ABSTRACT

Title of Dissertation:	EXPERIMENTAL ANALYSIS AND NUMERICAL MODELING OF IGNITION OF LIGNOCELLULOSIC BUILDING MATERIALS SUBJECTED TO GLOWING FIREBRAND PILES
	Jacques A. De Beer, Doctor of Philosophy, 2023
Dissertation directed by:	Professor Stanislav. I Stoliarov, Fire Protection Engineering

The prevalence and severity of Wildland-Urban Interface (WUI) fires is on the rise globally. Wildfires that spread into urban areas are known as WUI fires, with firebrand exposure a leading cause of structure losses during these WUI fire events. However, the complex ignition process of WUI building materials by glowing firebrand piles has not been fully resolved. The objective of this research was to develop a numerical ignition model capable of predicting the ignition probability of any horizontally-mounted flammable substrate when exposed to a pile of glowing firebrands. This development process was based on: extensive experimental data quantifying the mechanisms controlling the ignition process; a novel empirical firebrand pile heat flux model; and comprehensive pyrolysis models of three commonly-used lignocellulosic building materials.

Experiments were conducted in a bench-scale wind tunnel where a glowing firebrand pile of controlled geometry was deposited onto a horizontally-mounted substrate. Forced air flow velocities in the range of 0.9 – 2.7 m s^{-1} and two firebrand pile coverage densities (0.06 and 0.16 g cm^{-2}) were used, significantly expanding the range of conditions used in earlier laboratory-scale studies. The firebrand pile thermal exposure and burning intensity were quantified using time-resolved back surface temperature and combustion heat release rate data. Flammable substrate flaming ignition and extinction statistics, as well as burning intensity data, were also collected.

A custom inverse heat flux modeling technique, utilizing a solid-phase pyrolysis solver, ThermaKin, and infrared thermal imaging back surface temperature data, was employed to generate incident firebrand pile heat flux profiles directly underneath and in front of a glowing firebrand pile. The time-dependent firebrand pile heat flux behavior was captured using a three-step piecewise linear function. Further, a novel empirical firebrand pile heat flux model was developed, capable of generating time-dependent firebrand pile heat flux profiles over a range of forced air flows (0 – 4 m s^{-1}) and for all firebrand pile coverage densities and geometries.

A hierarchical modeling approach was used to develop a comprehensive pyrolysis model for each lignocellulosic substrate through inverse analysis of milligram- and gram-scale experimental data. All relevant kinetics, thermodynamics, and thermal transport properties of pyrolysis was parameterized.

Finally, a novel numerical ignition model used to predict the ignition probability of any flammable target substrate when exposed to a glowing firebrand pile under wind was

developed. A newly-defined dimensionless flame stability parameter was used as a material-independent criterion to characterize the ignition of a flammable substrate surface. The model captured the stochastic ignition behavior of flammable substrates by firebrand piles, as well as the reduced burning intensity of the piles deposited onto a flammable substrate surface. A logistic growth function was found to most accurately capture the ignition probability dependence on the dimensionless flame stability parameter and was, on average, capable of predicting the ignition probability within 14% of the experimental data. Further, using a critical dimensionless flame stability parameter, the absolute average difference between all experimental and predicted ignition timing and burning duration data was 11 and 26 s respectively.

EXPERIMENTAL ANALYSIS AND NUMERICAL MODELING OF IGNITION OF LIGNOCELLULOSIC BUILDING MATERIALS SUBJECTED TO GLOWING FIREBRAND PILES

by

Jacques Andre De Beer

Dissertation submitted to the Faculty of the Graduate School of the

University of Maryland, College Park, in partial fulfillment

of the requirements for the degree of

Doctor of Philosophy

2023

Advisory Committee:

Professor Stanislav I. Stoliarov, Chair
Professor Peter B. Sunderland
Professor Arnaud C. Trouve
Assistant Professor Shuna Ni
Professor James Baeder, Dean's Representative

Acknowledgments

First, I would like to thank both the De Beer and Kraus family for their unwavering support. Specifically, I would like to acknowledge the unwavering support and love from my partner, Alyssa. You have always been my number one supporter through the entirety of my graduate school career. I would like to thank my family in South Africa for all their encouragement and love during my time at Maryland. Through everything you were there to support me. I would like to specifically thank my late mother, Melinda, for everything she did for me. I would also like to thank the Kraus house for all their love and support. Mike, Lisa, Lindsay, and CJ, you are all amazing people that I am fortunate enough to call family.

Next, I would like to thank my advisor Dr Stanislav Stoliarov. Dr Stas, thank you for taking a chance on me when I joined the department 5 years ago. It has been an honor working with you. Your endless pursuit of knowledge and exceptional work ethic has made me push myself to the limit. I am a better researcher for this. Thank you for all the time you have invested in this project, this would not have been as much a success without your continued guidance and endless help. I look forward to implementing the knowledge you have passed on in my future career.

I would like to thank everyone in Stas's research group that I have had the pleasure of working with. I would like to specially acknowledge Joe Alascio, Emily Dietz, Alec

Lauterbach, and Sangkyu Lee. I would not have been able to complete this project within three years if it wasn't for all the help you provided. From spending countless hours in the lab, performing experiments, to wrapping our brains around GB's worth of data, thank you all! I would like to extend a special thank you to Josh, Yan, Isaac, Dushyant, Conor, Greg, Evan, Ahmed, Will, Lucas, Rebekah, Thomas, Bryce, and Ryan. You all know what you did, so thanks!

I would like to thank all of my committee members who have generously given their time to provide feedback and guidance in varying capacities during this doctoral research. My advisory committee consisted of: Dr Arnaud Trouve, Dr Peter Sunderland, Dr Shuna Ni, and Dr James Baeder. Thank you again for all the time you have set aside, it is greatly appreciated. I would also like to thank Dr Michael Gollner, Dr Alex Filkov, and Dr Gavin Horn for their valuable feedback which has inevitably strengthened the outcome of this research. I would also like acknowledge financial support from the U.S. National Institute of Standards and Technology (NIST) grant number 70NANB19H053 and the UL's Fire Safety Research Institute (FSRI).

Table of Contents

List of Figures

List of Tables

1 Introduction

1.1 Global wildfire problem

In recent years, the occurrence of large destructive, wildfire events has increased throughout the world. Countries like the United States of America (USA), Australia, Greece, Spain, Serbia, and Brazil are all experiencing wildfires seasons highlighted by a large number of structure losses, thousands of acres burned, and enormous suppression and evacuation costs. Wildfires that spread into urban areas are known as Wildland-Urban Interface (WUI) fires. Communities in the USA that are built within the WUI account for more than 43.4 million structures [1], with this number continuously increasing. In the USA, the number of wildfires (over the past 30 years) has remained relatively constant but the devastating effects of these wildfires including the acres burned and structures lost are on the rise. The National Interagency Coordination Center have estimated that wildfires inflict an estimated annual economic loss of approximately $ 78 billion in the USA [2].

The severity of a wildfire is typically quantified by the total number of acres burned but the number of structures destroyed during a wildfire is a metric that more accurately captures the socio-economic impact of a wildfire event. The California Department of Forestry and Fire Protection has indicated that the yearly structure loss rate in California is on the rise with more than 80% of all the documented structures losses over the past 30 years occurring within the last seven years spanning 2015 – 2021 [3]. The 2018 Camp Fire is one of the most destructive wildfires in USA history accounting for the loss of more than 18000 structures, 85 fatalities, and the evacuation of more than 50000 residents [4]. The Dixie Fire was one of the largest wildfires in the USA in 2021 resulting in the loss of more than 1300 structures [3]. In Australia, 3000 structures were lost during the 2019 – 2020 Black summer bushfires and required the evacuation of more than 60000 residents [5]. Globally, there is an immediate need to design structures in wildfire-prone communities that are more resilient to wildfires. In this work, the mechanisms responsible for the ignition of structural fuels during wildfire events will be elucidated and subsequently modeled. Mitigating the devastating impacts of wildfires within the WUI is crucial and therefore a proper understanding of these ignition mechanisms is required which will aid in the development of more accurate wildfire spread simulations.

1.2 Literature review

1.3 Main exposure pathways

Three main exposure pathways have been identified by which wildfires spread into and within the WUI: direct flame impingement, radiative exposure, and firebrand attack [6-9]. Radiation and direct flame impingement both involve heat transfer from the flame. In the case of flame impingement, direct flame contact with the flammable substrate is require for ignition [10]. For radiation, ignition can occur at a distance greater than the distant to which flames can extend. Ignition of flammable materials by firebrands typically occurs ahead of the fire front at a distance where ignition by radiation and direct flame impingement is not possible [6].

1.3.1 Firebrand exposure hazard

Post-fire studies indicate that firebrand exposure has contributed to the rapid spread of many wildfires and is often responsible for a large fraction of structure losses in the WUI [5], [11–14]. Firebrands are hot embers (on the order of millimeters to centimeters in size) that are liberated from the combustion of vegetation or burning structural components and have the potential to ignite recipient fuels kilometers ahead of the fire front [12], [15], [16]. Babrauskas [17] notes that embers are hot, carbon-based particles which are identified as firebrands when airborne. Three distinct processes have been identified to describe the behavior of firebrands: generation, transport, and ignition of target fuels [7], [18].

1.3.2 Firebrand generation

The generation of firebrands has been extensively studied. Firebrands can be generated from the combustion of building materials such as wood shingles, framing timber, and fences [19–21] as well as vegetative fuels including needles, pinecones, tree bark and twigs [22–26]. A series of studies using Korean pine (4 m in height) and Douglas Fir (2.6 m and 5.2 m in height) trees were conducted to better understand what the typical shapes of firebrands are when generated [25], [27]. The experiments were conducted using individual trees (in the absence of any forced air flow) which were ignited and allowed to burn. The generated firebrands were collected in water pans, dried, and then weighed and measured. More than 1300 firebrands were collected and it was concluded that the shape of the majority of firebrand were cylindrical with nearly 80% of the firebrands having a mass less than 0.2 g. The surface area of an individual firebrand was also characterized with most of the firebrands having a surface area smaller than 1 cm^2. A Suzuki and Manzello [28] study characterized the shape and mass of firebrands generated during an urban fire in Japan. The mass and surface area of more than 60% of the firebrands collected was less than 0.1 g and 2 cm^2 respectively.

Adusumilli et al. [22] investigated the firebrand generation propensity of different trees and shrubs having different heights. In this study, 71 individual trees and shrubs were burned using two trees species and one shrub. The tree species were Douglas-fir and ponderosa pine and the shrub species was sagebrush. The number of firebrands generated for each of the experiments was calculated as the summation of char marks visually present on a piece of fire-resistant fabric. Char marks would form when firebrands, having surface temperatures in excess of 300 ºC, were deposited onto the fabric. It was concluded that sagebrush produced six times more firebrands per kg of fuel consumed compared to the two tree species. The number of firebrands generated during an experiment was also found to increase with tree height. Woycheese found that the shape of firebrands generated from the burning of structural fuels were typically disk-like [29]. Suzuki and Manzello [30] performed a review of literature on the generation of embers from structural and vegetative fuels. Some of the important findings from the review are: the majority of firebrands have surface area less than 25 mm^2, firebrand masses are typically between 0.1 – 1.0 g, larger firebrands were generated at increased air flow velocities, and the structural material or species type significantly affects the size and mass of the generated firebrands

1.3.2.1 Firebrand transport

Once the firebrands have been generated, they are transported away from the wildfire in a process that involves the firebrands being lofted into the atmosphere due to the formation of buoyant plumes generated in the vicinity of the wildfire. Various studies focused on the transport of firebrands have been conducted and include both experimental work [31–35] and numerical modeling [36–38]. Once the firebrands have been lofted into the plume, they can be deposited onto target fuels several kilometers from the wildfire front.

Upon deposition, the temperature of the firebrands is still sufficiently high and therefore contribute to the ignition of the flammable target fuels. Ignition of target fuels by firebrands has received limited attention due to the complex, stochastic ignition behavior associated with firebrands being deposited onto or within flammable substrates. Some of the factors that affect the ignition of flammable materials by firebrands are: the thermal properties of the target fuel, the transient decomposition behavior of the firebrands, the air flows in proximity to the target surface on which the firebrands are deposited as well as the heat transfer interactions between the firebrands and the flammable target fuel.

1.3.3 Target fuels at risk to firebrand attack

Recipient fuels that have been identified as being susceptible to ignition by firebrands include both porous vegetation like mulch beds and cellulosic insulation as well as non-porous structural fuels like decks, fences, and roof shingles. The ignition of structural fuels by firebrands was of interest for this study.

1.3.4 Large-scale firebrands studies on structural fuels

Quantifying the mechanisms by which firebrands ignite WUI structural fuels is an important step towards hardening communities and structures against the threat of wildfires and serve as a motivation for this study. McArthur and Lutton [39] conducted some of the first large-scale work on the ignition of structural materials by firebrands. The study was performed to investigate the ignition susceptibility of structural components when exposed to firebrands generated during bush fire events. Wood cribs of varying sizes (0.8 – 12.0 g) as well as combustible debris including leaves and twigs were used to study the ignition susceptibility of building components (in the absence of any forced air flow). It was concluded that fuel moisture content significantly hindered the ignitability of the structural materials. For structural materials with low moisture content (5%), less than 1 g of combustible fuel was required for ignition. As the moisture content of the structural material increased, ignition was more difficult with even the largest wood crib size (12 g) unable to ignite the structural materials being studied.

Dowling [40] evaluated the ignition of Australian timber bridges by firebrands. Wood cribs were used to generate firebrands which were deposited into the 10 mm gap between bridge members. Firebrand masses ranging from 7 – 35 g were used in this study. A 7 g firebrand pile placed between the gaps of adjacent timber decking boards was sufficient to initiate smoldering ignition of the bridge boards. Advanced aging of the timber also contributed to the increase ignition susceptibility of the boards. It is worth mentioning that the state, glowing or flaming, of the firebrands deposited onto the bridge members was not specified in this study.

Manzello et al. [41] studied how the ignition of plywood and oriented strand board (OSB) by glowing firebrands was affected by a change in crevice angle and forced air flow velocity (either 1.3 m s^{-1} or 2.4 m s^{-1} when measured near the surface of the substrate). No ignition events were observed when using individual firebrands. However, when piles of firebrands were used, ignition of the plywood and OSB boards was observed when being exposed to a forced air flow of 2.4 m s^{-1}. The ignition probability of the boards increased as the crevice angle between adjoining boards decreased from 135° to 60° and as the forced air flow increased. The surface temperature of an individual firebrand was also measured using a thermal imaging camera and it was noted that the global temperature of the firebrand (the temperature over the entire firebrand surface) increased as the air flow increased from 1.3 m s^{-1} to 2.4 m s^{-1}. The emissivity of the firebrand surface was determined to be approximately 0.6 and was validated against a thermocouple mounted to the surface of the firebrand. It was concluded that ignition of the flammable substrates occurred when a sufficient number of firebrands were deposited onto a specific substrate material type and exposed to a sufficiently high air flow velocity. The contact area between the firebrands and the substrate also affected the ignition probability of the flammable substrate.

Manzello and Suzuki [41], [42] conducted a large-scale study evaluating the ignition of three different decking materials (Redwood, Western Red Cedar, and Douglas-fir) when subject to continuous wind-driven glowing firebrand attack. The initial study used a single constant forced air flow velocity of 6 m s^{-1} (measured as the bulk flow velocity from the wind tunnel fans). The structural component of interest was a mock-up decking assembly (1.2 m × 1.2 m) attached to a reentrant corner. Firebrands were continuously deposited onto the assembly using the NIST-developed Continuous Feed Firebrand Generator. Flaming ignition was documented for all three wood types. The ignition time and the mass of firebrands required for ignition of the target fuels increased with increasing material density. The average ignition times for Redwood, Western Red Cedar, and Douglas-fir were 756 s, 437 s, and 934 s respectively. The ignition time was defined as the time after which the first firebrand landed on the surface of the decking material. The second study was performed to evaluate how changing the bulk forced air flow velocity (6 m s^{-1} and 8 m s^{-1}) affected the ignition propensity of the same three decking materials. It was concluded that increasing the bulk airflow from 6 m s^{-1} to 8 m s^{-1} drastically decreased the mass of firebrands required for flaming ignition. At a 6 m s^{-1} bulk airflow velocity, 85 g – 278 g of accumulated firebrands (on the decking material surface) were required for flaming ignition. The mass of firebrands required for flaming ignition decreased to 7.5 – 24.1 g when using an 8 m s^{-1} bulk airflow velocity.

Suzuki et al. [43] investigated how the coupled effect of radiative heat flux and firebrand exposure affected the ignition susceptibility of a Douglas-fir decking assembly. The effect of air flow velocity was also evaluated. The decking assembly was continuously exposed to glowing firebrands. A quartz radiant panel (0.3 m × 0.3 m) was mounted 0.44 m above the assembly and was operated at a nominal incident heat flux of 8.5 kW m^{-2}. For the 6 m s^{-1} air flow tests, the number of firebrands required for ignition and time to ignition decreased when using the radiant panel. At the 8 m s^{-1} air flow, the significance of the radiant panel was negligible. It was suggested that the effect of air flow dominated the ignition susceptibility of the structural assembly at the elevated, 8 m s^{-1}, air flow velocity. Santamaria et al. [44] studied the ignition of redwood (by conduction) when exposed to piles of firebrands. In-depth temperature probes, located along the thickness of the material substrate were used track the transient heating of the substrate. It was concluded that 60 g of glowing firebrands (in the absence of any forced air flow) was required for ignition of a horizontally-mounted substrate.

All of these large-scale studies provide valuable information related to the ignition of structural components (and in most cases decking assemblies) by firebrand exposure. The key conclusions from these large-scale firebrand studies include: the ignition probability of solid fuels increased as the forced air flow and firebrand pile size increased; the solid target fuel ignition probability decreased as the moisture content of the fuel and the material density was increased. However, to be able to predict the ignition behavior of a material substrate when exposed to firebrands, a more detailed analysis of the heat transfer mechanisms between firebrands and the flammable substrate are required. An important parameter that is used to quantify the thermal exposure from the pile is the temperature and hence the heat flux insult from the firebrand pile impinging onto the material substrate.

1.3.5 Lab-scale firebrand pile thermal exposure studies

Hakes et al. [45] performed one of the first studies to investigate the transient heat fluxes from laboratory-fabricated firebrand piles onto a target substrate surface. Heat flux measurements were conducted using either a 1.27 cm OD water-cooled heat flux gauge or an array of thin-skin calorimeters that were positioned underneath the firebrand pile. The study investigated how the measured heat flux would be affected by a change in firebrand diameter (ranging from 6.35 mm to 12.75 mm), the presence of a forced air flow (1.83 m s^{-1}), and the firebrand pile size (ranging from 2.7 g to 9.6 g). The heat flux from individual firebrands were higher for larger firebrand diameters and was attributed to a larger thermal contact area between the firebrand and the face of the heat flux gauge. For firebrand piles, there was negligible dependence between the diameter of the firebrands and the measured heat flux. It was observed that the heat flux of the firebrand piles increased with increasing firebrand pile mass and air flow. Reradiation between firebrands and reduced convective cooling was postulated to dominate the heat flux dependence observed for different pile sizes. The peak heat flux of the 5.2 and 9.6 g firebrand piles was noted to increase by approximately 10 to 15 kW m^{-2} when increasing the airflow from 0 m s^{-1} to 1.84 m s^{-1}. The average peak heat flux for a known firebrand pile size and forced air flow was calculated as the average of all peak heat flux values from all repeat tests. The average peak heat fluxes for all firebrand pile sizes and air flow velocities were in the range of 15 kW m^{-2} to 25 kW m^{-2}. The ignition of OSB, when exposed to the studied range of firebrand pile masses and air flows was also investigated. No ignitions occurred at ambient airflows (0 m s^{-1}) but at an air flow of 1.84 m s^{-1}, flaming ignition of the OSB surface was observed.

Tao et al. [46] performed similar experiments to that of Hakes et al. [45] to characterize the thermal exposure from firebrands having different geometries and material compositions when exposed to a range of constant air flow conditions (0.5 – 1.4 m s^{-1}). Artificial cylindrical birch wood dowels as well as eucalyptus sticks and pine bark flakes were used to produce firebrands. It was noted that the peak heat flux of the smaller (more porous) firebrand piles increased with air flow. The continuous heat flux increase with air flow was observed when using smaller fluted dowels (diameter and length equal to 6.35 and 25.4 mm respectively). It was suggested that for more porous firebrand piles, increasing the airflow increased the convective heat losses from the pile but also allowed more oxygen to penetrate into the pile thereby increasing the pile oxidation rate. When using larger firebrands, the firebrand pile heat flux increased with airflow but was noted to decrease at elevated airflows. The decreased heat flux was attributed to convective cooling of the individual firebrands. It was hypothesized that a larger firebrand surface area being exposed to the incoming air flow resulted in increasing convective cooling of the brands. The peak average heat fluxes for all firebrands pile in this study were in the range of 8 kW m^{-2} to 45 kW m^{-2}.

Salehizadeh et al. [47] extended the work of Hakes et al. [45], characterizing the ignition of plywood, OSB, and cedar shingles when exposed to firebrand piles under wind. The firebrand pile heat fluxes from different pile masses when exposed to various air flow velocities (0.5 m s^{-1} to 2.0 m s^{-1}) was also quantified. Firebrand piles masses of 4 g, 8 g, and 16 g were used. The firebrand pile heat fluxes continuously increased as the air flow velocity was increased. The peak heat flux of an 8 g firebrand pile increased from approximately 12 to 37 kW m^{-2} as the airflow was increased from 0.5 to 2.0 m s^{-1}. Increased firebrand temperatures correlated with shorter target fuel ignition times and an increased ignition susceptibility.

Richter et al. [48] investigated the ignition propensity of three wood substrates in different crevice geometries when exposed to firebrand piles and different constant forced air flow velocities (0.5 m s^{-1} to 1.4 m s^{-1}). The crevice geometries included a crevice aligned with the direction of the flow (0º), a geometry perpendicular to the air flow (90º) and two intermittent angles with respect to the direction of the air flow (30º and 60º). Heat flux measurements were performed using a Schmidt-Boelter water-cooled heat flux gauge positioned in the center of the crevice with the face of the gauge mounted flush with the surface of the substrate. It was concluded that the ignition propensity of all three wood substrates increased with air flow as well as when changing from a flat (no crevice) to a crevice geometry. The peak-average firebrand heat fluxes increased from approximately 15 kW m^{-2} to 40 kW m^{-2} as the crevice configuration was rotated from 90º to 0º (for all air flow) and was attributed to increased reradiation between firebrands within the crevices and decreased convective losses along the perimeter of the pile.

Bearinger et al. [49], [50] investigated the transient heat flux distributions from individual firebrands of different geometries deposited onto a horizontal substrate using infrared thermal imaging and an inverse heat transfer analysis technique. The firebrand heat flux dependence on air flow velocity as well as firebrand orientation and substrate contact area was evaluated. A 0.8 mm thick stainless steel plate was used as a non-combustible material surrogate with both sides of the plate coated with high-emissivity (ε=0.97) Rust-Oleum paint. In the absence of a forced air flow, the peak-average heat fluxes for all firebrand geometries were approximately 30 kW m^{-2}. The highest heat fluxes, measured directly underneath the pile, were recorded for firebrands that had maximum contact with the steel plate. The firebrand peak-average heat fluxes increased (up to 85 kW m^{-2}) as the air flow was increased from 0.5 m s^{-1} to 2.0 m s^{-1}. The measured heat fluxes, for an individual firebrand exposed to a forced air flow, was higher at the air-flow facing edge of the firebrand due to increased oxidation of the firebrand.

1.3.6 Previous firebrand ignition modeling studies

Quantifying the thermal exposure conditions from firebrand piles is a key step towards developing models that can be used to accurately predict the ignition of firebrand-exposed target substrates. These models would then enable more accurate ignition predictions during actual wildfire events.

Various studies have been conducted in an effort to simulate the ignition behavior of target fuels when exposed to firebrands. One of the main challenges thought to hinder the accurate prediction of the ignition of fuels by glowing firebrands is the complex burning process describing the transition between smoldering and flaming combustion [18]. Santoso et al. [51] defines the transition from smoldering to flaming combustion as a rapid homogenous gas-phase ignition process that occurs after smoldering of the fuel. During smoldering combustion, the fuel is rapidly oxidized and in the presence of sufficient oxygen supply, a combustible mixture is formed. If the temperature of the combustible mixture is adequate, flaming ignition of the mixture occurs. Stoliarov et al. [52] studied the smoldering-to-flaming transition of polyurethane foams and defined the transition as the formation of a pyrolysis fuel zone adjacent to the smoldering region. In the pyrolysis zone, gaseous fuel is being produced and the production of said fuel is sustained by oxidation reactions occurring in the smoldering region. It was speculated that the smoldering region provides the heat required to sustain the anaerobic pyrolysis of the fuel as well as to ignite the pyrolyzate-oxidizer mixture. The oxidizer in these experiments was fresh air drawn upward along the length of a thermally decomposing foam sample.

1.3.6.1 Porous fuel bed ignition modeling studies

A majority of the ignition models have been developed for porous vegetative fuels citing the danger of mulching materials and roof attic insulation as materials susceptible to ignition by firebrands. For ignition of porous fuels by firebrands, the hot spot ignition theory is often used as a reasonable approximation of the particle size and temperature required for the ignition of a fuel [53] and typically ignition by an individual particle is studied. However, the hot spot theory does not account for the transient decomposition behavior of firebrands generated in real wildfires.

Warey et al. [54] developed an empirical model for the ignition of a pine needle fuel bed by an individual idealized firebrand. The ignition process of the fuel bed was attributed to the heat transfer from the firebrand and the heat required for ignition. The change in the shape of the firebrand as well as the fuel bed was assumed negligible. A linear correlation between the moisture content and ignition time of the fuel bed was presented. Wang et al. [55] modeled the ignition propensity of pine needle fuel beds when exposed to an individual hot steel particle and the effects of fuel bed moisture content and air flow velocity were investigated. The particle temperature required for ignition was found to increase with fuel bed moisture content and decrease with particle size. An empirical correlation for the ignition temperature of the fuel bed was presented and including the effect of moisture content and hot particle diameter.

Wessies et al. [56] is one of the few studies that has quantified the ignition propensity of porous fuels beds when subject to multiple continuously-decomposing firebrands. The ignition propensity of seven different cellulosic insulation materials when exposed to firebrands was evaluated. A simple heat and mass transfer model was developed to predict the ignition of porous cellulosic fuel beds by firebrands and included the prediction of: the firebrand temperature evolution, the fuel bed temperature, and the pyrolyzate mass flux. A criterion for ignition was also incorporated into the model. It was concluded that the heat transfer model was capable of simulating the experimental firebrand temperature data within 8%, on average. Further, the simulated ignition timing and firebrand temperature dependence on air flow was qualitatively similar to the experimental data.

1.3.6.2 Solid wood ignition modeling efforts

The ignition process of solid wooden fuels by firebrands is very different to the ignition processes of porous fuel beds. Only a handful of studies [57], [58] have attempted to simulate the ignition of solid fuels when exposed to firebrands due to the complex nature of the combustion and ignition process of solid fuel-firebrands systems. Conduction and radiation have both been identified as heat transfer processes that contribute to the ignition of solid fuels by firebrands [59].

Matveinko et al. [57] studied the ignition of three commonly-used wooden structural materials (Plywood, OSB, and chipboard) by firebrands. Experimental data related to the ignition timing dependence on air flow velocity and the number of firebrands used was collected. A mathematical model capturing the heat transport from a firebrand(s) to the surface of a wood substrate and evaporation of water from the wood during heating was developed. The heating of a surface exposed to a single or group of firebrands was simulated using an isothermal heating source. The number of firebrands required for ignition of all three materials was noted to decrease as the air flow was increased from 2.0 m s^{-1} to 2.5 m s^{-1}. It was found that ignition would only occur if the temperature of a single firebrand exceeded 850 K when using the mathematical model to match the experimental ignition probability behavior of a substrate when exposed to a single firebrand. The transient decomposition behavior of the firebrands was not modeled and the ignition locations were not specified. The accuracy of the model in predicting the experimental ignition timing data was not provided.

1.4 Motivation and research plan

The ignition of lignocellulosic structural materials found in the WUI when exposed to firebrands is a complex process that has yet to be fully quantified. Furthermore, an ignition model that is capable of accurately predicting the complex ignition behavior of firebrand-exposed structural materials has, to date, not been developed. This research seeks to provide detailed insight into the mechanisms controlling the ignition of flammable substrates by firebrands that can be implemented into a novel numerical ignition model. Although studies have identified parameters that affect the ignition propensity of firebrand-exposed structural materials such as air flow velocity, firebrand pile size, moisture content, and material density, the available experimental data is limited. A majority of the current ignition probability data is qualitative and material specific. Previous studies have quantified the temperature and heat flux values of individual firebrands and firebrand piles but have not been directly connected to ignition location and ignition susceptibility of a material. There is a recognized need for a systematic research study that is able to quantify the ignition behavior of WUI structural materials when exposed to a pile of glowing firebrands. The present study seeks to determine: the mechanisms responsible for the ignition of flammable substrates by firebrands; develop a custom firebrand pile heat flux model that is applicable for a wide range of experimental testing conditions; and for the first time, to develop a numerical ignition model that will enable ignition probability predictions for any arbitrary substrate when exposed to a pile of glowing firebrands.

The specific goals of this research are broadly defined as follows:

1. Retrofit a bench-scale wind tunnel to generate back substrate temperature, combustion heat release rate, modified combustion efficiency data, as well as gaseous flame ignition and extinction statistics;
2. Conduct an extensive experimental study to identify the experimental parameters that control the ignition susceptibility of common lignocellulosic structural materials when exposed to a pile of glowing firebrands;
3. Develop a comprehensive pyrolysis model for a set of lignocellulosic materials by implementing a hierarchical inverse modeling approach;
4. Develop an empirical firebrand pile heat flux model that can be used to generate transient firebrand pile heat flux profiles for a range of forced air flow conditions and firebrand pile sizes;
5. Develop a novel numerical ignition model that will capture the complex, stochastic ignition behavior of solid fuels when exposed to piles of glowing firebrands. The numerical ignition model will be developing using the experimental ignition

statistics, the custom empirical firebrand pile heat flux model, and multiple comprehensive pyrolysis models obtained for lignocellulosic materials.

1.5 Dissertation proposal outline

The remainder of this dissertation is structured in the following manner. In Section 2, a detailed description of the wind tunnel apparatus used to perform firebrand pile exposure experiments is provided. The gas analyzer and thermal imaging camera calibration methodology as well as the firebrand pile generation procedure is described. A section is also dedicated to the description of the materials used in this study. Chapter 3 outlines the measurements diagnostics used in the bench-scale wind tunnel that are used to collect data related to the deposition of a piles of glowing firebrands onto a horizontally-mounted lignocellulosic substrates. Transient back surface temperature measurements using a thermal imaging camera technique were used to quantify the firebrand pile thermal exposure when deposited onto different substrate materials. The burning dynamics of the firebrands as well as the target fuels when exposed to glowing firebrands were quantified using transient gas analyzer measurements. The identification of different ignition events when exposing a pile of firebrand to flammable materials is also discussed.

In Sections 4 through 6, wind tunnel testing results are presented in which the burning behavior of two different lignocellulosic structural materials, when exposed to pile of firebrands, is compared. The structural materials evaluated in these wind tunnel experiments are Western Red Cedar (WRC) and OSB. In Chapter 4, the material burning dynamics and thermal exposure profiles at constant forced air flows and known firebrand pile sizes are explored. In Chapter 5, the ignition probability dependence on firebrand pile airflow-facing edge length is explored. This was done in an effort to elucidate the ignition probability dependence of a flammable substrates on the edge length of the firebrand pile facing the incoming air flow. The effect of changing the edge length is analyzed by comparing ignition statistics and burning dynamics of the two structural materials. The firebrand pile thermal exposure profiles from different edge length piles are also compared. In Chapter 6, ignition and thermal exposure data generated for intermittent air flow conditions are presented. During actual wildfire events, variable surface air flow conditions are typical. The presence of frequent gusts are used as one of the primary criterions when issuing a red flag warning prior to an actual wildfire and it is therefore important to understand the ignition probability dependence of flammable substrates when exposed to variable air flow conditions.

Section 7 provided a detailed description of the hierarchical inverse modeling approached used to develop a comprehensive pyrolysis model for WRC. The hierarchical modeling includes inverse analysis of both milligram scale and gram-scale experiments. The significance of oxidation at the surface of lignocellulosic target substrate prior to flaming ignition is also discussed. Section 8 provides all the details relevant to the development of a comprehensive pyrolysis model for pressure-treated wood (PTW).

The development of a new, custom inverse firebrand pile heat transfer modeling technique is introduced in Section 9. The inverse heat flux modeling technique incorporates a solid-phase pyrolysis solver, ThermaKin, which was used to determine transient firebrand pile heat flux profiles underneath and directly in front of a glowing firebrand pile. For the first time, a generalized empirical firebrand pile heat flux model was developed and captures the effect of both forced air flow velocity and firebrand pile size. The generalized firebrand pile heat flux model can be used to construct transient incident heat flux profiles from a pile of glowing firebrands to the surface of a horizontally-mounted substrate. The accuracy of the generalized heat flux model is also validated against experimental firebrand pile heat exposure data.

In Section 10, a novel numerical ignition model used to predict the ignition probability of any horizontally-mounted lignocellulosic structural materials when exposed to a pile of glowing firebrands is discussed. The ignition model is based on experimental ignition statistics, the custom firebrand pile heat flux model, and the comprehensive pyrolysis models developed for the three lignocellulosic structural materials. Further, the numerically-generated and experimental ignition timing and burning duration statistics were compared to determine whether the ignition model was capable of capturing the flaming combustion behavior of a flammable substrate when subject to a pile of glowing firebrands

2 Experimental Setup and Procedures

2.1 Wind tunnel apparatus and diagnostics

The bench-scale wind tunnel used in this study included three main sections as shown in Figure 2-1. A similar wind tunnel setup has been used by previous firebrand pile thermal exposure studies [45–47]. The three main sections include: a contraction cone, test section, and exhaust. The 3D printed contraction cone consisted of a 0.27 m × 0.26 m inlet reducing to a 0.10 m × 0.26 m outlet. A honeycomb inset at the inlet followed by several mesh screens were used to both straighten and laminarize the flow into the test section.

The test section, constructed of 7 mm thick aluminum, having length and height equal to 0.4 m and 0.1 m, included a custom-built sample holder, the horizontally-mounted material sample, two cut-outs lined with borosilicate glass, a thermal imaging setup, and a gold-coated reflective mirror. The sample holder was used to mount a sample material sample within the test section. Samples with a size up to 0.185 m × 0.185 m could be tested. The top face of the sample was mounted flush with the bottom interior wall of the test section. The firebrand pile was deposited in the center of the top surface of the sample. Tracks located along the bottom exterior wall of the test section was used to position the sample holder such that the sample was located in the center of the test section. The sample holder was designed to accommodate sample thicknesses up to 4 cm. The bottom face of the material sample was exposed which allowed for back surface temperature measurements using an infrared FLIR E95 thermal imaging camera. Optical access to the top surface of the sample (mounted within the test section) was gained through the two borosilicate glass cutouts and was used for the visual identification of ignition events. The ignition events were recorded using two DSLR cameras. A reflective mirror, positioned on top of the test section, was used to redirect the view of the DSLR camera used to record the top view of a sample and the pile of firebrands during an experiment. The interior walls of the test section were painted with a high temperature black paint to reduce reflection effects.

The exhaust section of the wind tunnel included a 0.152 m OD Terrabloom high temperature booster fan and a 72-orifice gas analyzer probe (OD equal to 9.5 mm) installed 0.23 m downstream of the booster fan. The booster fan was connected to a fan speed adjuster, which allowed control of the air flow velocity within the test section over a range of 0.5 – 2.9 m s^{-1}. The sampling probe was connected to a California Analytical Instruments (CAI) ZPA non-dispersive infrared analyzer and was used for CO_2 and CO volumetric concentration measurements.

The air flow velocity was verified before the start of each experiment using a calibrated Omega HHF-SD1 hot wire anemometer. The air flow measurement was recorded at the center of the test section, 0.03 m above the surface of the sample. The airflow uniformity analysis was conducted at room temperature in the absence of a firebrand pile. It was determined that, throughout the cross section of the test section, the air flow velocity was nearly perfectly uniform (± 6%). The reader is directed to Alascio et al. [60] for a detailed discussion of the flow uniformity analysis. It was concluded that a single point anemometer measurement could be used as an accurate representation of the bulk flow speed within the test section.

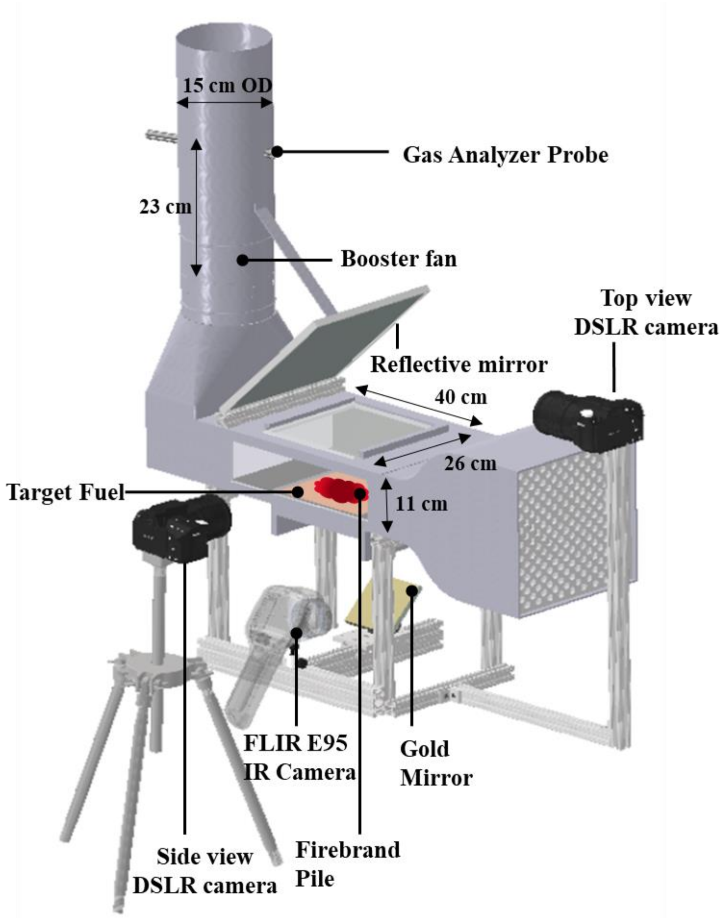

Figure 2-1. A schematic of the bench-scale wind tunnel setup used in this study (drawn to scale).

2.2 IR equipment and calibration

The thermal imaging system, installed on the bottom exterior of the wind tunnel, was used to measure the back surface of the material sample during a test as shown in Figure 2-2. The thermal imaging system included a FLIR E95 thermal imaging camera and a

0.1 x 0.1 m Edmund Optics square gold mirror with a surface flatness of $\lambda/10$. The FLIR E95 thermal imaging camera has an IR resolution of 464 x 348 pixels and was operated at 30 Hz measuring temperatures in the range of 0 - 650 °C. The gold mirror has an average reflectance of 0.96 within the 700 - 10 000 nm wavelength range. Due to geometric constraints imposed by the wind tunnel being positioned within a fume hood, the gold mirror was required to redirect the view of the thermal imaging camera. A support bracket was used to maintain a constant optical distance (0.4 m) between the thermal imaging camera and the back surface of the sample. The support bracket could be detached from the main wind tunnel frame and was used during calibration of the IR thermal imaging camera. The thermal imaging camera and the gold mirror were mounted to the support bracket using a panoramic ball head camera mount and a 45° optical mount respectively.

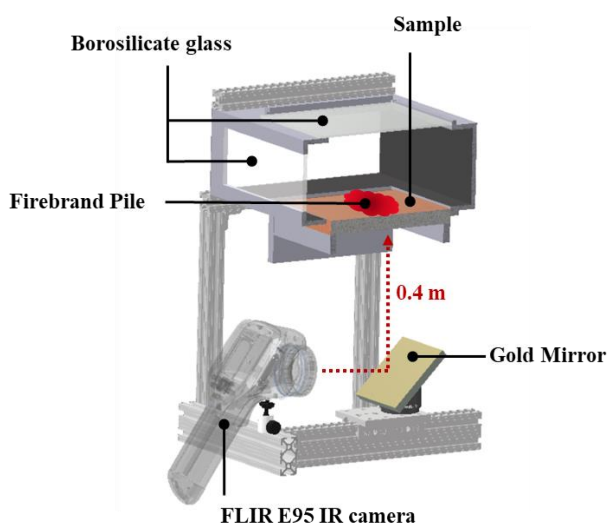

Figure 2-2. Exploded view of the thermal imaging system used for back surface temperature analysis.

A 80 cm^2 section of the back surface of each sample was painted with a MedTherm high-emissivity optical black coating (with a broadband emissivity of 0.94) to ensure accuracy of spatially resolved back surface temperature measurements for all wind tunnel experiments as shown in Figure 2-3.

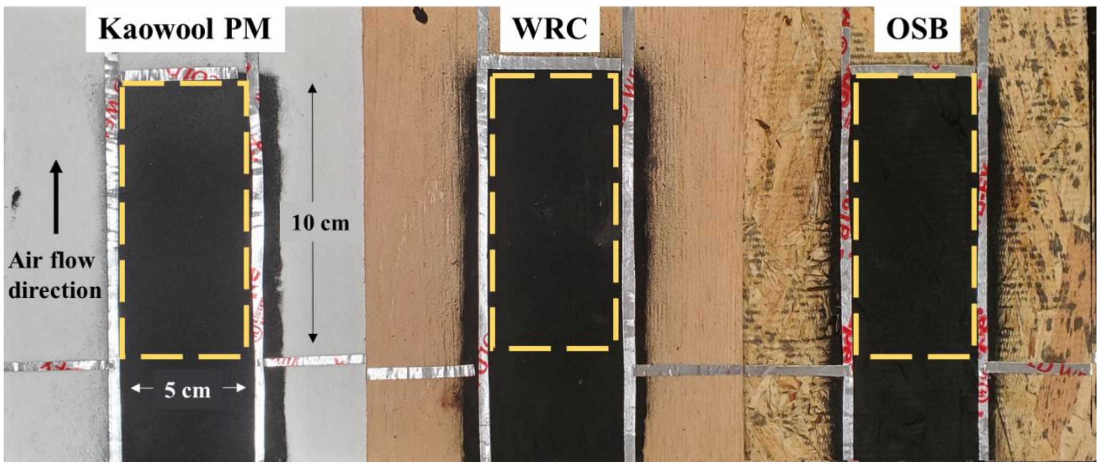

Figure 2-3. Representative examples of the back surface of a sample painted with the MedTherm optical black coating with a broadband emissivity of 0.94. The yellow dashed line boxes mark the region of firebrand deposition.

The emissivity of the optical black coating was validated against thermocouple temperature measurements obtained using a conical radiant heater. The conical radiant heater temperature was set to 890 ºC and corresponded to a nominal incident heat flux of 85 kW m^{-2} which was measured using a 9.53 mm OD NIST-calibrated water-cooled Schmidt-Boelter total heat flux gauge. The optical black coating was noted to remain affix to the bottom surface of the samples for the duration of the calibration experiments.

The thermal imaging system, which included the support bracket, was centered underneath the conical radiant heater. The top surface of the sample substrate was positioned 2 cm below the bottom lip of the conical heater. A 2.5 cm x 2.5 cm square section in the center of the back surface of the sample was painted with the MedTherm high-emissivity optical black coating. A 0.13 mm bead-diameter K-type thermocouple was positioned flush on the back surface of the sample and on top of the optical black coating. Proper contact between the thermocouple bead and the back surface of the sample was visually confirmed prior to the start of each calibration experiment.

The emissivity of the back surface of the target substrate, coated with the high emissivity optical black coating, was validated by matching the transient thermal imaging temperature profile with the transient thermocouple temperature profile. The surface emissivity (the optical black coating emissivity) of the bottom sample surface was iteratively changed until an adequate match between the IR and thermocouple data was obtained. An emissivity equal to 0.94 was found to adequately match the thermocouple data. The method of calibrating IR cameras by comparing IR temperature measurements to surface imbedded thermocouple measurements has also been successfully used in other studies [61], [62].

2.3 Gas analyzer equipment and validation

The gas analyzer system was used to measure the instantaneous volumetric concentration production rates of CO_2 and CO during an experiment. The gas analyzer system included: a stainless steel smooth-bore seamless sampling probe mounted within the exhaust outlet and aligned perpendicular to the direction of the air flow, and a CIA ZPA non-dispersive infrared gas analyzer. The gas analyzer probe contained two rows of 36, 1 mm OD, orifices each spaced 2 mm apart. A suction pump with an operating flowrate of 8 LMP, was used to transport the sampled effluent towards the gas analyzer. A soot filter was installed upstream of the suction pump and was used to remove any solid combustion residue. Two Drierite holders, downstream of the suction pump, were used to remove any excess moisture from the sampled effluent. 1.3 SLPM of sampled effluent was sent to the non-dipersive infrared gas analyzer with the remainder being purged to atmosphere. The gas analyzer was connected to a NI-9215 voltage input module for data generation and was operated at a frequency of 10 Hz.

The calibration of the gas analyzer was performed monthly using 12 mixture compositions spanning 0.01 – 0.2 vol.% CO_2 and 0.001 – 0.02 vol.% CO concentrations. High purity nitrogen and a known-composition calibration gas with 8 vol%. CO_2 and 0.8 vol%. CO were used to calibrate the gas analyzer. These concentration ranges were selected to correspond to those measured in preliminary firebrand deposition experiments. The performance of the gas sampling and measurement system was verified by introducing known amounts of CO_2 and CO directly into the test section and obtaining the concentration readings that were consistent with the introduced amounts at a range of set air flows. The calibration curve comparing CO_2 and CO concentration data to the corresponding voltage data is shown in Figure 2-4. It was observed that there was a 12 s gas measurement delay time between the gas analyzer probe (where gas is sampled) and the gas analyzer sensor.

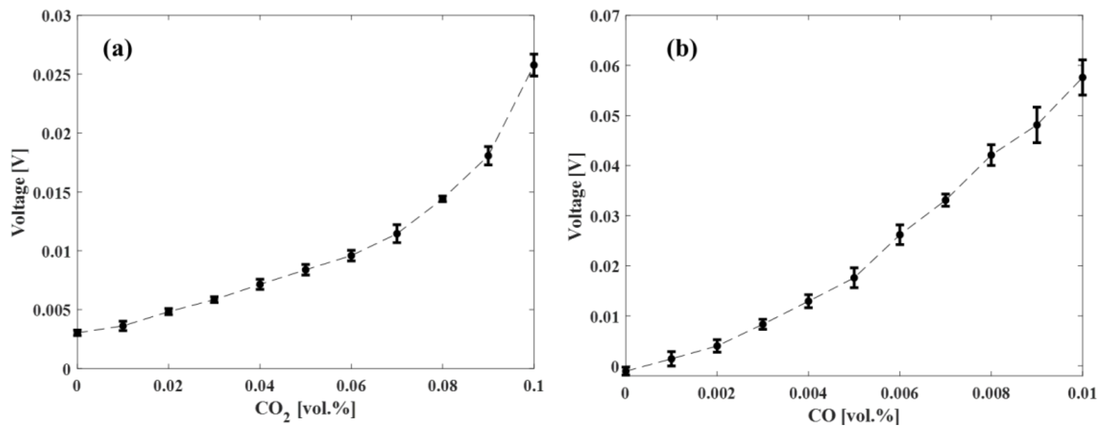

Figure 2-4. The gas analyzer calibration curves used to convert the voltage data output from the analyzer to the measured volumetric concentration (a) CO_2 and (b) CO measurements.

The gas sampling probe was installed one and a half exhaust diameters (23 cm) downstream of the booster fan with the orifices facing the direction of the flow. Adequate mixing of the combustion effluent, prior to reaching the gas analyzer probe, was validated using a methane Bunsen burner flame. The burner flame was positioned in the center and 3 cm above the bottom interior wall of the wind tunnel test section. The location of the burner outlet within the wind tunnel was representative of the location of the firebrand pile. A flowrate of 1.5 L min^{-1} of methane was used and the air flow velocity within the test section was set to 1.4 m s^{-1} prior to ignition of the methane flame. Air flows in excess of 1.4 m s^{-1} could not be tested as the flame would be blown out. The average steady volumetric production rate of CO_2 and CO from the methane flame were compared to the stiochomertically calculated volumetric production rates of complete combustion of methane. It was concluded that mixing of combustion effluent prior to reaching the sampling probe was sufficient as the difference between the experimental and measured CO_2 and CO volumetric concentrations were within 8% of one another.

2.4 Firebrand pile generation

All experiments were conducted using 6.35 mm outer diameter and 25.4 mm long oven-dried artificial birch wood cylindrical dowels to produce glowing firebrands with sizes representative of firebrands generated during actual wildfire events [20], [24–26]. The mass and projected area of a single birch wood dowel was 432 ± 20 mg and 1.61 ± 0.06 cm^2, respectively. The birch wood dowels were purchased from American Wood Crafters Supply and were dried in a convection oven, set at 102 ºC, for 24 hours. In this study, only firebrands that were in a glowing state were deposited onto the top surface of the material sample. Glowing firebrands were generated using a methodology similar to that used by Hakes et al. [45]. The glowing firebrands were prepared using a propane flame set to a flowrate of 1.8 SLPM. The dowels were placed in the center of a wire mesh basket and were pushed together to form a mounded pile which ensured even heating of all the dowels. The birch wood dowels were exposed to the propane flame for 40 seconds after which the propane flow was terminated (Figure 2-5 (a)). The firebrands were then left to transition to glowing firebrands (indicative of the absence of any visible flames) as shown in Figure 2-5 (b).

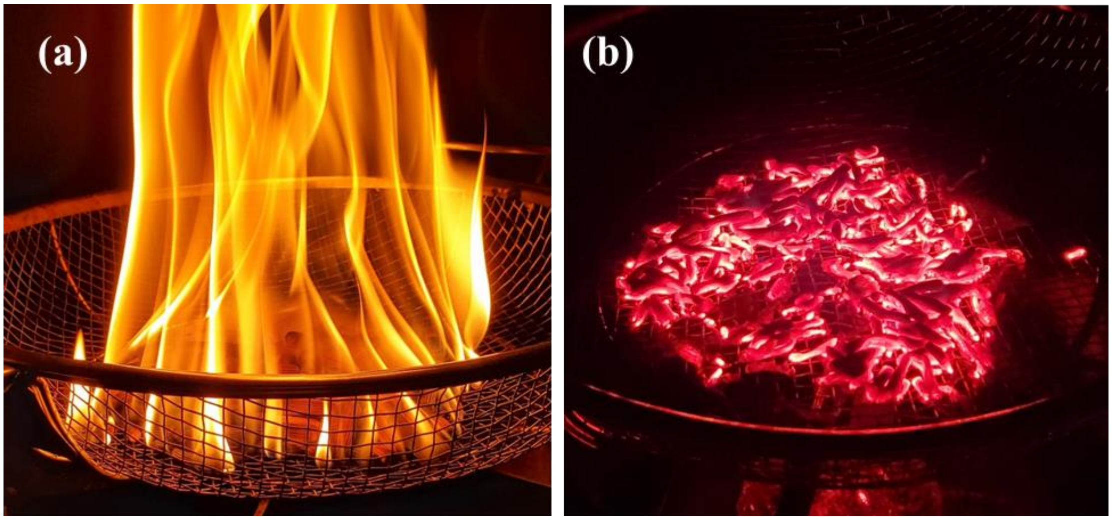

Figure 2-5. Glowing firebrand pile preparation technique. (a) State of the burning firebrands directly after switching the propane burner off, (b) state of the glowing firebrands prior to being deposited onto the target substrate within the wind tunnel.

The average mass and projected area for the glowing firebrands used in this study was calculated using the measurements of 15 individual firebrands. The firebrands that were used to calculate the average mass and projected area were placed in a water bath directly after being prepared. The firebrands were then removed from the water bath and dried in a convection oven for 24 hours before being weighed and measured. The mass of each firebrand was measured using a PN-2100A precision balance with an accuracy of 0.1 mg. The average mass and projected area of an individual firebrand were equal to 44.5 ± 10.8 mg and 0.63 ± 0.11 cm^2 respectively. The projected area of an individual firebrands was calculated as the product of its length and diameter. The firebrand mass and projected area uncertainty was determined using 15 individual firebrands and was calculated as the difference between the maximum and minimum value of each parameter.

The average mass and projected area of the firebrands used during this study are representative of firebrands generated during the burning of Douglas-fir trees and Korean pine. Suzuki [63] found that approximately 80% of all firebrands generated from the combustion of Douglas-fir and Korean pine had masses smaller than 0.1 g and project areas smaller than 3 cm^2. Suzuki et al. [64] studied the firebrand generation rates and sizes from burning Noble-fir trees under forced air flow conditions. It was concluded that even in the presence of a forced air flow, the mass and projected area of the majority of the firebrands collected were similar to the firebrands sizes noted when burning Douglas-fir and Korean pine in the absence of any forced air flow. It is worth noting that the heat fluxes from artificial firebrands have been found to be higher than the heat fluxes measured for wet and dry vegetative fuels [46], [50]. This suggests that firebrands generated from artificial dowels are a conservative surrogate for natural firebrands.

2.5 Wind tunnel air flow velocity validation

The air flow introduced into the wind tunnel test section was laminarized and straightened through a honeycomb mesh and a set of perforated plates that were installed within the reducer section of the wind tunnel. The flow profiles within the test section was characterized using an Omega HHF-SD1 hot wire anemometer having an operating range of 0.2 - 20 m s^{-1} and a sampling frequency of 1 Hz. A 12 cm x 12 cm area within the test section was used to measure the air flow at different heights and lengths within the test section of the wind tunnel. The 12 x 12 cm section included 25 different sampling points that were spaced 3 cm apart. At each of the sampling points, the air flow velocity was measured at five different heights, spaced 2 cm apart. The first height was located 1 cm above the top face of the substrate mounted within the test section. The air flow velocity at each sampling location and each height was time-averaged over a 30 second period. The air flow velocity within the tunnel was measured in the absence of a deposited firebrand pile. It was concluded that the air flow was uniform along the height of the wind tunnel. More details related to the characterization of the air flow can be found elsewhere [60].

Prior to the firebrand pile being deposited onto the horizontally-mounted substrate, the test section was open to atmosphere. The test section was only sealed once the firebrands were deposited. The time required for the air flow to stabilize once the test section had been sealed was evaluated. It was initially determined that in the absence of firebrands within the wind tunnel, the air flow being drawn into the wind tunnel stabilized within 10 seconds after sealing the test section with a piece of borosilicate glass. The fast stabilization time of the air flow velocity into the wind tunnel indicated that the firebrand pile burning dynamics could be calculated using a known, constant air flow velocity. The air flow stabilization time when firebrands were present within the wind tunnel was found to be equal to 13 s. It was concluded that the stabilization time when firebrands were deposited onto the substrate was not noticeable different from the stabilization time when no firebrands were deposited.

2.6 Target material selection and preparation

Four target materials were used in this study: a standard decking-thickness (2.1 cm) North Carolina Western Red Cedar (WRC) board, a 1.3 cm thick Georgia-Pacific Blue Ribbon PS2-10-compliant Oriented Strand Board (OSB) board, a 1.8 cm thick Pressure Treated Wood (PTW) board, and a 0.32 cm thick Kaowool PM ceramic fiber insulation board. Key thermophysical properties of these materials are summarized in Table 2-1. Kaowool PM was selected as a reference material for these experiments because of its inert, thermal-decomposition-resistant composition, and low thermal conductivity and low heat capacity that ensures minimal interference with the firebrand pile combustion process. At the same time, the Kaowool PM baords were sufficiently thin for the back surface temperature to approximately follow the temporal evolution of the heat flux from the firebrands to the target substrate surface. The characteristic conduction time of the Kaowool PM samples, estimated as the thickness squared divided by the thermal diffusivity taken at 350 °C, was found to be about 40 s.

WRC, OSB, and PTW are woods frequently used as structural materials. OSB is a dense engineered wood frequently used as a wall lining and roof covering material. WRC is a light weight, warp- and decay-resistant soft wood that is widely used in residential construction in the Western United States. PTW is an insect- and decay-resistant engineered wood that is frequently used in the built environment. WRC, OSB, and PTW have similar thermal properties but different densities and analyzing the ignition of these lignocellulosic materials by a pile of glowing firebrands provides information related to the ignition dependence of a flammable substrate on its density.

All lignocellulosic samples were conditioned in a desiccator maintained at room temperature (21 – 23 °C) and 20 – 25 % relative humidity for at least 48 hours prior to testing. Note that the WRC heat capacity and thermal conductivity listed in Table 2-1 were obtained for samples containing 15% moisture, all OSB and PTW thermal properties were obtained at 10% of moisture, while all thermal properties of Kaowool PM [65] corresponded to the dried samples. The mean density of each material was calculated in-house as the desiccated sample mass divided by its corresponding measured volume. The moisture content of each flammable material was calculated on a dry mass basis. The moisture content was calculated as the difference between the average desiccated and dry mass of each lignocellulosic material normalized by the average dry mass.

Table 2-1. Thermophysical properties of Kaowool PM, WRC, OSB and PTW

Material	Density ($kg\ m^{-3}$)	Heat Capacity ($J\ g^{-1}\ K^{-1}$)	Thermal Conductivity ($W\ m^{-1}\ K^{-1}$)	Moisture content (wt.%, dry basis)
Kaowool PM	232	1.07	$0.049 + 1.5 \times 10^{-5}\ T + 1 \times 10^{-7}\ T^2$ (T in °C)	0
WRC	394	1.7 (at 25 °C) [66]	0.11 (at 25 °C) [66]	4.6
OSB	664	1.6 (at 25 °C) [67]	0.12 (at 25 °C) [67]	7.0

PTW	527	1.21 (at 25 °C) [68]	0.12 (at 25 °C) [68]	7.0

The majority of the material samples were machined into 0.185 m × 0.145 m (in length and width) rectangles which ensured that the sample would fit within the sample holder. The remaining samples were machined into 0.185 m × 0.185 m squares. Aluminum tape was used to highlight the edges of the high-emissivity optical black coating applied to the materials' bottom surface. The aluminum tape would reflect light, highlighting the edges of the coated area. The highlighted edge included the 50 cm^2 firebrand pile deposition area as shown in Figure 2-3.

2.7 Testing condition combinations and test matrix

The experiments were performed at four different air flow velocities (0.9, 1.4, 2.4, and 2.7 m s^{-1}) and two different firebrand pile sizes. The air flow velocities used during this study were representative of air flow conditions at the surface of a horizontal structural material (like a decking slab) during actual wildfires and large-scale research studies [69]. The range of air flow velocities tested were also selected taking into account the maximum operational capability of the booster fan and noting that for air flows in the excess of 2.7 m s^{-1}, a large number of firebrands would be blown away from the initial deposition area hence compromising the expected firebrand pile coverage density. Previous bench-scale studies that have been conducted to quantify the thermal exposure from firebrand piles have used air flows up to 2.0 m s^{-1}. The firebrand pile thermal exposure at air flow velocities in excess of 2.0 m s^{-1} have yet to be quantified.

Two different firebrand pile sizes, shown in Figure 2-6, were used in the current study. These firebrand piles were characterized by a coverage density defined as the mass of deposited glowing firebrands at the start of an experiment per unit area of the surface they were deposited on. The unburned mass of artificial dowels required to generate the 0.06 and 0.16 g cm^{-2} glowing firebrand piles were 48 and 110 g respectively. The mass of firebrands generated for each of the firebrand pile coverage densities equated to 3 and 8 g respectively.

The smaller 0.06 g cm^{-2} firebrand pile coverage density corresponded to a single layer of firebrands on the surface and was approximately 0.7 cm in height. The larger, 0.16 g cm^{-2} firebrand pile corresponded to the maximum pile size that could be maintained on a flat horizontal surface at the maximum wind speed used in this study (2.7 m s^{-1}) and the pile height was approximately 2 cm. Hakes et al. [45] and Tao et al. [46] found that the firebrand pile heat fluxes started to plateau for firebrand piles masses in excess of 8 g. Therefore, the 0.16 g cm^{-2} firebrand pile was assumed as the firebrand pile coverage density where the maximum firebrand pile heat exposure would be observed. The firebrands were deposited onto a 5 cm × 10 cm area in the center of the substrate using a custom-built sheet metal funnel. In a majority of the experiments, the shorter dimension of the deposition area (5 cm) was perpendicular to the direction of the air flow introduced into the tunnel. Several additional experiments were performed for all materials with the longer dimension of the deposition area (10 cm) perpendicular to the direction of the incoming air flow. These additional tests were used to examine how changing the firebrand pile airflow-facing edge length impacted the ignition susceptibility of a flammable material. For all reported test results, the pile deposition area was maintained at 50 cm^2.

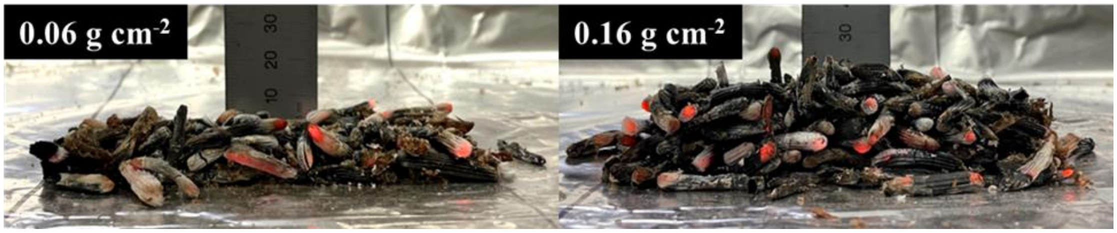

Figure 2-6. Height, in millimeters, of the two firebrand pile coverage densities positioned within the 50 cm^2 deposition area.

Three different types of experimental campaigns were investigated in this study using Kaowool PM, WRC, and OSB. The first experimental campaign (Campaign 1) included two different firebrand pile coverage densities and four constant continuous air flow velocities with the 5 cm firebrand pile length positioned perpendicular to the incoming air flow. For the second experimental campaign (Campaign 2), the firebrand pile edge length facing the air flow was doubled. The larger firebrand pile coverage (0.16 g cm^{-2}) density and a 2.4 m s^{-1} air flow velocity was used. In the third set of experiments (Campaign 3), an intermittent air flow (2.7 m s^{-1}) and a 0.16 g cm^{-2} firebrand pile coverage density was used. In Campaign 3, the 5 cm firebrand pile length was positioned to face the incoming air flow. Nine replicate tests were conducted for each testing condition combination and each material. The number of tests performed for each materials in each of the three experimental campaigns investigated in this study is summarized in Table 2-2.

In this dissertation, experimental data related Kaowool PM, WRC, and OSB being subjected to a pile of glowing firebrands are presented in detail. PTW experimental data was provided by Alec Lauterbach and was used during the development of a numerical ignition model (see Section 10).

Table 2-2: Number of tests performed for each testing condition combination during each experimental campaign.

Campaign number	Firebrand pile coverage density (g cm^{-2})	Test substrate	Air flow velocity (m s^{-1})			
			0.9	1.4	2.4	2.7
1	0.06	Kaowool PM	-	9	9	-
		WRC	-	9	9	-
		OSB	-	9	9	-
	0.16	Kaowool PM	9	9	9	9
		WRC	9	9	9	9
		OSB	-	9	9	9
2	0.16	Kaowool PM	-	-	9	-
		WRC	-	-	9	-
		OSB	-	-	9	-
3	0.16	Kaowool PM	-	-	-	9
		WRC	-	-	-	9
		OSB	-	-	-	9

2.8 Testing procedure

Each of the experiments for this study were performed in the bench-scale wind tunnel following the same procedure. Before the beginning of each experiment, a pre-determined mass of oven-dried birch wood cylindrical dowels were placed into a mesh-wire basket and the material sample was mounted within the test section of the wind tunnel. The air flow velocity within the tunnel was set by measuring the air flow at the center of the test section, 3 cm above the surface of the sample, using a calibrated hot-wire anemometer. The dowel pile, located within the wire-mesh basket, was then exposed to a propane burner flame and at the same time, the gas analyzer data logging system was initiated.

After 40 seconds, the propane flow was terminated and the burning dowels were left to transition to glowing firebrands. The video recordings of both DSLR cameras and the thermal imaging camera were initiated 110 seconds and 130 seconds after the dowels were initially exposed to the propane flame respectively. Once the dowels had all transitioned to glowing firebrands, they were deposited onto the top surface of the material sample using a custom built sheet-metal funnel. The bottom outlet area of the funnel was equal to firebrand pile deposition area (50 cm^2) and was placed in the center of the sample. The placement of the funnel ensured that the deposition of glowing firebrands onto the top surface of the sample was repeatable. The deposition area corresponded to the area of the back surface of the sample that was painted with the high-emissivity optical black coating. The funnel was then lifted out of the tunnel and a piece of 18 x 18 cm borosilicate glass was used to seal the top of the tunnel. This time corresponding to the test section being sealed with the borosilicate glass was selected as the start of an experiment for analysis purposes. The experiment was then left to proceed until all firebrands were consumed or the structural integrity of the sample was compromised.

3 Post-processing of Measurements and Video Recordings

3.1 Target material thermal imaging

The back surface temperatures of Kaowool PM, WRC, and OSB were recorded as a series of time-stamped two-dimensional temperature maps, which are, effectively, thermal imprints of the firebrand pile onto the target substrate. It was determined that, in all experiments, these back surface temperature maps significantly evolved in time with the hottest zone gradually shifting from the front of the pile facing the incoming air flow toward the tail end of the pile. This traveling behavior was also noted in earlier firebrand pile studies [47], [49]. To capture this temperature evolution, the back surface of the sample was divided into three zones, as shown in Figure 3-1. All zones were either 4 cm or 8 cm in width (the dimension perpendicular to the direction of the air flow) depending on whether a firebrand pile with an air flow facing edge length of 5 cm or 10 cm was used. The preleading zone (zone 1 in Figure 3-1) was located in front of the air flow facing edge of the pile and was 1.5 cm long. It extended 1 cm outside of the firebrand deposition area. The leading and middle zones (zones 2 and 3 in Figure 3-1) were 3 cm in length and were located directly underneath the firebrand pile.

The locations of these zones were selected to approximately match locations of ignition events, whose detection is discussed in Section 3.3. Previous firebrand pile thermal analysis studies measured the heat flux underneath a pile of firebrands and found that the location of the highest firebrand pile thermal exposure corresponds to the air flow-facing edge of the firebrand pile [50].

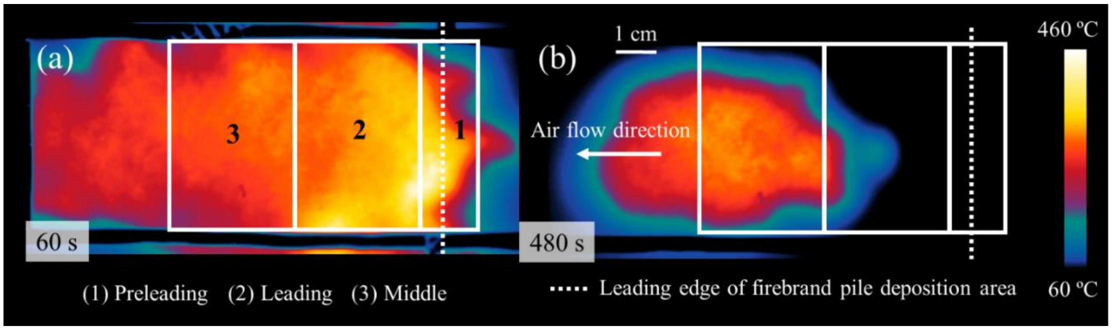

Figure 3-1. Back surface temperature maps obtained for a 0.16 g cm^{-2} firebrand pile deposited onto Kaowool PM and exposed to 2.4 m s^{-1} air flow at (a) 60 s and (b) 480 s after the start of the test.

The mean back surface temperature and the spatial temperature variation were computed by selecting 30 spots for the leading and middle zones and 24 spots for the preleading zone. Each spot contained nine pixels, which represents nine individual temperature measurements. The spot measurements were distributed approximately uniformly and randomly across one zone. No preference was given to hotter or colder regions within each zone. The exact locations of the spot measurements within a particular measurement zone differed between tests but the locations of the temperature measurement zones were the same. Using 30 or 24 spot measurements in each zone was determined to correctly capture both the mean zone back surface temperature and its spatial variation.

The data from nine repeated tests performed on the same target substrate under the same conditions were processed together to compute a single time-resolved mean temperature and time-resolved temperature variation for each zone. The spatial temperature variation was computed as two standard deviations rather than two standard deviations of the mean in an effort to more accurately capture the stochastic nature of the firebrand pile deposition process as well as the fact that a firebrand pile is a highly non-uniform heat source.

3.2 Species measurement and heat release rate calculations

Time-resolved CO_2 and CO volumetric fraction, $\phi^e_{CO_2}$ and ϕ^e_{CO}, profiles from individual tests were smoothed using a third order Savitsky-Golay filter with a frame length of 31 points, which corresponds to 3 s. The smoothed profiles were converted to mass production rates of CO_2 and CO, $\dot{m}^e_{CO_2}$ and $\dot{m}^e_{CO}$, expressed in g s^{-1} using the following expressions:

$$\dot{m}^e_{CO_2} = \rho_{CO_2}\dot{V}\left(\phi^e_{CO_2} - \phi^a_{CO_2}\right) \tag{3.1}$$

$$\dot{m}^e_{CO} = \rho_{CO}\dot{V}(\phi^e_{CO} - \phi^a_{CO}) \tag{3.2}$$

The mass densities of CO_2 and CO, ρ_{CO_2} and ρ_{CO}, were assumed to correspond to the standard conditions, 25 °C and 1 atm, and were equal 1.81 kg m^{-3} and 1.15 kg m^{-3}, respectively. $\dot{V}$ is the volumetric flowrate of air through the test section, which was computed as the product of the test section cross-sectional area (0.26 m × 0.1 m) and the set air flow velocity (m s^{-1}). $\phi^a_{CO_2}$ and ϕ^a_{CO} are the background or ambient volumetric fractions of CO_2 and CO obtained by averaging the concentration data collected during a 50 s time period preceding the deposition of firebrands. Carbon dioxide calorimetry [70], [71] was employed to compute the time-resolved combustion heat release rate, HRR, data expressed in kW m^{-2}:

$$HRR = \left(E_{CO_2}\dot{m}_{CO_2}^{e} + E_{CO}\dot{m}_{CO}^{e}\right)/A_{pile} \tag{3.3}$$

In this expression, E_{CO_2} and E_{CO} are the heats of combustion per unit mass of CO_2 and CO generated and are equal to 13.1 $\pm$ 1.5 and 11.1 $\pm$ 2 kJ g^{-1}, respectively; and A_{pile} is the firebrand deposition surface area in m^2. The firebrand pile deposition area was constant for all testing conditions combinations and was equal to the deposition area of the funnel (5×10^{-3} m^2). The *HRR* was normalized by the firebrand pile deposition area because preliminary experiments indicated that, for a firebrand pile of given coverage density, the HRR scales approximately linearly with A_{pile}.

In addition to HRR, the combustion dynamics observed in each test was characterized using the time-resolved modified combustion efficiency, MCE, data computed from the CO_2 and CO volumetric fractions:

$$\mathrm{MCE} = \frac{\left(\phi_{CO_2}^{e} - \phi_{CO_2}^{a}\right)}{\left(\phi_{CO_2}^{e} - \phi_{CO_2}^{a}\right) + \left(\phi_{CO}^{e} - \phi_{CO}^{a}\right)} \tag{3.4}$$

MCE is typically used to determine whether the combustion process occurs in the smoldering mode, which corresponds to an MCE = 0.65 – 0.80, or flaming combustion mode corresponding to an MCE > 0.90 [72]. The HRR and MCE temporal profiles were averaged for all tests performed on the same material under the same experimental conditions. The uncertainties in the time-resolved mean *HRR* and MCE values were computed from the scatter of the data as two standard deviations of the mean.

3.3 Visual ignition event identification

During a preliminary analysis of the video recordings collected in the wind tunnel experiments, two distinct types of ignition events were identified. The first ignition type corresponded to the formation of a faint, blue, unsteady flame on the top surface of the pile. The flame moved around and appeared and disappeared at short time intervals. A series of snapshots of this flame is shown in Figure 3-2. This ignition type was observed for all material substrates used and is referred to here as a firebrand pile ignition.

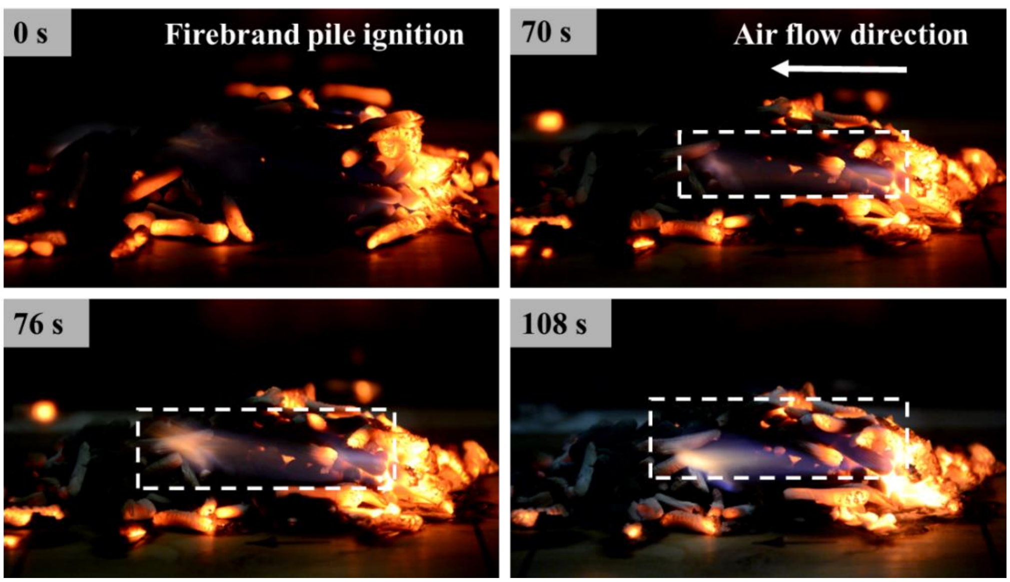

Figure 3-2. Time-stamped side-view images of a firebrand pile ignition observed at 0.16 g cm^{-2} firebrand pile coverage density and 2.4 m s^{-1} air flow velocity. The dashed-line rectangle indicates the location of the flame on top of the firebrand pile.

The second ignition type resulted in the formation of a relatively steady luminous diffusion flame attached to the surface of the substrate as shown in Figure 3-3. These ignition events were observed only in the flammable substrate experiments and, thus, are referred to as flammable surface ignitions.

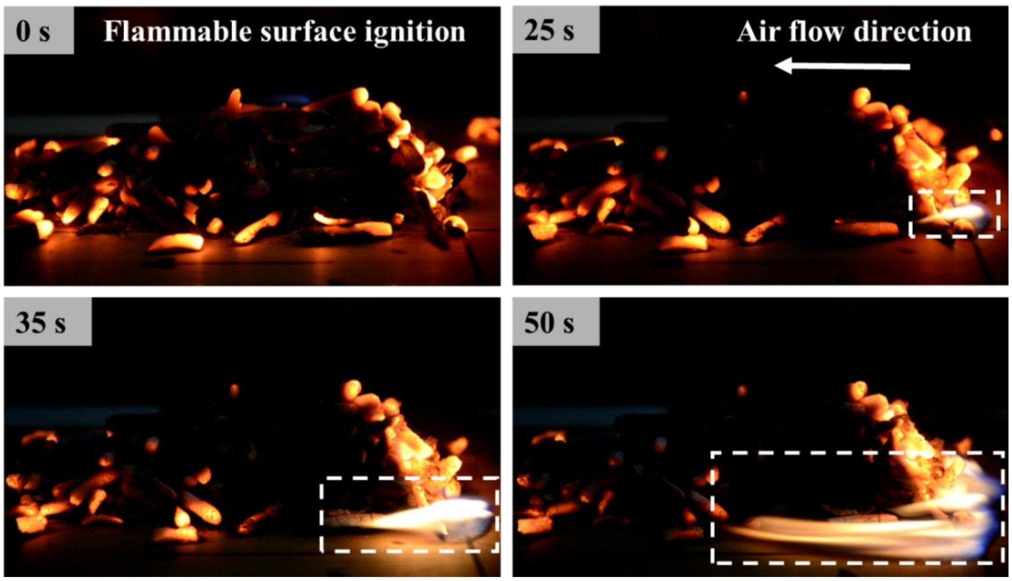

Figure 3-3. Time-stamped side-view images of a flammable substrate surface ignition observed at 0.16 g cm^{-2} firebrand pile coverage density and 2.4 m s^{-1} air flow velocity. The dashed-line rectangle indicates the location of the flame attached to the substrate surface.

The data on the location, time of ignition, and duration of burning were also collected, and corresponding mean values and uncertainties were computed. The uncertainties in the time of ignition and duration of burning were computed from the scatter of the data as two standard deviations of the mean.

4 Ignition and Combustion Dynamic Dependence on Firebrand Pile Coverage Density and Air Flow Velocity

Post-fire studies have found that when deposited onto non-porous structural elements, firebrands tends to accumulate in groups and can readily ignite recipient fuels. Both air flow velocity and firebrand pile size have been identified as parameters significantly affecting the ignition susceptibility of flammable recipient fuels by a pile of firebrands. The horizontal geometry that was considered for this study replicated structural configurations like decks and porched areas. The air flow velocities and firebrand pile covered densities used for this portion of the study are highlighted in Section 2.7. A 5 cm × 10 cm firebrand pile deposition area (with the 5 cm length perpendicular to the incoming air flow) was initially studied and the pile shape was representative of the elongated firebrand pile shapes that form on horizontal target substrates during large scale experiments [41], [42]. The firebrand pile deposition area used for all three substrate materials (WRC, OSB, and Kaowool PM) is highlighted in Figure 2-3. Kaowool PM (the reference, non-combustible substrate) was used to isolate the thermal exposure and burning dynamics of the firebrand pile. Firebrands were then deposited onto WRC and OSB (flammable substrates) to further elucidate the dependence of ignition susceptibility and burning behavior on material density.

4.1 Firebrand pile thermal exposure dependence on air flow velocity and firebrand pile coverage density

The Kaowool PM mean back surface temperature profiles obtained for all testing condition combinations within each temperature measurement zone using a glowing firebrand pile with an air flow facing edge length of 5 cm are shown in Figure 4-1. The temperatures start above ambient because of a 12 s delay between the initial deposition of the firebrand pile and sealing the wind tunnel test section, which corresponded to the formal test start time. Qualitatively, all these profiles exhibit the same trend consisting of a rapid increase followed by a gradual decrease in temperature. The rapid increase is likely to be associated with the increase in the rate of oxidation of the firebrand pile driven by an application of a forced air flow, which increases the supply of oxygen to the firebrand surfaces. The gradual decrease is probably due to the consumption of firebrands and formation of an ash layer on their surfaces, which acts as a mass transport barrier to oxygen and reduces the heat transfer from the firebrands to the material substrate.

It was also noted that the rate of temperature decrease in the middle zone was slower than the rate of temperature decrease in the preleading and leading measurement zone. The slower rate of temperature decrease in the middle zone can be attributed to the delayed consumption of firebrands in the middle zone as highlighted in Figure 3-1. After the peak back surface temperature is reached, the middle zone temperature holds steady for a prolonged period of time before decaying. The middle zone temperature plateau is potentially associated with reduced oxygen supply to the middle zone of the firebrand pile which results in a reduced firebrand pile consumption (oxidation) rate and an extended burning time.

Inverse modeling can be used to determine the incident heat flux from the firebrand pile to the target fuel using the mean back surface temperature profiles provided that the thermophysical properties of Kaowool PM are well defined [73]. This inverse heat transfer modeling technique is discussed in detail in Section 9 of this manuscript.

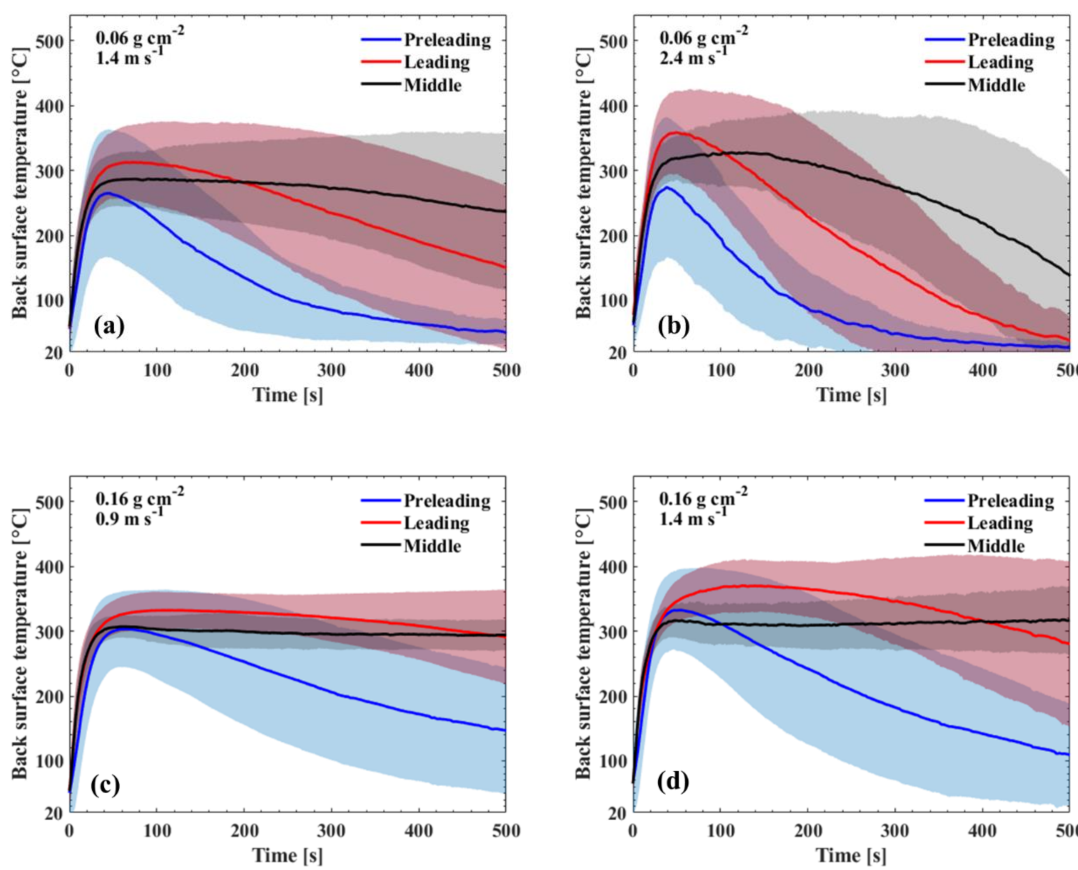

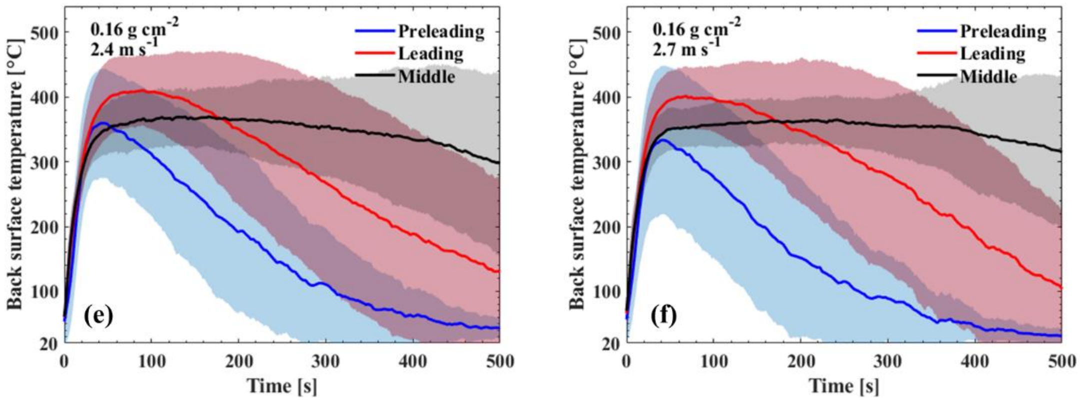

Figure 4-1. The mean Kaowool PM back surface temperature profiles obtained for a coverage density of 0.06 g cm^{-2} at an air flow velocity of (a) 1.4 m s^{-1} and (b) 2.4 m s^{-1} as well as a coverage density of 0.16 g cm^{-2} at an air flow velocity of (c) 0.9 m s^{-1}, (d) 1.4 m s^{-1}, (e) 2.4 m s^{-1}, and (f) 2.7 m s^{-1}. Firebrand piles with a 5 cm airflow-facing edge length were used. The shaded areas around the curves represent variations in these temperatures are expressed as two standard deviations.

In the current work, a peak-average back surface temperature was adopted as a quantitative measure of the intensity of the firebrand pile heat exposure to the target substrate. This peak-average back surface temperature was computed for each set of conditions by averaging the corresponding mean back surface temperature data over the period of 4 s that produced the maximum value of this average. These peak-average back surface temperature values computed for all zones and all testing conditions when depositing piles of firebrands onto Kaowool PM are summarized in Figure 4-2.

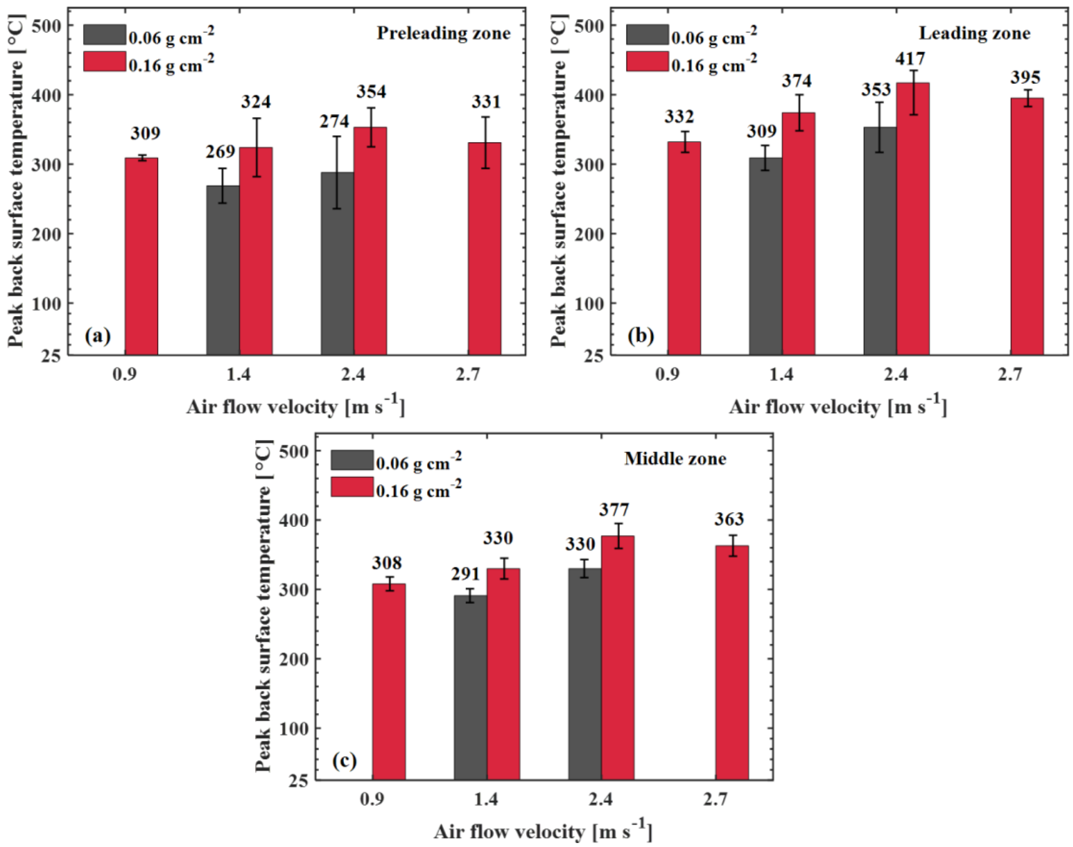

Figure 4-2. The peak-average Kaowool PM back surface temperature in the (a) preleading, (b) leading, and (c) middle zone under various testing conditions. Different bar colors correspond to different firebrand coverage densities. The error bars are calculated as two standard deviations. Firebrand piles with a 5 cm airflow-facing edge length were used.

The highest peak-average temperatures were observed in the leading zone, probably because it was fully covered by glowing firebrands that were exposed to the incoming air flow. The dependence of the peak-average back surface temperature on the air flow velocity exhibited the same qualitative trend in all zones. The peak-average back surface temperature increased as the air flow was increased up to 2.4 m s^{-1} and then gradually decreased upon further increase in the air flow. This trend can be explained by two competing effects: increasing the air flow increases the firebrand pile burning rate but also increases convective cooling of the firebrand pile. Increased convective cooling reduces the firebrand pile temperature and, consequently, heat flux to the target substrate. The data in Figure 4-2 also indicate that the peak-average back surface temperature systematically increased when increasing the firebrand pile coverage density. The peak-average back surface temperature increase with coverage density is indicative of increased heat transfer from the firebrand pile to the surface of the Kaowool PM board and is attributed to a larger number of firebrands being able to transfer heat to the surface of the Kaowool PM insulation board. The peak-average back surface temperature increase when increasing the firebrand pile coverage density was most significant in the preleading and leading zones.

4.2 Heating rate comparison for different flammable lignocellulosic substrate densities

The mean back surface temperature profiles with their corresponding spatial temperature variations obtained for all the studied conditions are shown in Figure 4-3 for WRC and Figure 4-4 for OSB. Firebrand piles with a 5 cm airflow-facing edge length were used. The peak-average back surface temperatures for WRC and OSB at each testing condition combination are significantly lower than the Kaowool PM peak-average back surface temperatures. The times to the peak back surface temperature for

WRC and OSB, after deposition of the firebrands, are significantly longer, primarily due to the fact that the WRC and OSB samples were at a minimum four times thicker than the 3.18 mm thick Kaowool PM insulation.

Qualitatively, all material substrate back surface temperatures profiles are similar. For WRC the initial temperature rise is associated with the deposition of glowing firebrands onto the substrate surface after which both the leading and preleading temperature profiles decay once the peak temperature has been reached. The decay is related to the decreasing burning intensity of the pile which results in the heat losses from the back surface of the substrate and in-depth lateral conduction dominating the heat transfer process. When a larger firebrand pile coverage density is deposited onto WRC, the middle zone back surface temperature profile was noted to increase even after a majority of the firebrands had been consumed. Delayed, in-depth smoldering of the flammable substrate was hypothesized to contribute to the observed back surface temperature rise in the middle zone after most of the firebrands were consumed.

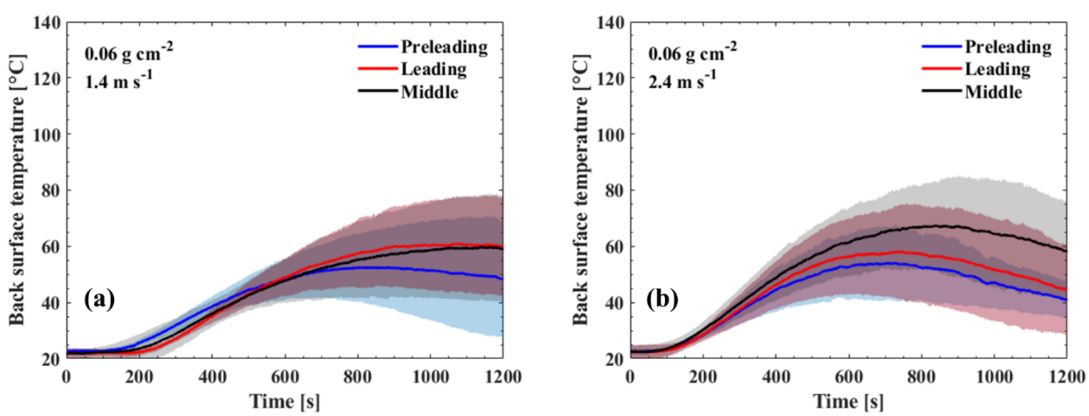

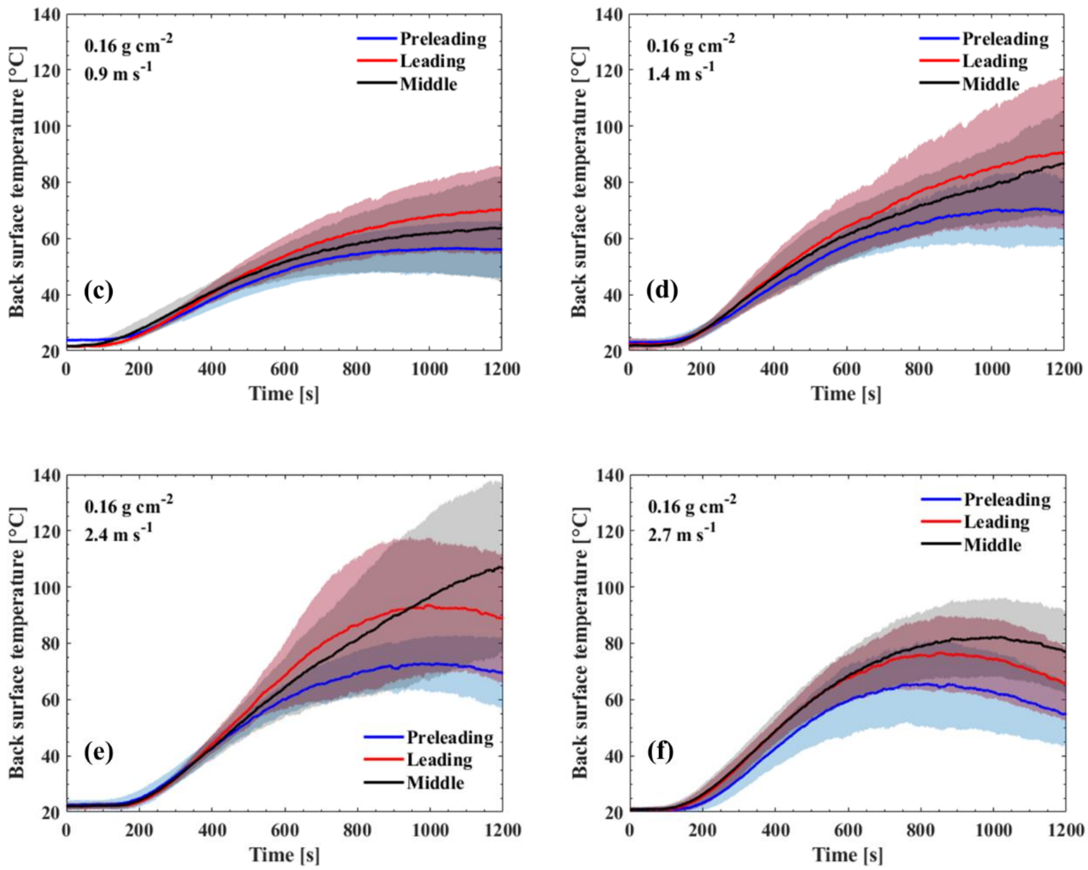

Figure 4-3. The mean WRC back surface temperature profiles obtained at a firebrand pile coverage density of 0.06 g cm^{-2} and an air flow of (a) 1.4 m s^{-1} and (b) 2.4 m s^{-1}. Temperature profiles at a 0.16 g cm^{-2} coverage density and an air flow velocity of (c) 0.9 m s^{-1}, (d) 1.4 m s^{-1}, (e) 2.4 m s^{-1}, and (f) 2.7 m s^{-1}. The shaded areas around the curves represent deviations in these temperatures expressed as two standard deviations.

The initial back surface temperature rise for OSB is also associated with the deposition of firebrands onto the surface of the substrate as shown in Figure 4-4. As the test progresses, the back surface temperature for all three measurement zones and for all testing conditions started to reach a plateau. However, unlike the WRC back surface temperatures decaying with time after reaching the peak temperature, all back surface temperature profiles (with the exception of the 0.06 g cm^{-2} firebrand coverage density exposed to a 1.4 m s^{-1} air flow velocity case) started to increase again. The secondary back surface temperature increase occurred approximately 400 s after the deposition of the firebrand pile and was hypothesized to be a result of in-depth oxidative smoldering that would continuously consume the OSB substrate. As a test progressed, the surface of the OSB smoldering front continually receded, moving towards the back surface of the OSB board and in some cases resulting in complete burn through of the board. The secondary temperature rise is therefore a result of the movement of the smoldering surface to the back surface of the OSB board.

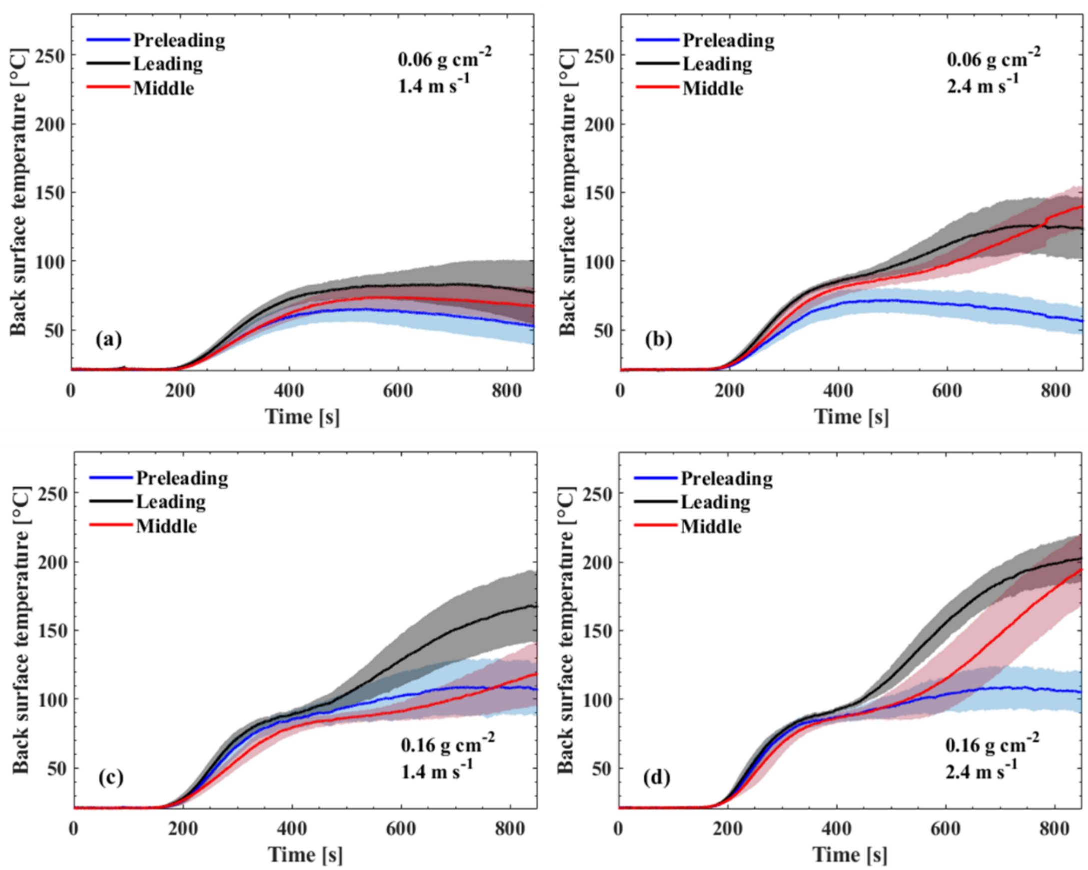

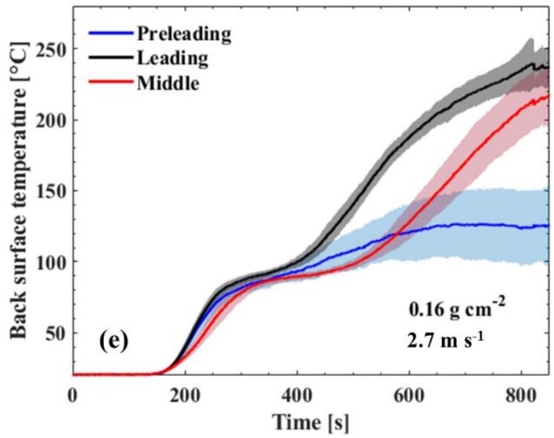

Figure 4-4. The mean OSB back surface temperature profiles obtained at a firebrand pile coverage density of 0.06 g cm^{-2} and an air flow of (a) 1.4 m s^{-1} and (b) 2.4 m s^{-1}. Temperature profiles at a 0.16 g cm^{-2} coverage density and an air flow velocity of (c) 1.4 m s^{-1}, (d) 2.4 m s^{-1}, and (e) 2.7 m s^{-1}. The shaded areas around the curves represent deviations in these temperatures expressed as two standard deviations.

Given that the WRC and OSB peak-average back surface temperatures were achieved after most of the firebrand pile was consumed, they no longer represent a good measure of the intensity of the firebrand pile heat exposure. Therefore, an average initial heating rate of the back WRC and OSB surface was used to quantify this intensity instead. The average heating rate was calculated over an 80 s time period starting at the time when the mean back surface temperature first exceeded 30 ºC. This particular time period was selected because for all WRC and OSB experiments during this period, the temperature rise was nearly perfectly linear. The results of the average heating rate calculations are summarized in Figure 4-5 for WRC and Figure 4-6 for OSB.

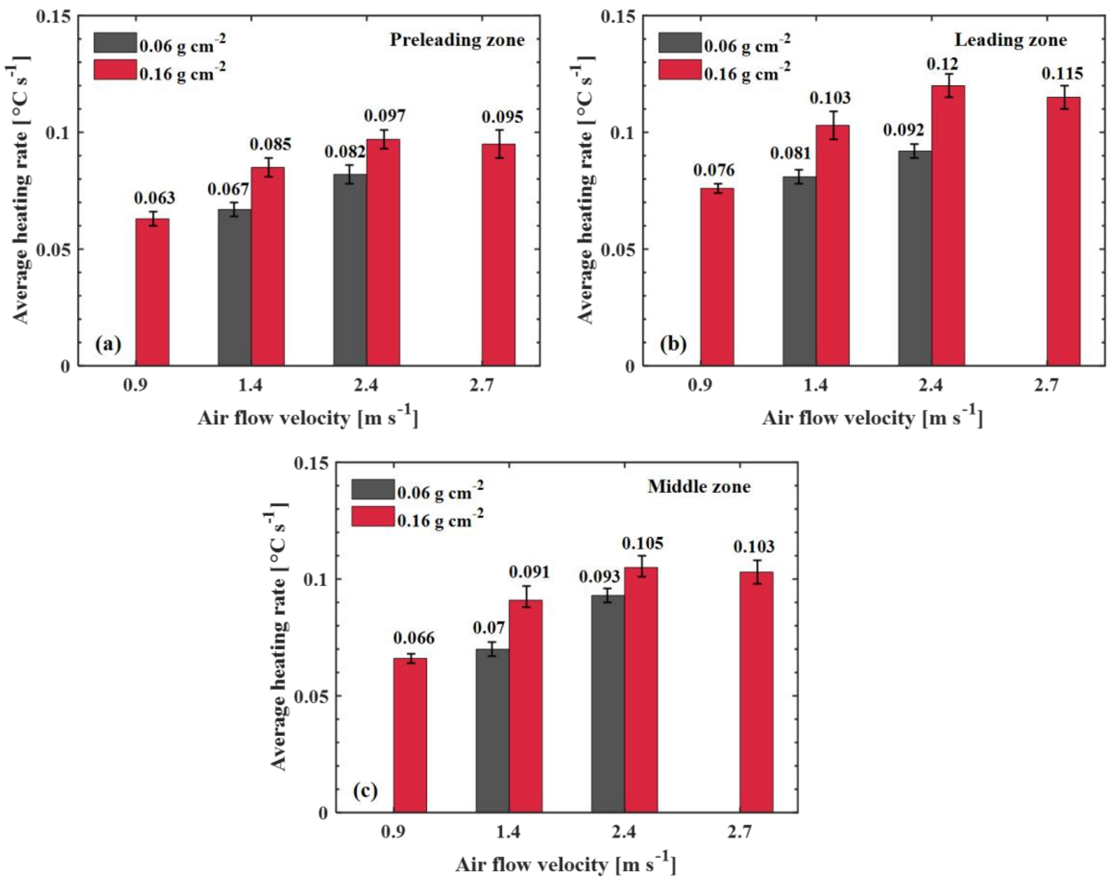

Figure 4-5. The average WRC heating rates in the (a) preleading, (b) leading, and (c) middle zone under various testing conditions. Different bar colors correspond to different firebrand coverage densities. The error bars are two standard deviations.

From Figure 4-5, the WRC heating rate data follow the same trends that were observed for the Kaowool PM peak-average back surface temperatures, which confirms that the same physical phenomena control the intensity of the firebrand heat exposure for both substrates. The WRC heating rate starts to gradually decrease as the air flow velocity exceeds 2.4 m s^{-1} highlighting the competition between the firebrand pile oxidation rate and the convective cooling of the pile. However, the OSB average heating rate data did not follow the same trends observed for the Kaowool PM peak-average back surface temperatures, continuously increasing as the forced air flow velocity was increased (as shown in Figure 4-6). No OSB tests were conducted at an air velocity of 0.9 m s^{-1}. This dissimilar dependency on air flow for the OSB heating rates when compared to the Kaowool PM peak-average back surface temperature data is hypothesized to be related to oxidation of the smoldering substrate surface exposed to the firebrand thermal insult. In the case of Kaowool PM and WRC, the main oxidation process is the oxidation of the firebrand pile. For OSB, the increased oxidation of the smoldering surface together with the oxidation of the firebrand pile could be related to the continual heating rate increase as the forced air flow velocity is increased.

It should also be noted that the difference in heating rate for OSB, for a known air flow, is more significant between the two firebrand pile loading sizes than for WRC. The difference in the heating rate of OSB when exposed to different firebrand pile loading sizes is most apparent in the preleading temperature measurement zone. The larger difference in heating rate is attributed to the thickness of the OSB board being smaller than WRC. Heat is more readily transferred from the top surface of the OSB board, on which the firebrands were deposited, to the bottom surface where thermal imaging measurements were performed during the time interval when the heating rate was calculated. For WRC, the rate of heat transfer between the top and bottom surface was slower thereby reducing the temporal accuracy of the back surface temperature measurements.

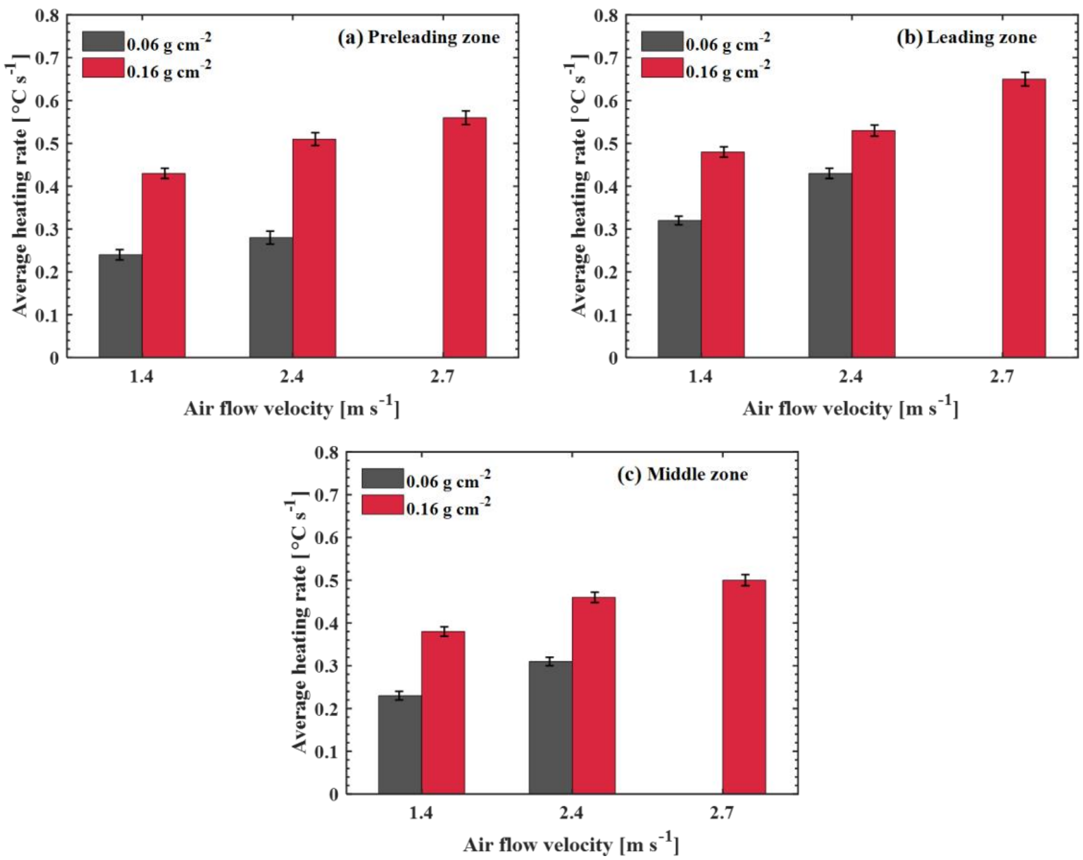

Figure 4-6. The average OSB heating rates in the (a) preleading, (b) leading, and (c) middle temperature measurement zone under various testing conditions. Different bar colors correspond to different firebrand coverage densities. The error bars are two standard deviations.

A direct comparison between the WRC and OSB average heating rates, for each testing combination, was not possible as the thickness of the two test substrates were different. Higher average heating rates for OSB compared to the average heating rates from WRC was mainly a result of the difference in thickness between the two materials. WRC and OSB had thicknesses of 21 mm and 11.5 mm respectively. It was also noted that the highest peak-average heating rate for WRC was documented when using a 0.16 g cm^{-2} firebrand pile coverage density and 2.4 m s^{-1} air flow velocity. However, for OSB the highest peak-average heating rate was documented when using a 0.16 g cm^{-2} firebrand pile coverage density and an air flow of 2.7 m s^{-1}. It is suggested that this difference is related to smoldering combustion intensity of the flammable material being higher for OSB.

4.3 Firebrand pile burning behavior dependence on air flow and firebrand pile size

The Kaowool PM mean HRR profiles obtained for a subset of studied testing condition combinations are shown in Figure 4-7. Firebrand piles with a 5 cm airflow-facing edge length were used. Since Kaowool PM is effectively inert, these profiles represent the firebrand pile combustion process. All Kaowool PM HRR profiles (for all testing condition combinations) are of similar shape consisting of a rapid increase followed by a gradual decrease. Just like in the case of the Kaowool PM mean back surface temperatures profiles shown in Figure 4-2, the rapid increase in HRR is likely to be associated with the increase in the firebrand burning intensity driven by the application of a forced air flow. The gradual decrease is likely to be associated with the continuous consumption of firebrands and formation of an ash layer on their surfaces, which may inhibit not only the heat transfer to the target substrate but also the diffusion of oxygen to the uncombusted portions of the firebrand pile.

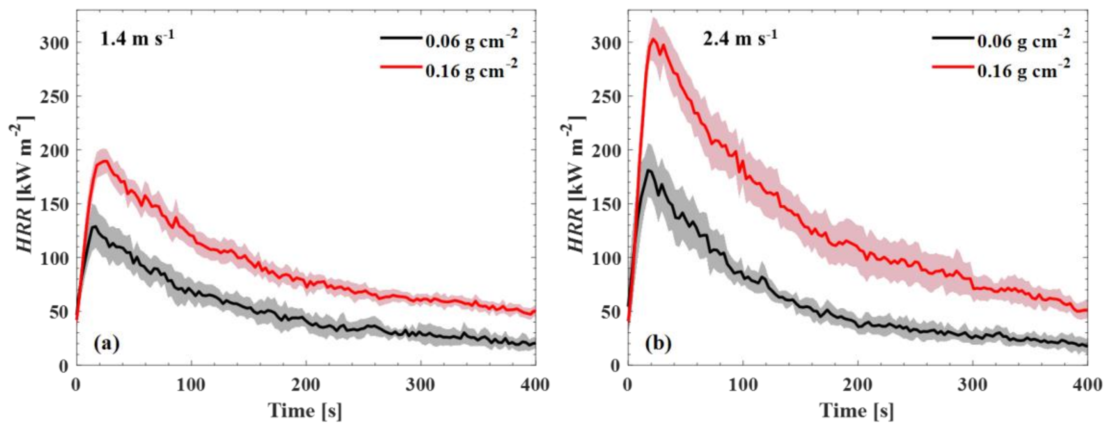

Figure 4-7. The mean Kaowool PM HRR profiles obtained for (a) 1.4 m s^{-1} air flow velocity and (b) 2.4 m s^{-1} flow velocity. Different line colors correspond to different firebrand coverage densities. The shaded areas around the curves are two standard deviations of the mean.

To analyze the impact of testing conditions (firebrand pile size and forced air flow velocity) on the burning intensity of the firebrand pile, peak-average HRR values were computed using the same approach that was used to compute the peak-average back surface temperatures discussed in Section 4.1. The peak-average HRR was used to quantify the burning intensity of the firebrands pile and values for all testing condition combinations are summarized in Figure 4-8.

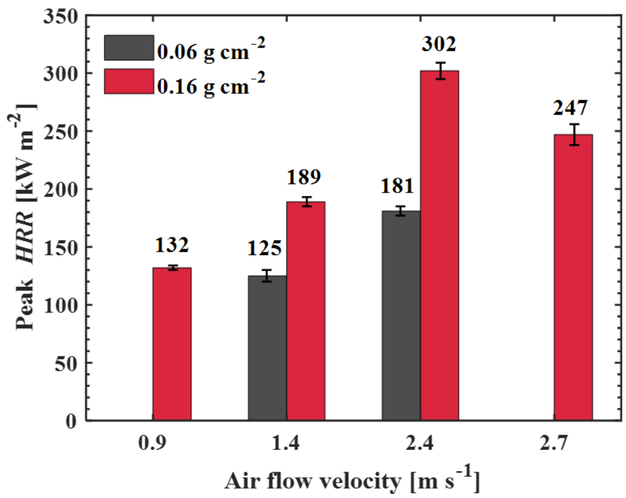

Figure 4-8. The Kaowool PM peak-average HRR values for all testing condition combinations. Different bar colors correspond to different firebrand coverage densities. The error bars represent two standard deviations of the mean.

The peak-average HRR exhibited qualitatively the same dependence on the air flow velocity as the peak-average Kaowool PM back surface temperature (shown in Figure 4-2). The peak-average HRR increased as the air flow velocity was increased up to 2.4 m s^{-1} and gradually decreased upon further increases in the forced air flow velocity. Just like in the case of the Kaowool PM peak-average back surface temperature measurements, this trend can be explained by a competition between an increasing supply of oxygen delivered by the increasing air flow into the wind tunnel and increased convective cooling of the firebrand surfaces. The increased forced airflow simultaneously increases the oxygen supply which thereby increases the firebrand burning rate (which HRR represents) but also reduces the firebrand temperature, which decreases the burning rate of the firebrand pile.

Also, similar to the Kaowool PM peak-average back surface temperature, the peak-average HRR (for a common forced air flow velocity) increased as the firebrand coverage density increased. For the smaller 0.06 g cm^{-2} firebrand pile coverage density, only a single layer of firebrands would be deposited onto the surface of the test substrate which resulted in a smaller fraction of firebrands being oxidized as opposed to the larger firebrand pile coverage density in which more firebrands would be oxidized at the air flow facing edge of the pile. The reduced burning of the smaller 0.06 g cm^{-2} firebrand pile is further validated by a lower Kaowool PM leading zone temperatures compared to the 0.16 g cm^{-2} firebrand pile back surface temperatures. The peak-average HRR increase is not proportional to the firebrand pile coverage density (highlighted in Figure 4-7) primarily because only a fraction of the firebrand pile was burning at a high intensity at any given time, as indicated by the Kaowool PM back surface temperature data discussed in Section 4.1.

The burning efficiency of a firebrand pile exposed to a constant air flow velocity was quantified by calculating the transient MCE as described in Section 3.2. The Kaowool PM mean MCE profiles, for all testing condition combinations were found to be effectively flat for the duration of the tests indicating no change in the mode of combustion as shown in Figure 4-9.

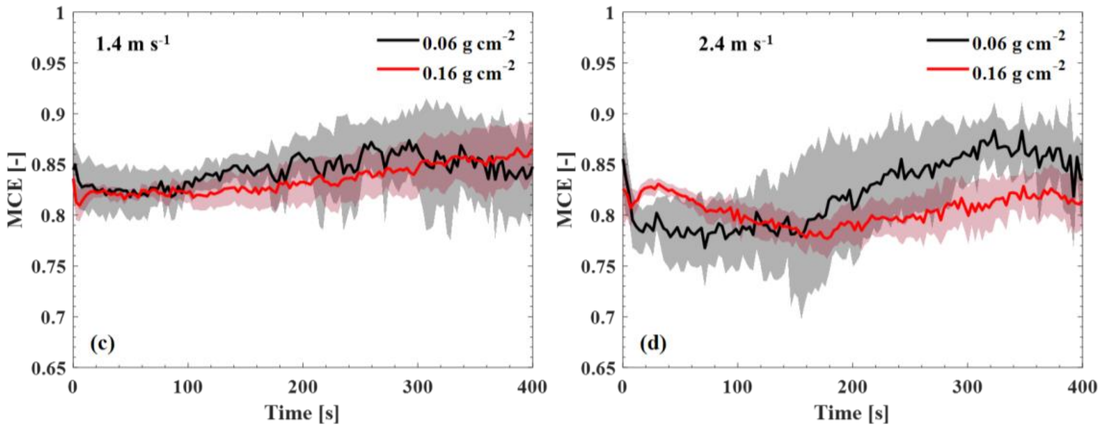

Figure 4-9. The mean Kaowool PM MCE profiles obtained for (a) 1.4 m s^{-1} air flow velocity and (b) 2.4 m s^{-1} flow velocity. Different line colors correspond to different firebrand coverage densities. The shaded areas around the curves are two standard deviations of the mean.

A time-averaged MCE value for each set of conditions was calculated to quantify burning efficiency of a firebrand pile of known coverage density when exposed to a constant air flow velocity. A time-average MCE value for each individual test was calculated using the first 400 s of each Kaowool PM transient MCE profile. Only the first 400 s of CO_2 and CO data were used to calculate the time-average MCE value as the firebrand piles were nearly fully consumed by this point. A mean MCE value for each firebrand pile testing combination was calculated as the average of all the individually calculated time-average MCE profiles for a specific testing condition combination as shown in Figure 4-10. The MCE experimental variation was calculated as two standard deviations of the mean.

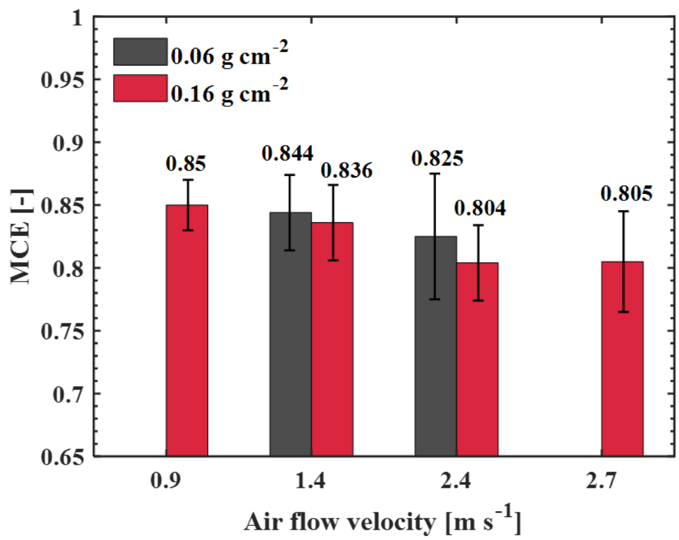

Figure 4-10. The Kaowool PM mean MCE under various testing conditions. Different bar colors correspond to different firebrand coverage densities. The error bars are two standard deviations of the mean.

The mean Kaowool PM MCE values for each firebrand pile testing condition combination were found to be in the range of 0.82 ± 0.06. These average MCE values are slightly above those usually associated with a pure smoldering process (MCE = 0.65 – 0.80) but also notably below a burning process indicative of well-ventilated flaming combustion (MCE > 0.90). This observation suggests that, in these experiments, glowing firebrand piles undergo a hybrid combustion process with smoldering taking place at the surface of the firebrands and some significant oxidation of the products of smoldering taking place in the gas phase in the vicinity of the firebrands. The firebrand pile ignition event is indicative of oxidation of the gaseous smoldering products (see Section 3.3). The data in Figure 4-10 also suggest that the

MCE decreases slightly as the forced air flow velocity is increased which can be related to the increased effect of convective cooling of the glowing firebrand pile.

4.4 *Burning behavior comparison for different flammable lignocellulosic substrate densities*

The global WRC and OSB mean *HRR* profiles are compared in Figure 4-11 and include the burning contribution of both the firebrand pile and the flammable substrate. The shape of the global HRR profile for both WRC and OSB for each testing condition combination was similar to that of the Kaowool PM firebrand pile HRR profiles. The initial rapid rise was attributed to the increased burning rate of the firebrand pile upon exposure of the forced air flow into the tunnel and is indicative of the firebrand pile driving the initial combustion process after deposition of the firebrands. The gradual decay represents the continual oxidation of the firebrand pile and heat losses to the underlying combustible substrate.

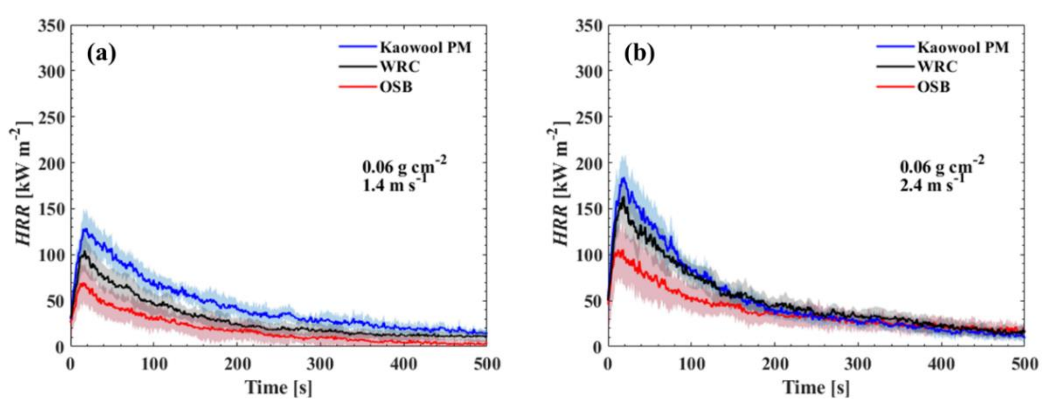

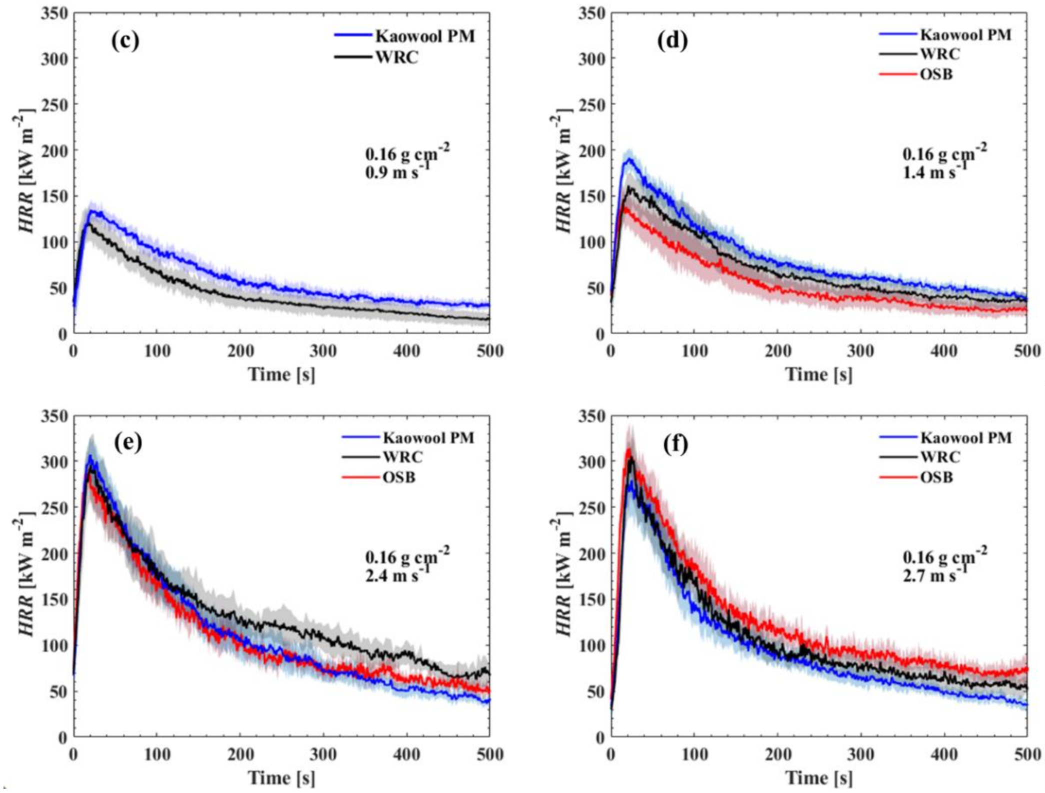

Figure 4-11. A comparison of the average global HRR profiles for all three material substrates at each testing condition combination. The variation shown in the shaded regions are calculated as two standard deviations of the mean

The peak-average HRR data were computed using the same approach used to calculate the peak-average back surface temperatures discussed in Section 4.1 and are summarized in Table 4-1. The peak-average HRR increased as the firebrand pile coverage density increased for a common air flow velocity regardless of the flammable substrate tested.

Table 4-1: The WRC, OSB, and Kaowool PM peak-average HRR data for all testing condition combinations used for comparison. The variation is calculated as two standard deviations of the mean

Firebrand pile coverage density	Air flow velocity (m s^{-1})	Kaowool PM	WRC	OSB
0.06 g cm^{-2}	1.4	125 ± 18	101 ± 21	68 ± 20
	2.4	181 ± 20	156 ± 23	101 ± 27
0.16 g cm^{-2}	0.9	132 ± 10	118 ± 16	-
	1.4	189 ± 14	158 ± 11	138 ± 20
	2.4	302 ± 17	291 ± 36	286 ± 15
	2.7	270 ± 28	300 ± 31	310 ± 21

For the 0.06 g cm^{-2} firebrand pile coverage density and both air flow velocities, the WRC and OSB peak-average HRR values are lower than the peak-average HRR profiles when depositing firebrands onto Kaowool PM. The burning intensity of the firebrand pile is reduced when depositing firebrands onto the flammable substrate surfaces because WRC and OSB both initially act as heat sinks, cooling the firebrands directly after deposition. The WRC peak-average HRR was also larger than the corresponding OSB values (for the 0.06 g cm^{-2} pile) indicating that firebrand pile heat losses to WRC were lower than for OSB. For the larger, 0.16 g cm^{-2} firebrand pile coverage density, the Kaowool PM peak-average HRR is larger than the corresponding WRC and OSB values when exposed to an air flow velocity up to 2.4 m s^{-1}. However, the peak-average HRR for WRC and OSB was larger than the corresponding peak-average Kaowool PM HRR data when exposed to a 2.7 m s^{-1} air flow velocity. It was also noted that at the 2.7 m s^{-1} air flow velocity, the OSB peak-average HRR was larger than the corresponding WRC value. This was suggested to be a result of increased oxidative smoldering of the OSB board underneath the firebrand pile.

When comparing the dependence of Kaowool PM peak-average HRR on airflow velocity, using the larger firebrand pile coverage density, the peak-average HRR increases with airflow up to 2.4 m s^{-1} and then decreases when the air flow velocity exceeded 2.4 m s^{-1}. The Kaowool PM peak-average HRR trend is analogous to trend describing the Kaowool PM peak-average back surface temperature, increasing up to an air flow of 2.4 m s^{-1} and then decreasing with any further air flow increases. The analogous trends further highlight the competition between the increased oxidation rate of the firebrand pile and the increased convective cooling of the pile at elevated air flows (in excess of 2.4 m s^{-1}). The WRC and OSB peak-average HRR dependence on air flow velocity (shown in Table 4-1) in monotonic and is attributed to the substrate smoldering contribution continually increasing. The impact of convective cooling on the burning intensity of the flammable substrates becomes less pronounced. Also, the relative effect of the flammable substrate acting as a heat sink becomes less important as the forced air flow velocity is increased.

The HRR profiles highlighting the contribution of WRC or OSB to the global combustion process were computed by subtracting the mean HRR profiles obtained in the Kaowool PM experiments (as shown in Figure 4-7) from the corresponding global mean HRR profiles for WRC and OSB. Assuming that the replacement of Kaowool

PM with a combustible substrate does not significantly alter the dynamics of the firebrand pile combustion processes, the HRR profiles shown in Figure 4-12 represent the contribution of WRC and OSB to the overall combustion process.

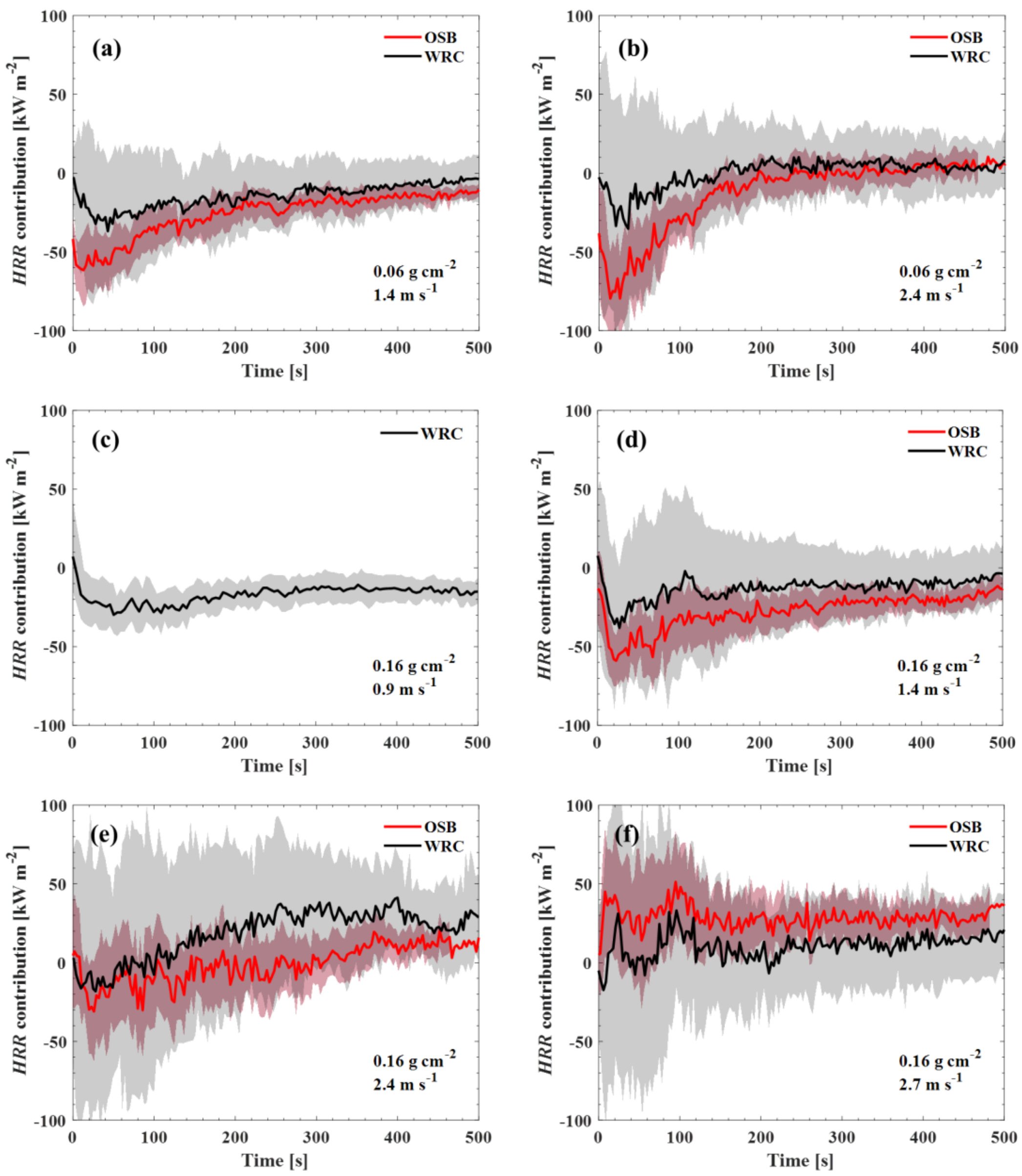

Figure 4-12. A comparison of the mean WRC and OSB HRR contribution profiles obtained for all testing condition combinations. The shaded areas around the curves are two standard deviations of the mean.

The fact that the flammable substrate HRR contribution data are slightly negative at the beginning of an overwhelming majority of experiments indicates that the higher thermal inertia of WRC and OSB (see Table 2-1) results in higher heat losses from the firebrand piles. Therefore, the piles burn with a slightly reduced intensity when deposited onto WRC or OSB with respect to those deposited onto Kaowool PM. After a negative dip, all mean HRR exhibit a gradual increase. At 0.16 g cm^{-2} firebrand coverage density and 2.4 and 2.7 m s^{-1} air flow velocities, the HRR increases to a positive value. However, even in these cases, the magnitude of the peak HRR remains at least 6.5 times smaller than the corresponding peak HRR data associated with the burning of the glowing firebrand pile, which means that the contribution of the flammable substrate to the overall burning process is very small. It was also noted that WRC (with the exception of the 0.16 g cm^{-2} firebrand pile exposed to a 2.7 m s^{-1} air flow) had a larger contribution to the overall combustion process than OSB. The initial negative HRR for WRC was also smaller when compared to OSB as WRC has a lower thermal inertia driven by the difference in density between the two materials.

The mean MCE profiles for WRC and OSB shown in Figure 4-13 represent the overall combustion process involving both firebrands and the flammable substrate. The flammable substrate MCE data are similar to the MCE data from the Kaowool PM experiments shortly after the deposition of the firebrands. However, unlike in the case of the Kaowool PM experiments, these profiles exhibit a slow but systematic downward drift eventually decreasing below 0.80 for all testing conditions. This trend suggests that, as the time of the experiment progresses and some of the flammable substrate converts to char, this char contributes to the burning process shifting the overall combustion towards pure smoldering. It is worth noting that depositing a firebrand pile onto a flammable substrate surface shifts the overall combustion process towards smoldering and the magnitude of the shift does not appear to depend on the exact material properties of the substrate. For a specific testing condition combination, the WRC and OSB average MCE profiles are below the time-average Kaowool PM MCE profile indicative of the hybrid flaming-smoldering behavior of the firebrand pile. The MCE profiles for both WRC and OSB were also noted to decrease as the air flow velocity and firebrand pile coverage density was increased. The final WRC and OSB MCE values, 400 s after deposition of the firebrand pile, for each firebrand pile coverage density gradually decreased as the air flow was increased. The gradual decrease of the final MCE values for WRC and OSB is hypothesized to be a result of increased engagement of the flammable substrate to the overall combustion process. The final MCE values for all the flammable substrate testing conditions ranged from 0.7 – 0.81.

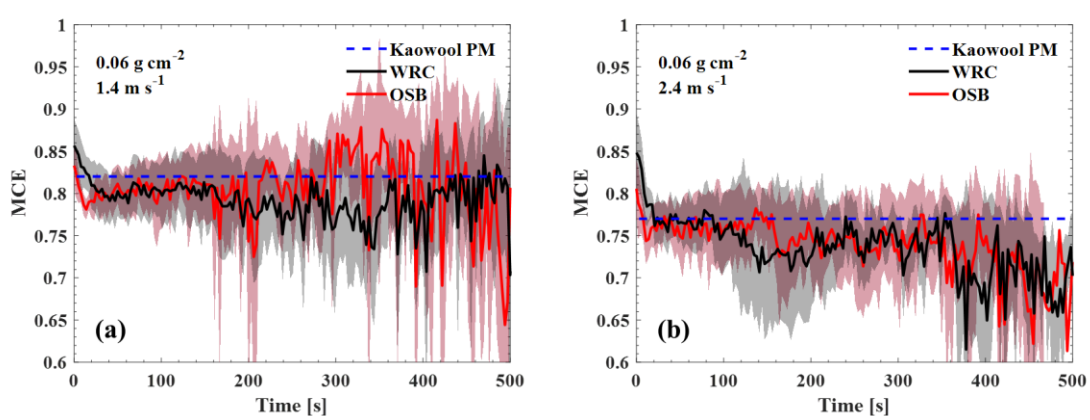

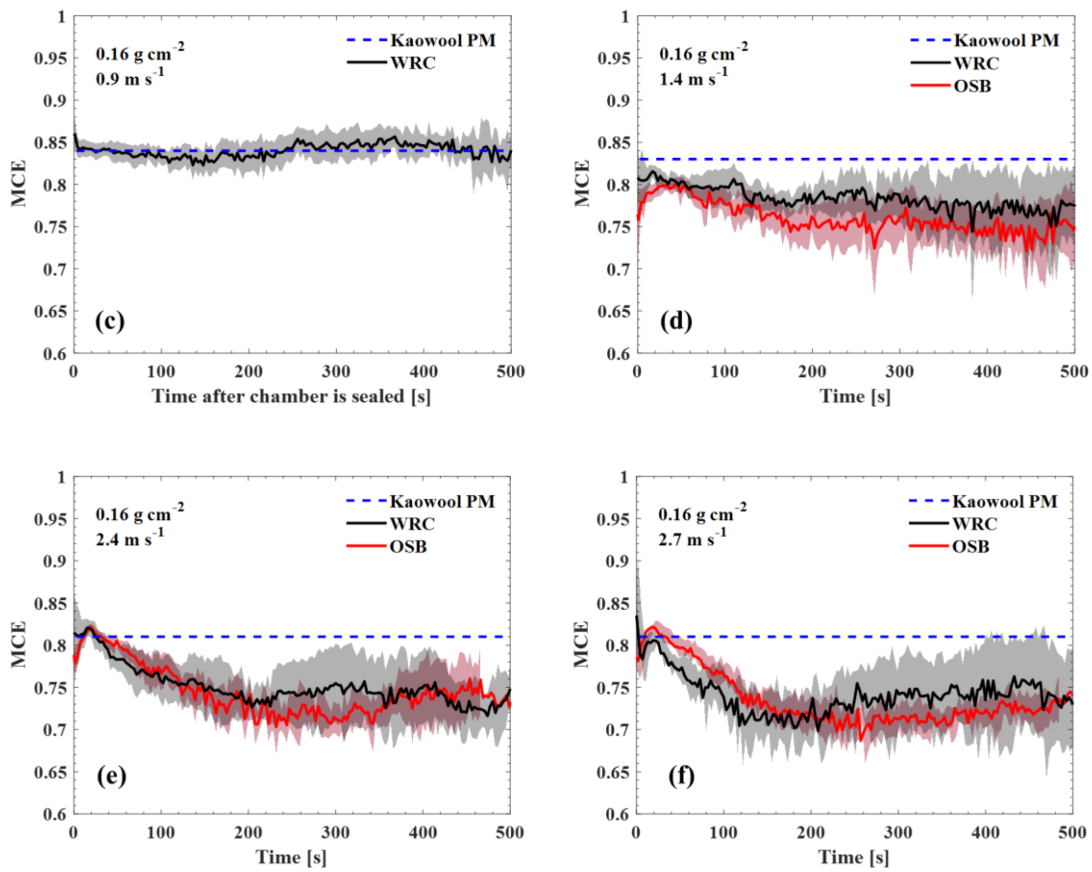

Figure 4-13. Comparison of the mean MCE profiles for all three materials at all testing condition combinations. Each profile is the average of 9 tests. The variation shown by the shaded regions are two standard deviations of the mean.

4.4.1 Ignition event identification using *HRR* and MCE

Two distinct ignition events were identified for this study: the ignition of the firebrand pile and the ignition of the surface of the flammable lignocellulosic substrate. The firebrand pile ignitions were observed in the Kaowool PM, WRC, and OSB experiments but did not register on any individual or mean *HRR* or MCE profiles.

Therefore, the formation of faint blue flames on the top surface of the piles did not have any apparent impact on HRR or MCE. The flammable substrate surface ignitions events, which corresponded to the formation of a luminous diffusion flame attached to the substrate surface, did lead to some small but detectable increases in the individual HRR profiles. Due to the fact that these ignitions were stochastic in nature, as further discussed in Section 4.5.2, these increases in HRR manifested themselves as increased uncertainties in the early mean HRR profiles (see

Figure 4-12) and were more prominent for WRC. The manifestation of the presence of surface ignition events in the HRR uncertainties was true when using a firebrand pile with the 5 cm length facing the incoming air flow. The presence of surface ignition events in the HRR signal will be discussed further in Section 5. The surface ignition flame was visually noted to spread away from its area of origin towards undecomposed portions of the flammable substrate. However, the flame from the firebrand pile ignition event remained in the area where is was initially observed. A representative example of each of the ignition event types is shown in Figure 3-2 and Figure 3-3.

4.5 *Ignition event statistics dependence on constant forced air flow and firebrand pile coverage density*

4.5.1 <u>Firebrand pile ignitions</u>

Information on the probability and timing of firebrand pile ignitions, and the duration of subsequent burning was considered. While this information was collected and processed, a decision was made not to analyze the firebrand pile ignition events in detail because, as was discussed in Section 3.3 the formation of a flame on the firebrand piles did not alter the dynamics of the combustion process. This flame did not grow or spread to the surface of the flammable substrate in any of the experiments. Therefore, in the absence of highly flammable substances in the immediate vicinity of the pile, it is very unlikely that this ignition could lead to further fire growth. All the ignition statistics for WRC and OSB are presented in Table 4-2 and Table 4-3 using firebrand piles with a 5 cm airflow-facing edge length.

Table 4-2. Firebrand pile ignition probability and timing statistics for Kaowool PM and WRC. The uncertainties were calculated as two standard deviations of the mean. The ignition and burn times reported without uncertainties correspond to a single ignition event observed in nine repeat tests.

Testing conditions	Ignition probability (%)		Ignition time (s)		Burn duration (s)	
	Kaowool	WRC	Kaowool	WRC	Kaowool	WRC
1.4 m s^{-1}, 0.06 g cm^{-2}	11	0	12	-	21	-
2.4 m s^{-1}, 0.06 g cm^{-2}	100	100	2 ± 1	5 ± 4	41 ± 17	56 ± 15
0.9 m s^{-1}, 0.16 g cm^{-2}	0	22	-	22 ± 20	-	59 ± 29
1.4 m s^{-1}, 0.16 g cm^{-2}	67	78	5 ± 4	9 ± 6	21 ± 6	58 ± 22
2.4 m s^{-1}, 0.16 g cm^{-2}	100	89	2 ± 1	4 ± 1	98 ± 45	108 ± 55
2.7 m s^{-1}, 0.16 g cm^{-2}	89	89	3 ± 1	3 ± 1	40 ± 12	47 ± 12

Table 4-3. Firebrand pile ignition probability and timing statistics for Kaowool PM and OSB. The uncertainties were calculated as two standard deviations of the mean. The

ignition and burn times reported without uncertainties correspond to a single ignition event observed in nine tests.

Testing conditions	Ignition probability (%)		Ignition time (s)		Burn duration (s)	
	Kaowool	OSB	Kaowool	OSB	Kaowool	OSB
1.4 m s^{-1}, 0.06 g cm^{-2}	11	11	12	7	21	5
2.4 m s^{-1}, 0.06 g cm^{-2}	100	78	2 ± 1	4 ± 2	41 ± 17	14 ± 6
1.4 m s^{-1}, 0.16 g cm^{-2}	67	67	5 ± 4	5 ± 1	21 ± 6	11 ± 3
2.4 m s^{-1}, 0.16 g cm^{-2}	100	100	2 ± 1	3 ± 1	98 ± 45	32 ± 21
2.7 m s^{-1}, 0.16 g cm^{-2}	89	89	3 ± 1	3 ± 1	40 ± 12	33 ± 12

As the data in Table 4-2 and Table 4-3 indicate, the firebrand pile ignition probability is not significantly affected when changing the flammable substrate material. In other words, the Kaowool PM and flammable substrate experiments performed under the same testing conditions yielded similar probabilities. The probability of the firebrand pile ignition on Kaowool PM was found to follow the same qualitative dependence on the air flow velocity as the Kaowool PM peak-average back surface temperature (see Figure 4-2) increasing as the forced air flow was increased up to 2.4 m s^{-1} and decreasing upon any further increase in the air flow. Changing the target substrate from Kaowool PM to WRC or OSB did result in slight increases in the times of ignition. When depositing firebrands onto WRC, the burning duration of the firebrand pile ignition event was longer than that compared to when firebrands were deposited onto Kaowool PM insulation. The increased duration of burning can be associated with WRC producing gaseous pyrolyzate when exposed to the glowing firebrand pile that helps sustain the flame over the firebrand pile. The burning duration for the firebrand pile ignition events when using OSB and for all testing condition combinations was shorter than when firebrands were deposited onto Kaowool PM. The decrease can be attributed to OSB more readily cooling the firebrand pile and not producing sufficient amounts of gaseous fuel that is in turn used to sustain the firebrand pile flame.

4.5.2 Flammable lignocellulosic substrate ignition events

4.5.2.1 Flammable substrate ignition location comparison

Maps of locations of the WRC and OSB surface ignitions obtained for all studied conditions in which surface ignitions were observed are shown in Figure 4-14 and Figure 4-15 respectively. The location of the surface ignition events observed for nine repeat tests at each testing condition combination have been divided into three categories, 0, 1, and 2: 0 indicates the absence of any surface ignition events, the presence of one surface ignition event in that region is indicated by the number 1, and the regions where two or more surface ignition events were noted are indicated by 2+. These maps indicate that an overwhelming majority of WRC and OSB surface ignitions occurred in front of the air flow facing edge or side edge of the firebrand pile. The majority of the surface ignitions were concentrated in the preleading temperature measurement zone. None of the WRC surface ignitions, at any conditions, were observed to occur directly underneath the pile. This was the case despite the fact that the leading zone (located directly underneath the pile) was subjected to the most intense heat feedback from the firebrands, as indicated by the peak-average Kaowool PM back surface temperature data shown in Figure 4-2.

The observation that a diffusion flame never formed on the flammable surface located under a continuous layer of firebrands can be explained by the lack of oxygen in the vicinity of surface underneath the pile. A significant amount of oxygen is consumed by the air flow facing edge of the smoldering firebrand pile, thereby reducing the oxygen concentration available at the substrate surface underneath the pile. The oxygen concentration within the firebrand pile decreases along the length of the pile as highlighted in Figure 4-2 where the oxidation of the firebrand pile is delayed as seen by the delayed temperature rise in the middle temperature measurement zone.

It appears that a sufficiently high intensity heat feedback from the firebrands combined with the availability of oxygen in the incoming air flow are the two factors that explain why the majority of ignitions occurred at the front and side edge of the pile. At the front edge, the heat feedback from the firebrand pile is clearly radiative in nature because the incoming air is cold. At the side edge, both radiation and convection from the firebrand pile may contribute to the WRC surface heating, although radiation is still likely to be dominant.

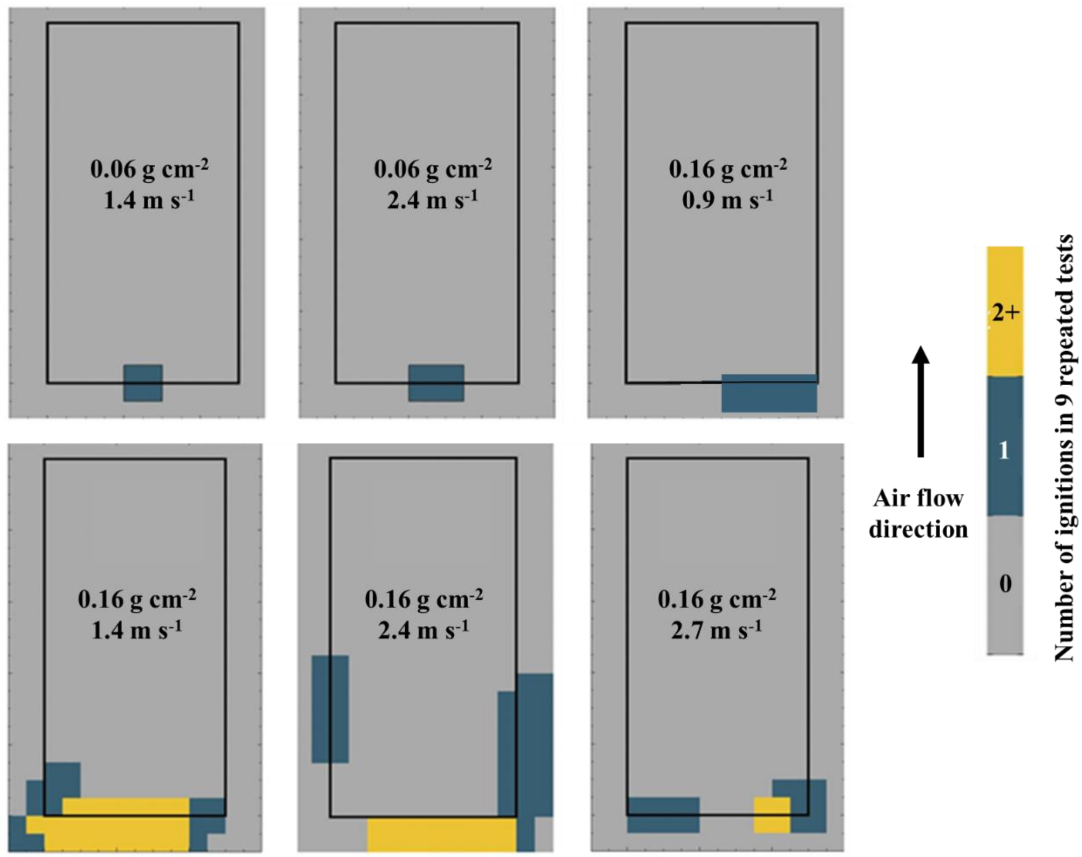

Figure 4-14. WRC surface ignition location maps drawn to scale for all testing condition combinations studied. The black rectangle outlines the location of the 50 cm^2 firebrand deposition area.

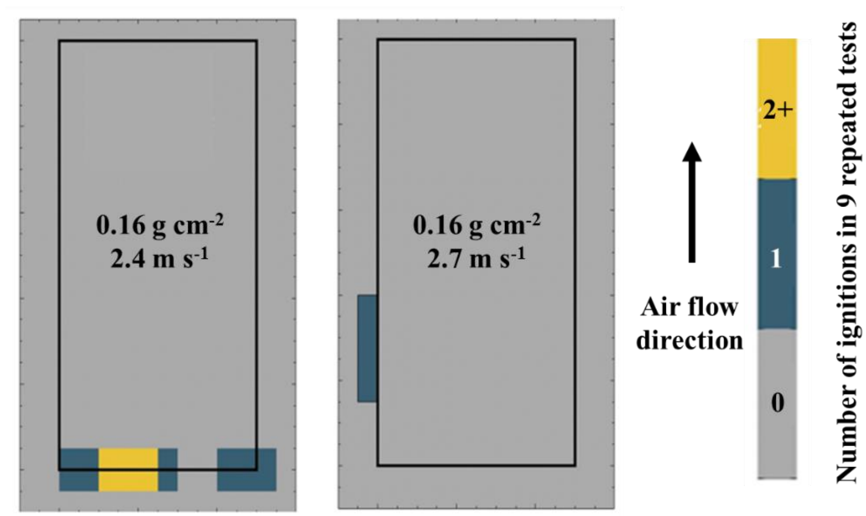

Figure 4-15. OSB surface ignition location maps drawn to scale. Surface ignition events were only observed when using the 0.16 g cm^{-2} firebrand pile coverage density. The black rectangle outlines the location of the 50 cm^2 firebrand deposition area.

4.5.2.2 Flammable substrate ignition probability dependence on material density, constant forced air flow and firebrand pile size

A comparison between the WRC and OSB surface ignition probability data is summarized in Figure 4-16. This is the mode of ignition that resulted in the formation of a stable (present for at least 5 s), luminous diffusion flame attached to the surface of the combustible substrate, as shown in Figure 3-2. In all tests, an ignition of a given type occurred only once or did not occur at all. Therefore, for each given set of conditions and each type of target substrate, the ignition probability was calculated as the ratio of the number of tests where a surface ignition event was observed to the total number of tests for each testing condition combination. For this study, nine tests were performed for each testing condition combination. In Figure 4-16, the substrate surface ignition event probability value is shown above each testing condition combination that was studied. An ignition probability value of zero indicates that no ignition events were observed at that testing condition combination.

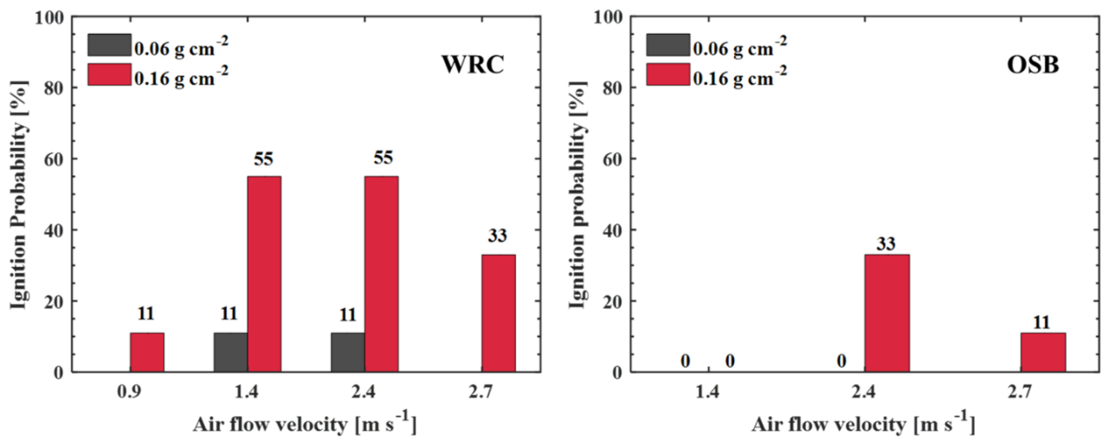

Figure 4-16. The probabilities of the WRC and OSB surface ignition computed for various experimental conditions from 9 tests performed at each set of conditions. Different bar colors correspond to different firebrand coverage densities.

The data indicate that the ignition probability of both substrates was significantly affected by both the forced air flow velocity and firebrand pile coverage density. It should be reiterated that only one surface ignition event was observed per test. The WRC ignition probability increased dramatically (up to a factor of 5) when the firebrand pile coverage density increased from 0.06 g cm^{-2} to 0.16 g cm^{-2}. For OSB, surface ignition events were only noted when using the larger 0.16 g cm^{-2} firebrand coverage density and when a forced air flow of 2.4 m s^{-1} and higher was employed (as highlighted in Figure 4-16). The largest OSB surface ignition probability increase between the two firebrand pile coverage densities was noted for a forced air flow of 2.4 m s^{-1}, increasing from 0 % to 33%. The WRC ignition probability, at each testing condition combination, was higher than that of OSB.

At 0.16 g cm^{-2} firebrand coverage density, the WRC and OSB ignition probability dependence on air flow velocity exhibited a trend qualitatively similar to that of the Kaowool PM peak-average back surface temperature (as shown in Figure 4-2). The ignition probability increased with the air flow increasing up to 2.4 m s^{-1} and decreased upon any further increases in the forced air flow. For both WRC and OSB, the highest ignition probability was obtained at an air flow velocity of 2.4 m s^{-1}. The reason for the decreased ignition probability at forced airflows in excess of 2.4 m s^{-1} is theorized to be attributed to: increased convective cooling at the airflow facing edge of the firebrand pile, and a faster removal of gaseous pyrolyzate from the region in front of the air-flow facing edge of the firebrand pile.

Given that the Kaowool PM peak-average back surface temperature may serve as a measure of the intensity of the heat feedback from the firebrands to the substrate, the similarity between the combustible substrate surface ignition probability and the peak-average back surface temperature trends indicates that, just like in the case of conventional, radiation-driven piloted ignition of solids [74], the ignition is driven by the heat flux onto the substrate surface as visually described in Figure 4-17 (a). However, unlike in the case of conventional piloted ignition of solids, the dependence of the probability of ignition on the heat flux observed in the current experiments is continuous rather than binary (i.e., a 0 % probability below the critical heat flux and 100 % probability above the critical heat flux). This continuous dependence is likely due to the fact that the firebrands serve as both a heat source and an ignition pilot (see Figure 4-17 (b)). The ignition of the flammable substrate surface is local and thus sensitive to the exact arrangement of the glowing firebrand pile. The fact that this arrangement was impossible to fully reproduce between repeat tests is what is thought to be responsible for the observed ignition stochasticity.

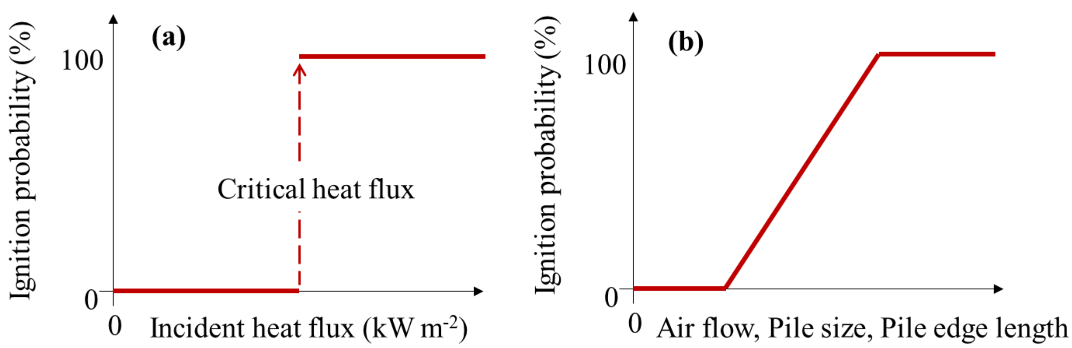

Figure 4-17: Visual representation of the (a) typical binary and (b) continuous ignition probability behavior of a flammable substrates

4.5.2.3 Ignition timing dependence on material density, constant air flow, and firebrand pile size

The data on the mean times of the WRC and OSB surface ignition and durations of burning are summarized in Figure 4-18. Timing data without any error bars are indicative of the occurrence of only one surface ignition event for a given testing condition. From Figure 4-18, it is noted that all WRC ignitions occurred within the first

74 s of firebrand exposure (considering the mean ignition times). For OSB, all surface ignition events occurred within the first 50 s of firebrand exposure. No clear ignition time trend between WRC and OSB could be resolved due to the limited number of surface ignition events for OSB. From Figure 4-18 (b), it should be noted that no OSB surface ignition events identified when using the smaller 0.06 g cm^{-2} firebrand pile and a forced air flow velocity of 1.4 m s^{-1}.

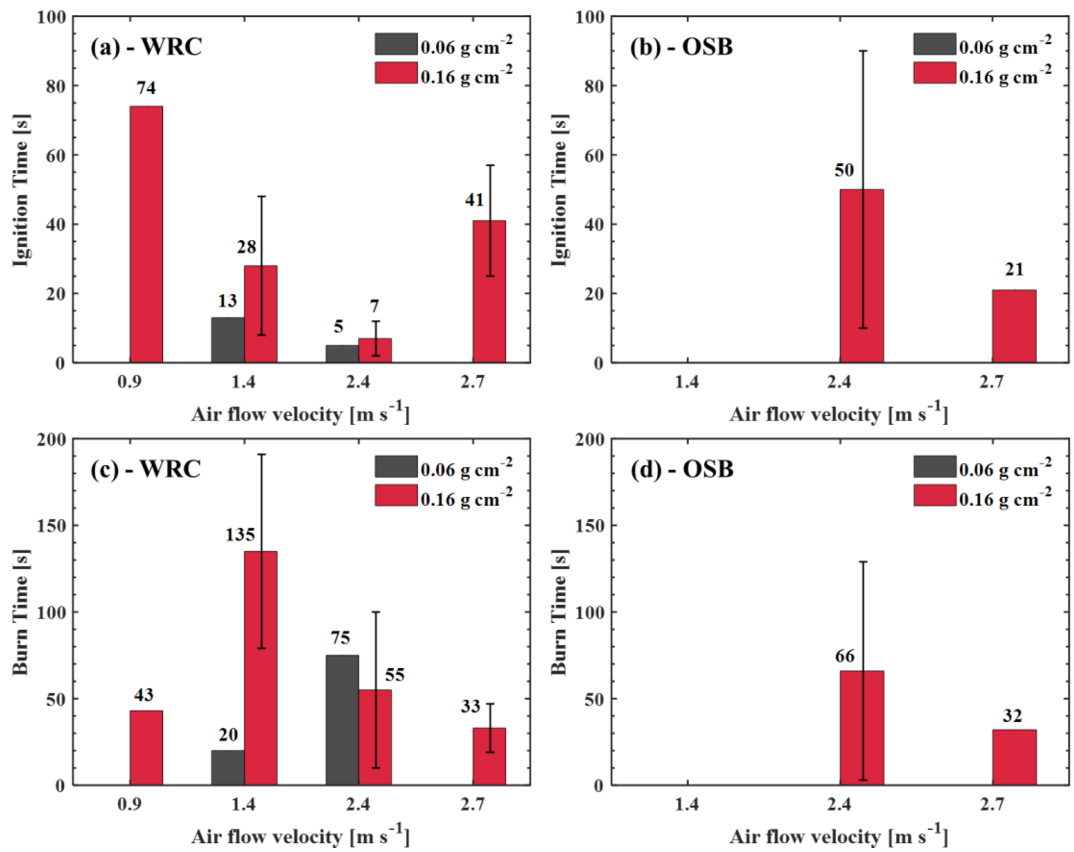

Figure 4-18. The WRC ((a), (c)) and OSB ((b), (d)) surface ignition times and burn durations computed for all testing condition combinations using nine repeat tests.

Different bar colors correspond to different firebrand coverage densities. The error bars are calculated as two standard deviations of the mean.

At the 0.16 g cm^{-2} firebrand coverage density, the mean times to ignition for WRC decreased monotonically with the air flow velocity increasing up to 2.4 m s^{-1} and increased upon further increase in the air flow. This trend shows an expected correlation with the heat feedback from the firebrands quantified through the Kaowool PM peak-average back surface temperature data (shown in Figure 4-2).

The dependence of the ignition time on the firebrand coverage density for WRC was impossible to resolve because of a small number of ignitions observed at 0.06 g cm^{-2}. The duration of burning observed for WRC, at the 0.16 g cm^{-2} firebrand coverage density, did exhibit a systematic trend increasing significantly with the air flow increasing up to 1.4 m s^{-1} and then decreasing at higher air flows. This trend does not fully correlate with the intensity of the heat feedback from the firebrands (which peaks at 2.4 m s^{-1} according to Figure 4-2) and suggests that the WRC surface flames were extinguished or blown off [75] at earlier times due to increased strain rates associated with higher forced air flows. Due to the limited number of OSB surface ignition events, no quantifiable trends could be elucidated.

5 Dependence of Ignition and Combustion Dynamics on Firebrand Pile Airflow-facing Edge Length

Currently, all experiments have been conducted using a 5 cm firebrand pile airflow-facing edge length which is, at a minimum, six times smaller [76] than the accumulated firebrand pile edge lengths observed in large scale tests. Additional experiments were performed to better understand how changing the airflow-facing edge length of the firebrand pile would affect the ignition probability (or frequency) of a horizontally-mounted target material (either WRC or OSB).

The maximum length of a sample substrate that could be mounted within the test section of the wind tunnel was 18.5 cm. A 10 cm firebrand pile edge length was therefore selected for the following reasons: the 10 cm pile edge length was the maximum length that could be used for thermal imaging measurements on Kaowool PM (when using the 10 cm × 10 cm gold mirror); a 10 cm pile edge length would expose 4 cm of the WRC or OSB substrate on the each side of the pile to the thermal insult from the firebrand pile; and the 10 cm edge length is closer in size to the firebrand pile edge lengths observed in large scale tests. Although the air-flow facing length of the firebrand pile was doubled for this set of experiments, the 50 cm^2 firebrand pile deposition area was not changed.

5.1 Flammable substrate ignition probability dependence on airflow-facing firebrand pile edge length

From the experiments conducted in Section 4, it was noted that the ignition probability dependence of the flammable substrate on the firebrand pile coverage density of the pile was near-linear (see Figure 4-16) .It was hypothesized that the ignition probability would also be directly dependent on the length of the firebrand pile edge facing the direction of the incoming forced air flow, increasing as the firebrand pile air flow-facing edge length was increased . To test this hypothesis, nine additional tests for each of the target substrates (WRC, OSB, and Kaowool PM) were performed using a constant air flow velocity of 2.4 m s^{-1} and a firebrand pile coverage density of 0.16 g cm^{-2}. An air flow velocity and coverage density of 2.4 m s^{-1} and 0.16 g cm^{-2} was selected for these experiments as this was the testing condition combination where the largest number of surface ignition events were observed for both WRC and OSB. The 5 cm × 10 cm firebrand deposition area (as shown in Figure 5-1) was rotated 90° with respect to the direction of the incoming air flow so that the longer dimension of the deposition area was perpendicular to (or facing) the incoming air flow. The firebrand pile deposition area was kept constant (50 cm^2) to enable direct comparison of the thermal exposure and gas analyzer burning dynamic data between the two firebrand pile edge lengths.

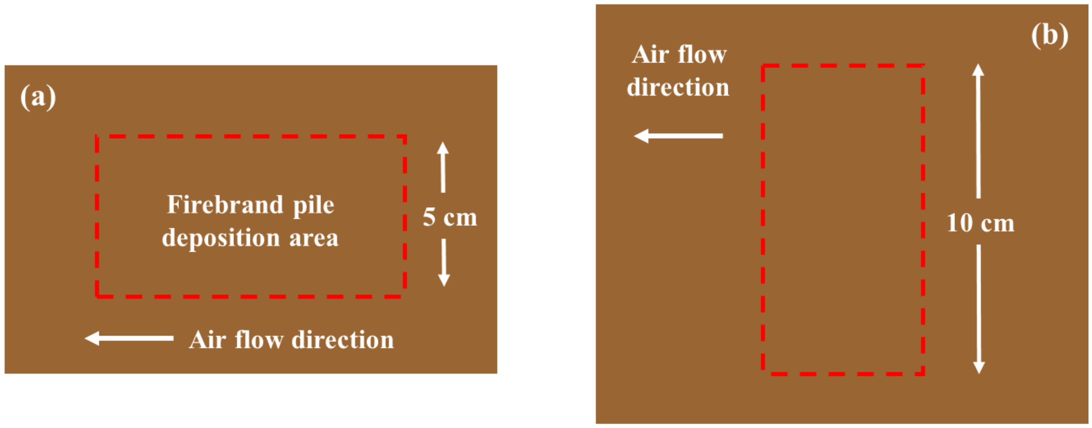

Figure 5-1. Schematic representing of the change in the length of the airflow-facing side of the firebrand pile from (a) 5 cm to (b) 10 cm.

5.1.1 Ignition probability statistics comparison for different firebrand pile edge lengths

Initially, WRC was used as the flammable test substrate to determine whether the number of ignitions at the surface of the WRC surface would change when changing the firebrand pile airflow-facing edge length from 5 cm to 10 cm. WRC was already identified to be more susceptible to ignition by glowing firebrands than OSB (see Figure 4-16). The surface ignition probability of WRC when exposed to a 0.16 g cm^{-2} firebrand pile and a 2.4 m s^{-1} air flow velocity was 55 % and was higher than the ignition probability observed for OSB (33 %) at the same testing condition combination.

The ignition probability for WRC and OSB increased dramatically as the length of firebrand pile edge was increased as shown in Figure 5-2. The ignition probability of WRC nearly doubled, increasing from 55 % to 100 %. A WRC surface ignition event was identified for each of the nine experiments. For one of the nine experiments, the WRC surface was noted to re-ignite but was not included in the surface ignition statistics. The ignition probability of OSB doubled, increasing from 33 % to 67 %, when the length of the airflow-facing edge of the firebrand pile was doubled from 5 cm to 10 cm. A single OSB surface ignition event was identified in six out of the nine experiments.

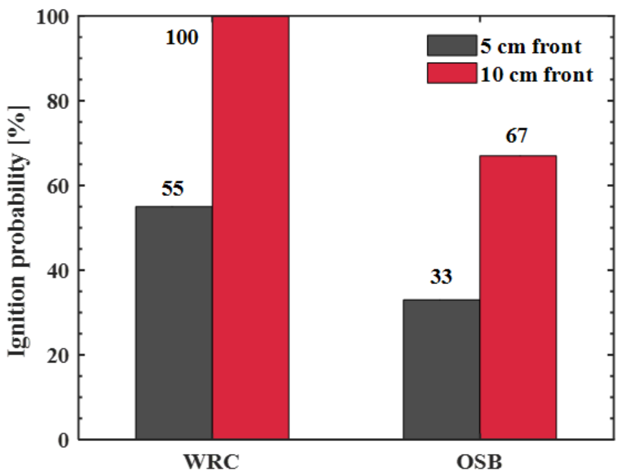

Figure 5-2. WRC and OSB surface ignition probability comparison when changing the firebrand pile perimeter length from 5 cm to 10 cm. The gray and red bars represent the ignition probability of the 5 cm and 10 cm firebrand pile perimeter respectively.

The increased surface ignition probability for both flammable substrates was attributed to an additional 5 cm of the WRC or OSB surface (mostly free of firebrands) being exposed to the thermal insult from the firebrand pile facing the incoming air flow. A larger surface area of the WRC and OSB board is able to thermally decompose and produce more gaseous fuel that can mix with the available oxidizer and potentially ignite. It is also postulated, that the increased number of glowing firebrands exposed to the incoming air flow (which are said to act as the pilot ignition source) contribute to the observed increased ignition probability of both flammable substrates.

5.2 Flammable surface ignition locations

All WRC and OSB surface ignition event locations (when using a 10 cm firebrand edge length) were located in front of and at the leading, air flow facing, edge of the firebrand pile as shown in Figure 5-3. The surface ignition locations for the 10 cm firebrand pile perimeter coincided with the surface ignition locations when using a 5 cm firebrand pile perimeter length as shown in Figure 4-14. Similar surface ignition locations for both pile edge lengths indicate that radiation from the air flow facing edge of the firebrand pile remains the dominant mode of heat transfer to the flammable substrate surface free of firebrands.

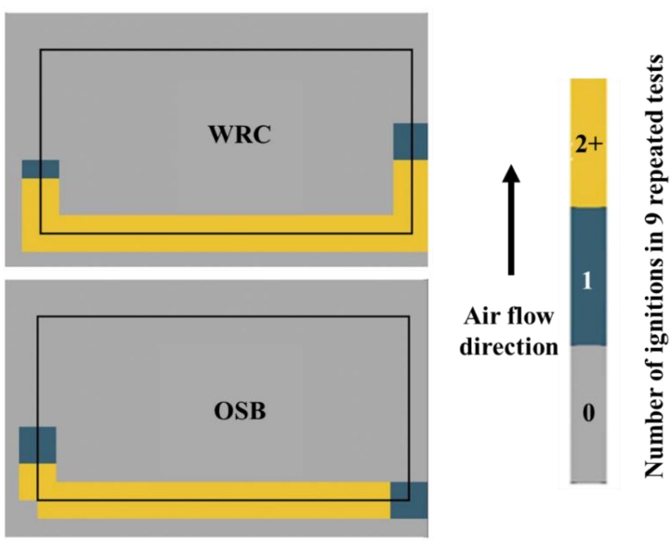

Figure 5-3. Substrate surface ignition locations for WRC and OSB when exposed to a 10 cm airflow-facing edge length firebrand pile.

5.3 Firebrand pile thermal exposure dependence of firebrand pile edge length

Experiments in which a 0.16 g cm^{-2} firebrand pile was deposited onto Kaowool PM insulation board were used to quantify the thermal exposure from the 10 cm airflow-facing edge of the firebrand pile. The firebrand pile thermal exposure at the front of the firebrand pile (free of firebrands) was evaluated. Most of the WRC and OSB surface ignitions were located in front of the firebrand pile and therefore the preleading temperature measurement zone was of interest. A 1.5 cm × 8 cm rectangular temperature measurement zone (as shown in Figure 5-4), positioned at the air flow facing edge of the firebrand pile, was used to isolate the thermal exposure from the 10 cm edge length firebrand pile. The temperature measurement zone extended 1 cm outside of the firebrand pile deposition area against the direction of the incoming air flow similar to the preleading temperature measurement zone used in Section 4.1. The entire 10 cm length was not used to measure the temperature due to a reduction in the firebrand coverage density at the edges of the pile. The mean back surface temperature and the temperature variation was computed similar to the methodology highlighted in Section 3.1.

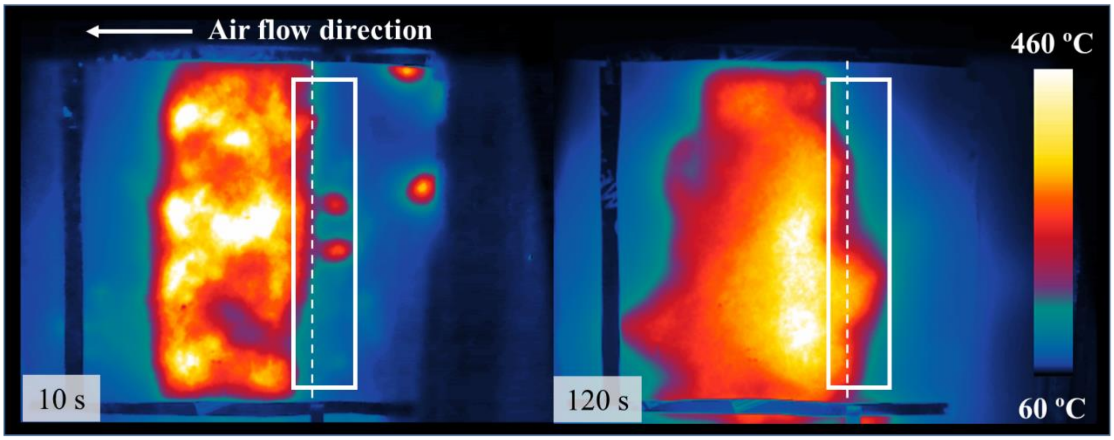

Figure 5-4. Back surface temperature maps obtained for a 0.16 g cm^{-2} firebrand pile deposited onto Kaowool PM and exposed to 2.4 m s^{-1} air flow (a) 5 s and (b) 90 s after deposition of the pile. The 10 cm firebrand pile perimeter length is perpendicular to the direction of the incoming air flow.

The transient back surface temperature profiles (generated in the preleading zone) for both firebrand pile edge lengths were compared as shown in Figure 5-5. Qualitatively, the transient temperature profiles exhibit the same trend consisting of an initial rapid increase after deposition of the firebrand pile and a gradual decrease. The rapid increase is attributed to the increased burning intensity of the firebrands upon the application of the forced air flow. The gradual temperature decrease is a result of the continuous consumption of the pile and the formation of an ash layer on top of the firebrands, which inhibits heat transfer to the target fuel.

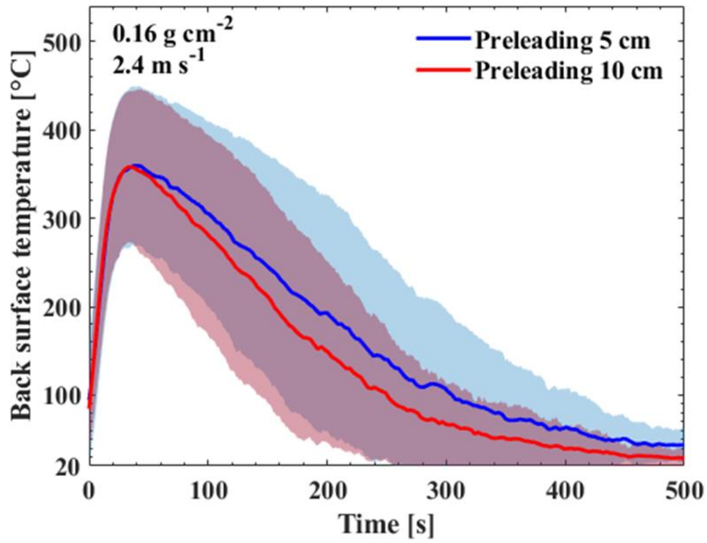

Figure 5-5. The mean Kaowool PM back surface temperature profiles obtained for a 0.16 g cm^{-2} firebrand coverage density and a 5 cm and 10 cm firebrand pile edge length. The shaded areas around the curves represent variations in these temperatures expressed as two standard deviations.

The initial temperature rise as well as the peak back surface temperature was noted to be nearly-identical between the two firebrand pile edge lengths. This initial similarity indicates that the firebrand pile heat exposure to the surface of a target substrate is not strongly-dependent on the length of the firebrand pile edge facing the incoming air flow. The temperature decay rate (after reaching the peak temperature) of the 10 cm edge firebrand pile was larger than the decay rate of the 5 cm perimeter firebrand pile. The larger decay rate is attributed to the increased oxidation rate of the firebrands in the 10 cm edge pile. A larger number of firebrands are exposed to the incoming air flow and subsequently oxidized compared to the number of firebrands being consumed when using a firebrand pile with a 5 cm edge length.

5.4 Dependence of ignition timing and ignition location on firebrand pile edge length

The ignition time and burning duration for both flammable substrates and both firebrand pile edge lengths were compared as shown in Figure 5-6. For the experiments where a WRC surface ignition event was identified, lateral surface flame spread along the length of the airflow-facing perimeter of the firebrand pile was observed. It is theorized that, for WRC, this lateral flame spread can be attributed to the increased burning duration. More gaseous pyrolyzate is being produced as a larger target material surface area in front of the pile is being thermally decomposed. The increased amount of pyrolyzate therefore assisted in sustaining the surface ignition flame. The lateral flame spread along the surface of the OSB in front of the firebrand pile was less prominent indicative of the burn duration for both firebrand pile edge lengths being nearly identical. The OSB surface flame location remained in close proximity to the point of initial ignition. From Figure 5-6, it was is noted that the WRC ignition time is shorter than the OSB ignition time for both firebrand pile air flow facing edge lengths.

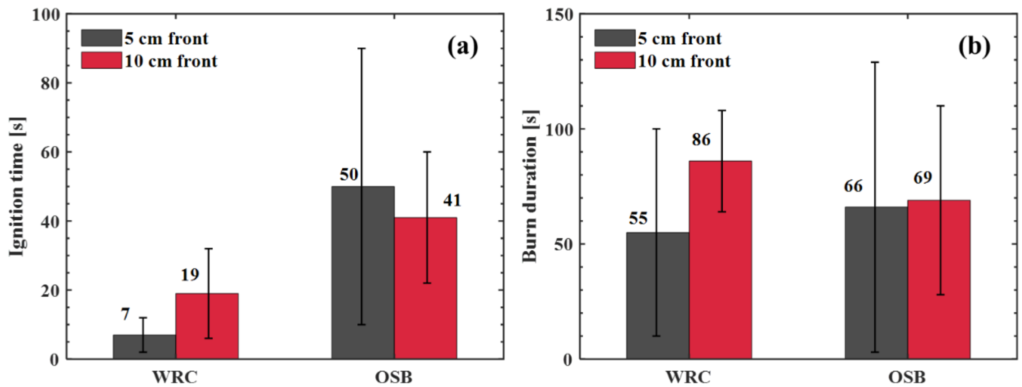

Figure 5-6. WRC and OSB (a) ignition time and (b) burn duration comparison when changing the firebrand pile perimeter length from 5 cm to 10 cm.

5.5 HRR dependence on firebrand pile edge length

The effect of changing the firebrand pile edge length was further analyzed considering the burning dynamics of the firebrands as well as the WRC- or OSB-firebrand pile system. The peak-average *HRR* was used as a measure to quantify the burning intensity of the firebrand pile-flammable substrate system. Initially, the peak-average Kaowool PM *HRR* values for both firebrand pile edge lengths were compared and are indicative of the burning intensity of only the firebrand pile. The peak-average *HRR* values were calculated by identifying the global maximum value and averaging 4 s of *HRR* data around the global maximum *HRR* value.

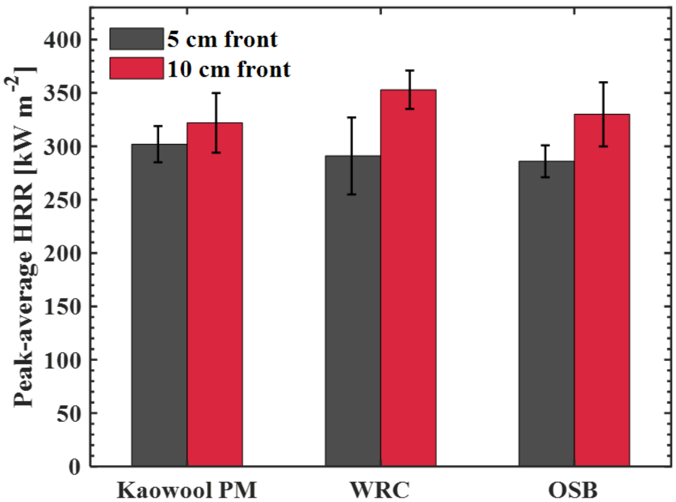

Figure 5-7. Comparison of the Kaowool PM, WRC, and OSB peak-average HRR values for the both firebrand pile air-flow facing edge lengths. A 0.16 g cm^{-2} firebrand pile coverage density and 2.4 m s^{-1} forced air flow velocity was used.

From Figure 5-7, it is noted that the firebrand pile peak-average *HRR* (deposited onto Kaowool PM) increased as the air flow-facing edge length was increased. The firebrand pile peak-average *HRR* increase can be attributed to an increased number of firebrands being oxidized when using the larger 10 cm firebrand pile edge length. The Kaowool PM peak *HRR* increased from 302 kW m^{-2} to 322 kW m^{-2} as the firebrand pile edge length was increased from 5 cm to 10 cm. A similar dependence on air flow-facing pile edge length was noted for the thermal exposure from the pile as highlighted in Figure 5-5. The peak-average *HRR* for both WRC and OSB (353 kW m^{-2} and 330 kW m^{-2}) when exposed to a 10 cm firebrand pile edge length is higher than the peak-average *HRR* for WRC (291 kW m^{-2}) and OSB (286 kW m^{-2}) when exposed to a 5 cm firebrand pile edge length using a 2.4 m s^{-1} air flow velocity. The peak-average *HRR* increase for both WRC and OSB can be attributed to the increased number of surface ignition events when using a 10 cm firebrand pile edge length. When a 5 cm edge length firebrand pile was used, the peak-average *HRR* for WRC was 11 kW m^{-2} lower than the corresponding Kaowool PM peak-average *HRR* when five WRC surface ignition events were identified. When using a 10 cm firebrand pile edge length, the WRC peak-average *HRR* was 31 kW m^{-2} higher than the corresponding Kaowool PM peak-average *HRR* and a WRC surface ignition event was noted for each of the nine tests as shown in Figure 5-3. The presence of a WRC surface flame is reflected by this additional 31 kW m^{-2} increase in the WRC peak-average *HRR* value. The surface flame increases the flaming combustion behavior of the firebrand pile-flammable substrate system which is reflected by an increased amount of CO_2 (being produced by the surface flame) which drives the higher peak-average *HRR* value. The OSB peak-average *HRR*, when using a 10 cm firebrand pile edge length, was only 8 kW m^{-2} higher than the corresponding Kaowool PM peak-average *HRR*. The smaller difference between the OSB and Kaowool PM peak-average *HRR* values can be attributed to presence of only six surface ignition events and the burn times of these OSB surface ignition events being shorter than what was noted for WRC.

Further, it is worth noting that the transient *HRR* profiles were qualitatively similar for all materials and the shape was not affected when the firebrand pile edge length was changed as shown in Figure 5-8. The *HRR* profiles included a sharp rise in the global

HRR of each profile directly after deposition of the firebrand pile followed by a gradual decay as the test progressed and firebrands were being continually consumed.

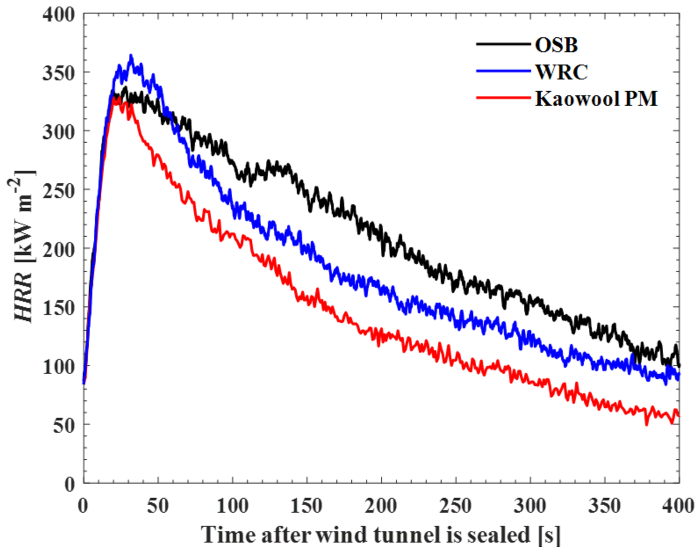

Figure 5-8. Average temporal combustion *HRR* profiles for Kaowool PM, WRC, and OSB at a 2.4 m s^{-1} air flow and 0.16 g cm^{-2} firebrand pile coverage density. Firebrand piles with a 10 cm air flow-facing edge length were used.

5.6 Flammable substrate combustion efficiency dependence of firebrand pile edge length

The difference in burning behavior for WRC and OSB when exposed to firebrand piles with different airflow facing edge lengths is further highlighted by their respective transient MCE profiles shown in Figure 5-9. For the first 150 s, the WRC MCE profile when exposed to a glowing firebrand pile with a 10 cm edge length is higher than the WRC MCE profile when exposed a firebrand pile with a 5 cm edge length. The higher WRC MCE in Figure 5-9 (b) shortly after deposition is attributed to the presence of a surface ignition event for each of the nine repeat tests. A surface flame is indicative of a more-complete combustion process producing larger amounts of CO_2 relative to the amount of CO being produced. A similar trend is noted when comparing the average transient OSB MCE profiles for both pile edge lengths where the OSB MCE profile for the 10 cm pile edge length is initially higher.

The 10 cm pile edge length MCE profiles start to gradually decrease with time, indicative of the extinguishment of the surface flame (approximately 75 s after firebrand pile deposition) and smoldering dominating the combustion process of both materials. At 500 s after deposition of the firebrand pile, the average MCE profiles for both perimeter lengths for each respective material start to converge to a value in the range of 0.74. The convergence is a result of reduced burning of the firebrand pile for both edge lengths (see Figure 4-12) and similar substrate smoldering rates.

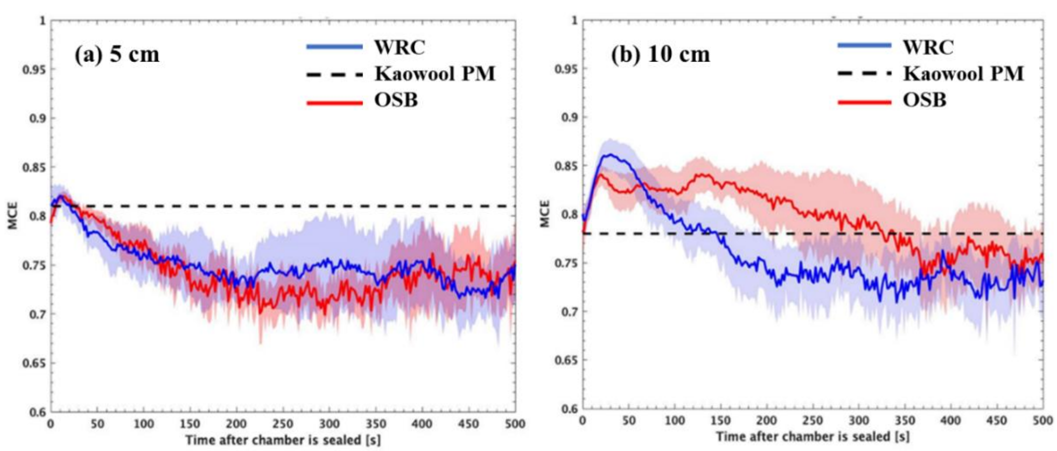

Figure 5-9. Transient average MCE profiles when a (a) 5 cm and (b) 10 cm firebrand pile perimeter length exposed to a 2.4 m s^{-1} continuous air flow velocity. A 0.16 g cm^{-2} firebrand pile coverage density was used for all the experiments.

6 Exploration of Impact of Airflow Intermittency on Ignition

Nine additional tests on each of the test substrates (WRC, OSB, and Kaowool PM) were performed using a 0.16 g cm^{-2} firebrand pile coverage density and exposing the firebrand pile to a single intermittent air flow velocity for a specified amount of cycles. A 5 cm × 10 cm firebrand deposition area was used. The shorter dimension of the deposition area (5 cm) was aligned perpendicular with the direction of the incoming air flow. Only one surface ignition event per test was observed when using a constant air flow velocity (see Section 4.5) and the above-mentioned firebrand pile orientation. This portion of the study was conducted to determine how the surface ignition probability of WRC and OSB would be affected when exposed to intermittent air flow conditions.

During initial exploratory testing using WRC, it was found that the air flow velocity emulating a gust condition, the duration of the gust, and the duration of time between gusts were all parameters that affected the reignition propensity of a flammable substrate. WRC was used for these initial exploratory tests due to it being more susceptible to ignition by firebrands than OSB (see Section 4.5.2.2).

The testing procedure that was selected for the intermittent air flow testing campaign was performed according to the following steps: a 0.16 g cm^{-2} firebrand pile was deposited onto the test substrate, using a custom-built funnel, while a known constant forced air flow was being continually introduced into the tunnel; the funnel was then lifted out of the tunnel and a piece of borosilicate glass was used to seal the tunnel, indicative of the test start time. The firebrand pile was initially exposed to a constant air flow for 60 s before the forced air flow was terminated (by switching the fan off). After the initial 60 s of constant air flow exposure, the fan was repeatedly switched off and then switched back on. This cyclic process would then be repeated 16 times after the initial 60 s constant air flow exposure condition.

During preliminary testing, four different timing intervals in which the forced air flow was introduced into the wind tunnel and then subsequently terminated were explored as presented in Table 6-1. This was done in an effort to determine which interval was more conducive to surface reignition events for a known forced intermittent air flow velocity. Reignition events were indicative of the repeat formation of a diffusion flame on the surface of a flammable substrate after the initial 60 s air flow exposure.

Two forced air flow velocities, 2.4 m s^{-1} and 2.7 m s^{-1}, were also initially compared. In all tests, the firebrand pile was initially exposed to a constant continuous forced air flow velocity for 60 s before the timing intervals before the intermittent air flows were implemented. The initial 60 second time period was selected with the knowledge that a majority of the surface ignition events, using a constant forced air flow velocity, occurred within the first 75 s after deposition of the firebrands onto the flammable substrate. The number of ignition events includes all surface ignitions documented during a single test.

Table 6-1: The testing condition combinations used during the initial exploratory testing campaign and their respective WRC surface ignition statistics.

Trial number	Air flow velocity (m s^{-1})	Constant force air flow on (s)	Constant force air flow off (s)	Number of ignition events	Reignition burn time (s)
1	2.7	60	60	5	7 ± 1
2	2.7	30	30	2	6
3	2.7	60	30	3	6 ± 2
4	2.7	20	10	10	7 ± 1
5	2.4	20	10	4	7 ± 2

As shown in Table 6-1, the most reignition events occurred when exposing the firebrand pile to a constant 2.7 m s^{-1} air flow velocity for 20 s and then switching off the fan for 10 s. This was selected as the set of air flow conditions that were used to generate all firebrand thermal exposure and ignition timing statistics. During the 10 s in which no forced air flow was applied to the pile, only buoyancy-driven entrainment of air into the tunnel was present. The average burn time for all the reignition events (ignitions occurring after the initial 60 s of firebrand exposure) were also very similar.

6.1 Firebrand pile thermal exposure dependence on air flow intermittency

The transient thermal exposure of the firebrand pile deposited onto Kaowool PM insulation board was examined to determine whether the thermal exposure form a pile of firebrands onto the surface of a flammable substrate was significantly altered when using intermittent air flow conditions. The same procedure highlighted in Section 3.1 was used to measure the back surface temperature of the Kaowool PM insulation board within the preleading zone (the zone in front of the air-flow facing edge of the firebrand pile). The average transient back surface temperature profile obtained when using an intermittent air flow along with the temperature profile obtained for a constant air flow is compared in Figure 6-1. The initial rate of back surface temperature rise as well as the average peak back surface temperature are nearly identical for both testing conditions. The peak average back surface temperature for the continuous and intermittent testing conditions are 300 and 313 °C respectively. For both air flow conditions (continuous or intermittent), the firebrand pile was exposed to the same constant 2.7 m s^{-1} air flow for the first 60 s of the test which explains why both the rate of temperature rise and peak back surface temperature are similar. After the peak back surface temperature was reached it was noted that the average back surface temperature profile of the intermittent air flow tests were higher than compared to the back surface temperature profile when using a continuous air flow. The higher back surface temperature profile for the intermittent air flow tests is attributed to the oxidation rate of a firebrand pile being slower as the air flow is periodically terminated. A larger number of glowing firebrands are still readily available to burn when the force air flow is continuously reintroduced into the tunnel.

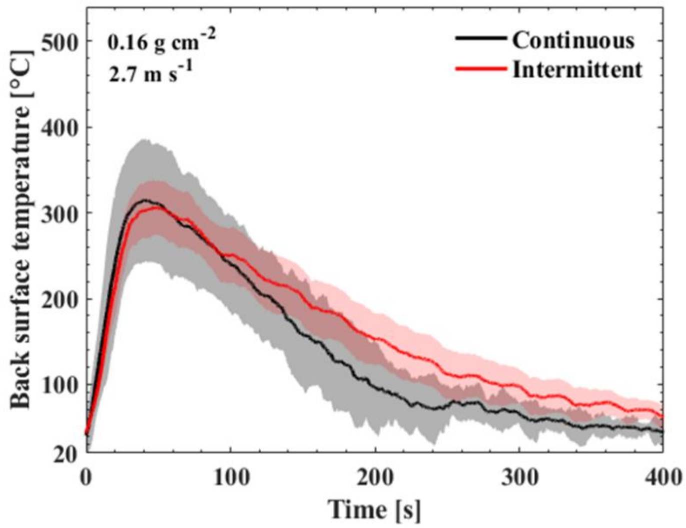

Figure 6-1. A comparison of the preleading zone average back surface temperature profiles when using a continuous and intermittent air flow velocity. The shaded areas represent the variation of each testing condition calculated as two standard deviations.

6.2 Flammable surface ignition time and burning duration dependence on air flow intermittency

Intermittent air flow ignitions statistics were collected and compared to the constant air flow statistics to determine the ignition timing dependence on air flow stability. The ignition statistics included the total number of ignitions during a test, the ignition time and burning duration of each surface reignition event, as well as the surface reignition probabilities in the presence or absence of a forced intermittent air flow. The total number of surface ignition events in nine repeat tests for WRC and OSB, when using a constant 2.7 m s^{-1} forced air flow and 0.16 g cm^{-2} firebrand pile coverage density, were equal to 3 and 1 respectively. The number of surface ignitions drastically increased for both flammable substrates when intermittent air flow conditions (at an air flow velocity of 2.7 m s^{-1}) were employed. The total number of WRC surface ignitions increased from 3 to 42 and for OSB the total number of surface ignition events increased from 1 to 19. All intermittent air flow tests were conducted using a firebrand pile with a 0.16 g cm-2 coverage density.

A timeline highlighting the surface ignitions events that occurred within the first 240 s seconds of three representative tests are shown in Figure 6-2 for WRC and Figure 6-3 for OSB. It is noted that a majority of reignition events occurred after the forced air flow into the tunnel was terminated (the absence of a forced airflow). A reigintion event was indicative of a stable diffusion flame located on the surface of the flammable substrate after the forced air flow was reintroduced into the wind tunnel. The percentage of surface ignition events that were noted to occur in the absence of a forced air flow was equal to 83 % (35 reignitions) for WRC and 74 % (14 reignitions) for OSB.

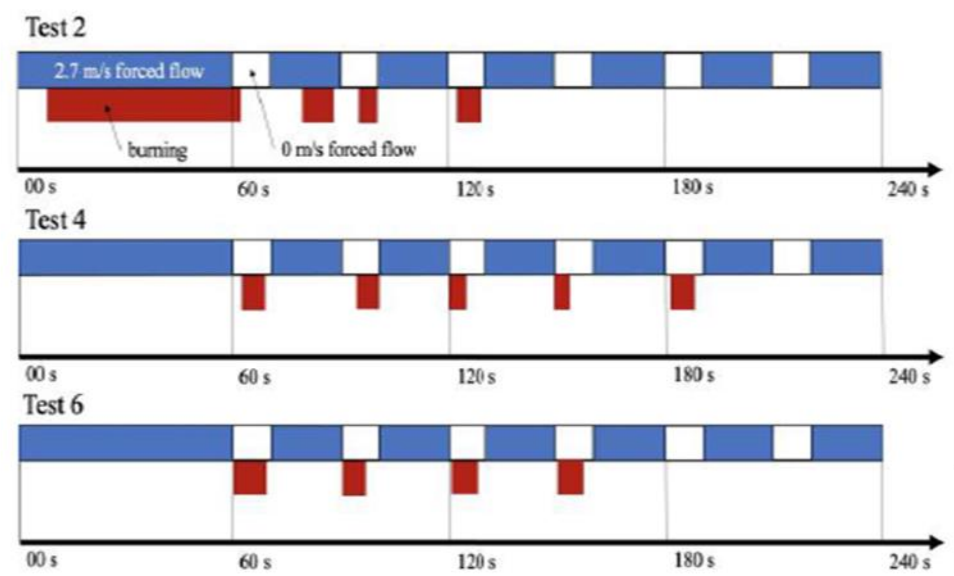

Figure 6-2. An ignition timeline when depositing a 0.16 g cm^{-2} firebrand pile onto WRC or (b) OSB and exposing the pile to an intermittent 2.7 m s^{-1} air flow velocity.

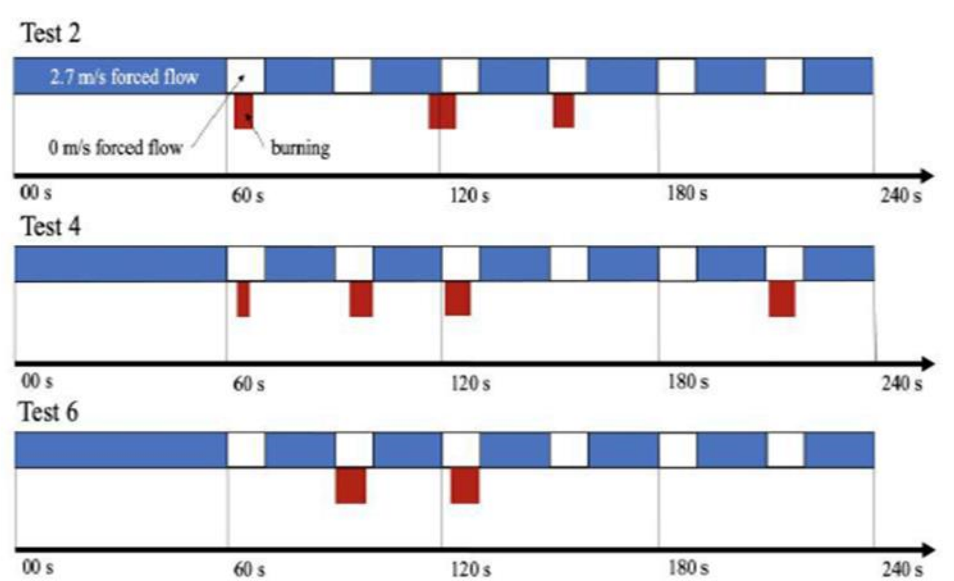

Figure 6-3. An ignition timeline when depositing a 0.16 g cm^{-2} firebrand pile onto and exposing the pile to an intermittent 2.7 m s^{-1} air flow velocity.

During a forced air flow period, the burning intensity of the firebrand pile is increased which in turn increases the rate at which the target fuel surface in front of the pile, free of firebrand, is being radiatively heated and subsequently pyrolyzed. However, at the high, 2.7 m s^{-1} air flow velocity, the gaseous fuel is being diluted and removed at a rate that is unfavorable for the formation of a flame at the surface of the target fuel in front of the firebrand pile. When the forced air flow is terminated, conditions conducive to ignition arise where sufficient amounts of gaseous fuel, at an elevated temperature, and oxidizer in front of the pile are able to mix and subsequently ignite. It is also postulated that the firebrands at the air flow facing edge of the firebrand pile also act as a potential high temperature pilot shortly after the forced air flow is terminated.

The majority of surface ignition flames would extinguish prior to the forced air flow being reintroduced into the tunnel (in the absence of a forced air flow). For WRC, 86 % of the surface reignition events and for OSB, 100% of the surface reignition events extinguished in the absence of the forced air flow. Immediately after the forced air flow was terminated, it was visually noted that the intensity of glowing of the pile decreased as shown in Figure 6-4. The vivid glowing of the air flow facing edge of the firebrand pile exposed to a forced air flow is shown in Figure 6-4 (a) and is highlighted by a bright yellow color. In Figure 6-4 (b), a firebrand pile ignition flame is observed directly after the forced air flow into the wind tunnel is terminated. Figure 6-4 (c) shows the reduced visual glowing of the firebrand pile 4 s after the forced air flow was terminated.

Figure 6-4. Firebrand pile glowing color differences during (a) the application of a forced air flow and (b), and (c) when the forced air flow into the wind tunnel has been terminated.

During the time intervals when no forced air flow was present, the burning intensity of the firebrand pile was noted to decrease as seen in Figure 6-4 (c). The reduction in the number of visually glowing firebrands was qualitatively indicative of reduced a firebrand pile burning intensity. Therefore, the majority of the surface flames extinguish in the absence of a forced air flow due to decreased heating of the target fuel surface in front of the firebrand pile. An insufficient mass flux of gaseous fuel being produced as well as lower temperature firebrands both attribute to extinction of the flame shortly (mean of 7 s) after the forced air flow is terminated. The ignition susceptibility of the surface of the target fuel decreased as the test progressed and was attributed to: the continual oxidation of the firebrand pile, during every forced air flow period, thereby decreasing the temperature of the firebrand pile as well as the thickening of the char layer on the flammable substrate surface which impedes heat transport to the in-depth undecomposed material.

The WRC and OSB ignitions statistics for continuous and intermittent air flow conditions were compared as shown in Table 6-2. The surface ignition events that occurred during the first 60 s of forced air flow exposure (after deposition of the firebrands) was not considered when calculating the mean number of surface ignition events during a single tests when intermittent air flow gust conditions were employed. One of the most compelling metrics is the mean number of surface ignition events that occurred during a single test when using continuous and intermittent gust air flow conditions. The mean number of surface ignition events drastically increases when gusting forced air flow conditions are used rather than when using a continuous forced air flow. The mean number of surface ignitions events for a single test when using a gust intermittent air flow for WRC and OSB was 13 and 19 times higher than when using a constant forced air flow. The drastic increase can be attributed the conditions in the absence of any forced air flow being more conducive to reignition of the flammable substrate. Sufficient amounts of gaseous pyrolyzate and oxidizer are able to mix and be ignited by the high-temperature firebrand pilot located at the air flow facing edge of the pile.

The maximum mean surface ignition time when using a constant forced air flow, considering all of the testing condition combinations for both flammable substrates, was 74 s after deposition of the firebrand pile. When intermittent air flow gusts were used, the fourth reignition event for WRC and the second reignition event for OSB occurred 170 s and 150 s after deposition of the firebrand pile. The probability that at least one surface ignition would occur at the surface of a flammable target substrate increases significantly when using an intermittent air flow condition. The surface ignition probability for WRC in the presence of an intermittent air flow was three times higher than when using a continuous air flow velocity. The surface ignition probability of OSB was six times higher when using an intermittent air flow.

Table 6-2: Comparison of surface ignition behavior between continuous and intermittent air flow conditions when using a 2.7 m s^{-1} forced air flow velocity and a 0.16 g cm^{-2} firebrand pile coverage density.

Substrate	Air flow type	Mean number of surface ignition per test	Probability of at least one surface ignition (%)	Average burn duration (s)
WRC	Continuous	0.33	33	32 ± 16
	Intermittent	4.3 ± 1.6	100	5.1 ± 1.0
OSB	Continuous	0.11	11	32
	Intermittent	2.1 ± 1.2	67	6.8 ± 1.7

The surface flame burning duration was significantly shorter when using an intermittent air flow and the intermittent air flow attributed to the rapid decrease of the firebrand pile heat exposure to the flammable substrate surface. Without the high temperature thermal exposure from the firebrand pile, the mass flux of gaseous fuel is decreased along with the temperature of the firebrand pilot. The average number of ignitions events, in a single test, for WRC and OSB increased when using an intermittent rather than a continuous air flow. It is postulated that a thinner char layer at the surface of the flammable substrate as well as the presence of high temperature firebrands exposed to the intermittent air flow contributed to the increased number of surface ignitions events.

6.3 *Flammable substrate surface ignition location*

Maps of the locations of both the WRC and OSB surface ignition locations when exposing the firebrand pile to an intermittent airflow are shown in Figure 6-5. These maps indicate that the majority of the surface ignition events for both WRC and OSB occurred in front or at the leading edge of the firebrand pile facing the incoming airflow. The surface ignition locations, when using an intermittent airflow, are similar to the ignition locations when exposing the pile to a continuous constant air flow velocity (see Figure 4-14). However, is should be noted that the ignition locations for the intermittent air flow conditions are also within the front 1.5 cm of the leading zone. This movement from the preleading to leading zone can be attributed to the continuous consumption of the firebrand pile during a test. The firebrand leading edge was noted to recede (see Figure 3-1) as it was being continually oxidized during each forced air flow period but the surface ignition event would still originate in front of the pile.

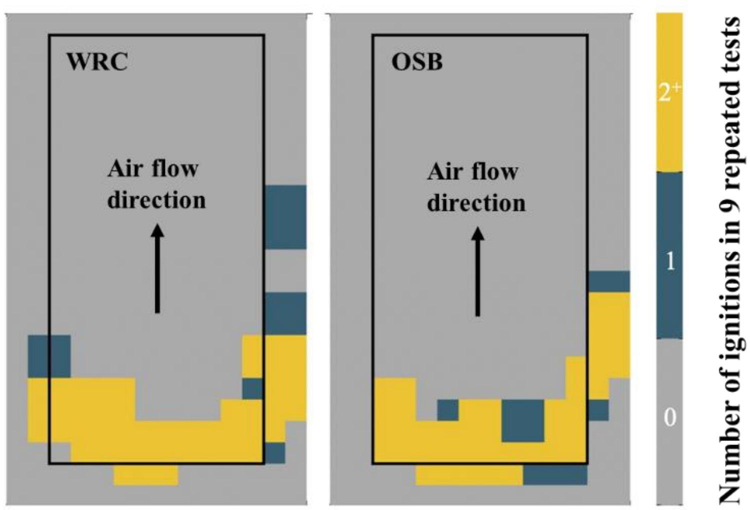

Figure 6-5. WRC (a) and OSB (b) ignition location maps drawn to scale for an intermittent 2.7 m s^{-1} air flow velocity and 0.16 g cm^{-2} firebrand pile coverage density. The black rectangle marks the location of the 50 cm^2 firebrand deposition area.

7 Pyrolysis Characterization of WRC

7.1 Description of the numerical pyrolysis solver, ThermaKin

A numerical solid-phase pyrolysis solver, ThermaKin [77], was used in this work for material property parametrization through inverse modeling of various milligram- and bench-scale experimental data, as well as for the development of a custom firebrand pile heat flux model and a novel numerical ignition model.

ThermaKin accounts for the chemical reactions, transient conduction (governed by temperature-dependent properties), absorption and emission of radiation, transport of gaseous pyrolyzate through the condensed-phase, and the swelling or contraction of the thermally-decomposing substrate. In ThermaKin, the substrate is geometrically defined by a series of layers with a predefined thickness and is chemically defined by specific thermodynamic and physical properties. ThermaKin can be used to solve multi-dimensional (up to 2D) pyrolysis and various burning problems. The ThermaKin modeling environment has been validated using previous investigations on both charring and non-charring polymers [78], [79].

In ThermaKin, the maximum amount of components is restricted to 50 with all components defined as being a gas, liquid, or solid. Chemical and physical properties are defined for each component and include: density, heat capacity, thermal conductivity, mass transport coefficient, emissivity, and absorption coefficient. The first four properties are temperature-dependent and are defined in Equation (7.1) where

p_0, p_1, p_2, and n are user-specified parameters. The emissivity and absorption coefficient are both defined by constant values.

$$property = p_0 + p_1 + p_n T^n \tag{7.1}$$

Chemical reactions in ThermaKin are defined as occurring between two reactants that produce zero to two products as shown in Equation (7.2). θ_i is the stoichiometric coefficient for each component specified as either a reactant or a product. h the evolved energy from each reaction which can also be defined as a temperature-dependent quantity as in Equation (7.1).

$$\theta_1 COMP1 + \theta_1 COMP2 \rightarrow \theta_1 COMP3 + \theta_1 COMP4 + h \tag{7.2}$$

Each reaction is governed by an Arrhenius-type reaction rate as defined in Equation (7.3). In Equation (7.3), A [$\left(\mathrm{m}^3\ \mathrm{kg}^{-1}\right)^{n-1}\mathrm{s}^{-1}$] is the Arrhenius pre-exponential coefficient (for an n order reaction) and the reaction activation energy indicated by E [J mol^{-1}]. R is the molar gas constant [J mol^{-1}K^{-1}] with T the temperature [K] and ξ_{COMP1} and ξ_{COMP2} the reactant concentrations in kg m^{-3}. If only one reactant is produced ξ_{COMP2} is set to unity. h_i [J kg^{-1}] is the heat absorbed or released in each reaction or phase transition.

$$r = A\, exp\left(-\frac{E}{RT}\right) \xi_{COMP1} \xi_{COMP2} \tag{7.3}$$

The rates of consumption or production (in unit volume) of the reactants and products is computed by the multiplication of the reaction rates with the corresponding mass-based stoichiometric coefficients. The heat flow (in unit volume) for each reaction is calculated as the product of the reaction rate by the heat of reaction specified as h. The heat flow becomes positive when the reaction is endothermic.

In the current ThermaKin simulations, the conservation of mass, as shown in Equation (7.4), will be used to capture the change in mass due to the presence of chemical reactions and gas transport at the boundaries of the substrate. Time is denoted by t, N_r represents the number of reactions, and θ_i^j the stoichiometric coefficients of each reaction.

$$\frac{\partial \xi_j}{\partial t} = \sum_{i=1}^{N_r} \theta_i^j r_i - \frac{\partial J_j{}^x}{\partial x} + \frac{\partial}{\partial x}\left(\xi_j \int_0^x \frac{1}{\rho}\frac{\partial \rho}{\partial t} dx\right) \tag{7.4}$$

The conservation of mass accounts for the consumption or production of a component, j, due to: reactions, mass transport of gaseous components within the condensed phase as shown in Equation (7.5), and mass transport associated with the contraction or expansion of the material with respect to the stationary boundary (x = 0). The gas transfer coefficient, λ, does not depend on the nature of the gas that is being transferred through the condensed phase.

$$J_g{}^x = -\rho_g \lambda \frac{\partial(\xi_g/\rho_g)}{\partial x} \tag{7.5}$$

The conservation of energy of the material, as specified in ThermaKin, is shown in Equation (7.6) and is expressed in terms of the material temperature.

$$\sum_{j=1}^{N} \xi_j c_j \frac{\partial T}{\partial t} = -\sum_{i=1}^{N_r} h_i r_i - \frac{\partial q_x}{\partial x} - \frac{\partial I_{ex}}{\partial x} + \frac{\partial I_{rr}}{\partial x} - \sum_{g=1}^{N_g} c_g \left(J_g{}^x \frac{\partial T}{\partial x}\right) + c\rho \frac{\partial T}{\partial x} \int_0^x \frac{1}{\rho}\frac{\partial \rho}{\partial t} dx \tag{7.6}$$

The conservation of energy accounts for the heat flow by thermal degradation of the material and phase transitions. The heat conduction term with the condensed phase, q_x, and the absorption and radiation from an external source is defined in Equation (7.7) and Equation (7.8) respectively. Radiant losses from the material to the environment are defined using Equation (7.9). The convective heat transfer associated with the transport of gaseous pyrolyzate through the condensed phase as well as heat flow associated with the expansion or contraction of the material is also captured in the energy conservation equation outlined in Equation (7.6). Heat transfer due to the expansion and contraction of the material is captured in the left-hand-side terms of Equation (7.6)

$$q_x = -k\frac{\partial T}{\partial x} \tag{7.7}$$

$$\frac{\partial I_{ex}}{\partial x} = -I_{ex}\sum_{j=1}^{N}\kappa_j\xi_j \tag{7.8}$$

$$\frac{\partial I_{rr}}{\partial x} = \frac{\epsilon\sigma T^4}{I_{ex}^0}\frac{\partial I_{ex}}{\partial x} \tag{7.9}$$

Equations (7.8) and (7.9) assume that the exchange of radiative heat between the material and the environment (I_{ex} and I_{rr}) is one-dimensional. The heat transfer between the gases and condensed phase components is assumed to be infinitely fast and is incorporated into Equation (7.6) using the convective heat flow terms (sixth term). The assumption is also made that the momentum transferred from the gases to the condensed phase material is negligible.

The symbols listed in Equation (7.6) are defined as follows: ρ [kg m^{-3}] denotes density, c [J kg^{-1}K^{-1}] is the heat capacity, k [W m^{-1}K^{-1}] is the thermal conductivity, κ [m^2 kg^{-1}] is the absorption coefficient, ϵ is the emissivity. I_{ex} [W m^{-2}] is defined as the radiation flux from external sources traveling within the material, the superscript 0 in I_{ex}^0 denotes net external radiation flux through the material boundary (incident flux minus the reflected flux), and σ [W m^{-2}K^{-4}] is the Stefan-Boltzmann constant. The external heat flux input into ThermaKin is defined by a set of piecewise linear functions. The mass transport of pyrolyzates at the interface between the top layer of the gas phase and the external environment is specified with a linear function.

In ThermaKin, both the mass and energy conservation equations are solved by dividing the material into finite volumes (or elements). The mass and temperature are quantities used to characterize the volume (or element). The transient behavior of the material is computed using small times steps, Δt. A Crank-Nicolson scheme [80] is used to for the time integration of the *x* dimension. Validation simulations have been performed [81] to determine the stability of integration in the *x* dimension. It was concluded that the *x* dimension integration is stable over a wide range of values for Δx and Δt and the accuracy of the results decreases as the time-step and *x*-dimension increments are increased. For the ThermaKin input, a time-step of 0.01 s and a dimension size of 5×10^{-5} m were found to represent a suitable initial guesses.

A hierarchical, inverse analysis methodology initially developed by Li et al. [80], [81] and elaborated on by McKinnon et al. [73], [82] and Gong et al. [83], [84] was used to parametrize the kinetics, thermodynamics, and thermal transport properties of pyrolysis of WRC. Parametrization of all pyrolysis properties was performed by inversely analysis of data collected from Thermogravemetric Analysis (TGA), Differential Scanning Calorimetry (DSC), Microscale Combustion Calorimetry (MCC), and Controlled Atmospheric Pyrolysis Apparatus (CAPA II) experiments using ThermaKin.

7.2 Simultaneous Thermal Analysis (STA)

7.2.1 <u>Overview of operation and model parameterization</u>

All STA experiments were conducted in a Netzsch 449 F3 Jupiter (shown in Figure 7-1) which is used to simultaneously generate TGA and DSC experimental data. The apparatus includes both a reference and a sample crucible which are exposed to user-defined heating program. Simultaneous measurements of mass evolution (TGA) and heat flow to the sample (DSC) as a function of time and temperature are performed. All STA experiments were performed in an inert nitrogen atmosphere to emulate typical atmospheric conditions at the surface of burning substrate underneath a diffusion flame.

The STA was routinely calibrated (every three months) using organic and inorganic compounds, with known melting points and heats of melting, to ensure that both a quantitative relationship between the measured and the true value of the thermocouple, measuring the temperature of the sample, and an accurate heating program was maintained. The calibration was performed for platinum-rhodium and aluminum oxide ceramic crucibles. The calibration for platinum-rhodium crucibles was performed using six organic compounds while five ultra-high purity metals were used for the ceramic crucible calibration. The calibration temperature ranged from 313 K to 1000 K.

Figure 7-1. Schematic of the Simultaneous Thermal Analysis (STA) apparatus.

All WRC samples tested in the STA using platinum-rhodium crucibles were prepared in the form of a powder using a second cut mill flat file. A 0.5 m by 0.3 m WRC board was used to generate multiple WRC powder samples. The board was separated into 15 0.1 m by 0.1 m squares and a powder mixture was generated for each of the WRC board squares. The mass of the powder samples used in the STA experiments were between 4 - 6 mg and were placed in a desiccator with Drierite for at least 48 hours prior to testing to ensure minimal moisture variations between samples. All platinum-rhodium crucible experiments were performed with lids. Each lid was perforated which allowed gaseous decomposition products to escape the crucible during an experiment.

10 STA experiments were conducting using platinum-rhodium crucibles at a heating rate of 10 K min^{-1} within an inert atmosphere maintained at a flowrate of 50 ml min^{-1} nitrogen. A heating rate of 10 K min^{-1} was selected to ensure that samples did not experience significant temperature or concentration gradients during an experiment, allowing for accurate isolation of thermal degradation kinetics and energetics. Before each experiment, a baseline test was performed using an empty sample crucible under identical testing conditions to account for any environmental differences, buoyancy effects, and asymmetry of the furnace and the crucibles.

When using ThermaKin to simulate the thermal decomposition behavior of WRC in the STA apparatus, the samples were modeled as being thermally thin and where simulated as a single spatial element (thickness = 5×10^{-5} m). The element temperature was forced to follow the experimental temperature by defining a sufficiently high convective coefficient of 1×10^{5} W m^{-2} K^{-1} at the boundary between the top surface of the element and the environment. The mass flow boundary conditions were defined in ThermaKin such that the gaseous pyrolyzates, produced during the thermal decomposition of the element, would instantaneously escape the top surface of the element. A hill climbing optimization algorithm, implemented as a Matlab script coupled with ThermaKin, was used to automate inverse analysis of the TGA data which generated data for all kinetic parameters used to predict the thermal decomposition of WRC. A goodness-of-fit criterion was adopted to serve as a target of optimization of the TGA data as highlighted in Equation (7.10). More details on the algorithm implementation can be found elsewhere [85].

$$GoF_M = 1 - \left(\frac{0.6}{MLR_{max,exp}} \sqrt{\frac{\sum_i^N \left(MLR_{i,exp} - MLR_{i,model} \right)^2}{N}} + \frac{0.4}{m_{max,exp}} \sqrt{\frac{\sum_i^N \left(m_{i,exp} - m_{i,model} \right)^2}{N}} \right) \quad (7.10)$$

The heating rate employed in the STA varied prior to reaching the nominal (prescribed) heating rate value. To account for this heating rate variation, the modeled heating rate was expressed as an exponentially decaying sinusoidal function as shown in Equation (7.11). a_1[K s^{-1}], a_2[s^{-1}], a_3 [s^{-1}] and a_4 [-] are constants fitted to capture the experimental data.

$$\frac{dT}{dt}(t) = a_1 \left\{ 1 - exp(-a_2 t) \left[cos(a_3 t) + a_4 sin(a_3 t) \right] \right\} \quad (7.11)$$

The values of the constants implemented in Equation (7.11) for three heating rates used for the operation of the STA apparatus are summarized in Table 7-1. All experimental heating rate profiles were fitted with a coefficient of determination larger than 0.95. The experimental and ThermaKin-simulated heating rates implemented in this study are shown in Figure 7-2.

Table 7-1: Parameters describing the evolution of the instantaneous heating rates employed in STA experiments

Nominal heating rate	a_1 (K s^{-1})	a_2 (s^{-1})	a_3 (s^{-1})	a_4 (-)
5 K min^{-1}	0.0835	0.0028	0.0052	-0.5788
10 K min^{-1}	0.1677	0.0033	0.0052	-0.7873
20 K min^{-1}	0.3177	0.0030	0.0028	-1.8980

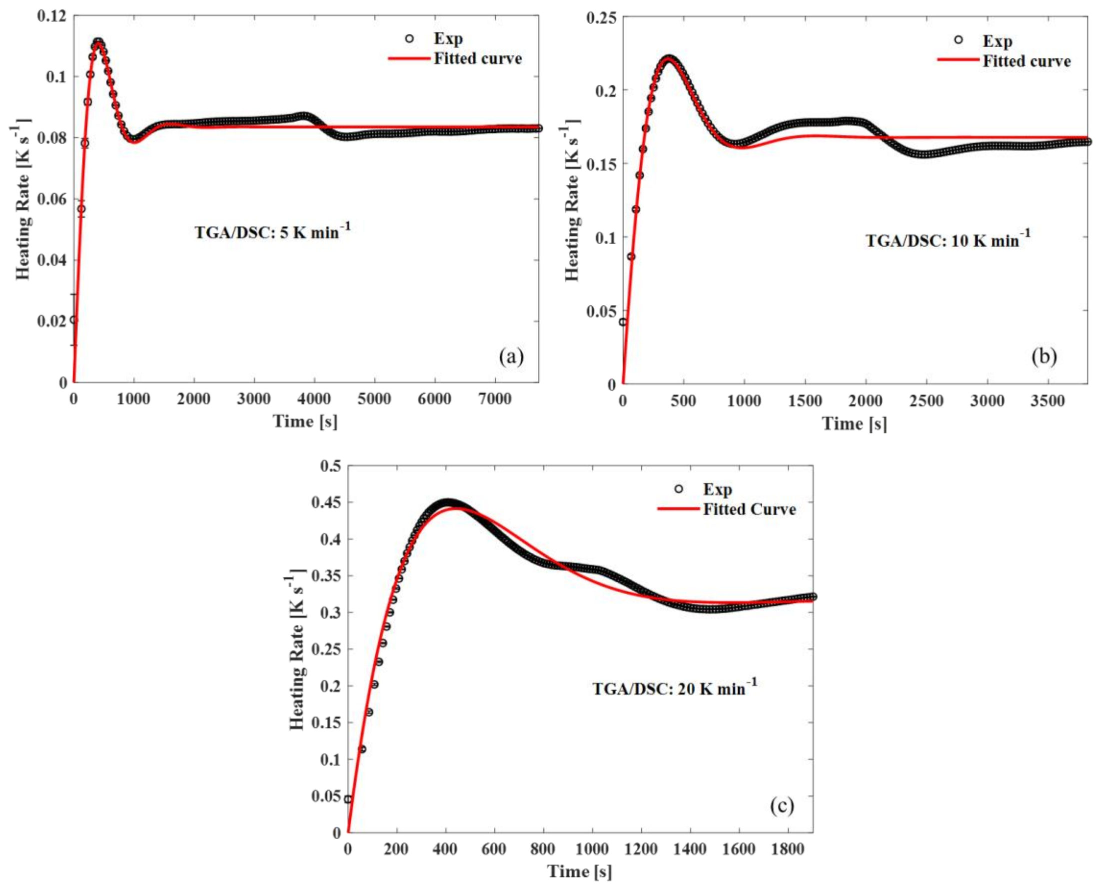

Figure 7-2. Averaged experimental and fitted heating rate profiles obtained for the TGA/DSC for a nominal heating rate of (a) 5 K min^{-1}, (b) 10 K min^{-1}, (c) 20 K min^{-1}.

7.2.2 STA data analysis and model development

The experimental mean mass, mass loss rate (MLR), heat flow, and integral heat flow normalized by the initial sample mass (m_o) obtained in the STA experiments performed at 10 K min^{-1} are shown in Figure 7-3. The uncertainties in the experimental data were calculated from the scatter of the data as two standard deviations of the mean. The experimental TGA data was reproducible for all 10 experiments while the scatter of the DSC data was found to increase with temperature due to the reduction in the sample mass which results in reduced contact between the sample and the bottom interior of the crucible and increasing baseline uncertainties.

Six consecutive reactions were identified to accurately capture the WRC MLR curve shown in Figure 7-3 (b): the first MLR peak below 400 K, the onset of mass loss at the axisymmetric shoulder of the main peak, an intermediate peak, the global MLR peak, a minor peak around 700 K and a slow decaying segment in the range of 800 K. The first peak is associated with the vaporization of chemically-bound water in the amount of 0.6 wt.%. The peaks associated with the second to fifth reaction were identified using the MLR and DSC heat flow curves and are located at 480 K, 600 K, 648 K and 710 K respectively. These and the last reaction can be attributed to the thermal decomposition of the WRC components.

From the DSC heat flow data shown in Figure 7-3 (c), the first 4 reactions are either endothermic or thermally neutral while the fifth reaction is exothermic. The presence of an exothermic step during the thermal decomposition of charring polymeric materials has been observed by Li and Stoliarov [86]. Wood pyrolysis, consisting of an endothermic phase followed by and exothermic phase has also been documented by Atreya et al. [87] and Gong et al. [83].

A methodology outlined by Gong et al [83] was considering during the ThermaKin modeling portion of this study for WRC. In [83], the thermal decomposition kinetics and heat flow properties for OSB were parametrized. The OSB thermal decomposition model was formulated using a series reaction scheme. A majority of earlier studies [88],

[89] on wood-based products have used parallel reaction schemes to simulate their thermal decomposition process. The assumption of parallel reactions is consistent with the multi-component nature of lignocellulosic solids. However, this requires knowledge of the composition of the undecomposed material. Usually, the composition of the undecomposed material is not known and is obtained through optimization. Therefore, a series of first-order reactions was used to simulate the decomposition of OSB which ensured that the mean experimental data was captured using a minimum number of adjustable parameters thereby reducing the complexity of the ThermaKin decomposition model. Hence, the thermal decomposition of WRC was also formulated as a series of first-order reactions. The WRC series reactions were optimized using the mass loss and mass loss rate data (see Figure 7-3(a) and (b)) as target measurements and are summarized in Table 7-2. It was determined that the WRC used in the STA experiments included 0.6% chemically-bound water.

Table 7-2: A reaction mechanism for the thermal decomposition of WRC

Reaction number	Reaction equation
1	Water → $Water_{vapor}$
2	WRC → 0.952 WRC1 + 0.048 Gas1
3	WRC1 → 0.627 WRC2 + 0.373 Gas2
4	WRC2 → 0.523 WRC3 + 0.477 Gas3
5	WRC3 → 0.721 WRC4 + 0.279 Gas4
6	WRC4 → 0.483 Char + 0.517 Gas5

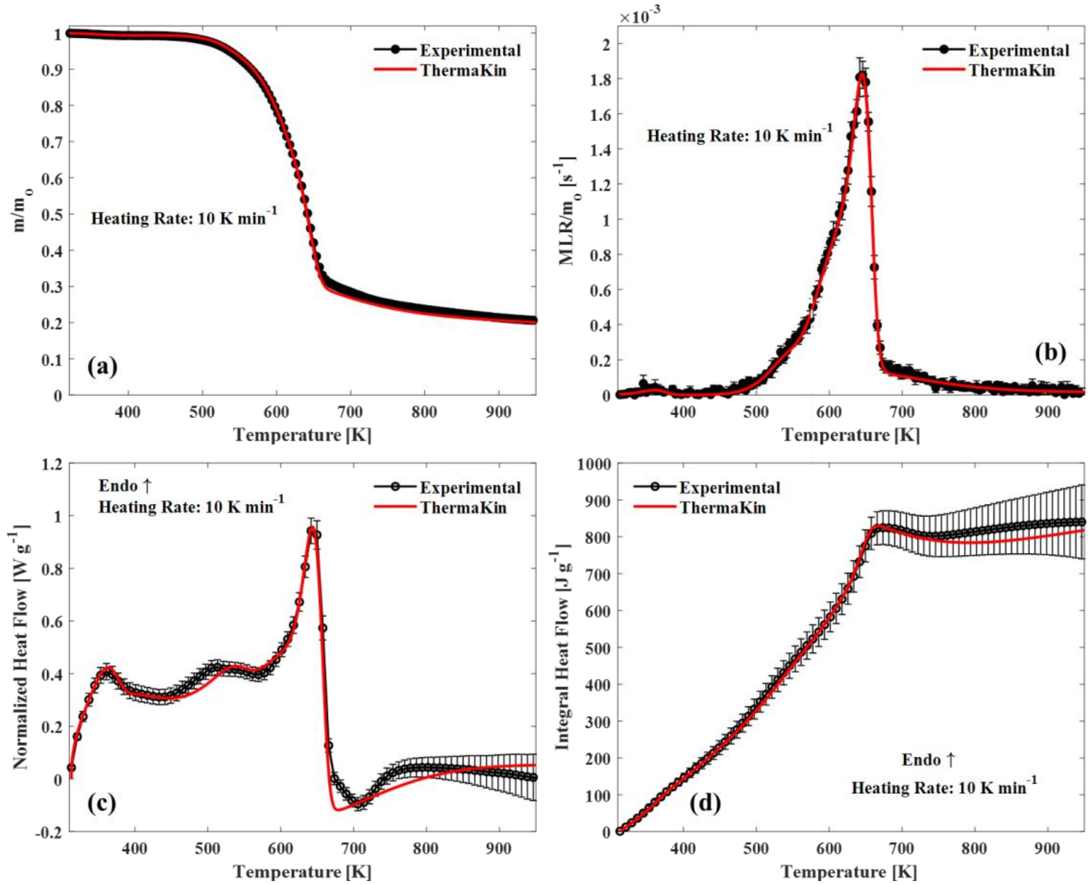

Figure 7-3. Experimental and simulated TGA ((a) and (b)) and the DSC ((c) and (d)) data obtained for WRC at 10 K min^{-1}.

The hill-climbing algorithm was used to optimize the Arrhenius reaction rate parameters (A and E), the reaction stoichiometric coefficients (θ_i), and the heats of reaction (h) to fit the mean experimental TGA data at 10 K min^{-1}. The modeled curves shown in Figure 7-3 capture the TGA and DSC well within the measurement uncertainties. The reaction parameters are summarized in Table 7-3. The Arrhenius reaction rate parameters and the heat of reaction of water vaporization was obtained from literature [83].

Table 7-3: Thermal decomposition reaction parameters obtained for WRC using the hill-climbing algorithm

Reaction number	A (s^{-1})	E (J mol^{-1})	h (J kg^{-1}) (exo)
1	1.55×10^4	4.35×10^4	-2.78×10^6
2	1.4×10^8	1.05×10^5	-2.6×10^4
3	2.57×10^6	1.01×10^5	-7.7×10^4
4	5.69×10^{18}	2.55×10^5	-2.8×10^5
5	5.48×10^{-2}	1.88×10^4	5×10^5
6	3.67×10^{-4}	5.46×10^3	3×10^3

The heat capacity is a user-defined parameter within ThermaKin which is required to simulate the heat flow of each liquid or condensed-phase component as a function of temperature. The heat capacity is calculated by dividing the measured heat flow (normalized transient DSC curve) by the instantaneous heating rate. The heat capacity of the WRC component (representing the undecomposed WRC material) was obtained from the DSC curve for the temperature range in between the vaporization of water (390 K) and the onset of decomposition of the undecomposed WRC material (450 K).

A separate set of five STA tests was performed using the WRC solid residue generated during the initial set of undecomposed WRC STA tests to obtain the WRC solid residue heat capacity. The WRC solid residue tests were performed using platinum-rhodium crucibles with lids. The undecomposed WRC tests could not be used to obtain the solid residue heat capacity due to contact issues between the sample and the bottom face of the crucible that originates at the higher temperature testing range.

The heat capacity of the residual char was obtained over the temperature range spanning 600 K to 800 K. The continual formation of char is captured in this specified temperature range. The heat capacity of the undecomposed WRC component was obtained from the segment of the DSC curve located between water vaporization and the onset of thermal decomposition as shown in Figure 7-4. The temperature-dependent heat capacity of the undecomposed WRC component and the char component was formulated using a linear fit. The heat capacity of water was obtained from literature [68].

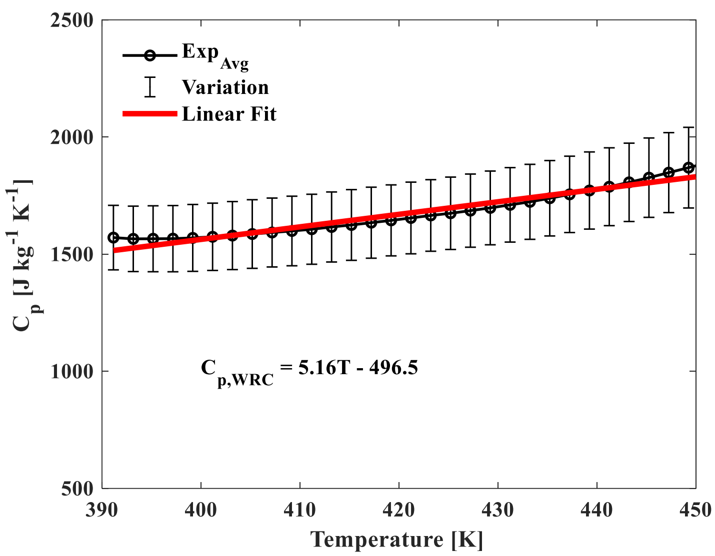

Figure 7-4. Linear fitting of WRC heat capacity as shown by the solid red line.

The heat capacities of the intermediate components were calculated by interpolating between the heat capacities of the undecomposed WRC and char component in equal steps (20%). As an example, the heat capacity of WRC1 was calculated as the summation of 80% of the undecomposed WRC heat capacity and 20% of the char heat capacity. The heat capacities of all the components are summarized in Table 7-4.

Table 7-4: Heat capacities of all condensed phase components

Component	C_p (J kg^{-1} K^{-1})
Water	5200 - 6.7T + 0.011T^2
WRC	-496.5+ 5.16T
WRC1	-214 + 4.22T
WRC2	69.4 + 3.29T
WRC3	350.9 + 2.35T
WRC4	633 + 1.42T
Char	915.8 + 0.48T

7.2.3 Thermal decomposition kinetics validation

Two additional heating rates were used to determine whether the WRC thermal decomposition model developed at 10 K min^{-1} could be used to simulate the decomposition behavior of WRC at a heating rate of 5 and 20 K min^{-1}. Ceramic crucibles (without lids) were used for these experiments to verify that neither the material nor configuration of the sample container affected the thermal decomposition of WRC. Figure 7-5 indicates convergence between the experimental and ThermaKin-simulated data. Therefore, the conclusion cane be made that the optimized thermal decomposition model can be used to accurately simulate the thermal decomposition behavior of WRC at other heating conditions. The accurate prediction of TGA mean experimental data further suggests that the presence of lids or changing the crucible material does not affect the WRC decomposition kinetics. The WRC thermal decomposition model also accurately predicts the final residue yield obtained in TGA experiments at other heating rates.

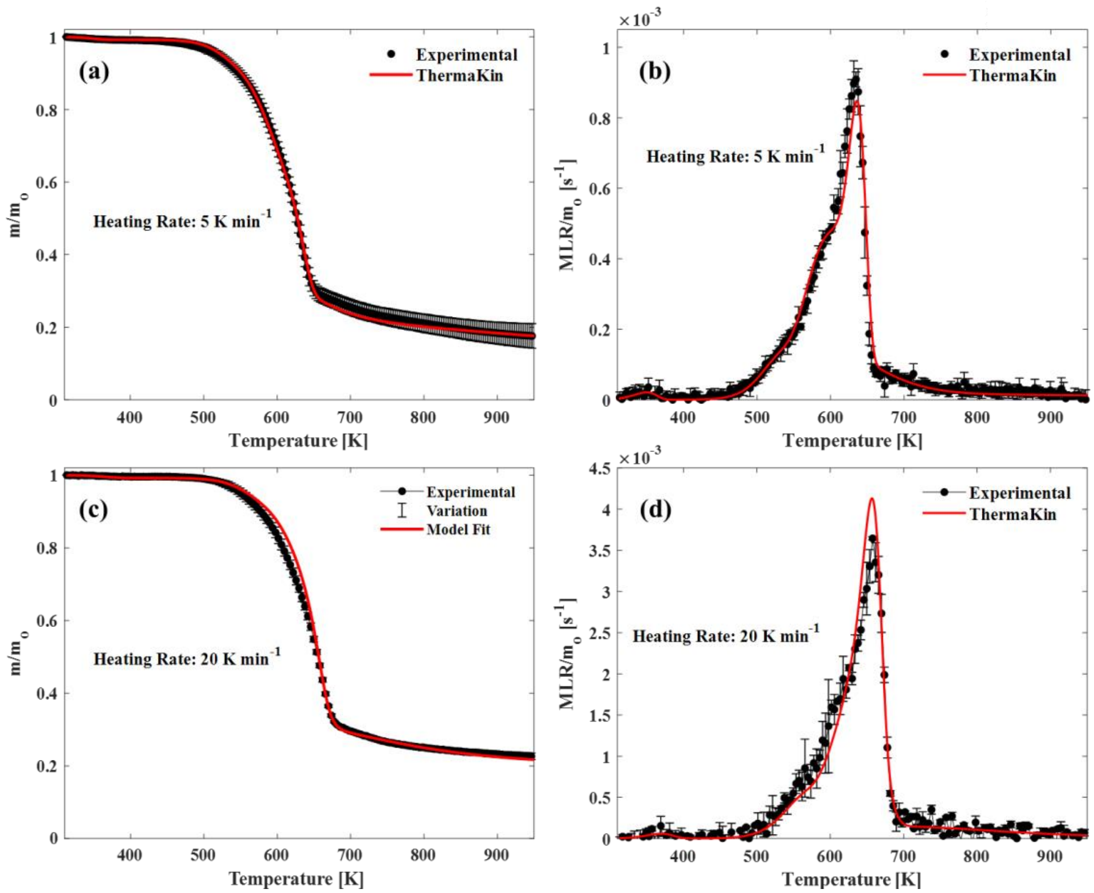

Figure 7-5. Experimental and predicted TGA data obtained for WRC at (a), (b) 5 K min^{-1} and (c), (d) 20 K min^{-1}.

7.3 Microscale Combustion Calorimetry (MCC)

MCC [90] is a milligram-scale flammability testing technique designed to obtain the heat release rate (HRR) [W g^{-1}] associated with the complete combustion of pyrolyzate gases evolving from the pyrolysis of a material within an environment similar to STA. A bisectional schematic of the MCC is shown in Figure 7-6. In the MCC apparatus, a milligram-scale sample is placed within a ceramic crucible and undergoes pyrolysis within an inert environment maintained using an 80 ml min^{-1} nitrogen purge flow. The sample is heated within the pyrolyzer zone at a heating rate of 10 K min^{-1} up to a maximum end temperature of 1023 K. The evolved pyrolyzate gases are transport upward towards the combustor zone, which is held at a constant, high temperature of 1173 K, and are mixed with a steady, 20 ml min^{-1} flow of O_2. The high temperature of the combustor ensures complete aerobic combustion of the evolved pyrolyzates.

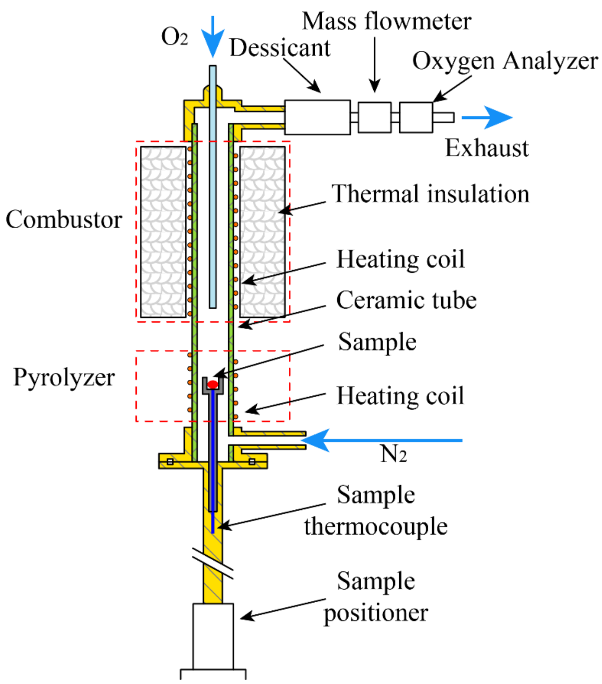

Figure 7-6. Rendering of the MCC apparatus

The MCC HRR is obtained using oxygen consumption calorimetry which incorporates both the flowrate and oxygen concentration percentage within the exhaust line, downstream of the combustor. The HRR was recorded as a function of time and pyrolyzing sample temperature. The exhaust flowmeter was calibrated against a Bios volumetric flow calibrator that measures the displacement time of a piston within a cylindrical annulus of known volume prior to testing. The automotive O_2 sensor was calibrated daily using a known flowrate of dry air with an O_2 concentration of 20.1 vol. %. The thermocouple positioned underneath the crucible was calibrated using four high-purity metals with known melting temperatures. The thermocouple was calibrated to compensate for the thermal lag between the bottom interior and bottom exterior face of the crucible. The accuracy of the MCC calibration was validated by conducting a set of MCC experiments using general purpose polystyrene as the sample material. The mass of the polystyrene ranged between 2.5 - 4 mg. The heat of combustion derived from the generated polystyrene HRR profile was found to be within experimental variation of the standard reference value of 39.7 ± 0.5 kJ g^{-1}.

Three WRC MCC experiments were performed with all samples weighing between 4 and 5 mg. Three experiments were deemed adequate as the MCC results were found to be highly reproducible. The samples were placed in a desiccator, which was kept at a relative humidity of 21 - 24% to ensure negligible moisture variations between samples, for at least 48 hours prior to testing. The samples were pyrolyzed in an anaerobic environment at a nominal heating rate of 10 K min^{-1}. The MCC experimental heating rate data along with the average simulated heating rate profile expressed as an exponentially decaying sinusoidal function, calculated using Equation (7.11), is shown in Figure 7-7. The parameters a_1, a_2, a_3, and a_4 used to capture the nominal MCC heating rate profile were equal to 0.1692 K s^{-1}, 0.0037 s^{-1}, 0.0042 s^{-1}, and -0.271 respectively.

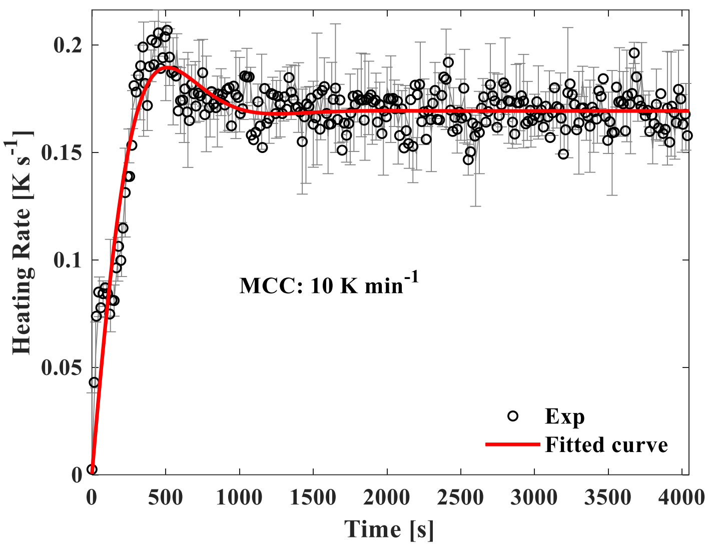

Figure 7-7. Averaged experimental and numerically-fitted MCC heating rate profile obtained at a nominal heating rate of 10 K min^{-1}

The complete heat of combustion of WRC (normalized by the initial sample mass) was calculated by integrating the normalized average HRR profile over the time frame corresponding to the temperature range from 450 K to 800 K. A trapezoidal integration technique was used to calculate the complete heat of combustion of WRC. The average complete heat of combustion of WRC was equal to 11.87 $\pm$ 0.71 kJ g^{-1}. The residue yield was calculated by measuring the final sample mass after the completion of each test and dividing it by the initial sample mass. The mean WRC residue yield (%) was calculated to be equal to 18.5 ± 3.4. The MCC solid residue yield was found to be consistent with STA solid residue yields.

The MCC average experimental HRR data was used to inversely analyze the heats of combustion of all gaseous intermediates defined in the WRC reaction scheme. First, the modeled TGA MLR data was directly compared to the MCC experimental HRR data as shown in Figure 7-8. A slight difference between the two profiles was identified and corrected by shifting the MCC HRR data by 12 K towards the higher temperature. The slight difference was attributed to a non-uniformity between the top and bottom surface temperature of the MCC sample. The top sample surface temperature was slightly higher due to additional radiant heating from the high-temperature combustor, a heating effect that was not fully captured by the sample temperature thermocouple located underneath the sample crucible.

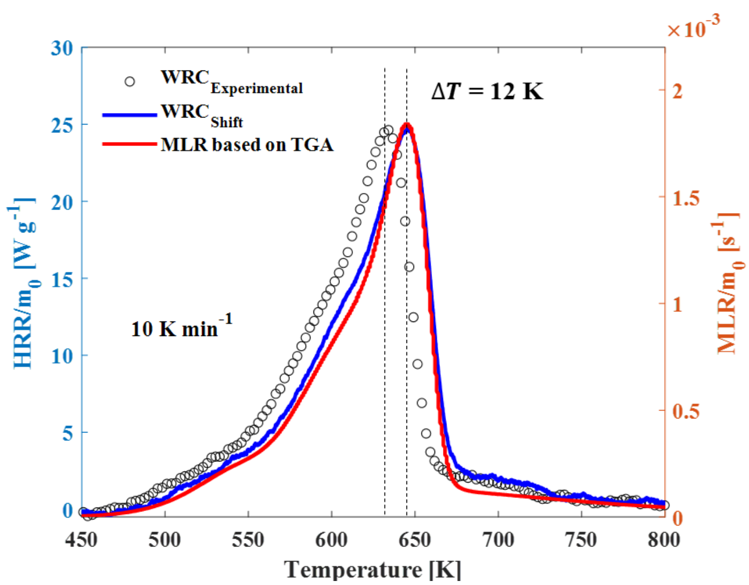

Figure 7-8. Comparison of original and shifted average experimental HRR data from MCC with the modeled MLR data from TGA experiments.

The average WRC HRR profile from the MCC experiments was predicted using MLR data, generated using ThermaKin, for all individual gaseous intermediates. In the ThermaKin, the thermal decomposition of WRC was captured using the heating rate shown in Figure 7-7. Initially, a single heat of combustion value (1×10^7 J kg^{-1}) was assigned to each of the gaseous intermediates to generate an average MCC HRR profile. The HRR of each gaseous intermediate was calculated by multiplying the heat of combustion value of each evolved gas with its corresponding normalized MLR. A fitting criterion was used to ensure an adequate match between the experimental MCC and ThermaKin-simulated HRR data was obtained. The criterion was developed in earlier studies [83] and comprised less than 5%, 5 K, and 5% difference in the maximum HRR, the temperature of the maximum HRR, and the final integral HRR value respectively. The fitting criterion was not satisfied when using a single heat of combustion value (1×10^7 J kg^{-1}) for all gaseous intermediates. Therefore, the heat of combustion value of each individual evolved gas was optimized until an adequate match between the experimental and ThermaKin-simulated HRR profile was obtain which satisfied the MCC fitting criterion. The heats of combustion values for all gaseous intermediate components are listed in Table 7-5.

Table 7-5: Heats of combustion values for all gaseous intermediate components.

Gaseous intermediate component	h_c (kJ g^{-1})
Gas1	11.5
Gas2	14.8
Gas3	13.6

Gas4	18.0
Gas5	5.0

The ThermaKin-simulated HRR and integral HRR profiles are compared with the corresponding experimental average MCC HRR profiles in Figure 7-9 (a). The experimental variation was calculated as two standard deviations of the mean.

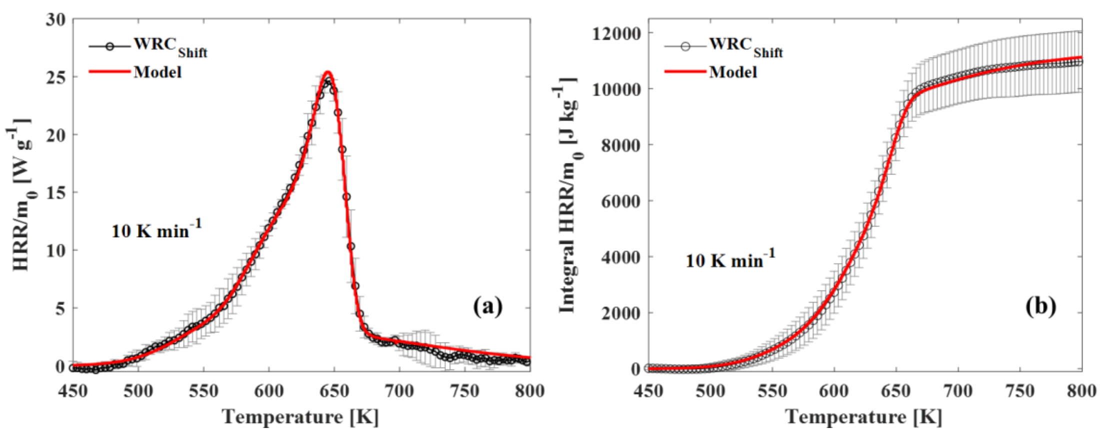

Figure 7-9. MCC (a) normalized HRR profile and (b) normalized integral HRR profile for WRC when using a nominal heating rate of 10 K min^{-1}. The experimental variation was calculated as two standard deviations of the mean.

From Figure 7-9 (a) is can be concluded that the experimental MCC HRR profile can be accurately predicted using the gaseous intermediate product heat of combustion values listed in Table 7-5 along with the MLR of each gaseous intermediate. Figure 7-9 (b) further validates this conclusion with an adequate match between the experimental and ThermaKin-simulated integral HRR being obtained.

7.4 Controlled Atmospheric Pyrolysis Apparatus (CAPA II)

The CAPA II apparatus, as shown in Figure 7-10 [91], is a bench-scale apparatus use to perform controlled-atmosphere experiments in which pyrolysis of the sample is driven by radiation. The top surface of an axisymmetric disk-shaped sample is subjected to radiation from a temperature-controlled conical heater. The radiation from the conical heater has been carefully characterized to account for changes in the angular orientation and position of the sample surface. The exterior wall of the gasification chamber is lined with a cooling system in which a steady flow of water ensures well-defined boundary conditions are maintained. The bottom sample temperature, T_{bottom}, as well as the sample mass loss as a function of time are continuously measured using a handheld FLIR E45 thermal imaging camera and a Sartorius high-precision (1 mg resolution) balance respectively. An average bottom sample temperature profile for each tests was generated using 12 spot measurements located along four radial planes (0, 1, 2, 3 cm) for each test. The reader is referred to the study by Swann et al. [91] where the back surface temperature data generation methodology is described in detail. The shape profile evolution of a sample was recorded with a Logitech webcam with optical access to the top surface of the sample gained via a quartz window. The gasification chamber is purged with 185 L min^{-1} of nitrogen to ensure that the atmosphere at the top surface of the sample, mounted within the gasification chamber, is maintained at an oxygen concentration below 1 vol. %. The near-anaerobic environment ensured negligible sample oxidation effects and emulates solid burning conditions underneath a diffusion flame [92]. The flow of nitrogen was homogenized using an array of glass beads which were placed within the gasification chamber and were located under the top surface of the sample.

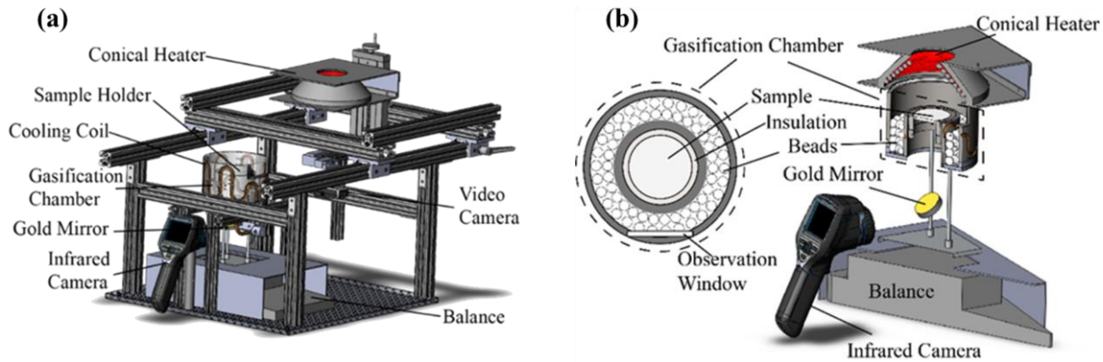

Figure 7-10. (a) Three-dimensional schematic of the CAPA II apparatus and (b) a close-up view of the thermal imaging system used in CAPA II experiments.

The sides of the WRC samples were insulated with rings cut out of Kaowool PM ceramic fiber board to generate near-adiabatic radial boundary conditions. A single layer of 0.025 mm thick copper foil was glued to the back surface of the WRC sample using a thin layer of epoxy. The mass of the epoxy used to adhere the copper foil to the bottom WRC surface did not exceed 0.2 g. The epoxy was used to ensure that adequate thermal contact between the surface of the WRC and the copper foil was maintained and to reduce the effect of potential sample swelling, and morphing. The back surface of the copper foil, facing the optical view of the IR camera, was painted with a MedTherm high-temperature, known-emissivity optical black coating with a broadband emissivity of 0.92 to ensure accurate back surface temperature measurements. The IR camera was focused on the copper foil using a circular gold mirror and the settings of the camera were adjusted to account for mirror transmission losses. A 0.76 cm thick piece of diamond-shaped aluminum mesh was positioned on top of the painted side of the copper foil which was used to structurally support the sample. The aluminum mesh was also painted with the high-temperature optical black coating.

A set of fine (0.025 m diameter bead) thermocouples positioned inside the gasification chamber and above the glass beads were used to measure the temperature of the nitrogen flowing over the top surface of the sample, T_{top}^{e}. The nitrogen temperature measurements would be used to compute convective losses at the top surface of the sample. T_{top}^{e} was measured at three different locations and at the same height inside the gasification chamber in an effort to capture the location dependence of T_{top}^{e} within the chamber. Another fine thermocouple was mounted along the interior wall of the gasification chamber and was in proximity to the bottom face of the sample. The temperature reading from this thermocouple, T_{bottom}^{e}, was used to compute convective and radiative heat feedback from the environment to the bottom surface of the sample.

The current CAPA II experiments were performed using WRC samples having an average thickness and radius of 0.91 cm and 3.4 cm respectively. The WRC samples were placed in desiccator for at least 48 hours prior to testing to minimize moisture content variation between samples. Two different incident radiant heat fluxes, 28.9 and 62.7 kW m^{-2}, were used during this study. The conical heater radiant heat flux was calibrated using a water-cooled Schmidt-Boelter heat flux gauge that was calibrated against a NIST-traceable reference. Duplicates tests were performed for each identified incident radiant heat flux and the results of these tests were used for thermophysical property parameterization and pyrolysis model validation.

7.4.1 CAPA modeling

The modeling of the CAPA II WRC experiments was performed using the most up-to-date version of the comprehensive pyrolysis solver ThermaKin. The reader is referred to Section 7.1 for a more detailed description of ThermaKin. ThermaKin was used in a one-dimensional mode to analyze and simulate CAPA II experimental data. The one-dimensional mode was deemed sufficient because the experimental data indicated that both T_{bottom} and the sample thickness remained uniform in the radial direction for the duration of all CAPA II tests. Unimpeded gas flow through the condensed phase was assumed and was captured by setting the gas transfer coefficient of all gaseous decomposition products equal to 2×10^{-5} m^2 s^{-1}. The top sample surface was simulated to have no resistance to gas flow while the bottom sample surface was simulated as being impenetrable to gas flow. All CAPA II simulations were performed using a 0.05 mm spatial discretization and a time step equal to 0.01 s. Increasing or decreasing the spatial discretization and time step by a factor of two did not produce significant simulation differences, which in turn indicated convergence of the CAPA II simulation results. Run times for CAPA II tests ranged from 15 – 25 minutes depending on the magnitude of the incident heat flux.

7.4.2 CAPA II boundary conditions

The convective heat losses from both the top and bottom surface of the material were computed using the experimentally measured $T_{top}^{e}$and T_{bottom}^{e} temperature data. The convective losses at the top surface of the sample, facing the conical radiant heater, were calculated using a previously determined convective coefficient [91] of 7.2 W m^{-2} K^{-1} and T_{top}^{e} which evolution in time was captured using Equation (7.12).

$$T_{top}^{e} = T_1^e \exp(T_2^e t) + T_3^e \exp(T_4^e t) + T_{HFG} \tag{7.12}$$

where T_1^e, T_2^e, T_3^e, T_4^e are all constants fitted to the experimental data, and T_{HFG} is constant indicative of the temperature of the water continuously flowing through the heat flux gauge, and t is the time during a test. These constants are unique to the constant incident heat flux used during a CAPA II test and are listed in Table 7-6.

Table 7-6: Parameters of Equation (7.12) representing the top surface environmental temperature, T_{top}^{e}, in CAPA II tests dependence on time

Incident heat flux (kW m^{-2})	T_1^e (K)	T_2^e (K s^{-1})	T_3^e (K)	T_4^e (K s^{-1})	T_{HFG} (K)
28.9	57.33	1.10×10^{-4}	-39.18	-2.04×10^{-2}	290
62.7	113.61	1.40×10^{-4}	-78.18	-1.99×10^{-2}	290

Linear empirical correlations capturing the dependence of each parameter listed in Equation (7.12) on incident heat flux were developed and allow interpolation and extrapolation of parameters at other incident heat fluxes. The linear correlations for each of the parameters listed in Equation (7.12) as presented in Table 7-7. The reader is directed to the Appendix section where a comparison between the experimental and predicted top surface temperature data is presented.

Table 7-7: Linear empirical correlations used to calculate each of the constants listed in Equation (7.12) for any CAPA II constant external incident heat flux.

Parameter	Linear empirical correlation
T_1^e (K)	$= 1.66(\text{Incident heat flux}) + 6.55$
T_2^e (K s^{-1})	$= (2 \times 10^{-6})(\text{Incident heat flux}) + (1 \times 10^{-5})$
T_3^e (K)	$= -1.14(\text{Incident heat flux}) - 3.82$
T_4^e (K s^{-1})	$= (-5 \times 10^{-5})(\text{Incident heat flux}) - 0.017$

The convective and radiative heat feedback between the environment and the bottom sample surface was computed using T_{bottom}^e which was approximated a piecewise linear expression as shown in Equation (7.13).

$$T_{bottom}^e = \begin{cases} b_1 t + b_2, & \text{when } t < t_c \\ b_{3,} & \text{when } t \geq t_c \end{cases} \tag{7.13}$$

where b_1, b_2, b_3, and t_c are constants fitted to the experimental data. The convective losses at the bottom surface were computed using a previously determined [91] convective coefficient equal to 4.0 W m^{-2} K^{-1}. Each of the parameters used to simulate the transient T_{bottom}^e behavior are listed in Table 7-8. Empirical correlations for the parameters used to simulate the T_{bottom}^e data was not required as these parameters could be manually generated through visual inspection.

Table 7-8: Parameters of Equation (7.13) representing the bottom surface environmental temperature, T^{e}_{bottom}, in CAPA II tests dependence on time

Incident heat flux (kW m^{-2})	b_1 (K s^{-1})	b_2 (K)	b_3 (K)	t_c (s)
28.9	0.035	303	317	400
62.7	0.085	308	342	400

7.4.3 CAPA II decomposition kinetics

The thermal decomposition kinetics of WRC was characterized in Section 7.2. The WRC samples used during CAPA II experiments consisted of 4.6 wt.% water (dry basis) and 95.4 wt.% of organic constituents and is cumulatively referred to as the undecomposed WRC component. The water content of the WRC samples used in CAPA II experiments was determined by oven-drying multiple desiccated WRC samples. The water content was calculated as the average difference in mass between the desiccated and oven-dried samples normalized by the average mass of the dried samples. The WRC decomposition reaction scheme is presented in Table 7-2 and are all of first order. The reaction parameters describing the thermal decomposition of WRC are presented in Table 7-3 and include the mass-based stoichiometric coefficients, pre-exponential factors (A), reaction activation energies (E), and heats of reaction (h). The heat capacities (c_p) of all components which include undecomposed WRC, the condensed-phase intermediates, and the char residue are presented in Table 7-4. The heat capacities of all WRC gaseous decomposition intermediates were set to be equal to 2100 J kg^{-1} K^{-1}, which has been determined to be the mean heat capacity for a group of C1 to C8 hydrocarbons measured at a temperature of 600 K [93]. The mean heat capacity of water vapor was obtained from literature [73]. The heats of combustion for all gaseous decomposition intermediates are presented in Table 7-5.

The development of a comprehensive WRC pyrolysis model was completed by quantifying all remaining condensed-phase thermophysical and optical properties using the results from CAPA II tests. It was assumed that all WRC condensed-phase components were opaque and therefore in-depth absorption of radiation was negligible. The broadband emissivity of each condensed-phase component was computed using the optical data collected by Forsth and Roos for plywood, a frequently-used engineered wood product [84]. The emissivity of plywood was observed to decrease from 0.81 to 0.70 as it underwent decomposition when exposed to a gray body radiation source set at 1153 K. The broadband emissivity of the virgin WRC and the char residue were selected as 0.81 and 0.70 respectively. The emissivities of all condensed-phase intermediates were computed by linear interpolation between 0.81 and 0.70. The emissivity of water was assumed to be the same as the undecomposed WRC component.

The thermal conductivities (k) of all condensed-phase components were determined using the mean T_{bottom} data collected from the 62.7 kW m^{-2} CAPA II tests. The T_{bottom} data would serve as a target measurement for optimization of each thermal conductivity value. The results from the CAPA II tests using a 62.7 kW m^{-2} incident heat flux were used because the WRC sample did not completely decompose in the 28.9 kW m^{-2}

CAPA II tests. The condensed-phase thermal conductivities were determined using an optimization algorithm implemented as a MATLAB script coupled with ThermaKin. The optimization algorithm was used to automate inverse analysis of CAPA II data with optimization convergence defined using a single goodness-of-fit criterion shown in Equation (7.14).

$$GoF_T = 1 - \sqrt{\frac{\sum_{i=1}^{N}\left(\frac{T_{Bottom,i}^{model} - T_{Bottom,i}}{T_{Bottom,i}}\right)^2}{N}} \tag{7.14}$$

where $T_{Bottom,i}^{model}$ and $T_{Bottom,i}$ are the simulated and experimentally-measured bottom sample surface temperatures respectively. N is the total number of experimental data points. A GoF_T equal to one implies a perfect match between the simulated and experimental bottom surface temperature data.

The WRC pyrolysis model used to simulate the CAPA II results was formulated by prescribing a uniform undecomposed WRC component density across the axial and radial plane of the sample. The mean density of WRC sample was found to be equal to 394 kg m^{-3}. For the CAPA II simulation, the density of the undecomposed WRC sample was adjusted to account for the approximately 4.6 wt.% water that contributes to the mass but not the volume of the sample. The adjustment resulted in a slightly lower density for the undecomposed WRC sample equal to 376 kg m^{-3}. It was determined from videos that the average expansion of WRC was about 0.3 mm or 3% of the original sample thickness. The expansion behavior was captured numerically by prescribing continually-decreasing condensed-phase component densities. The continual sample expansion was captured by reducing each solid-phase intermediate density by 3%. The densities of each solid-phase component used to simulate the CAPA II WRC bottom surface temperature profile at an incident heat flux of 62.7 kW m^{-2} are listed in Table 7-9.

The thermal conductivities of all condensed-phase components were assumed to be independent of temperature in an effort to minimize the number of adjustable parameters. The first two condensed-phase intermediates (WRC1 and WRC2) were assumed equal while the optimization algorithm was used to parametrize the remaining condensed-phase thermal conductivity values. The optimized thermal conductivity of each condensed phase component is presented in Table 7-9. It was assumed that the thermal conductivity of water and the undecomposed WRC component were equal.

Table 7-9: Densities and optimized thermal conductivities of the condensed-phase components of WRC.

Condensed-phase component	Density (kg m^{-3})	Thermal conductivity (W m^{-1} K^{-1})
WRC	376	0.128
WRC1	348	0.085
WRC2	218	0.085
WRC3	114	0.305
WRC4	82	0.580
Char	39	1.20

The optimized T_{bottom} and experimental bottom sample surface temperate profiles for CAPA II tests at a nominal incident heat flux of 62.7 kW m^{-2} are compared in Figure 7-11. The error bars in the experimental data were calculated from their scatter as two standard deviations of the mean. From Figure 7-11, it is noted that the optimized WRC thermal decomposition model captures the experimental CAPA II T_{bottom} data well.

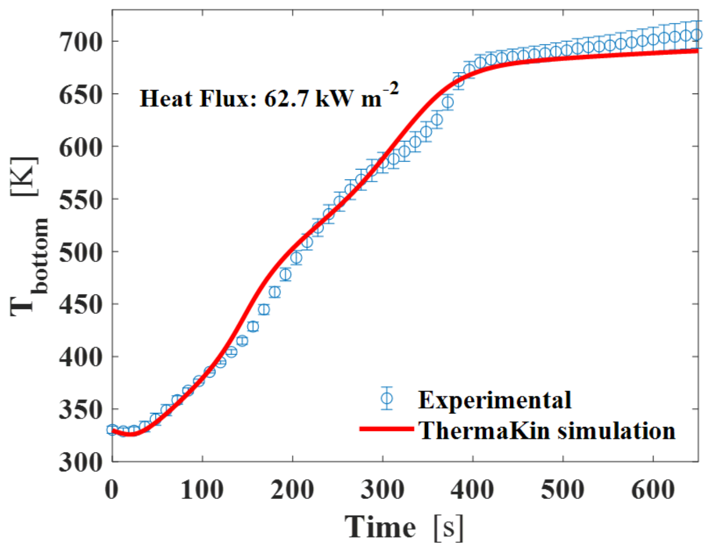

Figure 7-11. Experimental and simulated CAPA II bottom sample surface temperature profiles obtained at a nominal radiant heat flux of 62.7 kW m^{-2}.

7.4.4 CAPA II pyrolysis model validation

The remaining WRC CAPA II results which included the mass loss rate (MLR) at both incident heat fluxes and the mean T_{bottom} data obtained at the lower, 28.9 kW m^{-2} incident heat flux were used to validate the WRC pyrolysis model. Uncertainties for all the experimental data was calculated from their scatter as two standard deviations of the mean. Comparisons between the experimental and WRC model predictions are shown in Figure 7-12 and Figure 7-13. From Figure 7-12, it is noted that the optimized WRC pyrolysis model captures the magnitude of both the initial and secondary MLR peak as well as the overall shape of experimental MLR profile. For the 28.9 kW m^{-2} CAPA II experiments, the model captures the overall shape and magnitude of the MLR profile but slightly under-predicted the bottom surface temperature profile between the 300 and 800 s time range.

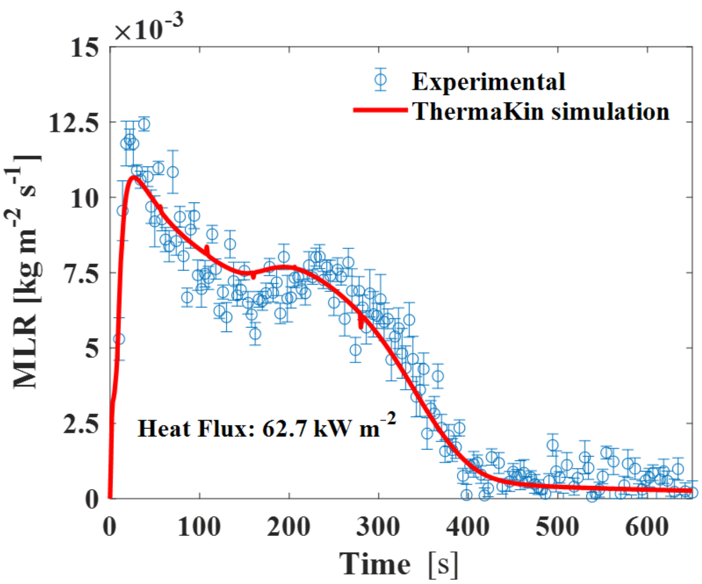

Figure 7-12. Experimental and ThermaKin-simulated CAPA II MLR profile comparison obtained at a 62.7 kW m^{-2} incident heat flux.

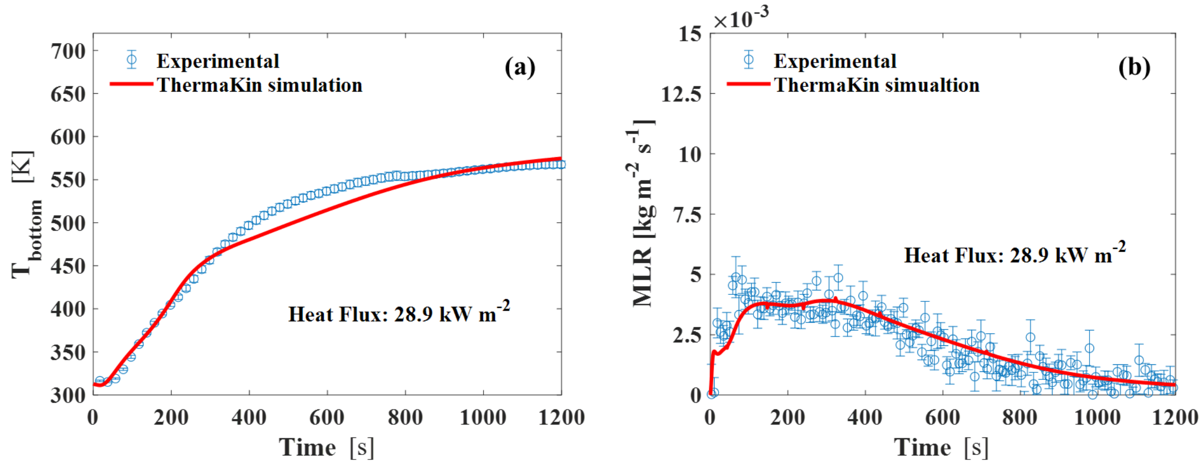

Figure 7-13. Experimental and ThermaKin-simulated CAPA II T_{bottom} and MLR profile comparison obtained at a 28.9 kW m^{-2} incident heat flux.

During the CAPA II experiments, it was observed that the samples would continuously shrink in the radial direction as shown in Figure 7-14. This shrinkage of the sample is thought to be the reason for the underestimation of the bottom surface temperature at the 28.9 kW m^{-2} heat flux and the mismatched timing of the second MLR peak at the 62.7 kW m^{-2} heat flux. As the sample shrinks, a larger area of the copper foil, mounted to the back of the sample, is directly exposed to the incident heat flux from the conical radiant heater resulting in higher back surface temperature measurements.

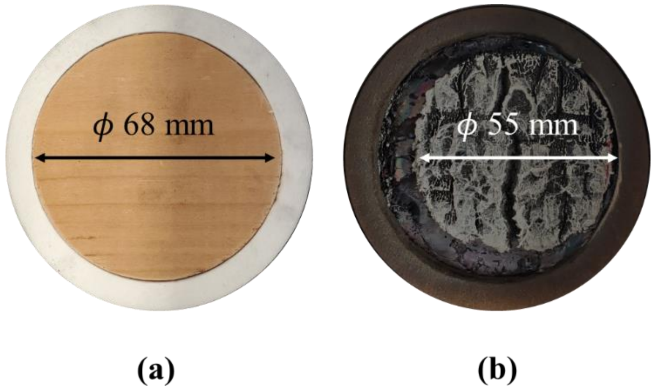

Figure 7-14. Snapshots of a WRC CAPA II sample (a) before and (b) after a test performed at an incident heat flux of 62.7 kW m^{-2}.

7.4.5 Effect of oxygen in CAPA II experiments

The comprehensive pyrolysis model used to capture the thermal decomposition behavior of WRC has developed using results from TGA, DSC, MCC, and CAPA II tests. All of these results were obtained by thermally decomposing WRC in an anaerobic environment. Nitrogen was used as an inert gas to maintain anaerobic conditions for all of these experiments. However, the ignition susceptibility of WRC when exposed to a pile of glowing firebrands was studied in an aerobic environment which constituted 21 vol. % O_2. Atmospheric air was the oxidizer used in the bench-scale wind tunnel experiments. Therefore, quantifying the potential contribution of oxidation at the surface of the WRC substrate prior to ignition of its surface is important to determine whether the surface oxidation process should be incorporated into the WRC comprehensive pyrolysis model.

The contribution of surface oxidation to the overall WRC thermal decomposition process was quantified using the results obtained from an additional set of CAPA II experiments that were performed in air (21 vol. % O_2). These aerobic CAPA II tests were performed in duplicates using the same incident heat flux exposure settings as in the anaerobic testing scenario (28.9 and 62.7 kW m^{-2}). The area-normalized mass loss rate and back surface temperature results for both the aerobic and anaerobic tests at the higher, 62.7 kW m^{-2} incident heat flux are compared in Figure 7-15. The MLR data was smoothed using a third order Savitsky-Golay filter with a frame length of 11 points which equates to a 5 s time frame. The average ignition time documented for the aerobic CAPA II tests was equal to 11 s.

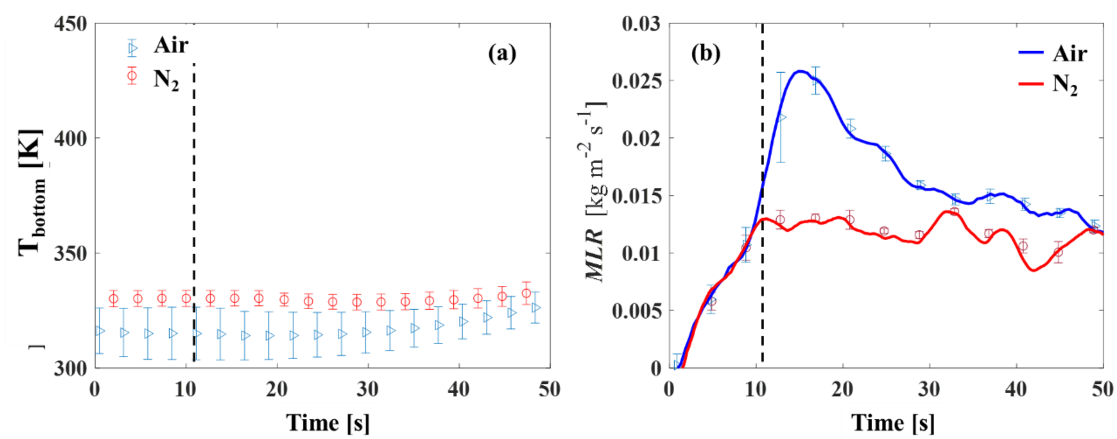

Figure 7-15. Comparison of the WRC (a) bottom surface temperature and (b) MLR comparison when exposing the sample surface to either N_2 or air. All data was collected at a nominal incident heat flux equal to 62.7 kW m^{-2}. The vertical dashed line indicates the onset of flaming ignition at the surface of the sample.

Oxidative pyrolysis is an exothermic process [94] that, if significant, would be highlighted by a rise of the WRC bottom surface temperature data prior to ignition and that is significantly faster than the CAPA II tests using nitrogen as the purge gas. The exothermic nature of oxidative pyrolysis at the surface of the sample prior to ignition would also be highlighted by a higher MLR. Figure 7-15 indicates that prior to flaming ignition, the effect of O_2 at the WRC surface is negligible even at a high heat flux of 62.7 kW m^{-2}. This is highlighted by small differences (0.03 kg m^{-2} s^{-1}) in the experimental MLR data at the point of flaming ignition and no noticeable rise of the bottom surface temperature data prior to ignition. The CAPA II MLR and bottom surface temperature profiles in nitrogen and air at an incident heat flux of 28.9 kW m^{-2} are compared in Figure 7-16. It should also be noted that the flaming ignition was not observed for any of the 28.9 kW m-2 tests. It is noted that initially there is a negligible difference between the MLR and bottom surface temperature profiles regardless of the oxygen concentration at the surface of the sample.

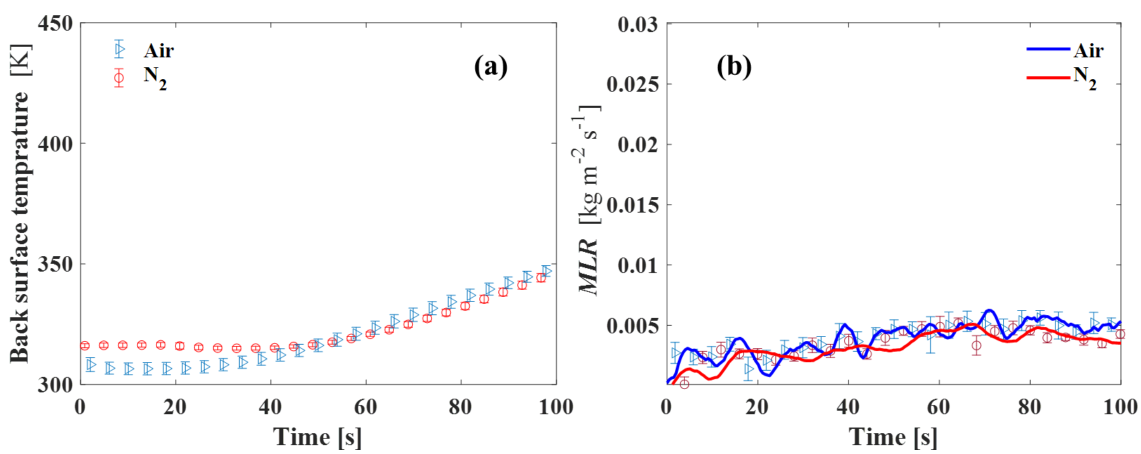

Figure 7-16. Comparison of the WRC (a) bottom surface temperature and (b) MLR comparison when exposing the sample surface to either N_2 or air. All data was collected at a nominal incident heat flux equal to 28.9 kW m^{-2}. The vertical dashed line indicates the onset of flaming ignition at the surface of the sample.

It was concluded that the contribution of oxidative pyrolysis at the surface of a WRC sample prior to flaming ignition could be assumed negligible. Further, it was assumed that the thermal decomposition behavior of WRC and any other lignocellulosic substrate could be adequately captured using its anaerobic pyrolysis model.

8 Pyrolysis Characterization of PTW

A comprehensive pyrolysis model was developed for a third lignocellulosic structural material, PTW. The comprehensive pyrolysis model for PTW was developed using the same hierarchical inverse modeling process used for WRC as presented in Section 7. In summary, a set of milligram-scale experiments (STA and MCC) are used to inversely analyze the thermal decomposition kinetics, reaction coefficients, heats of reactions, condensed-phase heat capacities, and the gaseous intermediates heats of combustion. Thereafter, gram-scale CAPA II experiments were performed to parametrize the thermal transport within the pyrolyzing sample and the developing char layer. MLR and bottom surface temperature data was inversely analyzed to quantify the density and thermal conductivity of the undecomposed PTW component as well as all other condensed-phase intermediates. All experimental and the milligram-scale pyrolysis model data was provided by Sangkyu Lee (Mechanical Engineering PhD student from the University of Maryland, College Park).

A five-step reaction scheme was sufficient to adequately resolve the STA PTW normalized mass loss and MLR data. The five-step reaction scheme and thermal decomposition kinetic parameters used to resolve the STA MLR are presented in Table 8-1. It was determined that the chemically-bound water content of the PTW samples used during milligram-scale analysis was equal to 1.9 wt.%.

Table 8-1: A reaction mechanism for the thermal decomposition of PTW as well as all relevant thermal decomposition kinetic parameters.

Reaction number	Reaction equation
1	Water → $Water_{vapor}$
2	PTW → 0.73 PTW1 + 0.27 Gas1
3	PTW1 → 0.429 PTW2 + 0.571 Gas2
4	PTW2 → 0.817 PTW3 + 0.183 Gas3
5	PTW3 → 0.769 Char + 0.231 Gas5

Table 8-2: Arrhenius-type reaction rate parameters obtained for PTW using a hill-climbing optimization algorithm

Reaction number	A [s^{-1}]	E [J mol^{-1}]	h [J kg^{-1}] (exo)
1	1.55×10^4	4.35×10^4	-2.8×10^6
2	1.92×10^7	1.06×10^5	-6.8×10^3
3	1.86×10^{11}	1.61×10^5	-1.7×10^5
4	1.79×10^5	1.01×10^5	-1.8×10^5
5	2.11×10^{-1}	3.44×10^4	2.0×10^5

The DSC heat flow data for PTW was captured by quantifying a temperature dependent heat capacity for water, the undecomposed PTW, and all other solid-phase intermediates. The temperature-dependent heat capacity data are presented in Table 8-3.

Table 8-3: Heat capacities of all condensed phase PTW components with T the experimental temperature

Component	Cp (J kg^{-1} K^{-1})
Water	$5200 - 6.7T + 0.011T^2$
PTW	$-302 + 4.93T$

PTW1	-77.4 + 4.11T
PTW2	160.8 + 3.07T
PTW3	389.9 + 2.18T
Char	623.6 + 1.22T

The MCC HRR data for PTW was inversely analyzed to quantify the heats of combustion (h_c) of all gaseous intermediates. The PTW h_c-values are summarized in Table 8-4.

Table 8-4: Individual heats of combustion of all gaseous intermediate PTW components

Gaseous intermediate component	h_c (kJ g^{-1})
Gas1	14.3
Gas2	16.5
Gas3	11.0
Gas4	4.0

CAPA II experiments were conducted to quantify the thermal conductivity, density, and emissivity of each condensed-phase PTW component. The PTW samples that were 0.9 cm thick and had a radius equal to 3.4 cm. The density of the undecomposed PTW sample was adjusted to account for the 7 wt. % water (dry basis) that contributes to the mass but not the volume of the sample. The adjustment resulted in a slightly lower density for the undecomposed PTW sample equal to 495 kg m^{-3}. The PTW water content was calculated by determining the average difference in mass between multiple desiccated and oven-dried PTW samples.

The densities of all solid-phase intermediates were further adjusted to account for the expansion of the sample (approximately 10 % or 0.9 mm) over the duration of a test. The CAPA II MLR and bottom surface temperature data for PTW were inversely analyzed and the results of this analysis are presented in Table 8-5.

Table 8-5: Densities and optimized thermal conductivities of the condensed-phase components of WRC.

Condensed-phase component	Density (kg m^{-3})	Thermal conductivity (W m^{-1} K^{-1})
PTW	490.1	0.145
PTW1	322.3	0.145
PTW2	138.3	0.26
PTW3	113.1	0.8
Char	86.9	1.0

Comparisons between STA, MCC, and CAPA II experimental data and ThermaKin simulations for PTW are presented in Figure 8-1. It is noted that inverse analysis of milligram- and bench-scale data used to parameterize the thermal decompstion of PTW provides adequate matches between the experimental data and ThermaKin simulations.

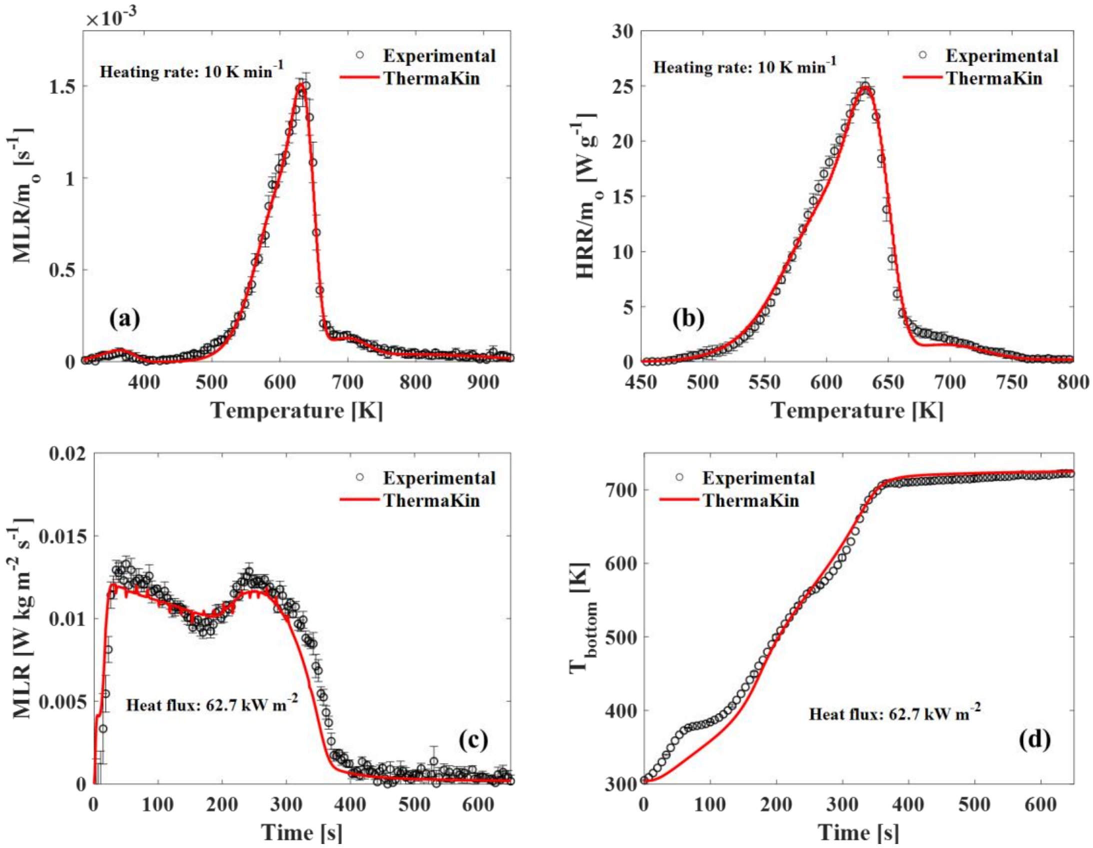

Figure 8-1. Comparisons between PTW experimental data and ThermaKin simulations profiles for (a) STA MLR, (b) MCC HRR, (c) CAPA II MLR, and (d) CAPA II bottom surface temperature

9 Inverse Firebrand Pile Heat Flux Modeling

The thermal exposure from a pile of firebrands to the surface of a flammable target substrate has been identified as a key parameter controlling ignition probability of a flammable lignocellulosic substrate. In Section 4.1, the back surface temperature of Kaowool PM insulation exposed to a glowing firebrand pile was used as a surrogate measurement to quantify the firebrand pile thermal exposure intensity dependence on air flow velocity and firebrand pile coverage density. In the current section, a custom inverse firebrand heat flux modeling technique will be developed and subsequently used to construct time-dependent firebrand pile heat flux profiles using Kaowool PM back surface temperature data as a target measurement. For the first time, a empirical heat flux model will be developed and that can subsequently be used to generate transient incident firebrand pile heat flux profiles for a wide range of air flow velocities and firebrand pile coverage densities. Quantifying the incident firebrand pile heat flux to the surface of a target substrate is critical when wanting to accurately predict the ignition of flammable substrates by a pile of firebrands.

9.1 Kaowool PM back surface temperature measurements

The thermal exposure from a pile of glowing firebrands to the surface of a horizontally-mounted substrate was isolated using 3.18 mm thick, non-combustible Kaowool PM ceramic fiber insulation. Kaowool PM has a low thermal conductivity and low heat capacity [65] (see Table 9-1) making its interference with the firebrand combustion process minimal. The mean density for Kaowool PM was calculated in-house using mass and volume measurements of ten 0.1×0.1 m^2, 3.18 mm thick Kaowool PM samples.

Table 9-1: Thermophysical properties of non-combustible Kaowool PM used to inversely analyze the incident heat exposure from a pile of glowing firebrands

Material	Density (kg m^{-3})	Heat Capacity (J g^{-1} K^{-1})	Thermal Conductivity (W m^{-1} K^{-1})	Absorptivity (m^2 kg^{-1})
Kaowool PM	232	1.07	$0.049 + 1.5 \times 10^{-5}\,T + 1 \times 10^{-7}\,T^2$ (T in °C)	10000

The Kaowool PM samples were sufficiently thin to allow for accurate tracking of the temporal evolution of the firebrand pile thermal exposure via IR thermal imaging back surface temperature measurements. The reader is directed to Section 2.2 where more detailed information related to the IR thermal analysis system can be found. The Kaowool PM back surface temperature data for all testing condition combinations was collected in two measurement zone: a zone in front of the airflow-facing edge of the firebrand pile (preleading zone) and a zone directly behind the preleading zone and located directly underneath the firebrand pile (leading zone) as shown in Figure 3-1. The preleading zone was located at the air flow facing edge of the firebrand pile and was 1.5 cm long. This zone extended 1 cm outside of the air flow-facing edge of the firebrand pile deposition area. The leading zone was 3 cm in length and was located underneath the firebrand pile and directly behind the preleading zone. Both zones were 4 cm wide, which is slightly lower than the total width of the firebrand pile.

An overwhelming majority of WRC and OSB surface ignition events originated within the preleading zone (see Figure 4-14 and Figure 4-15) while a majority of the firebrand pile ignitions events occurred on top of the firebrand pile located within the leading zone. The leading zone is also where the highest substrate back surface temperature was observed. A representative example of both a substrate surface and firebrand pile ignition event is shown in Figure 9-1. Nine repeat tests were used to compute a single time-resolved average back surface temperature profile for each testing condition combination. The spatial and test-to-test temperature variation at each time step was calculated as two standard deviations. The Kaowool PM back surface temperature data was generated using FLIR Tools™ software. More information related to the Kaowool PM back surface temperature data generation is presented in Section 3.1 of this manuscript.

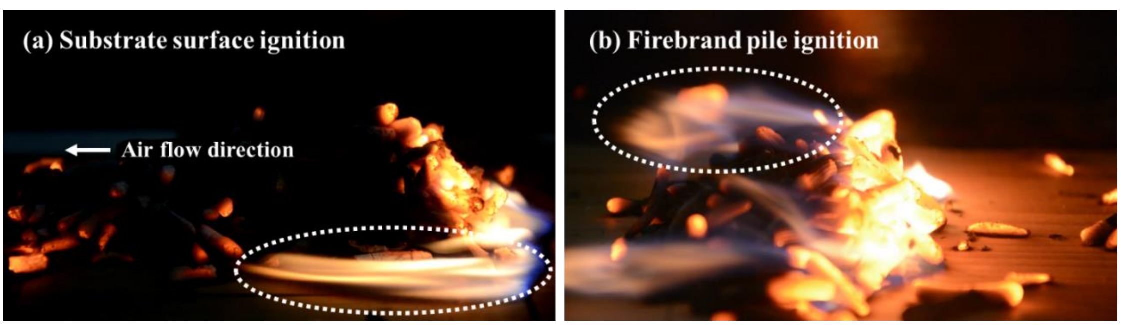

Figure 9-1. Representative examples of a (a) flammable substrate surface ignition event in the preleading zone and (b) a firebrand pile ignition event in proximity to the leading zone.

9.2 *Firebrand pile heat flux modeling*

The incident heat flux from a glowing firebrand pile to the surface of a flammable target substrate was determined in this work using a custom inverse modeling technique which relied on a solid-phase pyrolysis solver, ThermaKin. A detailed description of ThermaKin is presented in Section 7.1. For this inverse heat flux analysis modeling technique, one-dimensional ThermaKin simulations were performed. During inverse modeling of firebrand pile heat flux data, ThermaKin was only used as a heat transfer solver when inversely analyzing the firebrand pile incident heat flux to the surface of a target substrate. Generally, any one-dimensional heat transfer solver with flexible boundary conditions and temperature-dependent properties could be used.

The inverse heat flux modeling procedure consisted of matching a ThermaKin-generated Kaowool PM back surface temperature temporal profile with a target experimental Kaowool back surface temperature profile by iteratively changing the incident firebrand pile heat flux temporal dependence specified in the ThermaKin model. This inverse modeling required the knowledge of relevant Kaowool PM thermophysical properties summarized in Table 9-1, the emissivity of the Kaowool PM surface onto which a pile of glowing firebrands was deposited, and all external boundary conditions with the exception of the incident firebrand pile heat flux. The firebrand pile inverse modeling approach developed in this study concurs with the findings made from other studies [95], [96] that more than one system measurement is required when quantifying the heat flux data from temperature measurements.

9.3 *Validation of Kaowool PM thermophysical properties*

The inverse heat flux modeling requires an accurate definition of the properties that control heat transport inside the Kaowool PM board. Therefore, validation experiments and analysis were carried out to ensure that the properties listed in Table 9-1, which were originally provided by the manufacturer of this board, are valid.

Three experiments were performed where the 3.18 mm thick Kaowool PM insulation board (used in the firebrand pile wind tunnel experiments) was placed on the top of a 25.4 mm thick Kaowool PM insulation slab and subjected to controlled radiative heat flux from a conical radiant heater similar to that used in cone calorimetry [97]. The two pieces of insulation were joined using multiple strips of aluminum tape which ensured that adequate thermal contact between the two pieces of insulation was maintained.

Three fine wire (0.25 mm wire diameter) K-type thermocouples were placed in between the 3.18 mm thick Kaowool PM insulation board and the 25.4 mm thick Kaowool PM slab and were used to generate transient in-depth temperature measurements. The thermocouple beads were positioned within a 1 cm radius of the center of the Kaowool PM insulation. The conical radiant heater was operated at a nominal incident heat flux of 50 kW m^{-2}. The incident heat flux was measured using a NIST-traceable calibrated Schmidt-Boelter water-cooled heat flux gauge positioned in the center and 25 mm below the bottom surface of the heater. The top surface of the 3.18 mm thick Kaowool PM insulation, facing the conical radiant heater, was painted with a MedTherm high-emissivity optical black coating with a broadband emissivity of 0.94.

The ThermaKin simulation of this radiative heating experiment was carried out using the Kaowool PM properties listed in Table 9-1 and the emissivity of the radiation-exposed surface defined by the optical black coating (0.94). Natural convective losses from the top surface were taken into account using a convective heat transfer coefficient of 3.7 W m^{-2} K^{-1} [98] (corresponding to the center of a 10×10 cm^2 sample) and an ambient temperature of 293 K. A 0.01 s time step and 5×10^{-5} m element size was used for the numerical integration. Increasing or decreasing these integration parameters by a factor of two did not change the results indicating convergence. The same integration parameters were used in all wind tunnel experiment simulations discussed in the rest of this section. In-depth radiation absorption was assumed negligible. The mean in-depth experimental temperature history (average of all thermocouple signals collected in 3 repeated tests) and the ThermaKin-generated temperature history below the 3.18 mm thick painted Kaowool PM insulation board are compared in Figure 9-2. This comparison shows an excellent agreement between the experimental and simulation data confirming validity of the Kaowool PM thermophysical properties, as listed in Table 9-1.

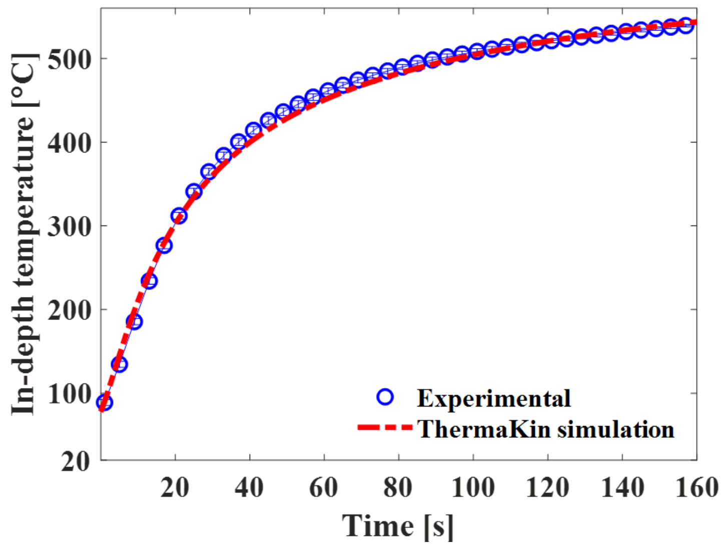

Figure 9-2. Comparison of the in-depth (3.18 mm) thermocouple and ThermaKin-simulated temperature profiles when exposed to 50 kW m^{-2} of incident radiant heat flux.

9.4 Inverse heat flux modeling setup and procedure

The Kaowool PM back surface temperature data has been used as an adequate surrogate to quantify the firebrand pile heat exposure dependence on the forced air flow velocity and firebrand pile size (see Section 4.1). Kaowool PM back surface temperature data has also been identified as an adequate target measurement that can be used during inverse modeling of the incident firebrand pile heat flux to a horizontally-mounted target substrate. It was also postulated that radiation is the dominant heat transfer mode from a pile of glowing firebrands to the surface of a target substrate (see Section 4.5.2). Therefore, the main assumption that was used during the inverse modeling of the heat flux from the firebrand pile was that, for both the preleading and leading zones, this heat flux was purely radiative in nature.

Preliminary ThermaKin simulations indicated that the Kaowool PM back surface temperature data collected from the wind tunnel experiments can only be captured when the heat flux from the firebrand pile is defined as a time-dependent function. In ThermaKin, the incident heat flux from an external heat source to the surface of a substrate can be simulated using the two available linear functions which can be time-dependent. In the case of the firebrand pile wind tunnel experiments, a range of piecewise linear functions of various levels of complexity was examined in an attempt to capture the time-dependent Kaowool PM back surface temperature behavior (see Figure 4-2).

It was determined that a three-step piecewise linear heat flux function was the simplest function that could be used to produce sufficiently high quality Kaowool PM back surface temperature predictions. A representative schematic of this piecewise linear heat flux function is shown in Figure 9-3. The transient nature of the piecewise linear heat flux function shown in Figure 9-3 is consistent with the actual burning behavior of a glowing firebrand pile. The shape of the Kaowool PM back surface temperature profiles (see Section 4.1) as well as the Kaowool PM burning intensity *HRR* profiles (see Section 4.3) confirm this transient firebrand pile burning behavior. The reader is further reminded that the burning intensity of the pile rapidly increased directly after deposition of the firebrands and was attributed to the pile being exposed to the fresh oxidizer being introduced into the tunnel. The firebrand pile burning intensity reached a peak and then started to decay as the test progressed. The back surface temperature and combustion *HRR* decay behavior is attributed to the continual consumption of the glowing firebrands.

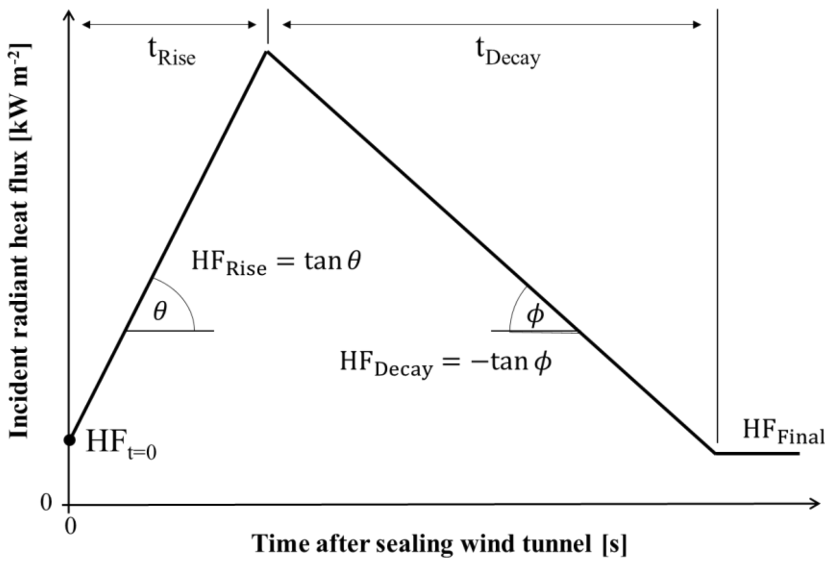

Figure 9-3. The dependence of the incident radiant heat flux on time used to represent the heat feedback from a glowing firebrand pile to a target substrate surface.

The parameters that define the piecewise linear heat flux function include: the heat flux rise rate (HF_{Rise}) [kW m^{-2} s^{-1}], the heat flux at the start of the test ($HF_{t=0}$) computed by multiplying HF_{Rise} by the delay time at the start of a test (12 s) [kW m^{-2}], the time to the peak heat flux (t_{Rise}) [s], the heat flux decay rate (HF_{Decay}) [kW m^{-2} s^{-1}], the final constant heat flux (HF_{Final}) [kW m^{-2}], and the time of decay from the peak to the final constant heat flux (t_{Decay}) [s]. t_{Decay} can be calculated knowing the peak incident heat flux value (a product of HF_{Rise} and t_{Rise}), HF_{Decay}, and HF_{Final}. t_{Decay} is equal to the difference between the peak heat flux value and HF_{Final} divided by HF_{Decay}. HF_{Final} was required to more accurately capture the complex cooling and decay behavior of a glowing firebrand pile during later stages of a test.

The convective and radiative heat losses at both the top and bottom Kaowool PM board surface used in the wind tunnel experiment were defined as follows. The top surface convective losses from the leading temperature measurement zone was assumed to be negligible because in this zone the substrate was completely covered by firebrands. The firebrand pile was treated as an impermeable obstruction to the air flow introduced into the wind tunnel. The convective losses from the top surface of the preleading zone were computed using well-known local forced flow correlations [68]. These correlations are summarized by Equations (9.1) and (9.2), where $h_{c,local}$ (W m^{-2} K^{-1}) is a local convective heat transfer coefficient, which is believed to provide a more accurate representation of the heat losses in the preleading zone than a global convection coefficient, which averages heat losses over the full length of the boundary layer.

$$h_{c,local} = \left(Nu_{local}\, k_{forced}\right)/L_{local} \tag{9.1}$$

$$Nu_{local} = 0.332 Re_{local}^{1/2} Pr^{1/3} \text{ for } (Re_{local} < 5 \times 10^5,\ Pr \geq 0.6) \tag{9.2}$$

The characteristic length, L_{local}, used to calculate each of the local convection coefficients was equal to 0.125 m as measured from the entrance of the test section of the wind tunnel to the center of the preleading zone. Re_{local}, Nu_{local}, and Pr are Reynolds, Nusselt and Prandtl numbers, respectively. k_{forced} is the thermal conductivity. All these quantities were computed assuming that the fluid is air at a film temperature of 493 K. This film temperature was determined as the mean of the ambient temperature of 293 K and the average substrate surface temperature measured underneath a pile of firebrands, 693 K [47], [48]. $h_{c,local}$ for each of the forced air flow velocities studied (0.9, 1.4, 2.4, and 2.7 m s^{-1}) were found to be equal to 5.1, 6.3, 8.3, and 8.8 W m^{-2} K^{-1}.

The convective losses from the bottom surface of the Kaowool PM board were defined using the natural convection correlations obtained from [68] and summarized by Equations (9.3) and (9.4).

$$h_{free} = \left(Nu_{free}\, k_{free}\right)/L_{free} \tag{9.3}$$

$$Nu_{free} = 0.27 Ra_{free}^{1/4} \text{ for } (10^5 \leq Ra_{free} < 10^{11}) \tag{9.4}$$

In these equations, h_{free} is the natural convection coefficient. L_{free} is the characteristic length set to 0.073 m, which is approximately half of the width of the Kaowool PM board. Nu_{free}, Ra_{free}, and k_{free} are the Nusselt number, Raleigh number and thermal conductivity, respectively. These quantities were computed for air at the film temperature of 433 K. This film temperature was determined as the mean of the ambient temperature (293 K) and the average Kaowool PM board back surface temperature measured in the tunnel experiments, 573 K. h_{free} was found to be equal to 4.8 W m^{-2} K^{-1}.

The final parameters required for the simulation of the Kaowool PM back surface temperature data collected in the wind tunnel experiments were the top and bottom insulation board surface emissivities. The bottom surface of the Kaowool PM boards used in these experiments were painted with the MedTherm optical black coating and thus the bottom surface emissivity was defined by the emissivity of the coating (0.94). The same approach could not be used for the top surface of Kaowool PM located underneath the firebrand pile because of a rapid thermal degradation of the coating when in direct contact with the glowing firebrands as shown in Figure 9-4. To address this issue, additional experiments and analysis were carried out to determine the emissivity of unpainted Kaowool PM board.

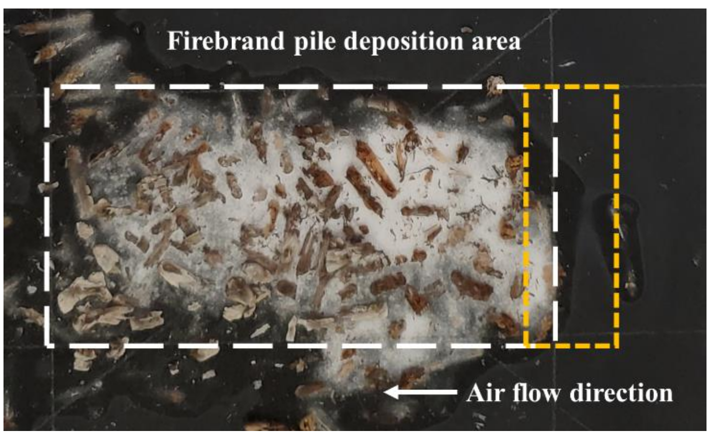

Figure 9-4. Representative example of the optical black coating on the top surface of the Kaowool PM insulation having degraded after coming into direct contact with any glowing firebrands. The white and yellow dashed lines represent the firebrand pile deposition area and the preleading temperature measurement zone.

First, a set of nine wind tunnel experiments was performed with both surfaces of the Kaowool PM board painted with the MedTherm optical black coating. These tests were conducted at 2.4 m s^{-1} forced air flow velocity and 0.16 g cm^{-2} firebrand pile coverage density. This is the testing condition combination where the largest number of WRC and OSB surface ignitions events were observed. The firebrand pile deposition area was orientated such that the 5 cm length of the rectangular deposition area was facing the incoming air flow into the wind tunnel. Subsequently, the preleading zone back surface temperature data collected in these tests were subjected to the inverse heat flux modeling. These test results were deemed suitable for the inverse modeling because both Kaowool PM surface emissivities were defined by the coating and the coating remained intact in the preleading zone, which contained few firebrands.

During this inverse modeling process, the parameters of the heat flux profile shown in Figure 9-3 were changed in small increments until the simulated Kaowool PM back surface temperature was found to capture the first 200 s of the mean experimental data with a coefficient of determination, R^2, higher than 0.96. The process of iteratively changing the heat flux parameters to obtain an adequate match between the ThermaKin-simulated and experimental data is shown in Figure 9-5. An adequate match between the simulated and experimental data is presented in Figure 9-5 (d). An adequate match also included qualitatively capturing the shape of the mean back surface temperature rise and decay, and being within 10 ºC of the peak back surface temperature. This 200 s time range was selected because all flammable surface ignition events (for both WRC and OSB) extinguished within the first 200 s of the test start time.

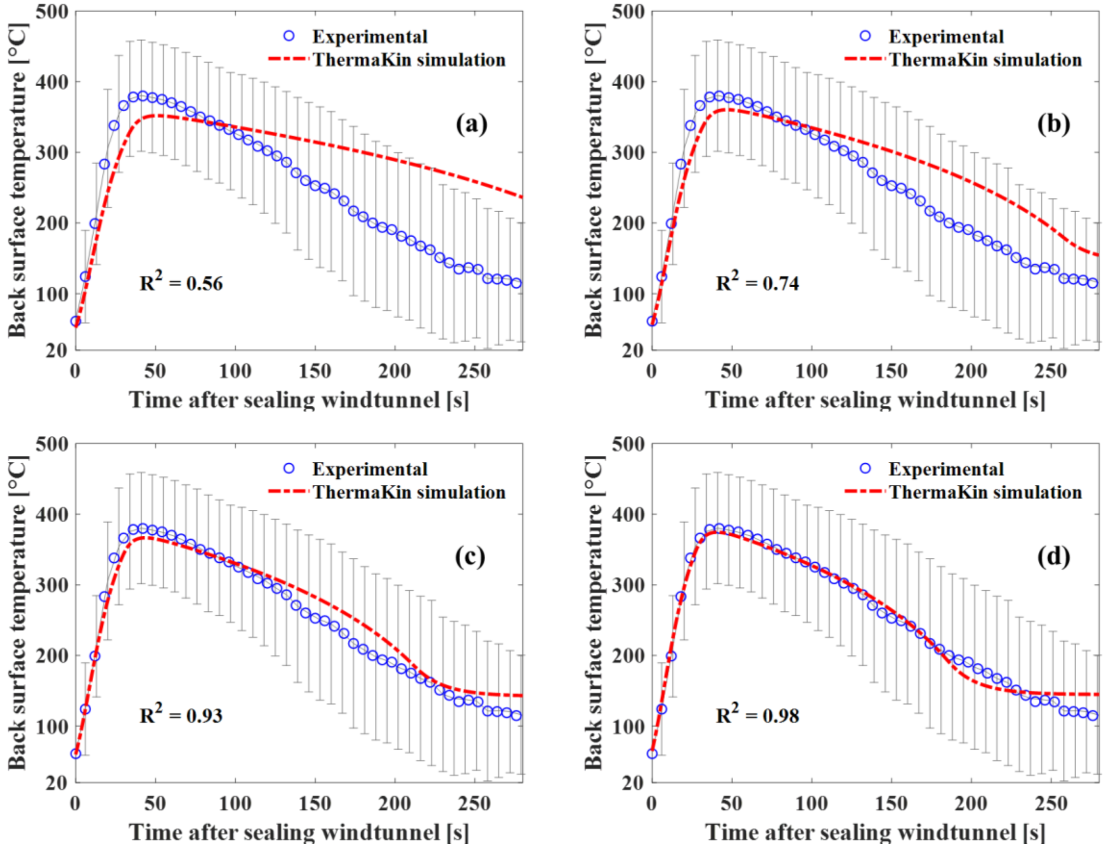

Figure 9-5. Iterative process used to obtaining an adequate match between the experimental and simulated Kaowool PM back surface temperature histories obtained for the preleading zone at 2.4 m s^{-1} air flow velocity and 0.16 g cm^{-2} firebrand pile coverage density. The top surface of the preleading zone was painted with the MedTherm optical black coating.

The heat flux parameters used to construct a piecewise linear function heat flux function that was in turn used to match the experimental painted Kaowool PM back surface temperature profile are summarized in Table 9-2. The uniqueness of these parameters was established by demonstrating, through exhaustive trial-and-error, that no other set of parameters could achieve the same level of agreement with the experimental data. Note that the experimental back surface temperature data exhibits a significant variation. This variation (expressed as two standard deviations) reflects primarily spatial variability in the firebrand pile thermal exposure associated with a discrete nature of the firebrand particles and changes in the exact spatial arrangement of these particles from test to test.

Table 9-2: Heat flux parameters used to construct a piecewise linear heat flux function that matches the coated Kaowool PM back surface temperature profile at a 2.4 m s^{-1} air flow and 0.16 g cm^{-2} firebrand pile coverage density.

Test condition	$HF_{t=0}$ (kW m^{-2})	HF_{Rise} (kW m^{-2} s^{-1})	t_{Rise} (s)	HF_{Decay} (kW m^{-2} s^{-1})	t_{Decay} (s)	HF_{Final} (kW m^{-2})
2.4 m s^{-1}, 0.16 g cm^{-2}	26	2.15	39	-0.50	152	8

During the next step, a comparison was made between the experimental preleading zone back surface temperature histories obtained under the same experimental conditions, 2.4 m s^{-1} air flow and 0.16 g cm^{-2} firebrand coverage density, using Kaowool PM boards with unpainted and painted top surfaces. This comparison is provided in Figure 9-6 and was required to determine whether emissivity of the optical black coating could be used to approximate the unpainted Kaowool PM top surface emissivity. Figure 9-6, it is noted that the unpainted Kaowool PM back surface temperature profile is slightly but systematically lower than the painted Kaowool PM back surface temperature profile. Therefore, it was concluded that the emissivity of the unpainted Kaowool PM surface is lower than that of the Kaowool PM surface painted with the MedTherm optical black coating.

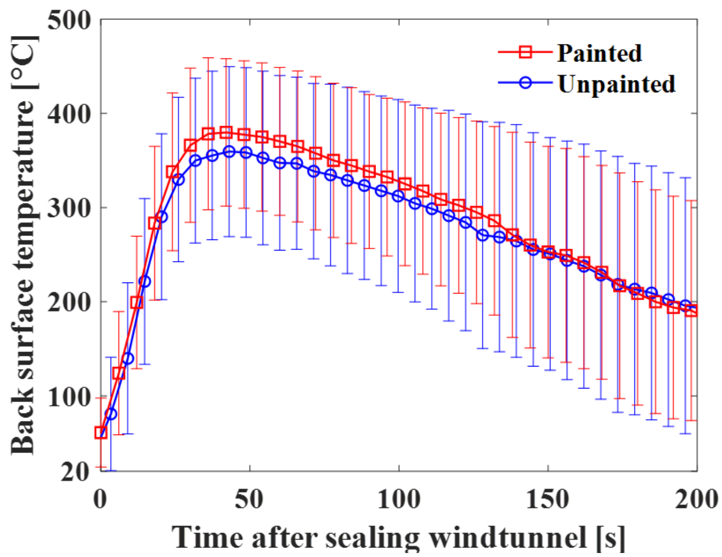

Figure 9-6. A comparison of the experimental preleading zone back surface temperature histories obtained under the same conditions (2.4 m s^{-1} air flow and 0.16 g cm^{-2} firebrand density) using painted and unpainted Kaowool PM top surfaces.

In the final step of this analysis, the unpainted Kaowool PM surface temperature data were used as a target for inverse modeling to determine the unpainted surface emissivity. This modeling relied on the knowledge of the firebrand incident heat flux profile, which parameters are summarized in Table 9-2, and the assumption that this profile is unaffected by the presence of the paint on the top surface of the Kaowool PM board. The emissivity values were adjusted in 0.01 increments until the best agreement between the experimental and simulated temperature profiles was achieved. This agreement is shown in Figure 9-7. It was obtained using a Kaowool PM surface emissivity value of 0.64.

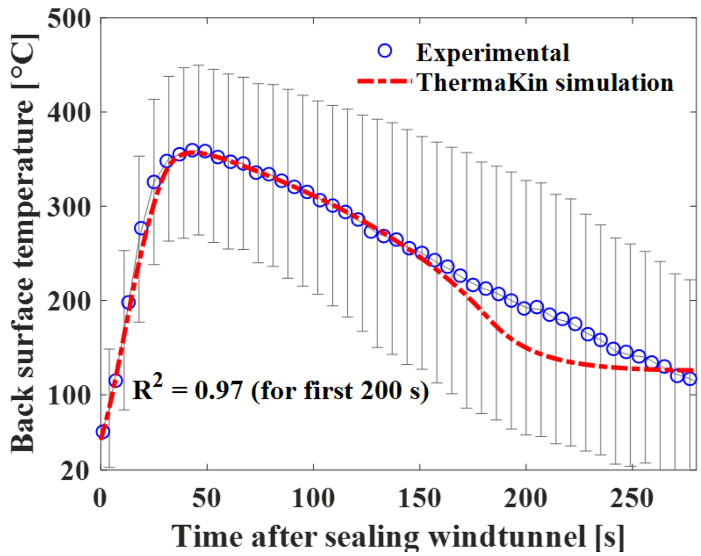

Figure 9-7. Experimental and simulated back surface temperature histories obtained for the preleading zone of the Kaowool PM board with an unpainted top surface at a 2.4 m s^{-1} air flow velocity and a 0.16 g cm^{-2} firebrand pile coverage density.

9.5 Piecewise linear heat flux functions for all other testing conditions combinations

Using the value of surface emissivity obtained for the unpainted Kaowool PM board, the preleading and leading zone back surface temperature data collected in the experiments at different air flow velocities and firebrand pile densities were analyzed to determine the corresponding parameters for each piecewise linear heat flux profile. The same approach that was used to obtain the heat flux profile parameters for the preleading zone at 2.4 m s^{-1} air flow velocity and 0.16 g cm^{-2} firebrand pile coverage density discussed in Section 9.4 was followed. Table 9-3 summarizes the results of this exercise obtained for both the preleading and leading zone. A representative ThermaKin conditioning and component file used to simulate the experimental unpainted Kaowool PM back surface temperature data in is presented in the Appendix section at the end of this manuscript.

Table 9-3: Heat flux parameter values used to construct the piecewise linear incident firebrand pile heat flux profiles in the preleading and leading temperature measurement zone for all test condition combinations studied.

Test condition	$HF_{t=0}$ (kW m^{-2})	HF_{Rise} (kW m^{-2} s^{-1})	t_{Rise} (s)	HF_{Decay} (kW m^{-2} s^{-1})	t_{Decay} (s)	HF_{Final} (kW m^{-2})
Preleading zone						
0.9 m s^{-1}, 0.16 g cm^{-2}	14	1.20	42	-0.13	329	8
1.4 m s^{-1}, 0.16 g cm^{-2}	19	1.56	41	-0.25	225	8
2.4 m s^{-1}, 0.16 g cm^{-2}	26	2.15	39	-0.50	153	8
2.7 m s^{-1}, 0.16 g cm^{-2}	23	1.90	37	-0.52	120	8
1.4 m s^{-1}, 0.06 g cm^{-2}	11	0.95	41	-0.23	149	5
2.4 m s^{-1}, 0.06 g cm^{-2}	15	1.19	39	-0.42	99	5
Leading zone						
0.9 m s^{-1}, 0.16 g cm^{-2}	16	1.30	42	-0.03	1566	8

1.4 m s^{-1}, 0.16 g cm^{-2}	20	1.61	46	-0.05	1300	8
2.4 m s^{-1}, 0.16 g cm^{-2}	27	2.18	51	-0.35	296	8
2.7 m s^{-1}, 0.16 g cm^{-2}	24	1.95	52	-0.28	335	8
1.4 m s^{-1}, 0.06 g cm^{-2}	13	1.04	46	-0.10	432	5
2.4 m s^{-1}, 0.06 g cm^{-2}	18	1.48	51	-0.4	177	5

The piecewise linear incident heat flux profiles constructed using a unique set of heat flux parameters for each studied testing condition combination listed in Table 9-3 are visually presented in Figure 9-8 for the preleading zone and in Figure 9-9 for the leading zone.

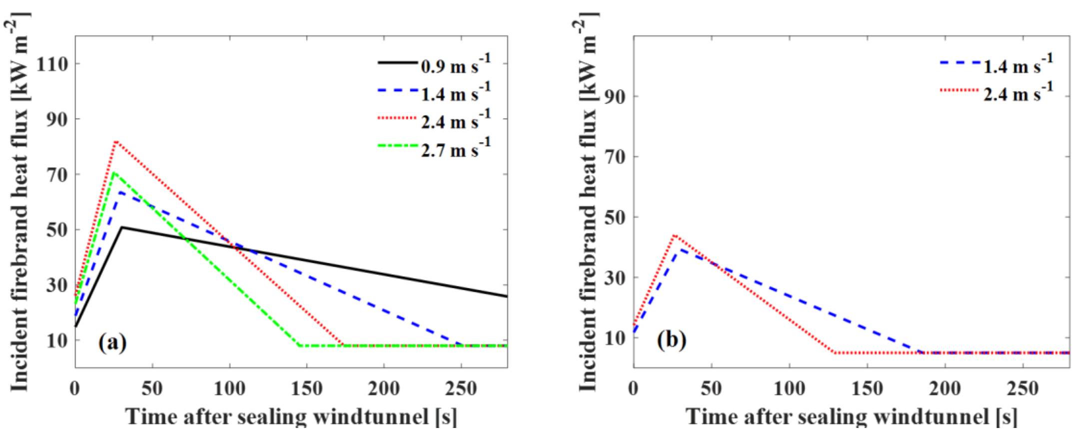

Figure 9-8. Preleading piecewise linear incident firebrand pile heat flux profiles for all studied forced air flow velocities at a (a) 0.16 g cm^{-2} and (b) 0.06 g cm^{-2} firebrand pile coverage density.

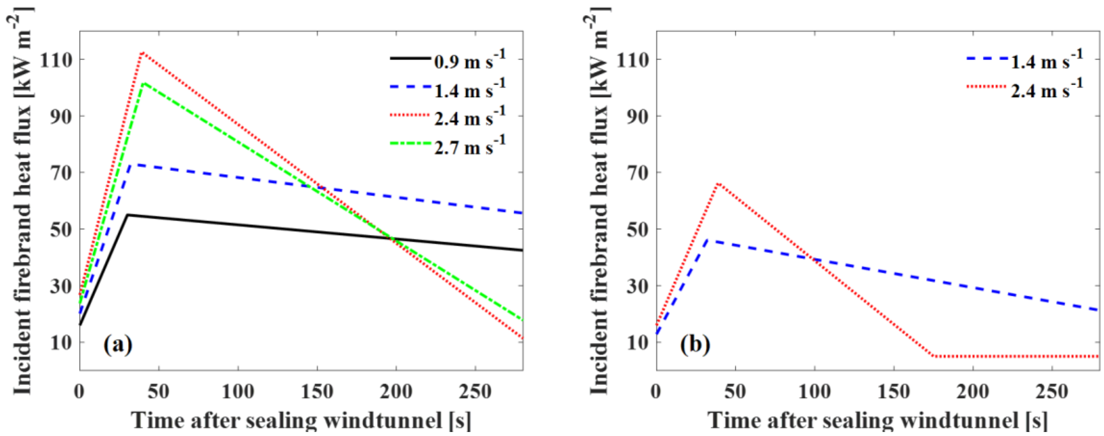

Figure 9-9. Leading piecewise linear incident firebrand pile heat flux profiles for all studied forced air flow velocities at a (a) 0.16 g cm-2 and (b) 0.06 g cm-2 firebrand pile coverage density.

Comparisons between the experimental and ThermaKin-generated Kaowool PM back surface temperature data in the both the preleading and leading measurement zone, for a representative set of testing condition combinations is presented in Figure 9-10 and Figure 9-11. All R^2 values were calculated using the first 200 s of ThermaKin-generated back surface temperature data. Additional inverse modeling was performed to estimate the variation in the firebrand heat flux that produces the variation in the Kaowool PM back surface temperature measured in the experiments. It was found that, on average (for all testing conditions and both zones) the experimentally observed variation in temperature corresponds to ± 40% variation in the heat flux around the mean. The large heat flux variation is a result of the stochastic nature of the firebrand pile deposition process. The stochastic firebrand pile deposition process is representative of the accumulation of firebrands on a horizontally-mounted substrate surface during large-scale firebrand exposure tests [44], [99].

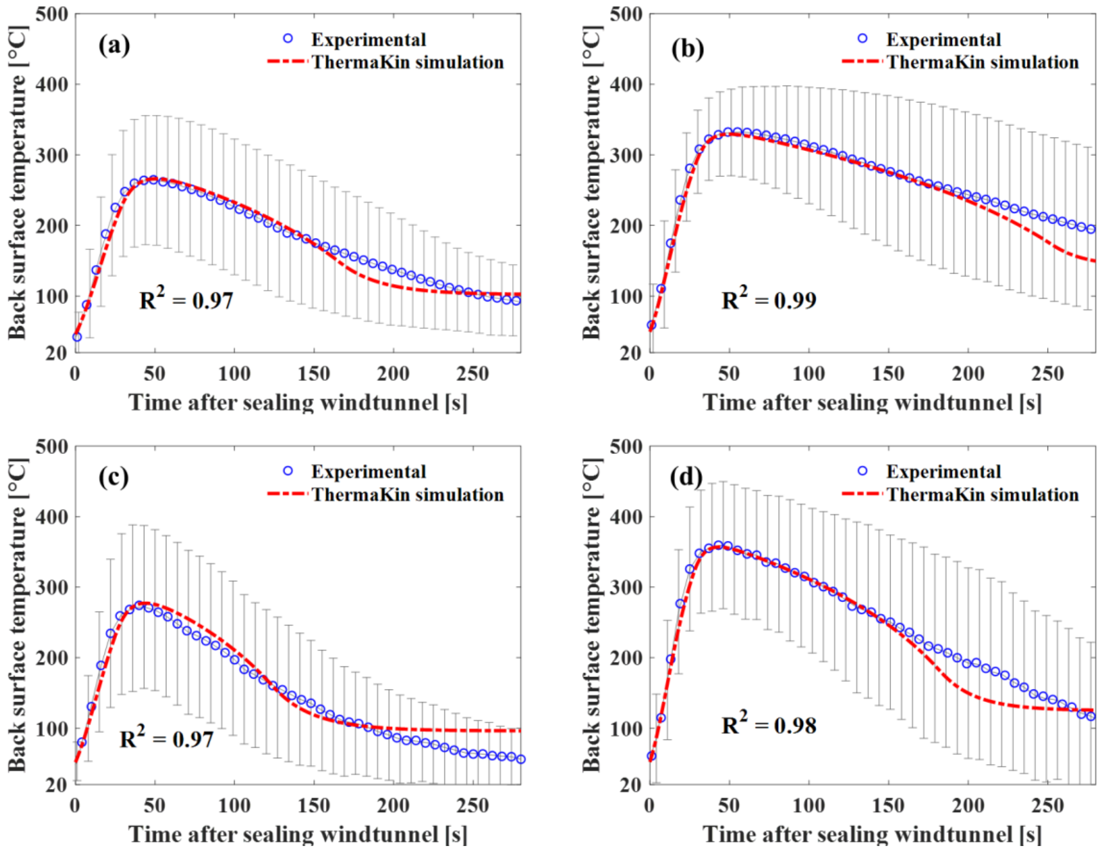

Figure 9-10. Comparisons between the experimental and ThermaKin-simulated average back surface temperature data in the preleading zone for a 1.4 m s^{-1} and 2.4 m s^{-1} air flow velocity and a firebrand pile coverage density of (a), (c) 0.06 g cm^{-2} and (b), (d) 0.16 g cm^{-2}.

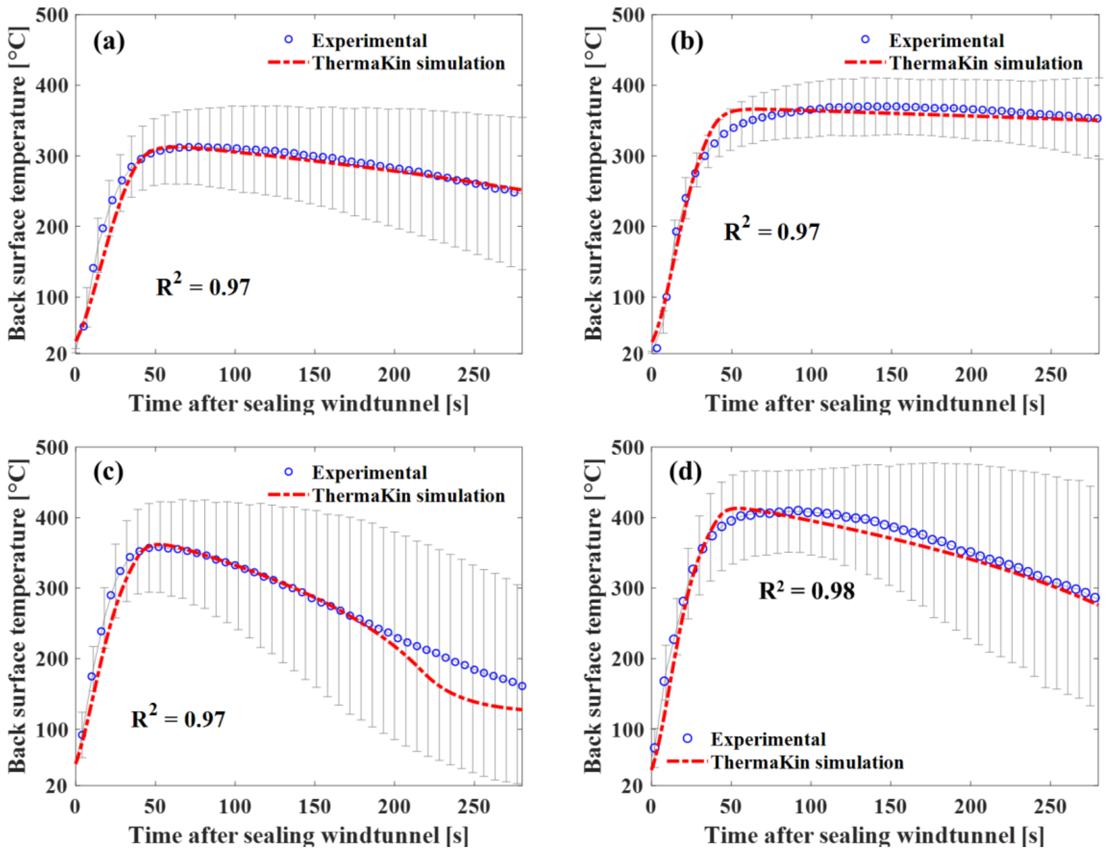

Figure 9-11. Comparisons between the experimental and ThermaKin-simulated average back surface temperature data in the leading zone for a 1.4 m s^{-1} and 2.4 m s^{-1} air flow velocity and a firebrand pile coverage density of (a), (c) 0.06 g cm^{-2} and (b), (d) 0.16 g cm^{-2}.

9.6 Comparison with previous firebrand pile thermal analysis studies

In previous firebrand pile thermal analysis studies [45–47, 49, 50], the time-averaged heat flux from a firebrand pile to the surface of a target substrate was used as a measure to quantify the firebrand heat flux intensity dependence on forced air flow and firebrand pile size. To enable comparison of the current results with these studies, average incident firebrand pile heat flux values for all testing conditions and both temperature measurement zones were computed from the modeled heat flux time dependencies. The average firebrand pile heat fluxes from the current study were calculated over a 100 s time frame, starting once the wind tunnel was sealed, and are presented in Table 9-4. The 100 s time frame was selected because all WRC and OSB surface ignitions occurred within the first 100 s of a test.

Table 9-4: Average incident heat flux values, calculated over a 100 s time frame, for all test condition combinations in both the preleading and leading temperature measurement zone.

Test condition	Preleading zone average heat flux (kW m^{-2})	Leading zone average heat flux (kW m^{-2})
0.9 m s^{-1}, 0.16 g cm^{-2}	38	43
1.4 m s^{-1}, 0.16 g cm^{-2}	46	53
2.4 m s^{-1}, 0.16 g cm^{-2}	58	80
2.7 m s^{-1}, 0.16 g cm^{-2}	47	69
1.4 m s^{-1}, 0.06 g cm^{-2}	28	35
2.4 m s^{-1}, 0.06 g cm^{-2}	30	44

Hakes et al. [45] and Salehizadeh et al. [47] measured the heat flux from a firebrand pile to the surface of an inert substrate using a water-cooled Schmidt-Boelter heat flux gauge positioned directly underneath the firebrand pile. The average firebrand pile heat flux measured by [45] over the first 100 s of the test, using a constant forced air flow of 1.84 m s^{-1} and a pile mass of 5 or 9 g, was approximately 20 kW m^{-2}. The average firebrand pile heat fluxes measured by [47] for airflows of 0.5 – 2 m s^{-1} and a 16 g pile mass ranged from 12 – 30 kW m^{-2} using a 100 cm^2 deposition area. The averaged heat fluxes determined under similar conditions in the current study are significantly larger. The large average heat flux difference can mainly be attributed to the use of a water-cooled heat flux gauge at is likely, to at least partially, quench smoldering firebrands in the vicinity of the gauge surface and thus reduce firebrand heat feedback. The interference of the current IR thermal analysis methodology with the combustion of the firebrands is minimal. The heat flux gauge was also placed in the center of the firebrand pile, however the preleading and leading zones are located closer to the air flow-facing edge of the pile and are known to be significantly hotter [50], [100].

Bearinger et al. [50] measured the heat flux from a firebrand pile to the surface of a thin stainless steel plate using IR thermal imaging back surface temperature data and an inverse heat transfer technique. A 3 g firebrand pile, exposed to a 2.0 m s^{-1} air flow, was deposited within a 20 cm^2 area on top of the stainless steel plate, which equated to a 0.15 g cm^{-2} coverage density. The resulting heat flux averaged over the same 100 s time period after the deposition of firebrands was found to be about 39 kW m^{-2}. This heat flux is closer to the current measurements (summarized in Table 9-4) but still about 40% lower at least partially due to the fact that Bearinger et al. [49] averaged their heat flux over the whole pile deposition area, whereas the current study focused on the hottest areas of the substrate defined by the preleading and leading zones [100]. The quenching of the firebrand pile as a result of using a stainless steel plate having larger conductive heat losses was hypothesized to further attribute to the lower heat flux values in comparison to the heat flux values from the present study.

9.7 Development of a time-dependent firebrand pile incident heat flux model

Firebrand pile heat flux profiles underneath (leading temperature measurement zone) and directly in front of (preleading temperature measurement zone) a glowing firebrand pile were determined. A set of firebrand pile heat flux correlations were developed to capture the dependence of each heat flux parameter (presented in Table 9-2) on forced air flow velocity and firebrand pile coverage density in the preleading and leading temperature measurement zone.

These heat flux correlations were developed to allow interpolation of the heat flux parameters within the range of testing conditions and to enable potentially extrapolation of the heat flux parameters outside of the range of air flows and pile coverage densities studied. The heat flux correlations were developed by labelling the forced air flow velocity exposed to a pile of glowing firebrands as ν (m s^{-1}) and the firebrand pile coverage density was ψ (g cm^{-2}).

9.7.1 Heat flux parameter dependence on ν

Each of the heat flux parameter's dependence on ν was evaluated using the heat flux parameter values (presented in Table 9-3) at ψ = 0.16 g cm^{-2}. HF_{Final} was set to be independent of ν. The heat flux parameters of the larger ψ were evaluated because more forced air flow conditions were studied at this larger coverage density. A second order polynomial was found to accurately represent each heat flux parameter's dependence on ν. The second order polynomial functions used to capture the ν

dependence of each heat flux parameter in the preleading- and leading temperature measurement zone are presented in Table 9-5. Graphs of the heat flux parameter values fitted with this second order polynomial function are shown in Figure 9-12 for the preleading temperature measurement zone and Figure 9-13 for the leading temperature measurement zone.

Table 9-5. Second-order polynomial functions that capture each independent heat flux parameter's dependence on ν.

Heat flux parameter	Correlation
Heat flux parameter ($\psi = 0.16\ \mathrm{g\ cm^{-2}}, \nu$)	
Preleading temperature measurement zone	
HF_{Rise} [kW m^{-2} s^{-1}]	$= -0.29(\nu)^2 + 1.49(\nu) + 0.1$
t_{Rise} [s]	$= -0.58(\nu)^2 - 0.50(\nu) + 43$
HF_{Decay} [kW m^{-2} s^{-1}]	$= -0.02(\nu)^2 - 0.13(\nu) - 0.01$
HF_{Final} [kW m^{-2}]	$= 8$
Leading temperature measurement zone	
HF_{Rise} [kW m^{-2} s^{-1}]	$= -0.32(\nu)^2 + 1.59(\nu) + 0.1$
t_{Rise} [s]	$= -1.02(\nu)^2 + 9.08(\nu) + 35$
HF_{Decay} [kW m^{-2} s^{-1}]	$= -0.05(\nu)^2 + 0.02(\nu) - 0.01$
HF_{Final} [kW m^{-2}]	$= 8$

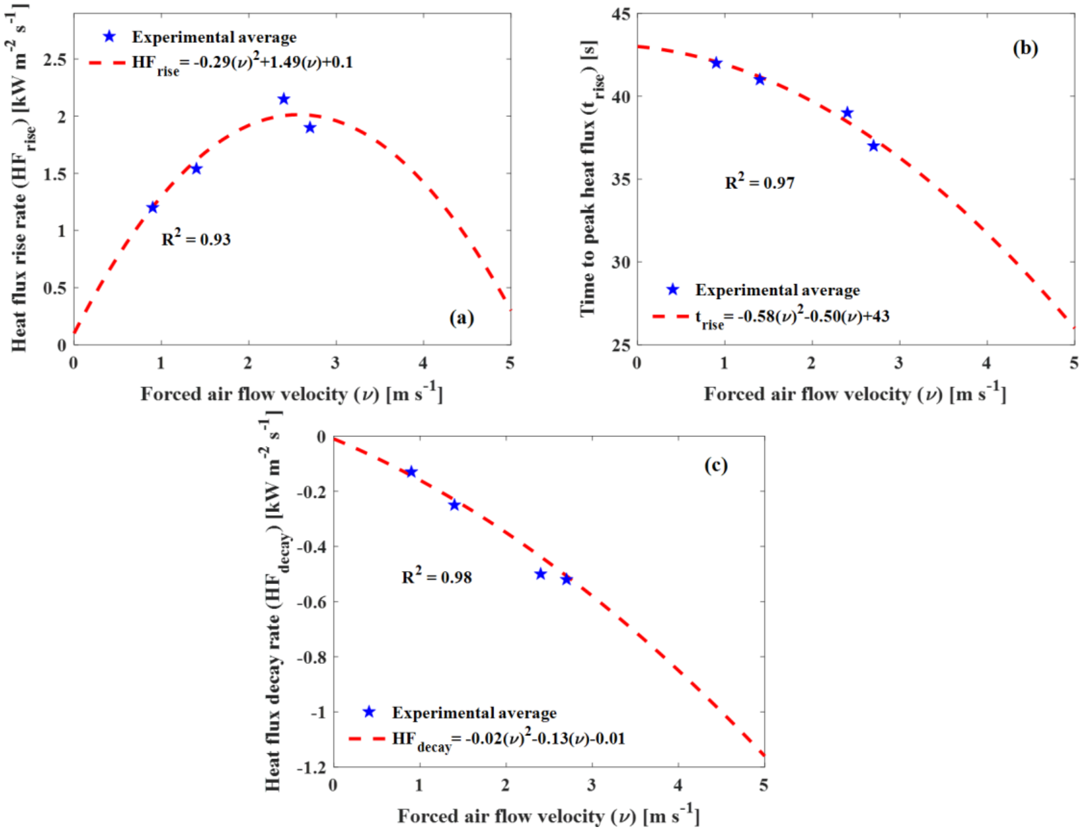

Figure 9-12. Second order polynomial functions used to capture each of the heat flux parameter's dependence on forced air flow velocity (ν) within the preleading temperature measurement zone when using a firebrand pile with a coverage density of 0.16 g cm^{-2}. (a) Heat flux rise rate (HF_{rise}), (d) Time to the peak heat flux (t_{rise}), and (c) Heat flux decay rate (HF_{decay}).

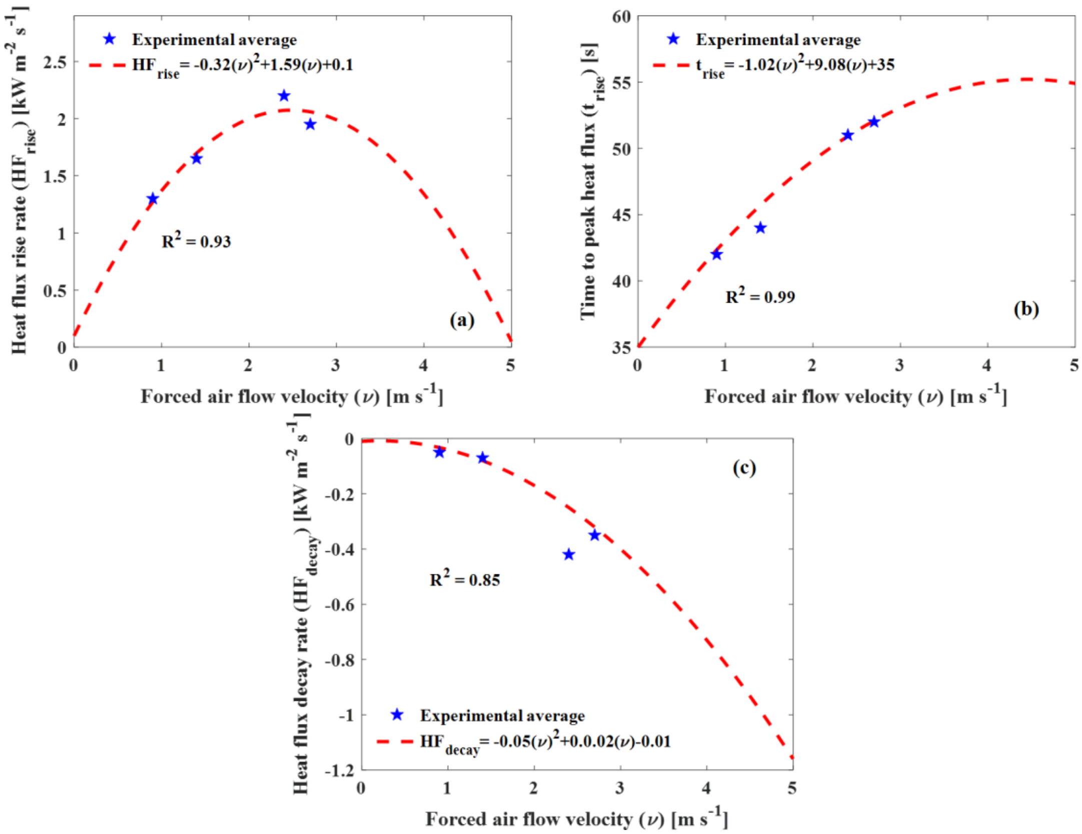

Figure 9-13. Second order polynomial functions used to capture each of the heat flux parameter's dependence on forced air flow velocity (ν) within the leading temperature measurement zone when using a firebrand pile with a coverage density of 0.16 g cm^{-2}. (a) Heat flux rise rate (HF_{rise}), (b) Time to the peak heat flux (t_{rise}), and (c) Heat flux decay rate (HF_{decay}).

9.7.2 <u>Heat flux parameter's dependence on ψ</u>

In this study, each heat flux parameter was quantified at two different firebrand pile coverage densities, ψ, (0.06 and 0.16 g cm^{-2}). However, at an ψ of 0.06 g cm^{-2}, the value of each heat flux parameter was only quantified at two ν-values (1.4 and 2.4 m s^{-1}). The dependence on ψ was constructed by taking into account an observation of Hakes et al. [45] that increasing the firebrand pile mass above 8 g, which approximately corresponds to ψ = 0.16 g cm^{-2}, produced no significant changes in the heat flux to the horizontal substrate. The values of each heat flux parameter at each ψ and the same ν were compared in an effort to capture each heat flux parameter's dependence on ψ. t_{Rise} was found to be independent of ψ. The rest of the heat flux parameters were normalized by the heat flux parameter value at ψ = 0.16 g cm^{-2} resulting in non-dimensional values that ranged from zero (at ψ = 0) to 1. The normalization ensured that the values of each heat flux parameter for a ψ larger than 0.16 g cm^{-2} would be equal to the heat flux value at a ψ = 0.16 g cm^{-2}. The normalized heat flux parameters were subsequently fitted with a hyperbolic tangent function, $F(\psi)$, which captures the limiting behavior of these parameters.

The firebrand pile heat flux decay rate parameter (HF_{Decay}) dependence on ψ in the leading temperature measurement zone was predicted using the reciprocal of the hyperbolic tangent function used to capture the ψ dependence of all other heat flux parameters. In the leading temperature measurement zone and for a common forced air flow velocity, it has been noted that the Kaowool PM back surface temperature decay rate of the larger 0.16 g cm^{-2} firebrand pile is slower than the decay rate of the smaller 0.06 g cm^{-2} firebrand pile (see Table 9-3). The slower decay rate of the larger firebrand pile can potentially be attributed to a larger firebrand pile insulation effect. For the larger, 0.16 g cm^{-2} firebrand pile, the glowing firebrands in contact with the target substrate (at the bottom of the firebrand pile) are partially shielded from the incoming air flow and the rate of consumption of these firebrands is lower than the firebrands at the surface. It is also hypothesized that the firebrands at the surface of the pile act as a mass transport barrier reducing the amount of oxidizer within the firebrand pile. For the smaller 0.06 g cm^{-2} pile, this mass transport barrier effect is less prominent compared to the larger pile resulting in an increased consumption rate of firebrands in contact with the surface of the substrate and environmental heat losses. The hyperbolic tangent functions used to capture the ψ dependence of each heat flux parameter in the preleading- and leading temperature measurement zone are presented in Table 9-6.

Table 9-6. Hyperbolic tangent functions that capture each independent heat flux parameter's dependence on ψ.

Heat flux parameter	Correlation
$F(\psi)$	
Preleading temperature measurement zone	
HF_{Rise}, HF_{Decay}, HF_{Final}	$= \tanh(12\psi)$
t_{Rise}	$= 1$
Leading temperature measurement zone	
HF_{Rise}, HF_{Final}	$= \tanh(12\psi)$
HF_{Decay}	$= (\tanh(12\psi))^{-1}$
t_{Rise}	$= 1$

The experimental average value of each heat flux parameter as a function of ψ, and the hyperbolic tangent functions used to predict each heat flux parameter's dependence on the ψ is shown in Figure 9-14 for the preleading zone and in Figure 9-15 for the leading zone.

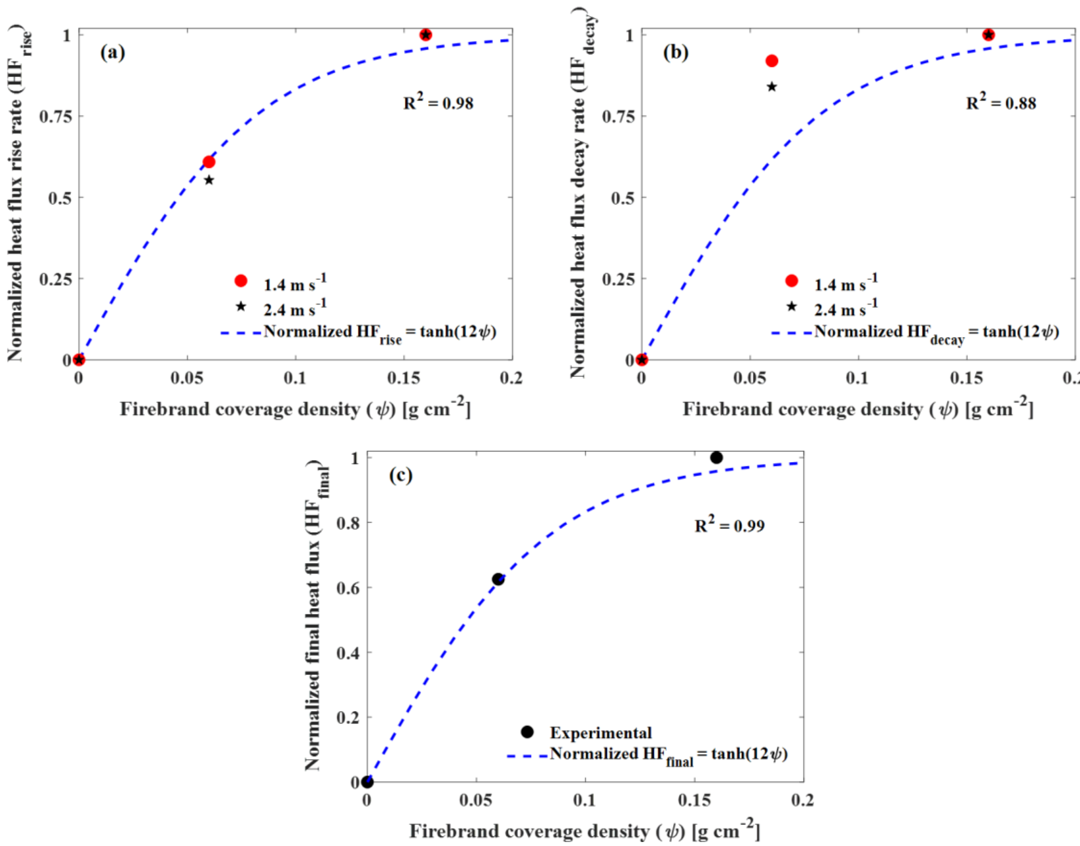

Figure 9-14. Hyperbolic tangent functions used to capture each of the normalized heat flux parameter's dependence on ψ within the preleading temperature measurement zone. (a) Heat flux rise rate (HF_{rise}), (b) Heat flux decay rate (HF_{decay}), and (c) Final constant heat flux (HF_{final}).

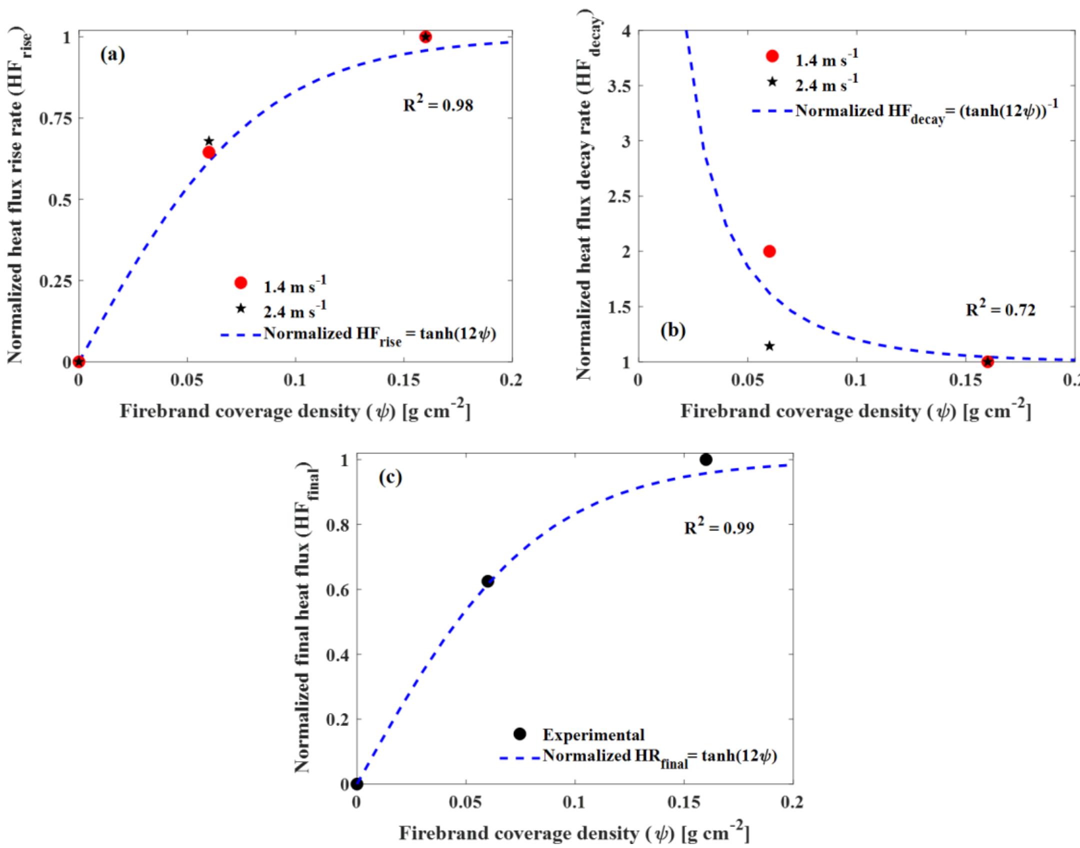

Figure 9-15. Hyperbolic tangent functions used to capture each of the normalized heat flux parameter's dependence on ψ within the leading temperature measurement zone. (a) Heat flux rise rate (HF_{rise}), (b) Heat flux decay rate (HF_{decay}), and (c) Final constant heat flux (HF_{final}).

From Figure 9-15 (b), it is noted that as the normalized heat flux decay rate dependence on coverage density in the leading zone starts to approach the limit of a 0 g cm^{-2}, the hyperbolic tangent function start to approach infinity. However, as the limit of a zero coverage density is reached, the burning behavior of the deposited firebrands will be different to what is typically expected of an accumulated pile of firebrands.

9.8 *Development of an empirical firebrand pile heat flux model*

Using the firebrand pile heat flux correlations presented in Table 9-5 and Table 9-6, an empirical heat flux model, as shown in Equation (9.5), was developed and can be used to generate a set of heat flux parameters that can be used to construct a transient incident firebrand pile heat flux profile as a function of forced air flow velocity and firebrand pile coverage density.

$$\text{Heat flux parameter } (\psi, \nu) = \text{Heat flux parameter } (\psi = 0.16 \text{ g cm}^{-2}, \nu) \times \mathrm{F}(\psi) \quad (9.5)$$

Each of the heat flux parameters used to construct the piecewise linear firebrand pile heat flux function can be calculated using Equation (9.5) which only requires that ν (m s^{-1}) and the ψ (g cm^{-2}) be specified. Further, the empirical heat flux model, shown in Equation (9.5) is applicable for ν ranging from 0 – 4.0 m s^{-1} measured at the surface of a substrate and any ψ.

9.9 *Empirical heat flux model accuracy verification*

A novel empirical firebrand pile heat flux model has been developed and can be used to generate a set of testing condition-specific heat flux parameters that are, in turn, used to construct a unique three-step piecewise linear firebrand pile heat flux function. The accuracy of the generalized heat flux model was evaluated by:

- Generating piecewise linear heat flux functions for all experimental testing condition combinations using the empirical heat flux model;

- Using the piecewise linear heat flux functions to simulate Kaowool PM back surface temperature profiles for each experimental ν and ψ condition in ThermaKin; and
- Comparing how well each ThermaKin-simulated Kaowool PM back surface temperature profile matches its respective experimental back surface temperature profile.

Comparisons between the preleading zone experimental Kaowool PM back surface temperature profiles and the simulated profiles using the generalized heat flux model are shown in Figure 9-16. An R^2-value was used to quantify the accuracy of the match between the experimental and ThermaKin-simulated back surface temperature data. An average R^2 of 0.92, calculated over the first 200 s of a test, was obtained from all testing condition combinations within the preleading and leading temperature measurement zones. The simulated preleading zone (Figure 9-16) and leading zone (Figure 9-17) peak-average back surface temperature values obtained using the empirical heat flux model were within 10 ºC and 19 ºC of the experimental peak-average back surface temperature data. The peak-average back surface temperature was calculated over a 4 s time frame around the global peak back surface temperature value.

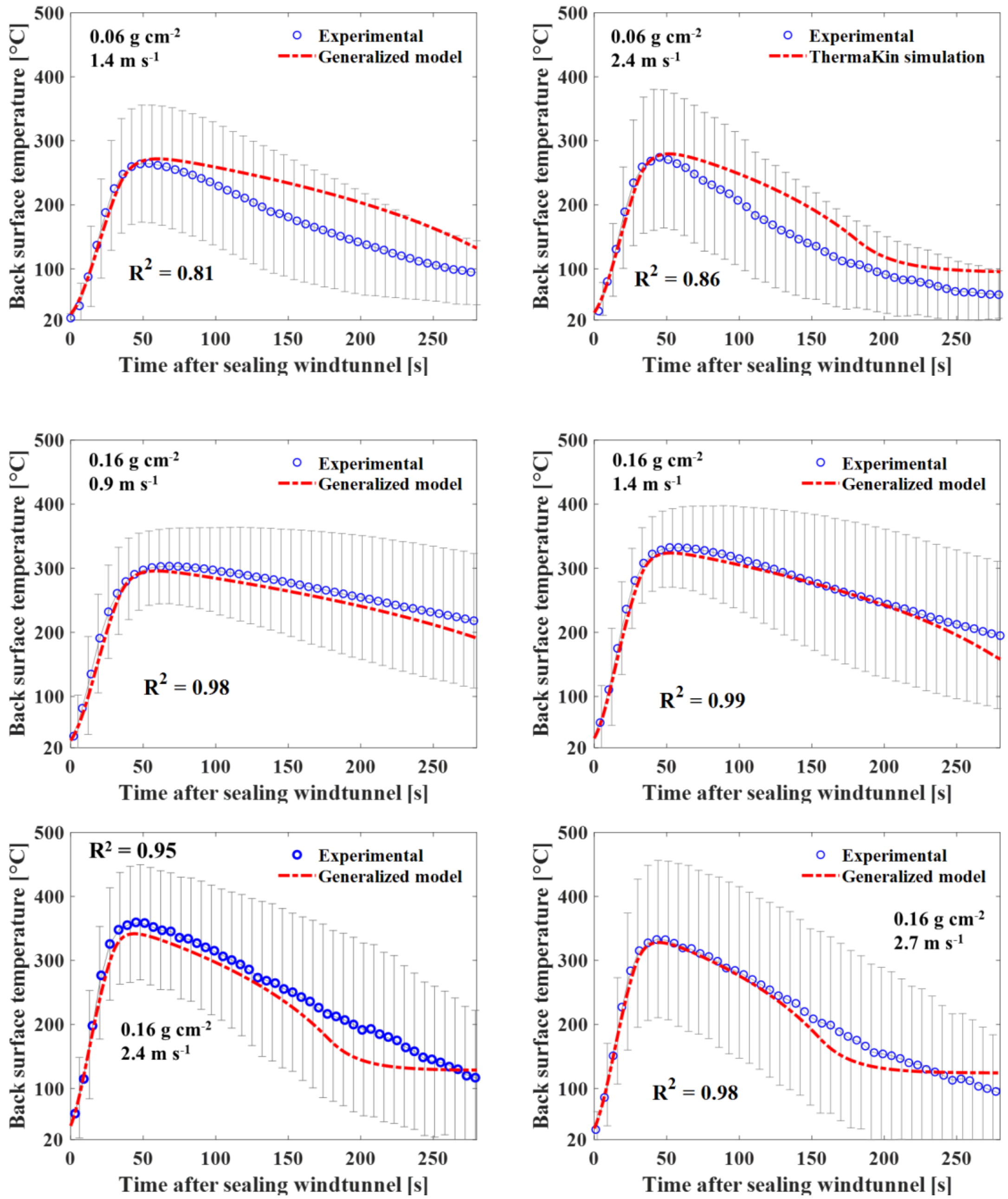

Figure 9-16. Comparison between experimental and generalized heat flux model-simulated Kaowool PM preleading back surface temperature profiles obtained at all testing condition combinations.

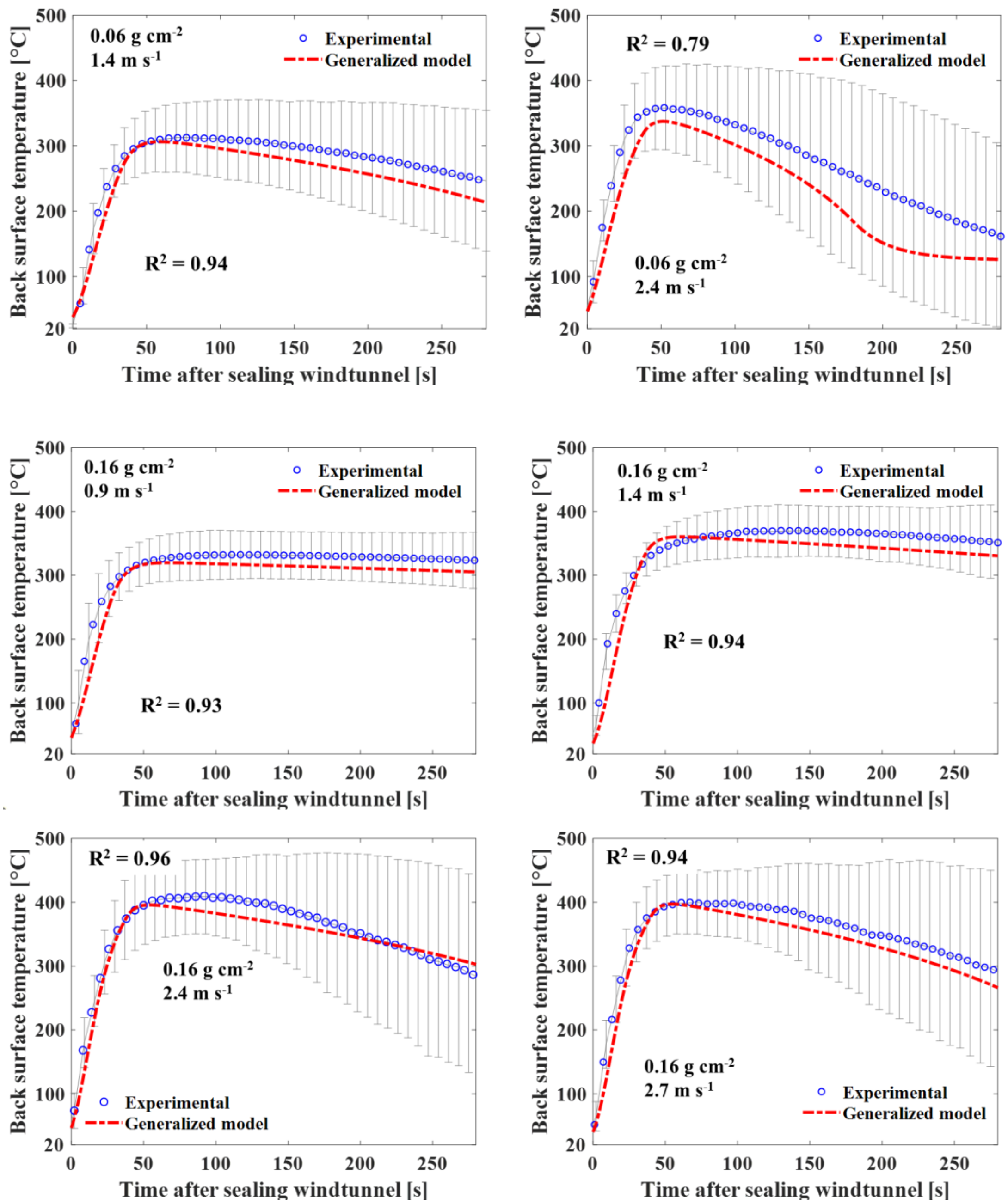

Figure 9-17. Comparison between experimental and generalized heat flux model-simulated Kaowool PM leading back surface temperature profiles obtained at all testing condition combinations.

9.10 Applicability of the empirical heat flux model for other firebrand pile airflow-facing edge lengths

An additional analysis was performed to determine whether changing the firebrand pile edge length facing the incoming air flow resulted in significant changes to the incident firebrand pile heat exposure to the surface of a target substrate. The result of this analysis will provide valuable information as to whether the empirical heat flux model is applicable to firebrand piles with air flow-facing edge lengths other than 5 cm. The effect of changing the firebrand pile edge length facing the incoming air flow from 5 cm to 10 cm was analyzed for all experimental testing condition combinations studied. The firebrand pile deposition area remained the same (50 cm^2) for all experiments. Kaowool PM back surface temperature comparisons in the preleading temperature measurement zone were analyzed as shown in Figure 9-18. A majority of the Kaowool PM back surface temperature data for a 10 cm firebrand pile airflow-facing edge length was provided by Alec Lauterbach (Fire Protection Engineering MS student from the University of Maryland, College Park).

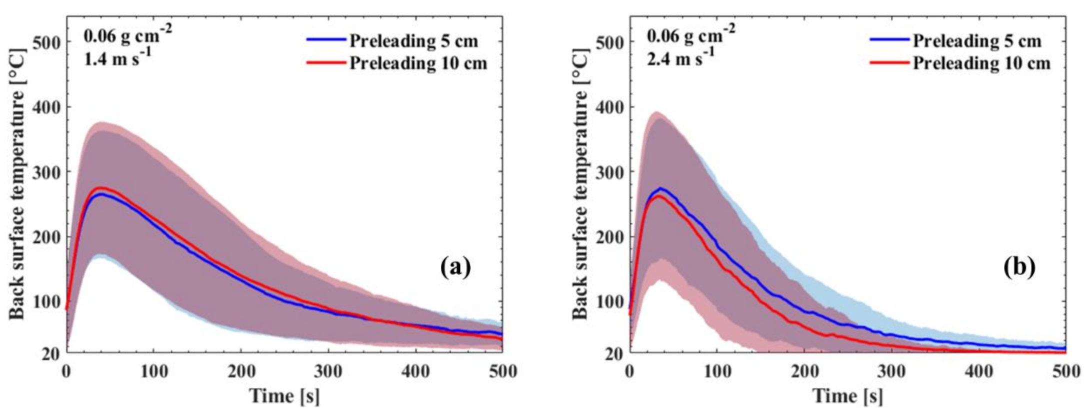

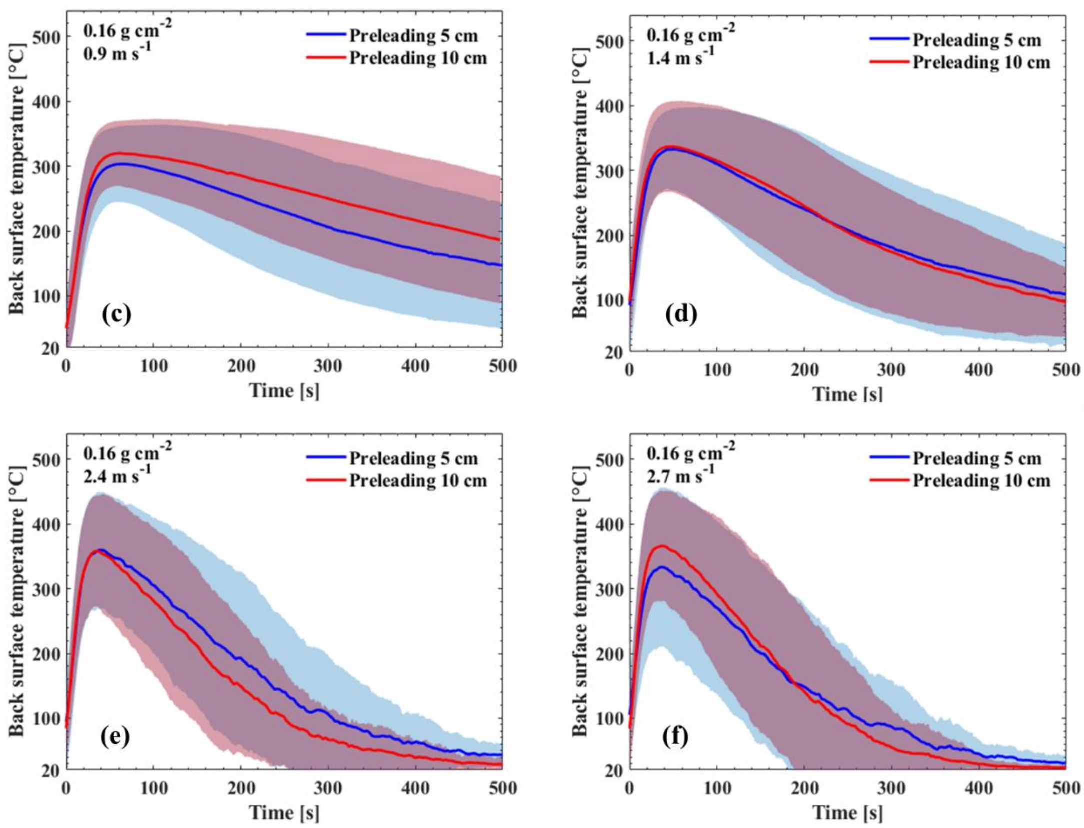

Figure 9-18. Comparisons of the Kaowool PM back surface temperature profiles from the preleading zone using a firebrand pile with either a 5 cm or 10 cm firebrand pile edge length. The variation was calculated as two standard deviations.

For both the preleading and leading zone comparison it was noted that the initial back surface temperature rate of rise for both firebrand pile edge lengths was nearly identical. However, the back surface temperature decay rate was typically slightly larger for the firebrand piles with a 10 cm airflow-facing edge length. The reader is directed to Section 5 for a more in-depth discussion on the increased decay rate for the larger firebrand pile edge length experiments. The mean peak-average back surface temperature data for both firebrand pile edge lengths and within the preleading and leading measurements zone are summarized in Table 9-7. The mean peak-average back surface temperature was calculated using the peak-average back surface temperature from each of the testing condition combinations. The peak-average back surface temperature for each testing condition combination was calculated using a 4 s time frame around the global peak back surface temperature value. The variation of the mean peak-average back surface temperature in each zone was calculated as two standard deviations of the mean.

Table 9-7: Comparisons of the mean peak-average back surface temperature data calculated using data from all testing condition combinations for both the 5 cm and 10 firebrand pile edge length measured within both the preleading and leading temperature measurement zone.

Firebrand pile edge length	Preleading zone (ºC)	Leading zone (ºC)
5 cm	313 ± 32	364 ± 31
10 cm	321 ± 36	362 ± 36

From Table 9-7, it is noted that the mean peak-average back surface temperature for both firebrand pile edge lengths and within the preleading and leading temperature measurement zone differ by 8 and 2 ºC respectively. Therefore, from this comparative analysis it can be concluded that the empirical heat flux model can be used to construct incident firebrand pile heat flux profiles for glowing firebrand piles with airflow-facing edge length other than 5 cm.

10 Development of an Ignition Model for Firebrand-exposed Flammable Materials

Traditionally, the ignitability of a non-porous (solid) fuel has been characterized by its ignition time or ignition temperature. Cone calorimetry [97] (ASTM E1354) is a well-known material flammability testing technique that is frequently used to quantify the ignitability of a variety of fuels (both liquid and solid). In cone calorimetry, the fuel surface is exposed to a known incident radiant heat flux and ignition is typically achieved with the use of a spark igniter pilot located above the fuel surface. Cone calorimetry can be used to determine the critical incident heat flux required for the ignition of a flammable substrate surface in the presence of a pilot ignition source as well as the ignition time. During conventional radiation-driven ignition like in cone calorimetry, the ignition behavior of a substrate is binary which means that ignition will always occur when the critical heat flux required for ignition is reached (i.e., a 0 % probability below the critical heat flux and 100 % probability above the critical heat flux).

In this study, it has been determined that the ignition of a solid, lignocellulosic structural material surface is driven by the incident heat flux from a pile of glowing firebrands. However, the surface ignition probability dependence of WRC, OSB, and PTW on the incident firebrand pile heat flux is continuous rather than binary in nature (see Figure 4-17). In other words, the ignition of the target substrate surface is not necessarily guaranteed once the critical incident heat flux required for ignition of the substrate surface is achieved. In this study, it has been found that the complex, continuous surface ignition behavior of target substrates exposed to a pile of glowing firebrands is dependent on:

- The magnitude of the forced air flow velocity;
- The magnitude of the firebrand pile coverage density;
- The air flow-facing edge length of the firebrand pile; and
- The material onto which the firebrand pile is deposited.

In this section, a novel numerical ignition model will be developed with the end of goal being used to predict the ignition probability of any flammable substrate when exposed to a pile of glowing firebrands having knowledge of only: the pyrolysis properties relevant to the thermal decomposition of the flammable substrate and the magnitude of the forced air flow velocity and firebrand pile coverage density. The ignition model will be developed using: the experimental surface ignition probability data for both WRC, OSB (see Section 4.5) and PTW (provided by Alec Lauterbach from the University of Maryland), the newly-developed empirical firebrand pile heat flux model (see Section 9), and the comprehensive pyrolysis models for WRC (see Section 7), OSB [83], [84], and PTW (see Section 8). Essentially, the goal of developingignition model will be

10.1 HRR as an adequate measure to quantify ignition of target substrates by a pile of glowing firebrands

The temperature at the surface of a solid fuel at the point of ignition often referred to as the ignition temperature (T_{ig}) [74], [101] is an ignition criterion that has been extensively used. The ignition temperature is however an empirical parameter and therefore, T_{ig} cannot be defined as a function of fuel properties or environmental conditions. Measuring the ignition temperature is also a tedious task and is often susceptible to large experimental variability.

The critical mass flux of volatiles at ignition ($\dot{m}''_{cr}$) was first identified by Bamford et al. [102] as an ignition criterion that could be used to more accurately captured the mechanisms associated with the ignition of solid fuels. Rasbash and Drysdale [103] used the $\dot{m}''_{cr}$ as a piloted ignition criterion to study the ignition of PMMA at both the flash and fire point. In the study by Rasbash and Drysdale, the fire point was found to be indicative of sufficient amounts of pyrolyzate being continuously produced to support the formation of a steady diffusion flame at the solid fuel surface. Lundström et al. [104] used the $\dot{m}''_{cr}$ as an ignition criterion to study the ignition behavior of small-scale fires. An ignition event was studied at both the flash and fire point using the Burning Rate Emulator (BRE) apparatus. In their study, the fire point was defined as the minimum volatile mass flux required to sustain a flame for at least 5 s.

Rich et al. [105] studied the dependence of $\dot{m}''_{cr}$ on fuel type and experimental conditions such as external incident heat flux and forced air flow velocity. All experiments were conducted in the FIST (forced ignition and flame spread test) apparatus which consists of a bench-scale wind tunnel fitted with a pair of parabolic strip heaters. The $\dot{m}''_{cr}$ at piloted ignition for the studied solid fuels was found to increase as the incident heat flux and forced air flow velocity increased over the range of 10 – 30 kW m^{-2} and 0.4 – 1.5 m s^{-1} respectively. It was also concluded that $\dot{m}''_{cr}$ was dependent on solid fuel composition.

Lyon and Quintiere [106] quantified the virtual heat release rate (HRR^*) as a unique, material-independent criterion to that can be used quantify the piloted ignition of solid fuels. The HRR^* was calculated as the product of the critical mass flux at ignition and the heat of combustion of the gaseous pyrolyzates. Therefore, HRR^* captures both the solid- and gas-phase mechanisms that are relevant to the piloted ignition of solid fuels. A HRR^* equal to 24 kW m^{-2} was found to be representative of a flash ignition process for a wide range of polymeric materials. Sustained ignition (fire point) was described as the near-stoichiometric burning of a diffusion flame on the surface of the solid fuel and was characterized by a HRR^* of approximately 66 kW m^{-2}.

In the current study, the ignition of a flammable substrate surface will be evaluated considering the process of the formation of a flame on a substrate surface as a competition between all heat generated during the combustion of the solid fuel and all heat losses. The HRR^* will be defined as the parameter that represents the heat generated during the combustion of a horizontally-mounted flammable substrate surface when exposed to a pile of glowing firebrands. All heat losses will be captured using a convective flame quenching heat flux which is representative of the heat losses inhibiting the formation of a flame on the substrate surface.

10.2 Virtual HRR data generation for an arbitrary solid fuels exposed to a pile of glowing firebrands

10.2.1 Lignocellulosic surface ignition probability data

The ignition of a flammable substrate surface in front of a 5 cm air-flow facing edge firebrand pile (that is free of firebrands) was selected in this study as the ignition event that was more likely to lead to fire growth due to direct engagement of the flammable target substrate and where an overwhelming majority of surface ignition events were observed. A majority of WRC and OSB wind tunnel tests were performed with the 5 cm length of the firebrand pile facing the incoming air flow. These WRC and OSB surface ignition statistics have been summarized in Table 10-1 for all testing condition combinations. It is worth reiterating that a surface ignition did not occurred more than once per test and therefore the ignition probability is calculated as the total number of ignitions normalized by the total number of tests (nine) per testing condition.

Table 10-1: Summary of surface ignition probability statistics for WRC and OSB using a firebrand pile with the 5 cm length positioned perpendicular to the direction of the incoming air flow.

Testing condition	WRC ignition probability	OSB ignition probability
1.4 m s^{-1}, 0.06 g cm^{-2}	0.11	0

2.4 m s^{-1}, 0.06 g cm^{-2}	0.11	0
0.9 m s^{-1}, 0.16 g cm^{-2}	0.11	-
1.4 m s^{-1}, 0.16 g cm^{-2}	0.55	0
2.4 m s^{-1}, 0.16 g cm^{-2}	0.55	0.33
2.7 m s^{-1}, 0.16 g cm^{-2}	0.33	0.11

An additional set of wind tunnel experiments were performed using PTW as the flammable target substrate. These PTW tests were performed with the 10 cm length of the firebrand pile facing the incoming air flow. Therefore, to enable a direct comparison with the WRC and OSB surface ignition probability data presented in Table 10-1 which is used for ignition model development, the PTW surface ignition probability data using a 10 cm firebrand pile edge length facing the incoming airflow (presented in Table 10-2) had to be converted to its 5 cm edge length equivalent (data courtesy of Alec Lauterbach from the University of Maryland, College Park). The firebrand pile deposition area was the same for all firebrand pile wind tunnel experiments (50 cm^2).

Table 10-2: Summary of surface ignition probability statistics for PTW using a firebrand pile with the 10 cm length positioned perpendicular to the direction of the incoming air flow.

Testing condition	PTW ignition probability
1.4 m s^{-1}, 0.06 g cm^{-2}	0.22
2.4 m s^{-1}, 0.06 g cm^{-2}	0.33
2.7 m s^{-1}, 0.06 g cm^{-2}	0.11
1.4 m s^{-1}, 0.16 g cm^{-2}	0.22
2.4 m s^{-1}, 0.16 g cm^{-2}	0.67

2.7 m s^{-1}, 0.16 g cm^{-2}	0.67

The surface ignition probability dependence on firebrand pile edge length facing the incoming air flow was determined by assuming that each 5 cm long firebrand pile edge length, facing the incoming air flow, can be evaluated as an independent heat and pilot ignition source. From Section 9.10, it was concluded that the incident firebrand pile heat exposure to the surface of a substrate is independent of firebrand pile edge length further validating the assumption of independent heat sources. The probability of a flammable substrate surface ignition event when exposed to a 10 cm and 5 cm firebrand pile airflow-facing edge length is presented in Equation (10.1) as $P_{ignition,10\ cm}$ and $P_{ignition,5\ cm}$ respectively.

$$P_{ignition,10\ cm} = 1 - \left(1 - P_{ignition,5\ cm}\right)^{n=4.4} \tag{10.1}$$

The power parameter, n, was optimized using experimental WRC, OSB, and PTW surface ignition probability data that was available for both the 5 cm and 10 cm firebrand pile edge lengths as presented in Table 10-3. An optimized value of 4.4 was determined for the power parameter, n. This optimized value was determined by calculating the absolute different between the 10 cm pile edge length experimental and predicted ignition probability data of each substrate and then averaging the absolute differences. The predicted ignition probability data was generated using Equation (10.1) and the experimental ignition probability data at a 5 cm firebrand pile edge length. The optimized power parameter corresponded to the parameter where the predicted 10 cm ignition probability data for WRC, OSB, and PTW was, on average, within ± 6% of the experimental ignition probability data

Table 10-3: Experimental preleading zone surface ignition probability data comparisons for WRC, OSB, and PTW at different firebrand pile edge length

Firebrand pile edge length	WRC 2.4 m s^{-1}, 0.16 g cm^{-2}	OSB 2.4 m s^{-1}, 0.16 g cm^{-2}	PTW 2.7 m s^{-1}, 0.16 g cm^{-2}
5 cm	0.55	0.33	0.22
10 cm	1.0	0.67	0.67

The experimental PTW surface ignition probability data for a 10 cm firebrand pile airflow-facing edge length along with the 5 cm predicted surface ignition probability data (obtained using Eqn. (10.1)) are presented in Table 10-4 for all testing conditions studied. The 5 cm ignition probability data listed in Table 10-4 will be used for ignition model development.

Table 10-4: PTW surface ignition probability statistics for the 10 cm experimental and 5 cm predicted firebrand pile airflow-facing edge length.

Testing condition	10 cm ignition probability	5 cm ignition probability
1.4 m s^{-1}, 0.06 g cm^{-2}	0.22	0.05
2.4 m s^{-1}, 0.06 g cm^{-2}	0.33	0.09
2.7 m s^{-1}, 0.06 g cm^{-2}	0.11	0.03
1.4 m s^{-1}, 0.16 g cm^{-2}	0.22	0.05
2.4 m s^{-1}, 0.16 g cm^{-2}	0.67	0.23
2.7 m s^{-1}, 0.16 g cm^{-2}	0.67	0.23

10.2.2 Firebrand pile burning intensity behavior when deposited on the surface of a flammable target substrate

In Section 4.4, the combustion heat release rate (*HRR)* of a glowing firebrand pile being deposited onto either inert Kaowool PM insulation or a flammable target substrate (WRC and OSB) was studied. It was observed that the firebrand pile burning intensity, quantified as a peak-average *HRR*, was reduced when the firebrand pile was deposited onto a flammable substrate surface rather than being deposited onto inert Kaowool PM insulation. It was concluded that both WRC and OSB initially acted as heat sinks, reducing the burning intensity of the firebrand pile directly after deposition. Therefore, to ensure that this reduced firebrand pile burning intensity behavior was captured in the ignition model, the incident firebrand pile heat flux, obtained using the empirical heat flux model from Section 9, was modified accordingly.

The reduction in the burning intensity of the pile when deposited onto a flammable substrate surface was quantified by normalizing the peak-average combustion *HRR* data for WRC and OSB by the peak-average combustion *HRR* data for Kaowool PM at each common testing condition as presented in Table 10-5. The peak-average combustion *HRR* was calculated over a 4 s time frame around the global maximum *HRR* value. This normalized *HRR* parameter will be labelled as the burning rate reduction ratio for the rest of this dissertation.

Any burning rate reduction ratio values greater than one were adjusted to be equal to one. A burning rate reduction ratio of one indicates that the burning intensity of the flammable substrate surface exposed to a pile of glowing firebrands overrides any heat sink effects. The burning rate reduction ratio value for WRC at a 0.9 m s^{-1} air flow and 0.16 g cm^{-2} was set to be equal to the 1.4 m s^{-1} WRC value at the same firebrand pile coverage density. This was done to ensure that the combustion *HRR* dependence on air flow was maintained (see Figure 4-8). The peak-average combustion *HRR* data along with the burning rate reduction ratio data for each flammable target substrate are presented in Table 10-5.

Table 10-5: Peak-average combustion *HRR* (kW m^{-2}) and burning rate reduction ratio data for Kaowool PM, WRC, and OSB.

Testing condition	Peak-average *HRR* (kW m^{-2})			Burning rate reduction ratio (-)	
	Kaowool PM	WRC	OSB	WRC	OSB
0.9 m s^{-1}, 0.16 g cm^{-2}	132	118	-	0.84	-
1.4 m s^{-1}, 0.16 g cm^{-2}	189	158	138	0.84	0.73
2.4 m s^{-1}, 0.16 g cm^{-2}	302	291	286	0.96	0.95
2.7 m s^{-1}, 0.16 g cm^{-2}	270	300	310	1.0	1.0
1.4 m s^{-1}, 0.06 g cm^{-2}	125	101	68	0.81	0.54
2.4 m s^{-1}, 0.06 g cm^{-2}	181	156	101	0.86	0.56

Linear empirical correlations were developed to capture the reduced burning intensity of a firebrand pile when deposited onto WRC and OSB over the full range of air flows that are applicable to the empirical firebrand pile heat flux model and for both firebrand pile coverage densities as shown in Figure 10-1.

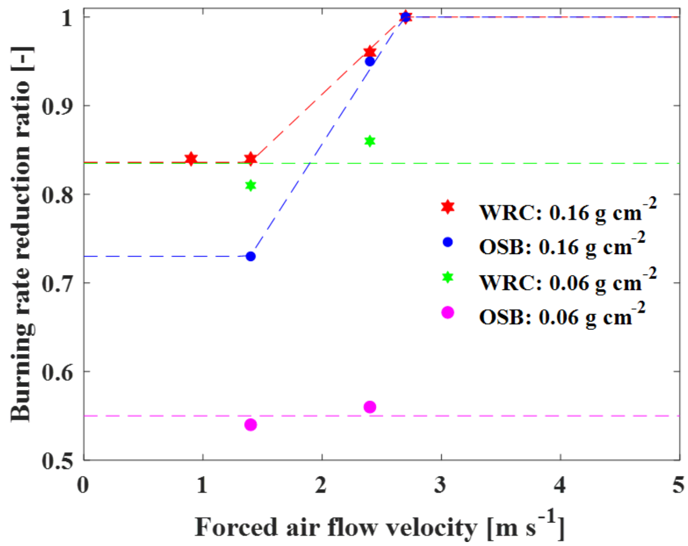

Figure 10-1. Burning rate reduction ratio data and linear empirical correlations for WRC and OSB at all experimental testing condition combinations studied.

The linear empirical correlations used to capture the reduced firebrand pile burning intensity when deposited onto WRC and OSB at a 0.16 g cm^{-2} firebrand pile coverage density are presented in Equation (10.2) and (10.3). The forced air flow velocity has been denoted as ν for purpose of analysis. The burning rate reduction ratio of both WRC and OSB at the smaller 0.06 g cm^{-2} firebrand pile coverage density was assumed constant over the entire range of air flow velocities applicable to the empirical firebrand pile heat flux model. The constant burning rate reduction ratio values for WRC and OSB were calculated as average of the burning rate reduction ratios for both air flows (1.4 and 2.4 m s^{-1}) and were equal to 0.84 and 0.55 respectively.

$$\text{Burning rate reduction ratio}_{\text{WRC}} = \begin{cases} 0.84 & \text{when } \nu \leq 1.4 \text{ m s}^{-1} \\ 0.13\nu + 0.65 & \text{when } 1.4 \text{ m s}^{-1} < \nu < 2.6 \text{ m s}^{-1} \\ 1.0 & \text{when } \nu \geq 2.6 \text{ m s}^{-1} \end{cases} \quad (10.2)$$

$$\text{Burning rate reduction ratio}_{\text{OSB}} = \begin{cases} 0.73 & \text{when } \nu \leq 1.4 \text{ m s}^{-1} \\ 0.21\nu + 0.44 & \text{when } 1.4 \text{ m s}^{-1} < \nu < 2.6 \text{ m s}^{-1} \\ 1.0 & \text{when } \nu \geq 2.6 \text{ m s}^{-1} \end{cases} \quad (10.3)$$

WRC was selected to represent the lignocellulosic substrate that reduces the firebrand pile burning intensity the least while OSB was assumed to represent the substrate with the largest heat sink effect. A thermally-thick ignition theory can be used to describe the ignition behavior of a horizontally-mounted flammable target substrate exposed to a pile of glowing firebrands within the wind tunnel. From the thermally-thick ignition theory [74], it is known that the incident heat exposure to a flammable substrate surface is related to the square root of the thermal inertia of said material and the difference between the ignition and ambient temperature.

The thermal inertia is calculated as the product of the material density, thermal conductivity, and heat capacity. The thermal inertia for undecomposed WRC and OSB were calculated using the optimized thermophysical properties from each of the flammable substrate's comprehensive pyrolysis models. The square root of the thermal inertia (J m^{-2} K^{-1} $s^{-0.5}$) for WRC and OSB were equal to 224 and 321 respectively. A binary thermal inertia criterion was used to determine whether an arbitrary lignocellulosic material will adopt either the heat sink behavior of WRC or OSB and was calculated as the average of these two values, 273 J m^{-2} K^{-1} $s^{-0.5}$. Therefore, if the square root of the thermal inertia of a flammable substrate is lower than 273 J m^{-2} K^{-1} $s^{-0.5}$ it will adopt the heat sink behavior of WRC otherwise it will adopt the heat sink behavior of OSB. The square root of the thermal inertia of PTW was calculated to be equal to 289 J m^{-2} K^{-1} $s^{-0.5}$ and hence the heat sink behavior of OSB was adopted.

This reduced firebrand pile burning intensity behavior was captured in the ignition model by adjusting the incident firebrand pile heat flux to the surface of a flammable target substrate. The incident heat flux was adjusted by only changing the magnitude of the heat flux rise rate (HF_{Rise}) parameter. The magnitude of this parameter was reduced using the burning rate reduction ratio fraction that is applicable to the air flow, firebrand pile coverage density, and material being evaluated. The modified HF_{Rise} was calculated as the product of the unmodified HF_{Rise} and the burning rate reduction ratio fraction. It was assumed that reduction of the firebrand pile burning intensity did not significantly affect the heat flux decay rate and the time to peak heat flux (t_{Rise}). The reader is directed to Figure 4-11, where the global combustion *HRR* profiles for Kaowool PM, WRC, and OSB are compared. It is visually noted that the flammable substrate combustion *HRR* rise rate is qualitatively lower than when Kaowool PM is used. Qualitatively, the combustion HRR decay rate is similar for all target substrates.

10.2.3 Flammable target substrates HRR^* data generation

Similar to the inverse firebrand pile heat flux model development using Kaowool PM insulation, a 1-D, radiation-driven ThermaKin simulation was developed for the deposition of a pile of glowing firebrands onto a flammable substrate surface. The flammable substrate ThermaKin simulation was used to generate WRC, OSB, and PTW MLR profiles for all experimental testing condition combinations. Radiant heat exposure from a pile of glowing firebrands onto the substrate surface in front of the pile was captured in ThermaKin using the modified firebrand pile incident heat flux profiles from Section 10.2.2. The adjusted heat flux profiles were used to capture the reduced burning intensity of a firebrand pile when deposited onto a flammable substrate and at each testing condition combination studied.

In the current ThermaKin simulations, natural convective losses at the bottom boundary of a flammable substrate were the same as that used when simulating the firebrand pile heat exposure to a Kaowool PM insulation surface (see Section 9.4). The forced convective losses within the preleading temperature measurement zone were calculated using Equations (9.1) through (9.2). All air properties used to calculate the local forced convection coefficients were taken at a film temperature of 493 K. This film temperature was determined as the mean of the ambient temperature of 293 K and the average substrate surface temperature measured underneath a pile of firebrands, 693 K [47], [48]. The forced convection coefficients at the top surface of a target substrate for all studied forced air flows (0.9, 1.4, 2.4, and 2.7 m s^{-1}) were equal to 5.1, 6.3, 8.3, and 8.8 W m^{-2} K^{-1}.

Each flammable substrate MLR profile was converted into a HRR^* profile by multiplying the MLR of each gaseous intermediate with its corresponding heat of combustion value obtained from inverse analysis of MCC data. WRC and PTW heats of combustion data are listed in Table 7-5 and Table 8-4. OSB heat of combustion data were determined by Gong et al. [84]. The physical properties and initial conditions used during the simulation of the flammable substrate MLR profiles in ThermaKin are presented in Table 10-6.

Table 10-6: Physical properties and initial conditions used during the simulation of the flammable substrate MLR profiles

Flammable substrate	Sample thickness (cm)	Moisture content (wt.%, dry basis)	Initial temperature (K)
WRC	21	4.6	293
OSB	11.5	7.0	293
PTW	18.6	7.0	293

Representative HRR^* profiles for WRC, OSB, and PTW at a 2.4 m s^{-1} air flow velocity and 0.16 g cm^{-2} firebrand pile coverage density as shown in Figure 10-2.

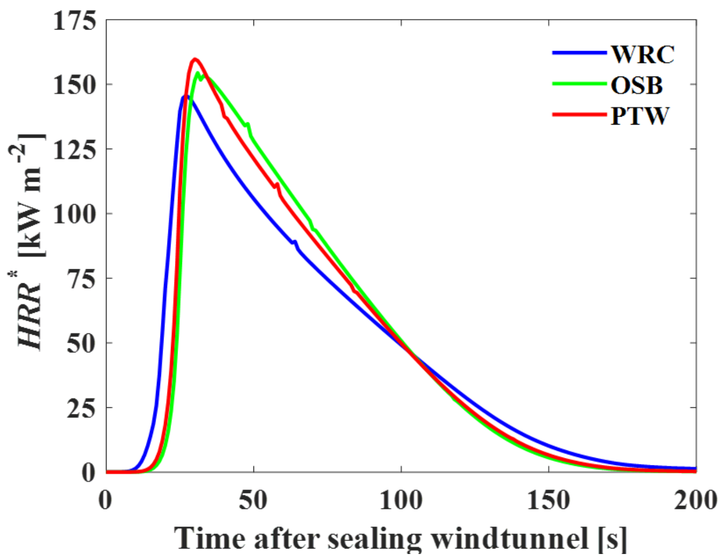

Figure 10-2. Transient HRR^* profiles for WRC, OSB, and PTW generated from the preleading temperature measurement zone at a 2.4 m s^{-1} air flow velocity and 0.16 g cm^{-2} firebrand pile coverage density. Firebrand piles with 5 cm edge lengths facing the air flow were used.

10.3 *Development of an ignition model used to predict the ignition probability of an arbitrary substrate when exposed to a pile of glowing firebrands*

As part of the development of the ignition model, a peak-average HRR^* value (kW m^{-2}) was calculated for each testing condition combination. The peak-average HRR^* value was calculated by applying a 60 s moving average to each of the simulated HRR^* profiles and then extracting a peak value. The 60 s averaging time frame was calculated using the mean burning duration statistics (presence of a flame on the surface of a flammable substrate) from all the WRC, OSB and PTW surface ignition events. The peak-average HRR^* values from each testing condition combination studied are presented in Table 10-7.

Table 10-7: Peak-average HRR^* values (kW m^{-2}) for all lignocellulosic flammable substrates and at all studied testing condition combinations.

Testing condition	WRC	OSB	PTW
0.9 m s^{-1}, 0.16 g cm^{-2}	40	-	-
1.4 m s^{-1}, 0.16 g cm^{-2}	71.5	31.4	36.9
2.4 m s^{-1}, 0.16 g cm^{-2}	104.3	115.8	112.1
2.7 m s^{-1}, 0.16 g cm^{-2}	100.3	112.9	111.7
1.4 m s^{-1}, 0.06 g cm^{-2}	14.9	0.02	0.06
2.4 m s^{-1}, 0.06 g cm^{-2}	17.1	0.02	0.05
2.7 m s^{-1}, 0.06 g cm^{-2}	-	-	0.02

It has been observed that the forced air flow velocity is a parameter that significantly affects the incident heat exposure from a pile of glowing firebrands to the surface of a flammable target substrate as well as the ignition susceptibility of a flammable substrate. Increasing the forced airflow increases the burning intensity of the firebrand pile but also increases the convective cooling of the pile. The competition of these two air flow affects have resulted in the incident firebrand pile heat flux starting to plateau around 2.4 m s^{-1} and then decreasing with the air flow increases above 2.7 m s^{-1}.

As previously mentioned, the ignition of a flammable substrate surface (formation of a flame of the substrate surface) was described as a competition between the heat generated during combustion of the flammable substrate and all heat losses. The peak-average HRR^{*} is indicative of all the heat generated during flaming combustion while all heat losses are a result of the convective cooling of the surface inhibiting the formation of a flame. A new material-independent peak-average flame stability parameter ($\overline{\Omega}_{\mathrm{peak}}$) will be presented in this dissertation research and will be used to characterize the ignition of a flammable substrate surface when exposed to a pile of glowing firebrands. The peak-average flame stability parameter is mathematically presented in Equation (10.4).

$$\overline{\Omega}_{\mathrm{peak}} = {}^{\mathrm{Peak} - \mathrm{average}\ HRR^{*}}\Big/_{\mathrm{Q}''_{\mathrm{convective}}} \qquad (10.4)$$

A flame quenching convective heat flux $Q''_{convective}$ was used to capture the forced convective losses within the preleading temperature measurement zone. $Q''_{convective}$ was calculated as the product of a forced convective heat transfer coefficient and the absolute difference between the flame quenching temperature (1573 K) and the ambient air temperature (293 K). The flame quenching temperature is indicative of the minimum temperature required to sustain flaming combustion at a flammable substrate surface.

The forced convective heat transfer coefficient value for each testing condition combination was calculated using Equations (9.1) through (9.2). All air properties used to calculate these local forced convection coefficients were taken at a film temperature of 933 K. The film temperature at the top surface was calculated using a flame quenching temperature of 1573 K [101] and an ambient temperature of 293 K. The forced convection coefficients at the top surface of a target substrate that are used to emulate the convective losses inhibiting the formation of a diffusion flame on the surface of said substrate when exposed to a pile of glowing firebrands at all studied forced air flows (0.9, 1.4, 2.4, and 2.7 m s^{-1}) were equal to 5.0, 6.2, 8.1, and 8.6 W m^{-2} K^{-1}. Subsequently, the $Q''_{\mathrm{convective}}$ heat flux values at each of the experimentally-studied forced air flow velocity (0.9, 1.4, 2.4, and 2.7 m s^{-1}) are equal to 6.3, 7.9, 10.4, and 11 kW m^{-2}.

The experimental ignition probability data for each of the lignocellulosic substrates and at each testing condition combination was plotted against all corresponding $\overline{\Omega}_{\mathrm{peak}}$-data (see Equation (10.4)) obtained from ThermaKin simulations as shown in Figure 10-3. The experimental ignition probability data shown in Figure 10-3 were generated using a firebrand pile with a 5 cm edge length facing the incoming air flow.

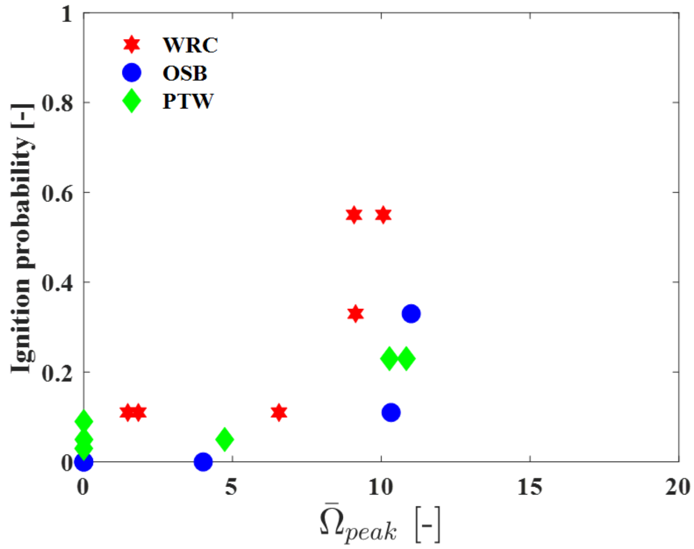

Figure 10-3. Experimental surface ignition probability of all studied lignocellulosic materials as a function of the peak-average $\bar{\Omega}_{\text{peak}}$-data at all experimental testing condition combinations. Firebrand piles with a 5 cm edge length facing the air flow were used to develop the numerical ignition model.

A logistic growth model function as shown in Equation (10.5) was found to be the function that best captured the ignition probability dependence on the $\bar{\Omega}_{\text{peak}}$-data. The logistic growth function is typically used to model the exponential growth of a variable having an upper limit, in this case an ignition probability of 1. The ignition probability behavior of a flammable substrate when exposed to a pile of glowing firebrands was found to start exponentially increasing for $\bar{\Omega}_{\text{peak}}$-values above 6.0. The ignition probability rate of rise would start slowing down as the upper limit of one was being approached. An ignition probability of one indicates that the surface of flammable substrate will ignite every time it is exposed to a pile of glowing firebrands at a known forced air flow velocity.

$$\text{Ignition probability}\left(\bar{\Omega}_{\text{peak}}\right) = 1/\left(1 + e^{\mu - \left(\bar{\Omega}_{\text{peak}}\right)/s}\right) \quad (10.5)$$

The logistic growth model parameters μ and s are known as the location and scale parameters and are both non-dimensional. The scale parameter, s, was fixed at a value of 1. Therefore, only the location parameter, μ, was fitted to the experimental ignition probability and $\bar{\Omega}_{\text{peak}}$-data and was determined to be equal to 10.8. The numerical ignition model is shown in Figure 10-4 as a dashed black line. The model was, on average, capable of predicting the ignition probability of a flammable substrate when exposed to a 5 cm edge length firebrand pile within 14% of its experimental equivalent at a common testing condition combination.

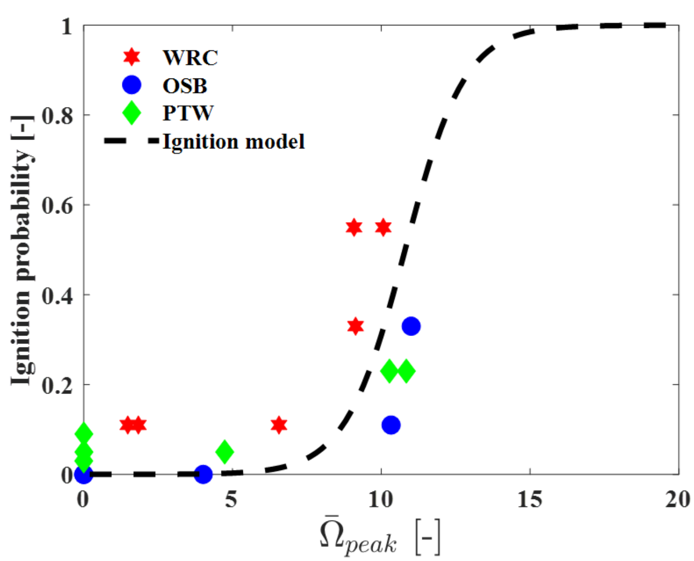

Figure 10-4. The ignition model, represented as a logistic growth model function that is used to predict the ignition probability of an arbitrary substrate when exposed to a pile of glowing firebrands. All data was collected for a 5 cm airflow facing edge length firebrand pile.

For the first time, a novel numerical ignition model (Equation (10.5)) has been developed that can be used to predict the ignition probability of an arbitrary flammable substrate when exposed to a pile of glowing firebrands. The model requires knowledge of the peak-average HRR^* (60 s moving average) of the arbitrary substrate which is obtained from ThermaKin simulations which incorporates both the empirical firebrand pile incident heat flux model and the comprehensive pyrolysis model of said substrate. For firebrand pile edge lengths between 0 and 10 cm, linear interpolation between the 0, 5, and 10 cm lengths can be employed to determine the ignition probability. It is assumed that the ignition probability at the 0 cm edge length is equal to 0. The process of obtaining the ignition probability of a pile with and airflow-facing edge length between 0 and 5 cm or between 5 and 10 cm includes:

- Using the numerical ignition model to obtain the ignition probability that corresponds to a known $\overline{\Omega}_{\mathrm{peak}}$ when exposed to a 5 cm airflow-facing edge pile;
- Using Equation (10.1) to generate the ignition probability corresponding to a 10 cm air flow facing edge length pile; and
- Calculating the ignition probability using linearly interpolating between 0 and 5 cm or 5 and 10 cm.

For firebrand pile edge lengths larger than 10 cm, the pile should be separated into individual 10 cm lengths assuming each 10 cm length acts as an independent firebrand pile. The ignition probability for each 10 cm airflow-facing edge length is determined using the numerical ignition model and Equation (10.1). The ignition probability of any remaining firebrand pile edge length smaller than 10 cm is obtained through linear interpolation.

10.4 Ignition and burn time predictions using the numerical ignition model

The numerical ignition model can be used to predict the probability of ignition of a flammable substrate surface when exposed to a pile of glowing firebrands under wind. An additional evaluation of the applicability of the ignition model was performed to determine whether the ignition time and flaming burning duration of an arbitrary material could also be accurately predicted. This evaluation was performed using all the experimental ignition timing and burning duration statistics of the three lignocellulosic materials at the 0.16 g cm^{-2} firebrand pile coverage density. The ignition timing and burning duration statistics at the smaller 0.06 g cm^{-2} firebrand pile coverage density were not used for this evaluation based on the fact that none of their HRR^{*} profiles exceeded 24 kW m^{-2}, the minimum HRR^{*} required for flash ignition at the surface of a flammable substrate [106]. Further, from Figure 10-4 it is noted that the ignition model predicts zero surface ignitions when using the smaller 0.06 g cm^{-2} pile even though, experimentally, single ignitions events where observed for select testing conditions and flammable substrates. The ignition timing and burning duration statistics from both 5 cm and 10 cm air flow facing firebrand pile edge length experiments were used during this analysis.

Numerical ignition timing and burning statistics were generated by identifying a critical instantaneous flame stability parameter ($\Omega_{\text{Instantaneous}}$) that most closely approximated the experimental ignition timing and burning duration data for all flammable substrates at each forced air flow velocity studied. $\Omega_{\text{Instantaneous}}$ was calculated using Equation (10.6) which is a function of the instantaneous HRR^* and the convective flame quenching heat flux $\text{Q}''_{\text{convective}}$

$$\Omega_{\text{Instantaneous}} = {}^{\text{Instantaneous } HRR^*}/_{\text{Q}''_{\text{convective}}} \tag{10.6}$$

A single $\Omega_{\text{Instantaneous}}$-value was used to generate all WRC, OSB, and PTW ignition statistics. Similarly, a single $\Omega_{\text{Instantaneous}}$-value was used to generate all WRC, OSB, and PTW burning duration statistics. The process of obtaining a $\Omega_{\text{Instantaneous}}$-value entailed changing the $\Omega_{\text{Instantaneous}}$-value in increments of 0.05 until the smallest absolute average difference between the experimental and numerical ignition timing and burning duration data was achieved.

The following procedure was used to generate numerically-predicted ignition timing and burning duration statistics from each flammable substrate $\Omega_{\text{Instantaneous}}$ profile: After the first identified critical $\Omega_{\text{Instantaneous}}$-value was first reached, the timing after sealing the wind tunnel corresponded to the ignition time. Similarly, once the second critical $\Omega_{\text{Instantaneous}}$-value was reached, the difference between the total timing after sealing the wind tunnel and the numerically-predicted ignition time corresponded to the burning duration. This procedure is graphically presented in Figure 10-5 for a WRC $\Omega_{\mathrm{Instantaneous}}$ profile at a 2.4 m s^{-1} air flow and 0.16 g cm^{-2} firebrand pile coverage density.

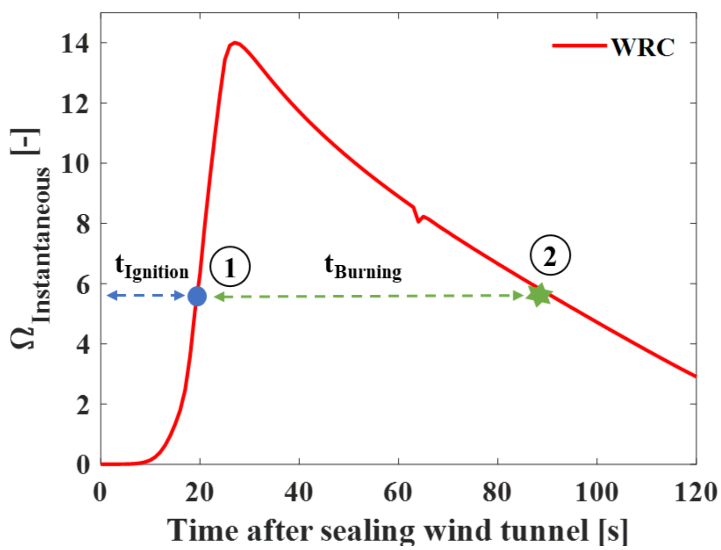

Figure 10-5: Graphical representation of the procedure used to generate ignition and burning duration statistics from a $\Omega_{\mathrm{Instantaneous}}$ profile. The $\Omega_{\mathrm{Instantaneous}}$ profile is of WRC exposed to a 0.16 g cm^{-2} firebrand pile and a 2.4 m s^{-1} air flow velocity. The dashed lines are indicative of the critical $\Omega_{\mathrm{Instantaneous}}$-value used during analysis.

The numerically-generated ignition timing data using a critical $\Omega_{\mathrm{Instantaneous}}$-value of 5.9 was found to most closely approximate the experimental ignition timing data. Further, it was also found that the numerically-predicted burning duration data using the same critical $\Omega_{\mathrm{Instantaneous}}$-value of 5.9 was found to most closely approximate the experimental burning duration data. The experimental and predicted ignition timing and burning duration data using a critical $\Omega_{\text{Instantaneous}}$-value of 5.9, are shown in Figure 10-6 and Figure 10-7, respectively. The experimental variation was calculated from the data scatter as two standard deviations of the mean.

From Figure 10-6, it was be concluded that, on average, the difference between the numerically-generated and experimental ignition timing of WRC, OSB, and PTW was equal to 11 s. Similarity from Figure 10-7, it was concluded that the difference between the numerically-generated and experimental burning duration was, on average, equal to 26 s.

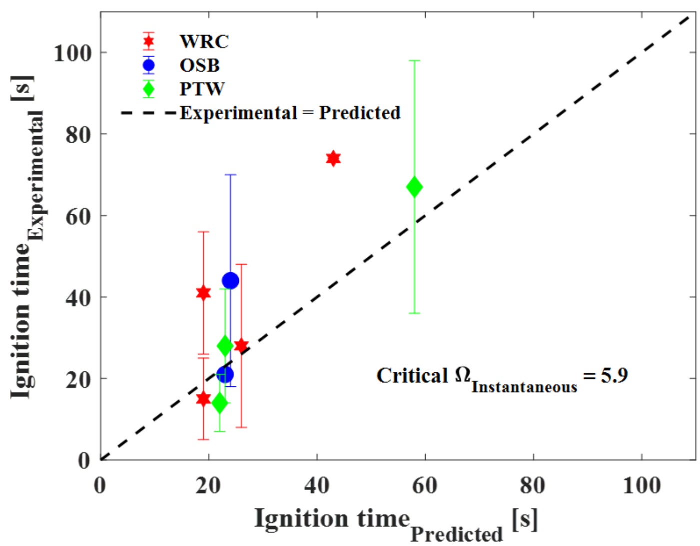

Figure 10-6: Comparison of experimental and numerically-generated ignition timing data for WRC, OSB, PTW when exposed to 0.16 g cm^{-2} firebrand pile and all air flows studied. Firebrand piles with 5 and 10 cm edge lengths were used.

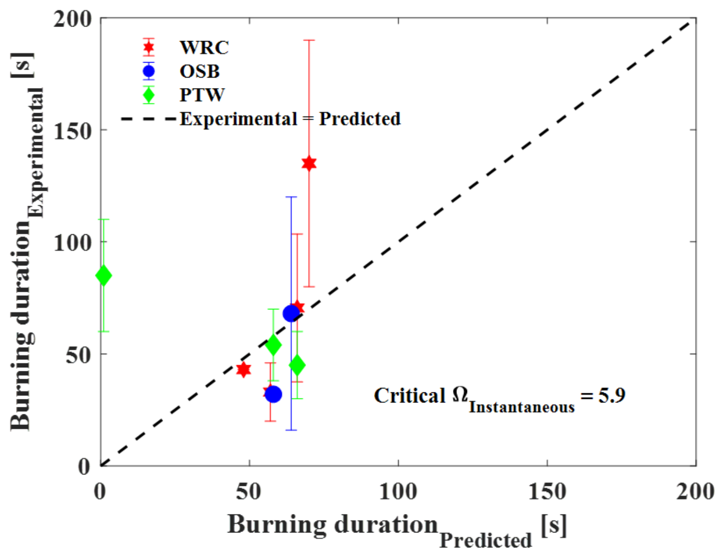

Figure 10-7: Comparison of experimental and numerically-generated burning duration data for WRC, OSB, PTW when exposed to 0.16 g cm^{-2} firebrand pile and all air flows studied. Firebrand piles with 5 and 10 cm edge lengths were used.

Additionally, an ignition and burning duration criterion was developed for scenarios where the peak $\Omega_{\text{Instantaneous}}$-value of an arbitrary flammable substrate exposed to a pile of glowing firebrands was smaller than the critical $\Omega_{\text{Instantaneous}}$-value of 5.9. In these scenarios, it was assumed that if ignition of the flammable substrate surface were to occur, the mean ignition timing and burning duration would be equal to 21 and 55 s, respectively. These data points were obtained considering the ignition and burning duration statistics for all WRC, OSB, and PTW which had a peak $\Omega_{\text{Instantaneous}}$-value smaller than the critical $\Omega_{\text{Instantaneous}}$-value of 5.9.

As has already been indicated, statistics from both the 5 cm and 10 cm firebrand pile edge length experiments were used during the comparison of the experimental and numerically-generated ignition and burning duration data. In Section 5.4 it was noted that for both WRC and OSB, increasing the firebrand pile edge length from 5 cm to 10 cm resulted in near-identical WRC and OSB ignition times and slightly larger burning durations. The similarity of ignition statistics for different firebrand pile edge lengths was attributed to the heat exposure from a firebrand pile to the surface of a flammable substrate being independent on firebrand pile edge length. Each 5 cm firebrand pile length could be treated as an independent heating source (see Section 10.2.1). For these reasons, the numerically-generated ignition timing and burning duration predictions are also applicable for any firebrand pile airflow-facing edge length.

11 Conclusions

The complex, stochastic ignition behavior of horizontally-mounted flammable substrates by a pile of glowing firebrands under wind was investigated using a detailed experimental and modeling framework. My primary contributions from this research study discussed in the dissertation are summarized below:

- Identifying and subsequently quantifying the mechanisms responsible for the ignition of lignocellulosic substrates when exposed to a pile of glowing firebrands using ignition statistics as well as combustion heat release rate and combustion efficiency data collected for an extensive set of experimental testing conditions.
- The development of a custom inverse modeling technique, using Kaowool PM back surface temperature profiles as an adequate target measurement, to construct piecewise linear firebrand pile heat flux functions.
- The development of a novel empirical heat flux model that can be used to construct incident firebrand pile heat flux profiles for a wide range of forced air flows (0 – 4 m s^{-1}) and all firebrand pile coverage densities.
- The development of novel numerical ignition model using a solid-phase pyrolysis solver ThermaKin to enable ignition probability predictions for an arbitrary target substrate subject to a pile of glowing firebrands of any size and geometry.

In this study, a bench-scale wind tunnel experimental protocol was designed to identify the mechanisms responsible for the ignition of horizontally-mounted lignocellulosic building materials when subject to a pile of glowing firebrands. The firebrand pile coverage density, geometry, and forced air flow velocity were all controlled in these experiments. Over 200 experiments were performed to collect data related to the intensity of heat exposure from the firebrand pile to the substrate surface and the combustion heat release rate and combustion efficiency of the firebrands or the flammable substrates. Ignition timing, location, and probability data were also collected for all substrates tested. Two distinct types of ignition events were identified. The first ignition type corresponded to the formation of a faint, blue, unsteady flame on the top surface of the pile; the second ignition type resulted in the formation of a steady, luminous diffusion flame attached to the surface of the substrate. The substrate ignitions were postulated to be most likely to lead to further fire growth. However, despite well controlled experimental conditions, surface ignition events were found to be stochastic in nature. The majority of substrate surface ignition events were found to occur in front of the air flow-facing edge of the firebrand pile.

The ignition dependence on material density was compared using Western Red Cedar (WRC) and Oriented Strand Board (OSB). The ignition probability of both flammable materials were significantly affected by the firebrand pile coverage density and forced air flow velocity magnitude. The probability of substrate ignition was found to increase by a factor of five for WRC and a factor of three for OSB when the firebrand pile coverage density was increased from 0.06 g cm^{-2} to 0.16 g cm^{-2}. The ignition probability dependence of WRC and OSB on air flow were similar and correlated with the firebrand thermal exposure intensity data which was quantified as the peak-average back surface temperature of a thin, inert Kaowool PM board as well as the firebrand pile heat release rate data. The probability of a substrate surface ignition increased with the air flow velocity increasing up to 2.4 m s^{-1} and then decreased upon further increase in the air flow velocity. The non-monotonic trend is suggested to be a competition between increasing oxygen supply promoting burning of the firebrands and increasing convective cooling of the firebrand surfaces. WRC was found to be more susceptible to ignition by glowing firebrands than OSB.

The ignition probability dependence of WRC and OSB on the firebrand pile edge length facing the incoming air flow was studied and compared. It was found that the ignition probability of WRC increased from 55 % to 100 % and OSB increased from 33 % to 67 % as the firebrand pile edge length facing the incoming air flow was increased from 5 cm to 10 cm. The increased ignition probability was postulated to be a result of the additional 5 cm of the flammable surface being exposed to the firebrand pile thermal insult which can produce more gaseous pyrolyzate that can potentially ignite as well as the increased number of firebrand pilots. The use of intermittent air flow conditions was studied and the ignition probability of WRC and OSB compared. The use of short high air flow velocity gusts (2.7 m s^{-1}) rather than a continuous air flow increased the number of surface ignition events during a single test. The probability of at least one ignition being observed when using an intermittent air flow increased from 33 % to 100 % for WRC and 11 % to 67 % for OSB when using a firebrand pile with a 5 cm airflow-facing edge length. The majority of WRC and OSB surface ignition events were noted to occur directly after termination of the air flow gust. It was postulated that the termination of the forced air flow allowed for the accumulation of sufficient amounts of gaseous fuel at the leading edge of the firebrand pile that could with mix with the fresh oxidizer and ignite.

Pyrolysis of two lignocellulosic substrates (WRC and PTW) was comprehensively parameterized using a hierarchical inverse analysis of small- and gram scale experimental data. Inverse analysis of experimental data was automated using a hill-climbing optimization algorithm, coupled with a comprehensive pyrolysis solver, ThermaKin. Thermogravimetric analysis (TGA) and differential scanning calorimetry (DSC) were used to parameterize the thermal decomposition reaction kinetics and thermodynamics. Microscale combustion calorimetry (MCC) was used to quantify the heat of combustion of all volatile intermediates during thermal decomposition. Controlled Atmosphere Pyrolysis Apparatus (CAPA II) experiments were performed and experimental data used to parametrize thermophysical properties, which included density and thermal conductivity. The development of two comprehensive pyrolysis models further validate the hierarchical inverse analysis methodology.

A custom inverse heat flux modeling technique using a pyrolysis solver, ThermaKin, was developed to quantify the incident firebrand pile heat exposure to the surface of a target substrate for a range of testing condition combinations. Kaowool PM back surface temperature data was used an adequate target measurement for the inverse heat flux modeling technique. A set of heat flux parameters were identified and used to capture the transient burning behavior of a pile of glowing firebrands. These testing condition-specific heat flux parameters were subsequently used to construct piecewise linear firebrand pile heat flux functions. A three-step piece wise linear function was found to be the simplest function that could accurately capture the transient burning behavior of a pile of firebrands. A coefficient of determination (R^2) was used to quantify the quality of the match between the experimental Kaowool PM and ThermaKin-simulated back surface temperature data. All Kaowool PM back surface temperature profiles in both the preleading and leading temperature measurement zone could be matched with an R^2 larger than 0.96, calculated over the first 200 s of a test. A novel empirical heat flux model was developed and could be used to construct a piecewise linear firebrand pile heat flux function for a wide range of air flows (0 – 4 m s^{-1}) and all firebrand pile coverage densities. The empirical heat flux model was developed using the heat flux parameters used to construct a piecewise linear heat flux function. It was found that a group of second-order polynomial functions could be used to accurately capture each heat flux parameter's dependence of air flow. A single hyperbolic tangent function was used to capture the firebrand pile heat flux dependence of firebrand pile coverage density. The applicability of the heat flux model was also validated and it was found that the firebrand pile heat flux model is independent of firebrand pile edge length. The simulated preleading and leading peak-average back surface temperature values obtained using the empirical heat flux model were within 10 and 19 ºC of the experimental peak-average back surface temperature data.

For the first time, a numerical ignition model was developed to enable ignition probability predictions of any arbitrary material subject to a pile of glowing firebrands. The novel ignition model was developed using the comprehensive pyrolysis models of three commonly-used lignocellulose building materials (WRC, OSB, and PTW) in combination with the empirical firebrand pile heat flux model. A peak-average dimensionless flame stability parameter was used to quantify the ignition of a flammable substrate surface by a pile of glowing firebrands. The newly-defined flame stability parameter is a material-independent parameter that captures both the gas- and condensed phases processes indicative of flaming ignition.

The numerical ignition model also captures the reduced burning intensity of a firebrand pile when deposited onto a flammable substrate surface. The ignition model was based on the formation of a flame on a substrate surface being represented as a competition between all heat generated during combustion and all heat losses. The heat generated during combustion was captured using a material-independent virtual heat release rate parameter while all heat losses were captured using a forced airflow-specific flame quenching convective heat flux. A logistic growth function was used to capture the ignition probability dependence of three lignocellulosic materials the newly-defined flame stability parameter. The ignition model was capable of predicting the exeprimntal ignition probability of all lignocellulosic materials tested within 14%, on average. A secondary analysis was performed in which the ignition model was used to generate WRC, OSB, and PTW ignition timing and burning duration statistics. A critical flame stability parameter value was used as a criterion to generate the ignition statistics. It was found that, on average, the numerically generated ignition timing and burning duration data was within 11 and 26 s of the experimental ignition data.

To further the understanding of the ignition of building materials by a pile of glowing firebrands, several topics have been recommended as the focus of future work. The first recommendation involves generating firebrand pile thermal exposure data at testing condition combinations and firebrand pile geometries other than what was evaluated in this study. This will undoubtedly improve the accuracy of the heat flux correlations used to construct time-dependent firebrand pile heat flux profiles which will also improve the accuracy of the ignition model. Further, generating experimental ignition probability and timing data for WRC, OSB, and PTW at other testing condition combinations would be extremely valuable to evaluate the accuracy of the numerical ignition model. Currently, the ignition model was developed using only a limited number of data points. Generating ignition probability data and pyrolysis models for other common building materials typically used in the WUI would help solidify the used of ignition model as a numerical tool to predict the ignition any flammable substrate when exposed to a pile of glowing firebrands. Finally, generating experimental data for other configurations where firebrands are known to accumulate during a wildfire such as a reentrant corner or vertical siding will further our understanding of the complex interactions between flammable solid substrates and pile of glowing firebrands under wind.

12 Appendix

12.1 ThermaKin files used during inverse analysis of firebrand pile heat flux data

Representative examples of the ThermaKin2Ds component and conditioning files used during inverse analysis of the Kaowool PM back surface temperature data

Component file used to simulate the uncoated Kaowool PM back surface temperature data for all testing condition combinations

```
COMPONENT: KAOWOOL_1
STATE: S
DENSITY: 232  0  0  0
HEAT CAPACITY: 1070 0  0  0
CONDUCTIVITY: 0.052 -4e-5 1e-7 2
TRANSPORT: 1e-30 0 0 0
EMISSIVITY & ABSORPTION: 0.64 10000

COMPONENT: KAOWOOL_painted
STATE: S
DENSITY: 232  0  0  0
HEAT CAPACITY: 1070 0  0  0
CONDUCTIVITY: 0.052 -4e-5 1e-7 2
TRANSPORT: 1e-30 0 0 0
EMISSIVITY & ABSORPTION: 0.94 10000

MIXTURES
S SWELLING: 0
L SWELLING: 0
G SWELLING LIMIT: 1e-30
PARALL CONDUCTIVITY: 0.5
PARALL TRANSPORT: 0.5
```

Condition file used to simulate the uncoated Kaowool PM back surface temperature data for all testing condition combinations

OBJECT TYPE: 1D

OBJECT STRUCTURE
****
THICKNESS: 0.00159
TEMPERATURE: 293
MASS FRACTIONS:
KAOWOOL_1 1

THICKNESS: 0.00159
TEMPERATURE: 293
MASS FRACTIONS:
KAOWOOL_painted 1

OBJECT BOUNDARIES
****

TOP BOUNDARY

MASS TRANSPORT: NO

OUTSIDE INIT TEMP: 293
OUTSIDE HEAT RATE: 0 0 0 0
CONVECTION COEFF: 8.25

EXTERNAL RADIATION: YES
TIME PROG1: 0.4e3 2.15e3 39
TIME PROG2: 84.25e3 -0.5e3 153
REPEAT: NO
ABSORPTION MODE: MAX

FLAME: NO

BOTTOM BOUNDARY

MASS TRANSPORT: NO

OUTSIDE INIT TEMP: 293
OUTSIDE HEAT RATE: 0 0 0 0
CONVECTION COEFF: 4.82

EXTERNAL RADIATION: YES
TIME PROG1: 429.4 0 6000
TIME PROG2: 0 0 0
REPEAT: NO
ABSORPTION MODE: MAX

12.2 CAPA II top and bottom experimental temperature and model prediction comparison

The temporal evolution of the top surface temperature in CAPA II experiments is experimentally tracked using a thermocouple at the level and in close proximity to the top surface of the sample. The temporal evolution of the bottom surface temperature is tracked using a thermocouple that is positioned inside the gasification chamber and directly below the bottom sample surface. The model predictions are used to account for convective losses at the top surface of the sample as well as convective and radiative losses at the bottom sample surface.

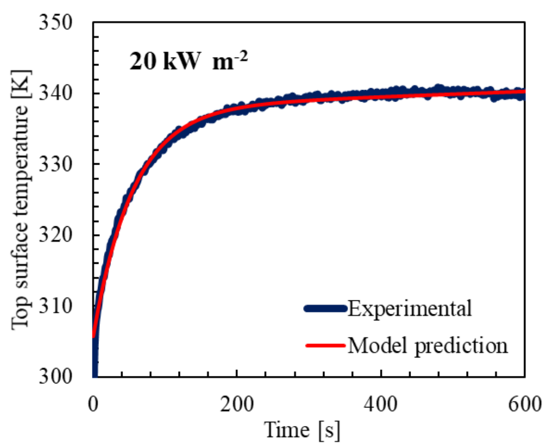

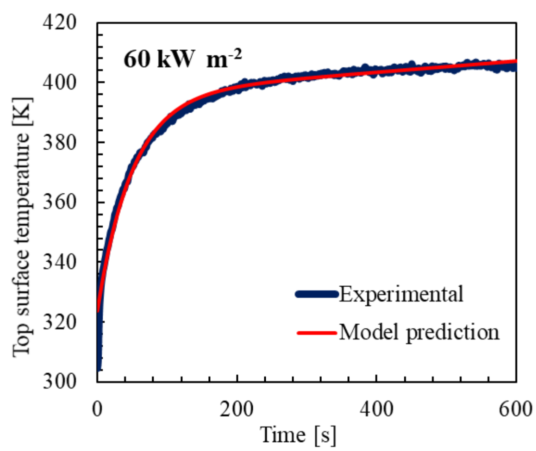

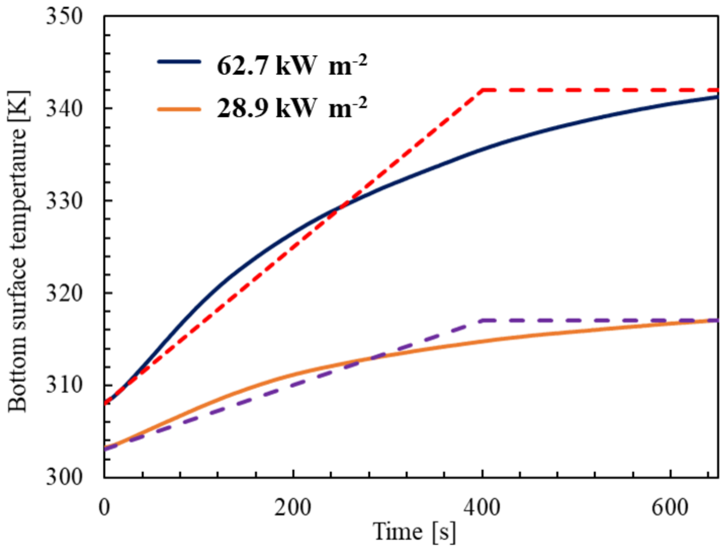

Figure 12-1. Visual representation of empirical fits used capture the time-dependent behavior of both the top and bottom CAPA II sample surface temperature

Bibliography

[1] V. C. Radeloff *et al.*, “Rapid Growth of the US Wildland-Urban Interface Raises Wildfire Risk,” *Proc. Natl. Acad. Sci. U. S. A.*, vol. 115, no. 13, pp. 3314–3319, Mar. 2018, doi: 10.1073/pnas.1718850115.

[2] National Interagency Coordination Center, “Wildland Fire Summary and Statistics Annual Report,” Boise, Idaho, 2022.

[3] CalFire, “Top 20 Most Destructive California Fires.” https://www.fire.ca.gov/media/t1rdhizr/top20_destruction.pdf

[4] T. Brown, S. Leach, B. Wachter, and B. Gardunio, “The Northern California 2018 extreme fire season,” *Bull. Am. Meteorol. Soc.*, vol. 101, no. 1, pp. S1–S4, 2020, doi: 10.1175/BAMS-D-19-0275.1.

[5] A. Filkov, D. Kasymov, V. Zima, and O. Matvienko, “Experimental Investigation of Surface litter Ignition by Bark Firebrands,” in *AIP Conference Proceedings*, Jan. 2016, vol. 1698. doi: 10.1063/1.4937859.

[6] S. E. Caton, R. S. P. Hakes, D. J. Gorham, A. Zhou, and M. J. Gollner, “Review of Pathways for Building Fire Spread in the Wildland Urban Interface Part I: Exposure Conditions,” *Fire Technol.*, vol. 53, no. 2, pp. 429–473, Mar. 2017, doi: 10.1007/s10694-016-0589-z.

[7] S. Nazare, I. Leventon, and R. Davis, “Ignitibility of Structural Wood Products Exposed to Embers During Wildland Fires: A Review of Literature,” Gaithersburg, MD, Apr. 2021. doi: 10.6028/NIST.TN.2153.

[8] W. E. Mell, S. L. Manzello, A. Maranghides, D. Butry, and R. G. Rehm, “The wildland-urban interface fire problem - Current approaches and research needs,” *Int. J. Wildl. Fire*, vol. 19, no. 2, pp. 238–251, 2010, doi: 10.1071/WF07131.

[9] A. C. Fernandez-Pello, “Wildland fire spot ignition by sparks and firebrands,” *Fire Saf. J.*, vol. 91, pp. 2–10, Jul. 2017, doi: 10.1016/j.firesaf.2017.04.040.

[10] J. D. Cohen and B. W. Butler, “Modeling Potential Structure Ignitions from Flame Radiation Exposure with Implications for Wildland/Urban Interface Fire Management,” 1998.

[11] J. D. Cohen and R. D. Stratton, “Home destruction examination: Grass Valley Fire, Lake Arrowhead, California,” 2008.

[12] A. Maranghides and W. Mell, “A Case Study of a Community Affected by the

Witch and Guejito Wildland Fires," *Fire Technol.*, vol. 47, no. 2, pp. 379–420, Apr. 2011, doi: 10.1007/s10694-010-0164-y.

[13] A. Maranghides, D. McNamara, R. Vihnanek, J. Restaino, and C. Leland, "A Case Study of a Community Affected by the Waldo Fire – Event Timeline and Defensive Actions," Gaithersburg, MD, Nov. 2015. doi: 10.6028/NIST.TN.1910.

[14] S. L. Manzello, S. Suzuki, and Y. Hayashi, "Enabling the study of structure vulnerabilities to ignition from wind driven firebrand showers: A summary of experimental results," in *Fire Safety Journal*, Nov. 2012, vol. 54, pp. 181–196. doi: 10.1016/j.firesaf.2012.06.012.

[15] E. Koo, P. J. Pagni, D. R. Weise, and J. P. Woycheese, "Firebrands and spotting ignition in large-scale fires," *International Journal of Wildland Fire*, vol. 19, no. 7. pp. 818–843, 2010. doi: 10.1071/WF07119.

[16] S. Stephens, D. Molina, R. Carter, and R. Martin, "Comparison of Fuel Load, Structural Characteristics, and Infrastructure Before and After the Oakland Hills Tunnel Fire," Albany, 2005.

[17] V. Babrauskas, "Firebrands and Embers," in *Encyclopedia of Wildfires and Wildland-Urban Interface (WUI) Fires*, S. Manzello, Ed. Cham: Springer, 2020, pp. 431–444.

[18] S. L. Manzello, S. Suzuki, M. J. Gollner, and A. C. Fernandez-Pello, "Role of firebrand combustion in large outdoor fire spread," *Progress in Energy and Combustion Science*, vol. 76. Elsevier Ltd, Jan. 01, 2020. doi: 10.1016/j.pecs.2019.100801.

[19] S. Suzuki, A. Brown, S. L. Manzello, J. Suzuki, and Y. Hayashi, "Firebrands generated from a full-scale structure burning under well-controlled laboratory conditions," *Fire Saf. J.*, vol. 63, pp. 43–51, Jan. 2014, doi: 10.1016/j.firesaf.2013.11.008.

[20] F. Hedayati, "GENERATION AND CHARACTERIZATION OF FIREBRANDS FROM SELECTED STRUCTURAL FUELS."

[21] S. L. Manzello and S. Suzuki, "Generating wind-driven firebrand showers characteristic of burning structures," *Proc. Combust. Inst.*, vol. 36, no. 2, pp. 3247–3252, 2017, doi: 10.1016/j.proci.2016.07.009.

[22] S. Adusumilli, J. E. Chaplen, and D. L. Blunck, "Firebrand Generation Rates at the Source for Trees and a Shrub," *Front. Mech. Eng.*, vol. 7, Jun. 2021, doi: 10.3389/fmech.2021.655593.

[23] T. Hudson, R. Bray, D. Blunck, W. Page, and B. Butler, “Effects of fuel morphology on ember generation characteristics at the tree scale,” *Int. J. Wildl. Fire*, vol. 29, no. 11, pp. 1042–1051, 2020.

[24] A. Filkov *et al.*, “Investigation of firebrand production during prescribed fires conducted in a pine forest,” *Proc. Combust. Inst.*, vol. 36, no. 2, pp. 3263–3270, 2017, doi: 10.1016/j.proci.2016.06.125.

[25] S. L. Manzello, A. Maranghides, J. R. Shields, W. E. Mell, Y. Hayashi, and D. Nii, “Mass and Size Distribution of Firebrands Generated from Burning Korean Pine (Pinus koraiensis) Trees,” *Fire Mater.*, vol. 33, no. 1, pp. 21–31, 2009, doi: 10.1002/fam.977.

[26] S. L. Manzello, A. Maranghides, W. E. Mell, T. G. Cleary, and J. C. Yang, “Firebrand production from burning vegetation,” *For. Ecol. Manage.*, vol. 234, p. S119, Nov. 2006, doi: 10.1016/j.foreco.2006.08.160.

[27] S. L. Manzello, A. Maranghides, and W. E. Mell, “Firebrand Generation from Burning Vegetation,” *Int. J. Wildl. Fire*, vol. 16, no. 4, pp. 458–462, 2007, doi: 10.1071/WF06079.

[28] S. Suzuki and S. L. Manzello, “Characteristics of Firebrands Collected from Actual Urban Fires,” *Fire Technol.*, vol. 54, no. 6, pp. 1533–1546, Nov. 2018, doi: 10.1007/s10694-018-0751-x.

[29] J. P. Woycheese, “WOODEN DISK COMBUSTION FOR SPOT FIRE SPREAD INTERFLAM 2001 WOODEN DISK COMBUSTION FOR SPOT FIRE SPREAD,” 2001.

[30] S. Suzuki and S. L. Manzello, “Firebrand production from building components fitted with siding treatments,” *Fire Saf. J.*, vol. 80, pp. 64–70, Feb. 2016, doi: 10.1016/j.firesaf.2016.01.004.

[31] D. K. Thompson *et al.*, “Quantifying Firebrand Production and Transport Using the Acoustic Analysis of In-Fire Cameras,” *Fire Technol.*, vol. 58, no. 3, pp. 1617–1638, May 2022, doi: 10.1007/s10694-021-01194-y.

[32] K. Zhou, S. Suzuki, and S. L. Manzello, “Experimental Study of Firebrand Transport,” *Fire Technol.*, vol. 51, no. 4, pp. 785–799, Jul. 2015, doi: 10.1007/s10694-014-0411-8.

[33] A. Tohidi and N. B. Kaye, “Comprehensive wind tunnel experiments of lofting and downwind transport of non-combusting rod-like model firebrands during firebrand shower scenarios,” *Fire Saf. J.*, vol. 90, pp. 95–111, Jun. 2017, doi: 10.1016/j.firesaf.2017.04.032.

[34] K. Himoto and T. Iwami, “Generalization framework for varying characteristics of the firebrand generation and transport from structural fire source,” *Fire Saf. J.*, vol. 125, Oct. 2021, doi: 10.1016/j.firesaf.2021.103418.

[35] E. Koo, R. Linn, P. Pagni, and C. Edminster, “Modeling firebrand transport in wildfires using HIGRAD/FIRETEC,” *Int. J. Wildl. Fire*, vol. 21, no. 4, pp. 396–417, 2011.

[36] A. Tohidi and N. B. Kaye, “Stochastic modeling of firebrand shower scenarios,” *Fire Saf. J.*, vol. 91, pp. 91–102, Jul. 2017, doi: 10.1016/j.firesaf.2017.04.039.

[37] R. Wadhwani, D. Sutherland, A. Ooi, and K. Moinuddin, “Firebrand transport from a novel firebrand generator: numerical simulation of laboratory experiments,” *Int. J. Wildl. Fire*, vol. 31, no. 6, pp. 634–648, 2022.

[38] O. A. Ivchenko, A. V. Tiutin, G. P. Nadejkina, A. V. Kirichenko, and K. E. Pankin, “An approach to estimating the range of wild fire firebrands transportation by wind,” in *IOP Conference Series: Earth and Environmental Science*, Feb. 2022, vol. 979, no. 1. doi: 10.1088/1755-1315/979/1/012158.

[39] N. A. McArthur and P. Lutton, “Ignition of Exterior Building Details in Bushfires: An Experimental Study,” *Fire Mater.*, vol. 15, no. 2, pp. 59–64, 1991.

[40] V. P. Dowling, “Ignition of Timber Bridges in Bushfires,” 1994.

[41] S. L. Manzello and S. Suzuki, “Exposing Decking Assemblies to Continuous Wind-Driven Firebrand Showers,” *Fire Saf. Sci.*, vol. 11, pp. 1339–1352, 2014.

[42] S. L. Manzello and S. Suzuki, “Experimental investigation of wood decking assemblies exposed to firebrand showers,” *Fire Saf. J.*, vol. 92, pp. 122–131, Sep. 2017, doi: 10.1016/j.firesaf.2017.05.019.

[43] S. Suzuki and S. L. Manzello, “Investigating Coupled Effect of Radiative Heat Flux and Firebrand Showers on Ignition of Fuel Beds,” *Fire Technol.*, vol. 57, no. 2, pp. 683–697, Mar. 2021, doi: 10.1007/s10694-020-01018-5.

[44] S. Santamaria, K. Kempna, M. El, and H. Efectis, “Investigation of Structural Wood Ignition by Firebrand Accumulation,” 2015. [Online]. Available: https://www.researchgate.net/publication/302413245

[45] R. S. P. Hakes, H. Salehizadeh, M. J. Weston-Dawkes, and M. J. Gollner, “Thermal Characterization of Firebrand Piles,” *Fire Saf. J.*, vol. 104, pp. 34–42, Mar. 2019, doi: 10.1016/j.firesaf.2018.10.002.

[46] Z. Tao, B. Bathras, B. Kwon, B. Biallas, M. J. Gollner, and R. Yang, “Effect of Firebrand Size and Geometry on Heating from a Smoldering Pile under Wind,”

Fire Saf. J., vol. 120, Mar. 2021, doi: 10.1016/j.firesaf.2020.103031.

[47] H. Salehizadeh, R. S. P. Hakes, and M. J. Gollner, "Critical Ignition Conditions of Wood by Cylindrical Firebrands," *Front. Mech. Eng.*, vol. 7, Mar. 2021, doi: 10.3389/fmech.2021.630324.

[48] F. Richter, B. Bathras, J. Barbetta Duarte, and M. J. Gollner, "The Propensity of Wooden Crevices to Smoldering Ignition by Firebrands," *Fire Technol.*, 2022, doi: 10.1007/s10694-022-01247-w.

[49] E. D. Bearinger, J. L. Hodges, F. Yang, C. M. Rippe, and B. Y. Lattimer, "Localized heat transfer from firebrands to surfaces," *Fire Saf. J.*, vol. 120, Mar. 2021, doi: 10.1016/j.firesaf.2020.103037.

[50] E. Bearinger, B. Y. Lattimer, J. L. Hodges, C. Rippe, and A. Kapahi, "Statistical Assessment of Parameters Affecting Firebrand Pile Heat Transfer to Surfaces," *Front. Mech. Eng.*, vol. 7, Jul. 2021, doi: 10.3389/fmech.2021.702181.

[51] M. A. Santoso, E. G. Christensen, J. Yang, and G. Rein, "Review of the Transition From Smouldering to Flaming Combustion in Wildfires," *Frontiers in Mechanical Engineering*, vol. 5. Frontiers Media S.A., Sep. 18, 2019. doi: 10.3389/fmech.2019.00049.

[52] S. I. Stoliarov, O. Zeller, A. B. Morgan, and S. Levchik, "An experimental setup for observation of smoldering-to-flaming transition on flexible foam/fabric assemblies," *Fire Mater.*, vol. 42, no. 1, pp. 128–133, Jan. 2018, doi: 10.1002/fam.2464.

[53] R. M. Hadden, S. Scott, C. Lautenberger, and C. C. Fernandez-Pello, "Ignition of Combustible Fuel Beds by Hot Particles: An Experimental and Theoretical Study," *Fire Technol.*, vol. 47, no. 2, pp. 341–355, Apr. 2011, doi: 10.1007/s10694-010-0181-x.

[54] A. Warey, "Influence of thermal contact on heat transfer from glowing firebrands," *Case Stud. Therm. Eng.*, vol. 12, pp. 301–311, Sep. 2018, doi: 10.1016/j.csite.2018.04.018.

[55] S. Wang, X. Huang, H. Chen, and N. Liu, "Interaction between flaming and smouldering in hot-particle ignition of forest fuels and effects of moisture and wind," *Int. J. Wildl. Fire*, vol. 26, no. 1, pp. 71–81, 2016.

[56] S. S. Wessies, M. K. Chang, K. C. Marr, and O. A. Ezekoye, "Experimental and Analytical Characterization of Firebrand Ignition of Home Insulation Materials," *Fire Technol.*, vol. 55, no. 3, pp. 1027–1056, May 2019, doi: 10.1007/s10694-019-00818-8.

[57] O. Matvienko, D. Kasymov, E. Loboda, A. Lutsenko, and O. Daneyko, “Modeling of Wood Surface Ignition by Wildland Firebrands,” *Fire*, vol. 5, no. 2, Apr. 2022, doi: 10.3390/fire5020038.

[58] N. Wickramasinghe and M. Khalid, “Potential of Modeling Firebrand Load on Structure in Wildland Urban Interface,” Melbourne, Australia, 2019.

[59] D. Bean and D. L. Blunck, “Sensitivities of Porous Beds and Plates to Ignition by Firebrands,” *Front. Mech. Eng.*, vol. 7, Aug. 2021, doi: 10.3389/fmech.2021.653810.

[60] J. A. Alascio and S. Stoliarov, “Firebrand Pile Thermal Characterization and Ignition Study of Firebrand Exposed Western Red Cedar,” 2021.

[61] S. D. Briles and G. A. Bennett, “Calibration procedure developed for IR surface-temperature measurements,” 1989, pp. 147–151. doi: 10.1109/stherm.1989.76082.

[62] M. Golabczak, A. Golabczak, and A. Konstantynowicz, “Calibration of infrared (IR) camera for heat generation monitoring during abrasive electrodischarge grinding,” *Materwiss. Werksttech.*, vol. 48, no. 5, pp. 335–341, May 2017, doi: 10.1002/mawe.201600756.

[63] S. L. Manzello, A. Maranghides, J. R. Shields, W. E. Mell, Y. Hayashi, and D. Nii, “Mass and size distribution of firebrands generated from burning Korean pine (Pinus koraiensis) trees,” *Fire Mater.*, vol. 33, no. 1, pp. 21–31, 2009, doi: 10.1002/fam.977.

[64] S. Suzuki and S. L. Manzello, “Investigating Conifer Tree Combustion in the Presence of an Applied Wind Field,” *Combust. Sci. Technol.*, pp. 1–18, Aug. 2022, doi: 10.1080/00102202.2022.2112034.

[65] I. T. Leventon, J. Li, and S. I. Stoliarov, “A Flame Spread Simulation Based on a Comprehensive Solid Pyrolysis Model Coupled with a Detailed Empirical Flame Structure Representation,” *Combust. Flame*, vol. 162, no. 10, pp. 3884–3895, Oct. 2015, doi: 10.1016/j.combustflame.2015.07.025.

[66] R. Ross, “Wood Handbook: Wood as an Engineering Material,” 2021.

[67] K. Kruse, C. Dai, and A. Pielasch, “An analysis of strand and horizontal density distributions in oriented strand board (OSB).”

[68] F. Incorpera, D. De Witt, T. Bergman, and A. Lavine, *Fundamentals of heat and mass transfer*, 6th ed. John Wiley & Sons, Inc, 2007.

[69] M. E. Alexander and M. G. Cruz, “Evaluating a model for predicting active

crown fire rate of spread using wildfire observations," *Can. J. For. Res.*, vol. 36, no. 11, pp. 3015–3028, Nov. 2006, doi: 10.1139/X06-174.

[70] H. Biteau *et al.*, "Calculation methods for the Heat Release Rate of Materials of unknown Composition," in *Fire Safety Science*, 2008, pp. 1165–1176. doi: 10.3801/IAFSS.FSS.9-1165.

[71] A. Tewarson, Ed., *SFPE Handbook of Fire Protection Engineering*, 2nd ed. Quincy, MA: The National Fire Protection Association Press, 1995.

[72] L. W. A. Chen *et al.*, "Emissions from Laboratory Combustion of Wildland Fuels: Emission Factors and Source Profiles," *Environ. Sci. Technol.*, vol. 41, no. 12, pp. 4317–4325, Jun. 2007, doi: 10.1021/es062364i.

[73] M. B. McKinnon and S. I. Stoliarov, "Pyrolysis Model Development for a Multilayer Floor Covering," *Materials*, vol. 8. pp. 6117–6153, 2015. doi: 10.3390/ma8095295 LK - https://umaryland.on.worldcat.org/oclc/7181568169.

[74] J. G. Quintiere, *Fundementals of Fire Phenomena*. Chichester, England: John Wiley, 2006.

[75] S. R. Turns, *An Introduction to Combustion: Concepts and Applications,* 3rd ed. New York: McGraw-Hill, 2012.

[76] S. Suzuki and S. L. Manzello, "Investigating the Effect of Structure to Structure Separation Distance on Firebrand Accumulation," *Front. Mech. Eng.*, vol. 6, Jan. 2021, doi: 10.3389/fmech.2020.628510.

[77] S. Stoliarov, I. Leventon, and R. Lyon, "Two-Dimensional Model of Burning for Pyrolyzable Solids," 2013.

[78] S. I. Stoliarov, S. Crowley, R. N. Walters, and R. E. Lyon, "Prediction of the burning rates of charring polymers," *Combust. Flame*, vol. 157, no. 11, pp. 2024–2034, 2010, doi: 10.1016/j.combustflame.2010.03.011.

[79] S. I. Stoliarov, S. Crowley, R. E. Lyon, and G. T. Linteris, "Prediction of the burning rates of non-charring polymers," *Combust. Flame*, vol. 156, no. 5, pp. 1068–1083, May 2009, doi: 10.1016/j.combustflame.2008.11.010.

[80] J. Li, J. Gong, and S. I. Stoliarov, "Development of pyrolysis models for charring polymers," *Polym. Degrad. Stab.*, vol. 115, pp. 138–152, 2015, doi: 10.1016/j.polymdegradstab.2015.03.003.

[81] J. Li, J. Gong, and S. I. Stoliarov, "Gasification experiments for pyrolysis model parameterization and validation," *Int. J. Heat Mass Transf.*, vol. 77, pp. 738–744, 2014, doi: 10.1016/j.ijheatmasstransfer.2014.06.003.

[82] M. B. McKinnon, Y. Ding, S. I. Stoliarov, S. Crowley, and R. E. Lyon, "Pyrolysis model for a carbon fiber/epoxy structural aerospace composite," *J. Fire Sci.*, vol. 35, no. 1, pp. 36–61, Jan. 2017, doi: 10.1177/0734904116679422.

[83] J. Gong, H. Zhu, H. Zhou, and S. I. Stoliarov, "Development of a pyrolysis model for oriented strand board. Part I: Kinetics and thermodynamics of the thermal decomposition," *J. Fire Sci.*, vol. 39, no. 2, pp. 190–204, Mar. 2021, doi: 10.1177/0734904120982887.

[84] J. Gong, H. Zhou, H. Zhu, C. G. McCoy, and S. I. Stoliarov, "Development of a pyrolysis model for oriented strand board: Part II—Thermal transport parameterization and bench-scale validation," *J. Fire Sci.*, vol. 39, no. 6, pp. 477–494, 2021, doi: 10.1177/07349041211036651.

[85] G. J. Fiola, D. M. Chaudhari, and S. I. Stoliarov, "Comparison of Pyrolysis Properties of Extruded and Cast Poly(methyl methacrylate)," *Fire Saf. J.*, p. 103083, 2020, doi: https://doi.org/10.1016/j.firesaf.2020.103083.

[86] J. Li and S. I. Stoliarov, "Measurement of kinetics and thermodynamics of the thermal degradation for non-charring polymers," *Combust. Flame*, vol. 160, no. 7, pp. 1287–1297, Jul. 2013, doi: 10.1016/j.combustflame.2013.02.012.

[87] A. Atreya, P. Olszewski, Y. Chen, and H. R. Baum, "The effect of size, shape and pyrolysis conditions on the thermal decomposition of wood particles and firebrands," *Int. J. Heat Mass Transf.*, vol. 107, pp. 319–328, Apr. 2017, doi: 10.1016/j.ijheatmasstransfer.2016.11.051.

[88] K. Y. Li, X. Huang, C. Fleischmann, G. Rein, and J. Ji, "Pyrolysis of medium-density fiberboard: Optimized search for kinetics scheme and parameters via a genetic algorithm driven by Kissinger's method," *Energy and Fuels*, vol. 28, no. 9, pp. 6130–6139, 2014, doi: 10.1021/ef501380c.

[89] J. Ira, L. Hasalová, V. Šálek, M. Jahoda, and V. Vystrčil, *Thermal Analysis and Cone Calorimeter Study of Engineered Wood with an Emphasis on Fire Modeling*, vol. 56, no. 3. 2020. doi: 10.1007/s10694-019-00922-9.

[90] A. International, "Standard Test Method for Determining Flammability Characteristics of Plastics and Other Solid Materials Using Microscale Combustion Calorimetry." doi: https://doi-org.proxy-um.researchport.umd.edu/10.1520/D7309-20.

[91] J. D. Swann, Y. Ding, M. B. McKinnon, and S. I. Stoliarov, "Controlled atmosphere pyrolysis apparatus II (CAPA II): A new tool for analysis of pyrolysis of charring and intumescent polymers," *Fire Saf. J.*, vol. 91, pp. 130–139, Jul. 2017, doi: 10.1016/j.firesaf.2017.03.038.

[92] O. Korobeinichev *et al.*, “An experimental study of horizontal flame spread over PMMA surface in still air,” *Combust. Flame*, vol. 188, pp. 388–398, Feb. 2018, doi: 10.1016/j.combustflame.2017.10.008.

[93] J. D. Swann, Y. Ding, and S. I. Stoliarov, “A quantitative comparison of the pyrolysis and combustion behavior of plasticized and rigid poly(vinyl chloride) using two-dimensional modeling,” *Fire Saf. J.*, vol. 111, p. 102910, 2020, doi: https://doi.org/10.1016/j.firesaf.2019.102910.

[94] C. Lautenberger and C. Fernandez-Pello, “A model for the oxidative pyrolysis of wood,” *Combust. Flame*, vol. 156, no. 8, pp. 1503–1513, 2009, doi: 10.1016/j.combustflame.2009.04.001.

[95] J. V Beck, “Surface Heat Flux Determination using an Integral Method,” 1968.

[96] K. Strąk, B. Maciejewska, and M. Piasecka, “The heat transfer coefficient determination with the use of the Beck-Trefftz method in flow boiling in a minichannel,” *EPJ Web Conf.*, vol. 180, p. 02099, 2018, doi: 10.1051/epjconf/201818002099.

[97] A. International, “Standard Test Method for Heat and Visible Smoke Release Rates for Materials and Products Using an Oxygen Consumption Calorimeter.” doi: https://doi-org.proxy-um.researchport.umd.edu/10.1520/E1354-17.

[98] C. G. McCoy, J. L. Tilles, and S. I. Stoliarov, “Empirical Model of flame heat feedback for simulation of cone calorimetry,” *Fire Saf. J.*, vol. 103, pp. 38–48, Jan. 2019, doi: 10.1016/j.firesaf.2018.11.006.

[99] S. Suzuki and S. L. Manzello, “Experimental investigation of firebrand accumulation zones in front of obstacles,” *Fire Saf. J.*, vol. 94, pp. 1–7, Dec. 2017, doi: 10.1016/j.firesaf.2017.08.007.

[100] J. A. De Beer, J. A. Alascio, S. I. Stoliarov, and M. J. Gollner, “Analysis of the thermal exposure and ignition propensity of a lignocellulosic building material subjected to a controlled deposition of glowing firebrands,” *Fire Saf. J.*, vol. 135, Feb. 2023, doi: 10.1016/j.firesaf.2022.103720.

[101] D. T. A.-T. T.- Drysdale, “An introduction to fire dynamics LK - https://umaryland.on.worldcat.org/oclc/759865320.” Wiley, Chichester, West Sussex, 2011. [Online]. Available: http://www.books24x7.com/marc.asp?bookid=46817

[102] C. Bamford, J. Crank, D. Malan, and A. Wilson, “The combustion of wood: Part I,” *Proc. Camb. Philol. Soc.*, vol. 42, no. 2, p. 166, 1946.

[103] D. J. Rasbash, D. D. Drysdale, and D. Deepak, “Critical heat and mass transfer

at pilot ignition and extinction of a material," *Fire Saf. J.*, vol. 10, no. 1, pp. 1–10, 1986, doi: 10.1016/0379-7112(86)90026-3.

[104] F. V. Lundström, P. B. Sunderland, J. G. Quintiere, P. van Hees, and J. L. de Ris, "Study of ignition and extinction of small-scale fires in experiments with an emulating gas burner," *Fire Saf. J.*, vol. 87, no. October 2016, pp. 18–24, 2017, doi: 10.1016/j.firesaf.2016.11.003.

[105] D. Rich, C. Lautenberger, J. L. Torero, J. G. Quintiere, and C. Fernandez-Pello, "Mass flux of combustible solids at piloted ignition," *Proc. Combust. Inst.*, vol. 31 II, pp. 2653–2660, 2007, doi: 10.1016/j.proci.2006.08.055.

[106] R. E. Lyon and J. G. Quintiere, "Criteria for piloted ignition of combustible solids," *Combust. Flame*, vol. 151, no. 4, pp. 551–559, 2007, doi: 10.1016/j.combustflame.2007.07.020.

[107] P. L. Andrews, "The Rothermel Surface Fire Spread Model and Associated Developments: A Comprehensive Explanation," 2018.